LAND - ATMOSPHERE COUPLING IN CLIMATE MODELS OVER NORTH AMERICA; UNDERSTANDING INTER-MODEL DIFFERENCES

by

©Almudena García García
agarciagarci@mun.ca

A Thesis submitted to the School of Graduate Studies
in partial fulfillment of the requirements for the degree of

Doctor of Philosophy

October, 2020

Department of Environmental Science
Memorial University of Newfoundland
St. John's, Newfoundland
and Labrador, Canada

Abstract

The interactions between the lower atmosphere and the land surface are associated with weather and climate phenomena such as the duration, frequency and intensity of extreme temperature and precipitation events. Thus, the representation of land-atmosphere interactions in climate model simulations is crucial for projecting future changes in the statistics of extreme events as realistically as possible. Given the importance of the land-atmosphere interaction, the purpose of the thesis is to evaluate climate simulations performed by General Circulation Models (GCMs) and Regional Climate Models (RCMs) and examine the role of the Land Surface Model (LSM) component and the horizontal resolution over North America. For this purpose, I analyze a large set of simulations from GCMs and RCMs used by the fifth assessment report of the Intergovernmental Panel on Climate Change (IPCC) as well as my own simulations performed by the Weather Research and Forecasting (WRF) model. Results show that GCM simulations present large uncertainties in the representation of land-atmosphere interactions in comparison with observations. This work also reveals a dependence of the simulated land-atmosphere interactions on the LSM components used in regional and global simulations. Additionally, the LSM component is identified as an important source of uncertainty in the simulation of extreme temperature and precipitation events. Increasing the horizontal resolution also affects the simulation of

land-atmosphere interactions, which lead to the intensification of precipitation, evapotranspiration and soil moisture at low latitudes; that is increased latent heat flux, soil moisture, and precipitation. The impact of both factors, horizontal resolution and the LSM, is larger in summer in agreement with the summer intensification of land-atmosphere interactions reported in the literature. The comparison of model simulations and observations indicates that the use of the most comprehensive LSM component available in WRF, the Community Land Model version 4 (CLM4), leads to a better representation of temperature climatologies. In contrast, finer horizontal resolutions are associated with larger biases in the WRF simulation of precipitation climatology, due to the overestimation of precipitation in the WRF model. Due to the large effect of the LSM component on the simulation of near-surface conditions shown in this dissertation, the use of simple version of LSM component in GCMs, RCMs or reanalyses can be an important limitation in climate simulations and reanalysis products.

Acknowledgments

This thesis would not have been possible without the help of many people.

To my supervisory committee; Dr. Hugo Beltrami, who despite being very busy, always found time to advise and guide me when I needed. I admire him for his ideas, comments and suggestions that always yielded interesting conversations. Dr. Joel Finnis, who has always helped me when needed, especially during my short stay in St. John's. Dr. Sue Ziegler who has also provided me with her best advise. Thanks all of you for your guidance and support.

To my co-authors; Francisco José Cuesta Valero who has always been willing to discuss about scientific ideas and my code and English problems. Dr. Jason Smerdon for his help and countless edits of my manuscripts. He has always been very generous with his time. Dr. Fidel González Rouco and Dr. Elena García Bustamante, who in addition to help me to develop my ideas in more interesting ways, have made me feel very supported.

To all institutions and individual groups that make their code and data available; the World Climate Research Program's Working Group on Coupled Modelling, the Mesoscale and Microscale Meteorology (MMM), the National Center for atmospheric Research (NCAR), the National Oceanic and Atmospheric Administration (NOAA), the Climatic Research Unit (CRU) at the University of East Anglia, and the Oak

Ridge National Laboratory Distributed Active Archive Center (ORNL DAAC).

To my labmates and friends, for listening to me each time that I have got angry about the job and the computer, and to all the new people that I have met in Canada. Thank you for being very kind to me.

To my parents, brother, brother-in-law, sister, nice and nephew, Juan, Sole, Juan Andrés, Matías, Míriam, Diana and Alberto, and to my grandparents! Thank you for supporting me to continue my studies in a country far away from home, despite it is very difficult for you. And finally, to my partner Francisco José, thanks for your support all these years.

Contents

List of Tables

List of Figures

List of Abbreviations

CE Common Era.

CMIP5 5^{th} phase of the Coupled Model Intercomparison Project.

CMIP6 6^{th} phase of the Coupled Model Intercomparison Project.

CO_2 Carbon Dioxide.

CORDEX Coordinated Regional climate Downscaling Experiment.

CRU Climatic Research Unit.

DAYMET Daily Surface Weather Data.

DJF December, January and February.

ESM Earth System Model.

ETCCDI Expert Team on Climate Change Detection and Indices.

GCM General Circulation Model.

GHF Ground Heat Flux.

GLACE Global Land-Atmosphere Coupling Experiment.

GMT Generic Mapping Tools.

GST Ground Surface Temperature.

HFX Sensible Heat flux.

IPCC Intergovernmental Panel on Climate Change.

JJA June, July and August.

LAI Leaf Area Index.

LH Latent Heat flux.

LNET Net Longwave radiation.

LS3MIP Land Surface Snow and Soil Moisture Model Intercomparison Project.

LSM Land Surface Model.

MAM March, April and May.

NA North America.

NARR North American Regional Reanalysis.

PILPS Programme for Intercomparison of Land-surface Parametrization Schemes.

PR Precipitation Rate.

PRE accumulated precipitation.

RCM Regional Climate Model.

RCP Representative Concentration Pathway.

RMSE Root Mean Square Error.

RNET Net Radiation.

SAT Surface Air Temperature.

SM Soil Moisture.

SNET Net Shortwave radiation.

SNW Surface Snow Amount.

SON September, October and November.

ST Surface Temperature.

TASMAX daily maximum SAT.

TASMIN daily minimum SAT.

US United States.

VAC Vegetation-Atmosphere Coupling

WRF Weather Research and Forecasting.

.

Chapter 1

Introduction

1.1 Background

Climate is changing across our planet. The current difference between the incoming and outgoing shortwave and longwave radiation has been leading to a small positive energy imbalance that increases the global heat content of the Earth's system (Hansen et al., 2005, 2011). The Earth's energy imbalance is affected by both natural and human forcings (Hansen et al., 2005). For example, natural fluctuations in solar activity and volcanic eruptions influence the energy imbalance by changing the incoming and outgoing radiation (Trenberth et al., 2014). Human activities are responsible for this energy imbalance through emissions of greenhouse gasses and aerosols, which influence atmospheric chemistry and lead to changes in the absorbed, scattered and reflected radiation. Additionally, human activities can modify the Earth's energy imbalance, for example modifying surface albedo through changes in vegetation, land surface properties, snow cover and sea ice (Cubasch et al., 2013).

The Earth's energy imbalance influences weather and climate processes with important consequences for the environment and society. Examples are the changes in probability of occurrence, duration and intensity of temperature and precipitation

extremes (Hartmann et al., 2013). Regional Climate Models (RCMs) and General Circulation Models (GCMs) are currently the most useful tools available for the future projection and study of climate change. These tools allow us to explore ways human activities affect the Earth's climate and to project this knowledge into the future in order to provide information for mitigation and adaptation strategies. Climate models are becoming more sophisticated over time, improving their representation of the Earth's climate and producing useful information about climate change. Climate models used by the fifth Assessment Report of the Intergovernmental Panel on Climate Change (IPCC) include numerous model components to simulate climate dynamics (Taylor et al., 2012). These climate models typically include an atmospheric model component, an ocean model component and a Land Surface Model (LSM) component, among others (e.g. components responsible for the simulation of the cryosphere and the carbon cycle). Although the new generation of climate models have shown improvements in the representation of the Earth's climate subsystems, the uncertainty in their climate projections is still large (Flato et al., 2013).

The interactions between the lower atmosphere and the land surface determine the strength of land-atmosphere coupling, whose representation in climate models is currently attracting considerable interest among scientists. The lower atmosphere and the land surface are hydrologically and energetically coupled, thus land surface variations in temperature, moisture, albedo, etc., affect and are affected by atmospheric processes acting on daily to seasonal scales through exchanges of water and energy (Bonan, 1995; Lawrence et al., 2007; Phillips et al., 2014; Smerdon et al., 2004, 2006a). For instance, variations in surface heat fluxes induced by soil moisture availability yield variations in precipitation (Koster et al., 1995; Wang et al., 2010a). Additionally, other exchanges take place at the land surface, such as exchanges of matter in the form of gasses related to biogeochemical cycles, which also alter weather

and climate evolution (Lawrence et al., 2007; Schuur et al., 2001; Skopp et al., 1990; Stark et al., 1995).

Land-atmosphere coupling has been associated with changes in the mean state of several variables, but also in their variability, and in the probability, magnitude, and duration of temperature and precipitation extremes (Guo et al., 2013; Hirschi et al., 2011; Lorenz et al., 2015). Some specific events that have been related to changes in land-atmosphere interactions are: the Dust Bowl drought in the United States (US) (Hu et al., 2018b), the 2003 European heat wave (Fischer et al., 2007) and the 2010 Russian Heatwave (Hauser et al., 2016). Due to the strong effect of land-atmosphere interactions on the climate system, the representation of land-atmosphere coupling has been employed as a criterion for the evaluation of climate model performance (Dirmeyer et al., 2006a; Ferguson et al., 2012; Henderson-Sellers et al., 1995; Knist et al., 2016; Koster et al., 2006b; Seneviratne et al., 2013). However, evaluating climate models using metrics based on land-atmosphere coupling is difficult due to the challenges of measuring land-atmosphere interactions and the lack of observational data above and below the ground surface useful for the evaluation of land-atmosphere interactions (Guo et al., 2006; Seneviratne et al., 2008; Seneviratne et al., 2010).

1.1.1 Water and energy balance at the surface

The coupling between the land surface and the lower atmosphere is driven by the water and energy balance at the air-ground interface. The water balance (Figure 1.1) for a surface soil layer without lateral water exchanges can be represented by:

$$\frac{dS}{dt} = PRE - E - Q, \tag{1.1}$$

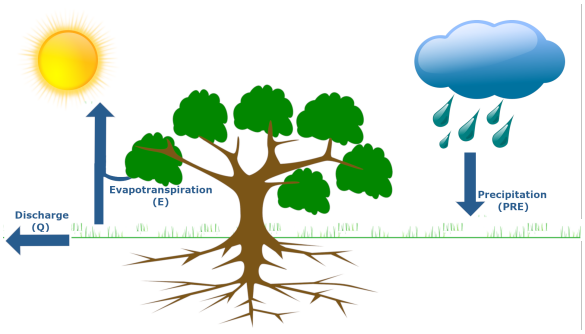

Figure 1.1: Components of the water balance at the surface for an infinitesimally small ground surface layer. PRE is precipitation, E is evapotranspiration from soils and vegetation, and Q is river discharge including surface runoff and groundwater flow.

where $\frac{dS}{dt}$ is the change in water content within the surface soil layer (soil moisture, surface water, snow, ice and ground water). PRE is precipitation, Q is the river discharge (surface runoff and groundwater flow), and E is evapotranspiration, including soil evaporation, vegetation evaporation, vegetation transpiration, snow sublimation and evaporation from surface water (Seneviratne et al., 2010; Wang et al., 2012a). The term $\frac{dS}{dt}$ tends to zero for an infinitesimally small soil layer at annual and longer time scales, however, its value may not always be negligible depending on the region (Hobbins et al., 2001; Teuling et al., 2009; Wang et al., 2012a).

The energy balance for a similar surface soil layer can be represented by:

$$\frac{dH}{dt} = RNET - LH - HFX - GHF, \tag{1.2}$$

where $\frac{dH}{dt}$ is the energy variation within the surface soil layer, including terms associated with the soil water content, such as temperature change, phase changes from freezing or melting soils and from snow melting systems. RNET is the net radiation absorbed by soil defined as the sum of incident downward and upward shortwave ($S\downarrow - S\uparrow$) and longwave ($L\downarrow - L\uparrow$) radiation (Equation 1.3).

$$RNET = S\downarrow - S\uparrow + L\downarrow - L\uparrow . \tag{1.3}$$

LH in Equation 1.2 is the latent heat flux, defined as the energy used in evapotranspiration (E in Equation 1.1). HFX is the sensible heat flux and GHF is the ground heat flux to deeper soil layers. These surface fluxes are given by the following equations (Bonan, 2002):

$$a)\ LH = -\frac{\rho C_p}{\gamma r_w}(e_a - e_*[T_s]), \quad b)\ HFX = -\frac{\rho C_p}{r_H}(T_a - T_s), \quad c)\ GHF = \kappa\frac{\Delta T}{\Delta z}, \tag{1.4}$$

where ρ is the density of air, which varies with temperature and humidity, C_p is the heat capacity of the air at constant pressure, γ is the psychrometric constant, which depends on C_p, pressure and the latent heat of vaporization or sublimation; r_w and r_H are resistances that depend on wind speed and surface state, e_a is the vapor pressure of air, $e_*[T_s]$ is the saturation vapor pressure at the surface temperature (T_s) and T_a is the air temperature. In the ground heat flux equation (Equation 1.4c), κ represents the thermal conductivity of the soil, varying with soil composition and water or ice content and $\frac{\Delta T}{\Delta z}$ is the temperature gradient between the surface and a soil layer at z.

The term $\frac{dH}{dt}$ from the energy balance equation tends to zero for an infinitesimally small ground surface layer at annual and longer time scales (Bonan, 2002; Seneviratne et al., 2010; Wang et al., 2012a). Thus, the energy balance at the surface can be described as shown in Figure 1.2. Additionally, the reflected shortwave radiation ($S\uparrow$ in Equation 1.3) is equal to $\alpha S\downarrow$, where α is the surface albedo, while the outgoing longwave radiation ($L\uparrow$) is defined as $L\uparrow \propto \sigma T_s^4$, where T_s is surface temperature and σ is the Stefan-Boltzmann constant. The incoming longwave radiation ($L\downarrow$) includes the longwave radiation emitted from the atmosphere due to atmospheric temperature and the proportion of the outgoing longwave radiation that is reflected by atmospheric mass to the surface, due to the effect of greenhouse gases, such as water vapor and

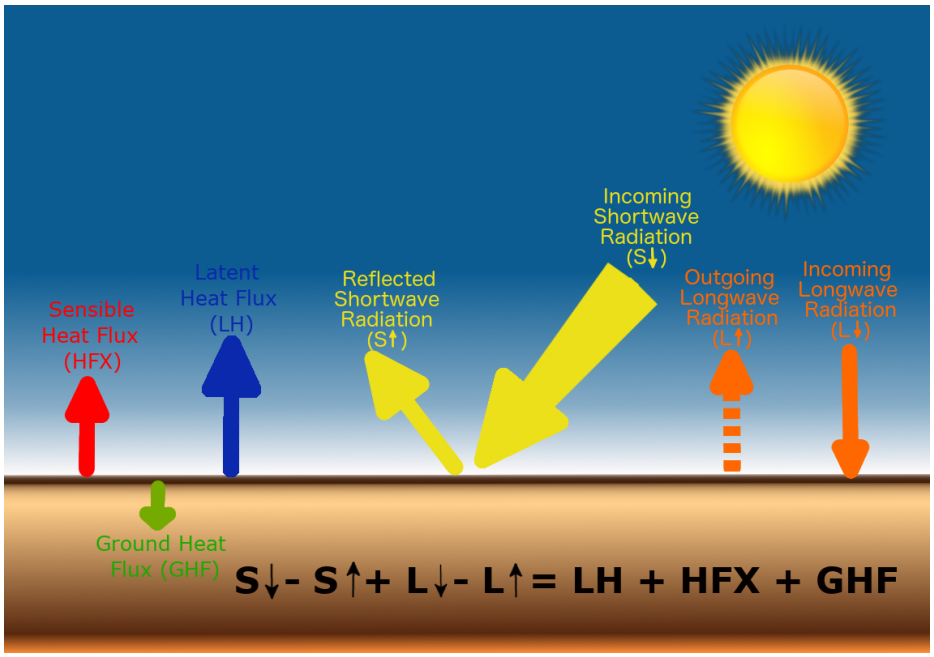

Figure 1.2: Components of the energy balance at the surface for an infinitesimally small ground surface layer. S↓, S↑ are the incident downward and upward shortwave radiation. L↓, L↑ are the incident downward and upward longwave radiation. LH is the latent heat flux, HFX is the sensible heat flux and GHF is the ground heat flux at the surface.

atmospheric Carbon Dioxide (CO_2) (Bonan, 2002; Seneviratne et al., 2010; Wang et al., 2012a).

As seen in Equations 1.1 and 1.2, the water and energy balance at the surface are coupled through the evapotranspiration (E) and latent heat flux (LH) terms. The evapotranspiration term corresponds to the water transferred from the land surface to the atmosphere through wind turbulence. This exchange of water involves a phase change of water or ice into water vapor, which absorbs energy from the soil surface (LH), leading to the cooling of the soil (Mao et al., 2015; Seneviratne et al., 2010; Wang et al., 2012a). Evapotranspiration has two limiting factors: soil water content and available energy. Variations in one of the two limiting factors determine the amount of water that is exchanged with the atmosphere and the required energy in the process, considering the given near-surface conditions and land cover. Variations in

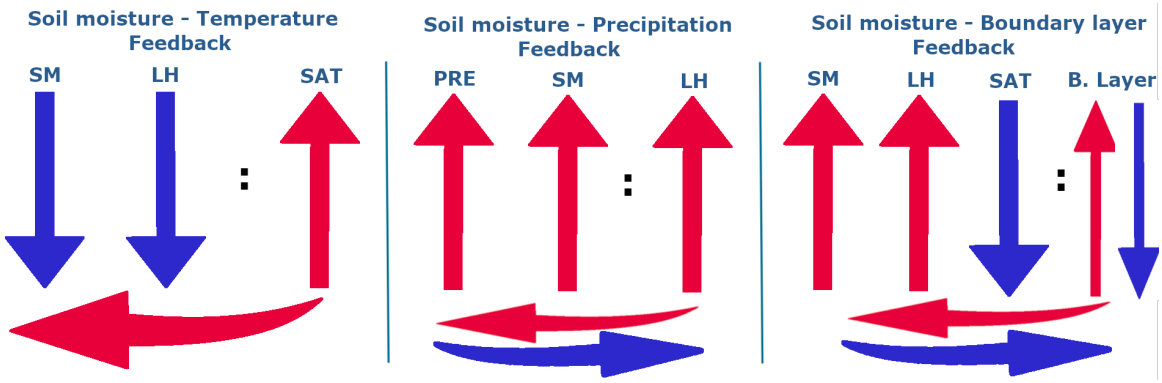

Figure 1.3: Soil moisture - climate feedbacks: soil moisture - temperature feedback (left), a decrease in soil moisture limits latent heat flux affecting the partition of energy into latent and sensible heat flux, and therefore affecting surface temperatures. Soil moisture - Precipitation (center), an increase in precipitation leads to an increase in soil moisture enhancing latent heat flux and affecting the formation of clouds and precipitation. Soil moisture -Stability of the planetary boundary layer (right), the previous soil moisture feedbacks modify atmospheric conditions (temperature and water content) affecting the depth and stability of the planetary boundary layer.

soil moisture induce evapotranspiration changes in soil-moisture limited areas, while in areas where soil moisture is plentiful but available energy is the limiting factor, high (low) net radiation increases (decreases) evapotranspiration (Koster et al., 2004a; Seneviratne et al., 2006).

Soil moisture plays a key role in several weather and climate processes through its impact on the water and energy balance at the surface in soil-moisture limited regions. Studies based on observational data and models' outputs have shown the impact of soil moisture on air temperature, the stability of the atmospheric boundary layer and precipitation rates in summer (e.g. Hirschi et al., 2011; Jaeger et al., 2011; Koster et al., 2003; Santanello-Jr. et al., 2011). Our knowledge about the processes that explain soil moisture - climate feedbacks is still developing, but can be summarized in three main processes (Figure 1.3): i) soil moisture - temperature feedback: decreased soil moisture alters the surface energy balance, limiting the latent heat flux component and leading to more available energy for the sensible and ground heat fluxes, induc-

ing an increase in surface air and soil temperatures. Increased temperature implies higher vapor pressure deficit and evaporative demand, leading to a potential increase in evapotranspiration and possibly a further decrease in soil moisture, closing the loop of soil moisture and surface air temperature (Berg et al., 2015; Herold et al., 2016; Hirsch et al., 2014b; Jaeger et al., 2011; Lorenz et al., 2016). ii) Soil moisture - precipitation feedback (i.e. moisture recycling): higher precipitation rates at the surface lead to higher soil moisture anomalies in unsaturated soils when infiltration is possible. Higher soil moisture can lead to higher evapotranspiration in areas where soil moisture is the limiting factor (Cook et al., 2006; Koster et al., 2003, 2004a; Lorenz et al., 2016). However, a negative relationship between soil moisture and evapotranspiration can also be found, because increasing evapotranspiration decreases soil moisture. The final change in evapotranspiration resulting from these competing processes will affect precipitation rates (Seneviratne et al., 2010). Some studies employing climate models have reported a correlation between soil-moisture/evapotranspiration and precipitation, which may be positive or negative depending on the region (Ek et al., 2004; Hohenegger et al., 2009). iii) Soil moisture - stability of the atmospheric boundary layer feedback: soil moisture locally affects the growth and entrainment of the atmospheric boundary layer by moistening/drying and cooling/heating the lower atmosphere through changes in the energy partition at the surface (Santanello-Jr. et al., 2007). Also, changes in the atmospheric boundary layer's depth and state may lead to the formation or disappearance of clouds, inducing variations in precipitation and affecting the water and ice content of soils, which can alter soil moisture recycling (Ek et al., 2004; Santanello-Jr. et al., 2007, 2011). In addition to the soil moisture impact on climate, soil moisture anomalies have been related to biogeochemical cycles, such as the carbon and nitrogen cycles, through relationships with vegetation transpiration, photosynthesis, and microbial activities (Dirmeyer et al., 2006b; Lawrence

et al., 2007; Schuur et al., 2001; Skopp et al., 1990; Stark et al., 1995).

The available energy at the surface can be limited by changes in surface albedo, leading to variations in the outgoing shortwave radiation. Several processes lead to changes in surface albedo, e.g. variations in the water content of the soil, changes in land cover and land uses. A high albedo increases the outgoing shortwave radiation at the surface, limiting the energy available for moistening and heating the lower atmosphere by latent and sensible heat fluxes, and therefore, limiting soil moisture impact on temperature, precipitation and stability of the atmospheric boundary layer (Ban-Weiss et al., 2011; Lejeune et al., 2017; Wild et al., 2015).

Other surface processes affect the water and energy balance, such as variations in wind speed and direction or the presence of dust in the lower atmosphere. Changes in land cover and land uses vary surface roughness, which leads to changes in the direction and velocity of wind. These wind changes influence the energy partition at the surface by altering soil moisture content and latent and sensible heat fluxes (see Equation 1.4a and 1.4b), therefore, limiting the water and energy exchanges between the lower atmosphere and the shallow subsurface (Wild et al., 2010; Zhou et al., 2016a). Dust also influences the radiation budget and precipitation by direct and indirect effects on the surface energy budget (Cook et al., 2008; Solmon et al., 2008). Dust absorbs and scatters the incoming solar radiation, limiting the net radiation absorbed by the soil, and the energy available for evapotranspiration. The dust-induced limitation in evapotranspiration may affect precipitation by the feedbacks described above.

1.1.2 Impacts of land surface processes on land-atmosphere interactions

As mentioned above, land surface processes alter the water and energy balance at the surface, i.e. land-atmosphere interactions, through changes in near-surface soil and air conditions (temperature, soil moisture, radiation, etc.) and land properties (roughness, albedo, dust, etc.). During the last decade, vegetation cover has received much attention due to its effect on land-atmosphere interactions. Changes in vegetation cover, such as deforestation, modify the carbon cycle due to a reduction of photosynthesis activity and the return of stored carbon to the ground and the atmosphere as material decays and burns. Additionally, vegetation activity alters the water and energy exchanges between the shallow subsurface and the lower atmosphere by changing albedo, evapotranspiration and surface roughness (Krinner et al., 2005). The effect of changes in vegetation on climate varies geographically and temporally, depending on the type of land cover; grass, forest, agriculture terrains, etc. The effect of deforestation and afforestation on climate at local and regional scales as well as at different temporal scales from monthly to centennial has been studied using satellite data and climate models (Garnaud et al., 2015; Li et al., 2016; Pu et al., 2012; Wilhelm et al., 2015). These studies have reported a latitudinal pattern in the impact of deforestation on temperature, inducing a warming in tropical areas and a cooling in boreal regions (Li et al., 2016). This latitudinal pattern is mainly caused by the competing effects of albedo and evapotranspiration on temperature (Pu et al., 2012; Zscheischler et al., 2015). Several studies have also shown a local impact of deforestation on annual temperature and monthly rainfall anomalies over the Amazonian basin (Lejeune et al., 2015; Lorenz et al., 2014). Usually, changes in land cover imply shifts in soil moisture regimes, thus the impact of vegetation changes on climate is often

associated with soil moisture feedbacks (Alessandri et al., 2008; Meng et al., 2014).

Snow cover influences the energy and water balance at the surface by changing surface albedo, altering the reflected solar radiation and consequently the net radiation absorbed by the ground. The decrease in energy induced by snow's high albedo affects the energy partition at the surface, decreasing the turbulent heat flux exchanges between the lower atmosphere and the ground surface (Bonan, 2002). Additionally, melting of snow and soil ice generates an energy sink in spring due to the large amount of latent heat required to freeze and thaw snow cover and soil water (Gouttevin et al., 2012; Koven et al., 2013). Snow cover acts as an insulator between the shallow subsurface and the lower atmosphere (Goodrich, 1982b; Sokratov et al., 2002). Changes in the energy partition at the surface, arising from the insulating effect of snow and the increase in soil water content caused by snow and ice melting, affect climate dynamics following the previously mentioned soil moisture - climate feedbacks (Thomas et al., 2016).

1.1.3 Land-atmosphere interactions in a changing climate

Anthropogenic activities are expected to affect numerous processes associated with land-atmosphere interactions. Changes in greenhouse gases, land cover, and land uses may lead to shifts of climate and soil moisture regimes resulting in changes in the strength and the location of areas with strong land-atmosphere coupling (Dirmeyer et al., 2012; Seneviratne et al., 2013). This in turn has been linked to variations in the mean state and variability of near-surface conditions, as well as in the frequency, intensity and duration of extreme temperature and precipitation events (Guo et al., 2013; Hirschi et al., 2011; Lorenz et al., 2015). The relationship between land-atmosphere interactions and extreme events has been demonstrated using observational data and climate model simulations in many regions of the world (Dirmeyer et al., 2013c; Koster

et al., 2003; Phillips et al., 2014; Wang et al., 2010a). For example, analyses based on observational data indicate a strong relationship between precipitation deficits and hot extremes (Hauser et al., 2016; Hirschi et al., 2011; Mueller et al., 2012) and a negative relationship between preceding soil moisture conditions and summer monthly maximum temperatures in Europe (Herold et al., 2016). The importance of soil moisture for the projections of heat waves has also been shown in modeling studies (Berg et al., 2015; Decker et al., 2015; Lorenz et al., 2016). Additionally, the strength of land-atmosphere coupling may increase under changing climate conditions, leading to intensified impacts of land use and cover changes in the future (Dirmeyer et al., 2014).

Climate model projections under different greenhouse gas emission scenarios suggest several changes in climate and soil moisture regimes around the world, which may alter land-atmosphere interactions. These shifts of climate regimes are not only induced by increased atmospheric greenhouse gas concentrations, but also by any modification of the climate system resulting in significant soil moisture changes, such as variations in aerosols concentrations due to volcanic eruptions (Mao et al., 2015; Seneviratne et al., 2006). Future shifts of climate regimes lead to changes in the location of transitional climates, and thus, to changes in the areas with strong land-atmosphere coupling (Guo et al., 2006; Koster et al., 2002). A poleward shift of climate regimes has been identified in the Northern Hemisphere consistent with the projected changes in radiation, temperature, and soil moisture (Flato et al., 2013). For example, soil-moisture shifts have been identified over Central Europe, and North Eastern United States (Flato et al., 2013). The future transitional climate zones may become areas with enhanced land-atmosphere interactions and therefore increased climate variability. However, soil moisture may both lead to an increase or decrease in climate variability, depending on the original climate regime (Seneviratne et al., 2010).

Land-atmosphere interactions have also been related to some inter-model differences and uncertainties in the simulation of climate change impacts on natural and human systems. Several studies have identified the representation and understanding of land-atmosphere interactions as key elements for climate predictability at several temporal and spatial scales, and for advances of many climate applications important for society such as seasonal forecasting and climate change modeling (Berg et al., 2015; Hirschi et al., 2014; Lorenz et al., 2016; Seneviratne et al., 2008).

1.1.4 Representation of land-atmosphere interactions within climate models

Due to the relationship between land-atmosphere interactions and climate conditions, and the expected changes in the strength and location of areas with strong land-atmosphere coupling, the representation of land-atmosphere interactions within climate models has been used as a criterion for the evaluation of climate models' performance (Dirmeyer et al., 2006a; Ferguson et al., 2012; Henderson-Sellers et al., 1995; Knist et al., 2016; Koster et al., 2006b; Seneviratne et al., 2013). Thus, previous intercomparison studies using global and regional climate models as well as assessments of model simulations against observations indicate the inter-model differences and difficulties in representing land-atmosphere interactions. However, sources leading to model uncertainties in representing land-atmosphere interactions are still unclear. The following subsections review prior analyses of climate model outputs in terms of land-atmosphere interactions.

Inter-model comparison projects

Land-atmosphere coupling within climate models is the net result of all interactions between the described processes at the air-ground interface. Therefore, the represen-

tation of land-atmosphere coupling within a climate model depends on the parameterizations of the atmosphere and LSM components, the information shared between components, and the assumptions taken to simulate near-surface processes associated with land-atmosphere interactions, such as vegetation and snow covers, soil moisture, and precipitation (Ferguson et al., 2012; Guo et al., 2006; Koster et al., 2002, 2006b; Xue et al., 2004). For example, there are large differences among models in simulating vegetation cover that may affect the representation of land-atmosphere interactions; some LSM components represent different types of vegetation at each grid-cell, allowing the evolution of vegetation with a dynamical model and the simulation of natural forest fires (e.g. Oleson et al., 2010), while other LSM components consider the dominant vegetation type at each grid-cell, simulating a constant vegetation cover with time (e.g. Tewari et al., 2004).

The number of analyses comparing the strength and location of areas with strong land-atmosphere coupling in several climate models is extensive. For instance, the world climate research Programme for Intercomparison of Land-surface Parametrization Schemes (PILPS) was developed in the 1990s to investigate the uncertainties in the behavior of LSM components and their effects on climate simulations (Henderson-Sellers et al., 1995, 1996). PILPS compared offline simulations from approximately 20 LSMs at several locations and found that although the models were forced by the same external forcing data, each LSM component yields a different surface state at inter-annual scales. In the following decade, the Global Land-Atmosphere Coupling Experiment (GLACE) (Guo et al., 2006; Koster et al., 2006b) evaluated the role of the land state in numerical weather and climate predictions using 12 different GCMs from a new generation of models. This analysis showed a large variability between GCMs while also identifying regions where land-atmosphere interactions exhibited a strong effect on climate for most of the simulations. Most recently, a new multimodel

experiment was carried out using the experimental protocol of GLACE and the general circulation models from the 5^{th} phase of the Coupled Model Intercomparison Project (CMIP5). This new experiment (GLACE-CMIP5) (Seneviratne et al., 2013) found a strong impact of soil moisture on climate variables such as temperature and precipitation, but also its contribution to the intensity, frequency and duration of extreme events (Lorenz et al., 2016; Seneviratne et al., 2013).

Currently, the research community is developing a new inter-model comparison project as part of the 6^{th} phase of the Coupled Model Intercomparison Project (CMIP6). This new project (Land Surface Snow and Soil Moisture Model Intercomparison Project (LS3MIP)), is designed to provide a comprehensive assessment of land surface, snow and soil moisture feedbacks on climate variability and climate change, and to diagnose systematic biases in LSM components used within state-of-the-art climate models (Hurk et al., 2016).

Comparison of climate model simulations and observations

Among the literature, we also find studies focused on the comparison of climate model simulations with observations. For example, Dirmeyer et al. (2006a) compared results from GLACE GCMs with observational data at a few locations and suggested that most of the GCMs used in GLACE do not represent land-atmosphere interactions accurately. However, the representation of land-atmosphere interactions for the multimodel mean of the experiments was more closely aligned with observations than individual results from the GLACE GCMs. An analysis of land-atmosphere interactions was also developed by Ferguson et al. (2012) using a set of GCMs, reanalyses and satellite data to evaluate the ability of offline simulations from LSM components and reanalysis products to reproduce the strength and location of areas with strong land-atmosphere coupling. Their results indicate that satellite data yield a substan-

tially weaker coupling over the globe relative to LSM components and reanalyses, concluding that both GCMs and reanalyses overestimate land-atmosphere coupling.

Other analyses based on model outputs and observations have related the uncertainties in climate projections to the different representation of land-atmosphere interactions within climate models (Guo et al., 2006; Seneviratne et al., 2008; Seneviratne et al., 2010). These analyses remain limited by the challenges of measuring land-atmosphere interactions and the lack of observational data above and below the ground surface. Thus, more studies comparing climate models and new observations are required to confirm the role of the different representation of land-atmosphere coupling in the uncertainties in climate projections (Orlowsky et al., 2010).

Differences in terms of land-atmosphere interactions arising from the use of General Circulation Models and Regional Climate models

GCMs and RCMs consist of model components which simulate climate subsystems. At a minimum, contemporary GCMs include an atmospheric model component, an ocean model component, a land surface model component, a sea-ice component and a component for connecting all of them ("coupler"). Thus, GCMs independently replicate atmosphere, ocean and land surface processes, as well as coupled processes limited by the simulated physics of the model components and the coupler connecting them. By contrast, most of RCMs are less complete, including an atmospheric model component and a land surface model component, therefore providing atmosphere-land coupled simulations over specific regions. Since RCMs do not perform simulations over the entire globe and over the ocean, the computational resources required for running a RCM are generally lower than for a GCM, allowing the performance of regional simulations with finer horizontal resolutions. However, climate information from GCM simulations or reanalysis products is required as initial and boundary conditions for

performing RCM simulations. Several studies have shown the importance of land-atmosphere interactions in simulating climate variability, trends and extreme events in GCM and RCM simulations (Berg et al., 2015; Jaeger et al., 2011; Jeong et al., 2014; Lorenz et al., 2016). Results from both types of climate models suggest a dependence of the represented land-atmosphere interactions on the LSM components coupled to each model (Ferguson et al., 2012; Guo et al., 2006; Koster et al., 2002, 2006b; Xue et al., 2004).

RCMs use outputs from GCMs as boundary conditions in order to increase the resolution of their climate simulations over specific regions (downscaling). Since land-atmosphere interactions have an important local component, some studies hypothesize a possible improvement in the representation of land-atmosphere interactions within RCMs due to the use of finer resolutions in their simulations in contrast to GCM simulations (see Lejeune et al., 2015 for a brief discussion). However, as far as I know there are no studies testing that hypothesis by comparing the performance of global and regional climate models using metrics based on land-atmosphere interactions.

1.2 Research Focus

The literature review included in this chapter illustrates the impact of land-atmosphere interactions on the simulation of near-surface conditions as well as the large uncertainties in the representation of land-atmosphere interactions within climate models. This thesis aims to provide new knowledge of the factors leading to discrepancies in climate model representation of land-atmosphere interactions, focusing on the following questions:

- Are land-atmosphere interactions properly represented within the global climate models used by the fifth assessment report of the IPCC?

- What factors lead to model differences in the representation of land-atmosphere interactions? Do they also contribute to uncertainties in near-surface conditions?

- How does horizontal resolution affect the representation of land-atmosphere interactions within climate models? Are land-atmosphere interactions better represented within RCMs than within GCMs due to the use of finer horizontal resolution?

Answering these research questions has been the focus of investigation in the three scientific articles included in Chapters 2, 3, and 4. Each article/chapter provides information on a particular research question. The objectives of these studies are detailed below.

1.2.1 Manuscript 1: Characterization of air and ground temperature relationships within the CMIP5 historical and future climate simulations

This article presents the evaluation of the CMIP5 climate model simulations, using a metric based on the representation of land-atmosphere interactions. This metric focusses on the thermal component of land-atmosphere interactions, and is defined as the difference between soil and air temperatures. The relationship between air and ground temperatures results from the solution of the water and energy balance at the surface, and depends on the processes that take place at the surface. The use of this simple metric allows the evaluation of model simulations against meteorological observations over North America, providing information about the ability of climate models to reproduce the relationship between air and soil temperatures. Additionally, this article examines the factors leading to model differences, identifying the LSM

component and the associated representation of land cover as possible contributors to model uncertainties.

1.2.2 Manuscript 2: Land Surface Model influence on the simulated climatologies of temperature and precipitation extremes in the WRF v.3.9 model over North America

The research presented in Manuscript 1 suggests that the LSM component is the main factor leading to GCM differences in the representation of the thermal component of land-atmosphere interactions. Since this article used GCM climate simulations provided by the CMIP5 project, the large number of structural differences and similarities between this set of GCMs prevented the attribution of model differences to the LSM component, thus presenting this result as an hypothesis in the manuscript. Manuscript 2 explores this hypothesis and examines possible implications for the simulation of extreme temperature and precipitation events. For this purpose, I designed a modeling experiment using an RCM to perform a set of simulations that only differ in the LSM component used. This modeling approach allows the identification and LSM-attribution of uncertainties in the simulation of land-atmosphere interactions and extreme events. Additionally, the uncertainties arising from the LSM component are compared with the uncertainties in a set of RCM simulations participating in the Coordinated Regional climate Downscaling Experiment (CORDEX) project, enabling the study of the applicability of these results to other model ensembles.

1.2.3 Manuscript 3: Effect of horizontal resolution on near-surface climate in the WRF v3.9 model over North America

Previous works on the representation of land-atmosphere interactions within climate models suggest that the simulation of energy and water exchanges between the lower atmosphere and soil surface may be better represented in RCM simulations than in GCM simulations, due to the associated increase in horizontal resolution and the more detailed representation of complex topography. The main objective of Manuscript 3 is to test that hypothesis, evaluating the effect of increasing horizontal resolution on the climatology of the surface energy balance and therefore on the climatology of near-surface conditions. Additionally, the influence of horizontal resolution on the energy balance is tested using different LSM components. Thereby, this manuscript presents the analysis of simulations with different horizontal resolutions and LSM components performed by the same RCM, allowing the comparison of uncertainties arising from the LSM choice and from horizontal resolution separately. The comparison of this set of simulations with observations of near-surface conditions allows to identify the contribution of these two factors to the bias in climate simulations.

1.3 Co-Authorship Statement

The manuscript included in Chapter 2 and entitled "Characterization of Air and Ground Temperature Relationships within the CMIP5 Historical and Future Climate Simulations" was published in *Journal of Geophysical Research: Atmosphere* and co-authored by F.J. Cuesta-Valero (Memorial University of Newfoundland - St. Francis Xavier University), H. Beltrami (St. Francis Xavier University), and J.E. Smerdon

(Columbia University). The research question studied in this manuscript arose from a conversation with all the authors. As the principal author, I was responsible for reviewing the literature, obtaining the data from the available archives indicated on the text, analyzing the data, presenting and interpreting the results, and writing the manuscript. The co-authors gave guidance in the interpretation of results, and reviewed the written manuscript several times before submission. The manuscript was critically reviewed by four anonymous reviewers. I was responsible for replying the reviewers comments and for modifying the manuscript accordingly, obtaining feedback from my co-authors.

The manuscript included in Chapter 3 entitled "Land Surface Model influence on the simulated climatologies of temperature and precipitation extremes in the WRF v.3.9 model over North America" was submitted to *Geocientific Model Development* and co-authored by F.J. Cuesta-Valero (Memorial University of Newfoundland - St. Francis Xavier University), H. Beltrami (St. Francis Xavier University), J.F. González-Rouco (Universidad Complutense de Madrid), E. García-Bustamante (Research Center for Energy, Environment and Technology, CIEMAT), and J. Finnis (Memorial University of Newfoundland). The research question included in this manuscript arose from the results of the article included in Chapter 2, as an experiment to test its main hypothesis. Thus, I was responsible for designing the modeling experiment, installing the RCM on the server, downloading the required data, performing the model simulations, analyzing the data, presenting and interpreting the results, and writing the manuscript. The co-authors gave guidance in the interpretation of results, and reviewed the written manuscript several times before submission.

The manuscript included in Chapter 4 entitled "Effect of horizontal resolution on near-surface climate in the WRF v3.9 model over North America" is in preparation for submission and co-authored by F.J. Cuesta-Valero (Memorial University of Newfound-

land - St. Francis Xavier University), and H. Beltrami (St. Francis Xavier University). As in the case of the second article, the research question examined here, arose from the results included in Chapter 2 and Chapter 3. Thus, I was responsible for designing the modeling experiment, downloading the required code and data, performing the model simulations, analyzing the data, presenting and interpreting the results, and writing the manuscript. The co-authors gave guidance in the interpretation of results, and reviewed the written manuscript.

1.4 Thesis Overview

This thesis is prepared in manuscript format, thus the thesis research is divided into three main chapters, which correspond to three articles that have either been published, submitted, or in preparation for publication. The first chapter includes a general introduction to the topic and the literature review of previous works in this area of expertise. The second chapter presents the contents of the published article entitled, "Characterization of Air and Ground Temperature Relationships within the CMIP5 Historical and Future Climate Simulations". The third chapter is constituted by the contents included in the article entitled, "Land Surface Model influence on the simulated climatologies of temperature and precipitation extremes in the WRF v.3.9 model over North America", which has been already submitted to a peer-review scientific journal. The fourth chapter contains the third manuscript included in this thesis, in preparation for submission and entitled, "Effect of horizontal resolution on near-surface climate in the WRF v3.9 model over North America". The tables and figures included in the supplementary information of each article are presented in separate appendices: Appendix A for Chapter 2, Appendix B for Chapter 3, and Appendix C for Chapter 4. The fifth chapter of this thesis summarized the conclusions

reached in the three presented studies and includes a discussion about implications of the research and possible future working lines. Each chapter associated with scientific articles includes an individual bibliography, while a general bibliography is presented at the end of the document.

Chapter 2

Characterization of Air and Ground Temperature Relationships within the CMIP5 Historical and Future Climate Simulations

This chapter is based on the contents of the published article:

García-García, A. et al. (2019). Characterization of Air and Ground Temperature Relationships within the CMIP5 Historical and Future Climate Simulations. *Journal of Geophysical Research: Atmospheres*(124), 3903–3929. DOI: https://doi.org/10.1029/2018JD030117

Abstract

The relationships between air and ground surface temperatures across North America are examined in the historical and future projection simulations from 32 General Circulation Models (GCMs) included in the 5^{th} phase of the Coupled Model Intercomparison Project (CMIP5). The difference between surface air (approx. 2 m) and ground surface (10 cm) temperatures is affected by simulated snow cover, vegetation cover and precipitation by means of changes in soil moisture and soil properties. In winter, the differences between air and ground surface temperatures, for all CMIP5 simulations, are related to the insulating effect of snow cover and soil freezing phenomena. In summer, large Leaf Area Index (LAI) and large precipitation rates correspond to smaller differences between air and ground temperatures for the majority of simulations, likely due to induced changes in latent and sensible heat fluxes at the ground surface. Our results show that the representation of air-ground coupling, analyzed using the difference between ground and air surface temperatures as a metric, differs from observations, the North American Regional Reanalysis (NARR) product and among the CMIP5 GCM simulations. The CMIP5 models differ by amounts that depend on the employed land-surface model. The large variability among GCMs and the marked dependence of the results on the choice of the land-surface model illustrate the need for improving the representation of processes controlling the coupling of the lower atmosphere and the land surface in GCMs as a mean of reducing the variability in their representation of weather and climate phenomena.

2.1 Introduction

The land surface and the lower atmosphere are hydrologically and energetically coupled. Atmospheric variations directly alter soil conditions through changes in temperature, precipitation, and moisture. Meanwhile, soil moisture and temperature also affect surface fluxes at daily to seasonal scales. For example, variations in surface fluxes induced by soil moisture anomalies yield variations in precipitation (Koster et al., 1995; Ruiz-Barradas et al., 2005; Schlosser et al., 2002; Wei et al., 2010; Welty et al., 2018). Other near-surface processes also influence atmospheric phenomena, such as the influence of dust on the radiation budget and precipitation by absorption and scattering of incoming solar radiation (Cook et al., 2008; Solmon et al., 2008). For the purpose of this study, we will refer to the collection of these interacting processes between the land and atmosphere as air-ground coupling. The degree of air-ground coupling has been associated with the evolution of meteorological phenomena such as the duration and intensity of heat waves, droughts, heavy precipitation episodes, and other extreme events (Fischer et al., 2007; Ruiz-Barradas et al., 2005; Seneviratne et al., 2006; Seneviratne et al., 2010; Zhang et al., 2008a). These phenomena exert a strong socioeconomic impact on society, highlighting the importance of understanding air-ground coupling for assessments of the effect of climate change on these extremes (Seneviratne et al., 2006). Air-ground coupling has also been identified as a determining factor for the evolution of temperature-dependent soil processes, such as changes in ground heat content (Cuesta-Valero et al., 2016), and permafrost and soil carbon stability (Koven et al., 2013).

General Circulation Models (GCMs) and Regional Climate Models (RCMs) have been used for studying the effects of air-ground coupling on climate dynamics, finding a relationship between air-ground coupling and precipitation anomalies in Africa,

North America, India, and Europe (Cook et al., 2006; Dirmeyer et al., 2009; Guo et al., 2006; Jaeger et al., 2011; Koster et al., 2004, 2006b; Seneviratne et al., 2008; Zeng et al., 2010). Additionally, previous studies have shown a relationship between air-ground coupling and surface temperature, mostly associated with changes in warm temperature extremes or summer temperature variability, in the above mentioned regions, eastern China, Europe, Australia, and Russia (Fischer et al., 2007; Hauser et al., 2016; Hirsch et al., 2014; Koster et al., 2006a,b; Seneviratne et al., 2008; Seneviratne et al., 2006; Zhang et al., 2008b). The coupling between the land and atmosphere within GCMs and RCMs is the net result of all the interactions between the described processes at the air-ground interface. The degree of air-ground coupling within a climate model is therefore dependent on the parameterizations of the atmosphere and land-surface models and the manner in which they are coupled (Ferguson et al., 2012; Guo et al., 2006; Koster et al., 2002, 2006b; Xue et al., 2004). The simulation of near-surface processes also affects air-ground coupling by increasing or decreasing energy and water exchanges between the land surface and the lower atmosphere. For example, snow cover acts as an insulating layer, decreasing the exchange of energy between the ground and atmosphere (Broxton et al., 2017; Zhang, 2005), while vegetation cover enhances evapotranspiration, which increases the surface energy and water exchanges (Bonan, 2002). Precipitation increases the water content of the soil, enhancing evapotranspiration when energy is not a limitation and cooling the ground, particularly in summer (Lin et al., 2003; Seneviratne et al., 2010; Smerdon et al., 2004).

Due to the strong influence of air-ground coupling on climate dynamics, the characterization of the relationships between the land and atmosphere has also been employed as a criterion for evaluating the performance of climate models (Ferguson et al., 2012; Henderson-Sellers et al., 1995; Knist et al., 2016; Koster et al., 2006b; Seneviratne et al., 2013). For instance, the Global Land-Atmosphere Coupling Experiment

(GLACE) (Guo et al., 2006; Koster et al., 2006b) evaluated the role of the land state in numerical weather and climate predictions using 12 different GCMs. This analysis showed large variability between GCMs and identified regions where air-ground coupling exhibited a strong effect on climate for most of the simulations. Dirmeyer et al., 2006 compared the results from GLACE GCMs with observational data at a few locations and suggested that most of the GCMs used in GLACE do not represent air-ground coupling correctly. However, the representation of the air-ground coupling for the multimodel mean of the experiments was more closely aligned with observations than results of GLACE GCMs separately. An analysis of air-ground coupling was also developed by Ferguson et al., 2012 using a set of GCMs, reanalyses, and satellite remote sensing data to evaluate the ability of offline simulations from Land Surface Models (LSMs) to reproduce air-ground coupling as derived from observations. Their results indicate that remote sensing data yield a substantially weaker coupling over the globe relative to LSMs, concluding that these GCMs and reanalyses overestimate the magnitude of air-ground coupling. A new multimodel experiment was carried out using the experimental protocol of GLACE and global climate models from the Coupled Model Intercomparison Project, Phase 5 (GLACE-CMIP5) (Seneviratne et al., 2013). This new experiment found a strong impact of soil moisture on climate variables such as temperature and precipitation, but also its contribution to the intensity, frequency and duration of extreme events (Lorenz et al., 2016; Seneviratne et al., 2013). All these studies follow different approaches to analyze air-ground coupling, using different metrics such as correlation coefficients and differences between ground surface and atmosphere variables; air-ground coupling assessments are also carried out comparing climate simulations with and without prescribed values of soil variables, removing the effect of land-atmosphere feedbacks (Dirmeyer et al., 2006, 2013; Ferguson et al., 2012). Previous analyses have also evaluated air-ground coupling by comparing offline

simulations with observational data using different metrics. The challenges of measuring elements of air-ground coupling that characterize relevant processes and the lack of observational data above and below the ground surface, nevertheless, present a limitation in comparing and evaluating model simulations against observations (Guo et al., 2006; Seneviratne et al., 2008; Seneviratne et al., 2010).

Temperature is one of the variables with longer and broader observational data records in comparison with other variables employed in the air-ground coupling literature, such as surface heat fluxes. In this study, we employ the difference between Ground Surface Temperature (GST) at 10 cm and Surface Air Temperature (SAT) as a metric for the evaluation of air-ground coupling. Changes in air and soil temperatures are the consequence of energy and water partitioning at the surface, thus making differences between the two temperatures a useful metric for the evaluation of air-ground coupling within climate models (Koven et al., 2013; Smerdon et al., 2006). We use the set of simulations that were used to evaluate and to understand the impacts of climate change by the last assessment report of the Intergovernmental Panel on Climate Change (IPCC) and to inform the 21^{st} Conference of the Parties (COP21) international climate agreement in December 2015 in Paris (Christoff, 2016; IPCC, 2013). This set of simulations was carried out using 32 GCMs, included in the 5^{th} phase of the Coupled Model Intercomparison Project (CMIP5), coupled to 12 different land surface models and 18 different atmospheric models with the same external forcings (Taylor et al., 2012). This allows for the analysis of model discrepancies attributed mostly to each model component and the shared information between them. The relationship between air and ground temperatures is also evaluated as represented within the NARR product (Mesinger et al., 2006). The use of this metric based on air and soil temperatures allows the comparison between models, reanalysis, and observations over a 27 years period at annual and seasonal scales over North

America. Additionally, we use the CMIP5 climate simulations to study the influence of present and future changes in near-surface processes such as snow cover, vegetation cover, precipitation and soil moisture on the representation of air and ground temperature relationships.

2.2 Data

2.2.1 CMIP5 GCM simulations

The simulations used herein are those included in a set of coordinated climate model experiments known as CMIP5 (Taylor et al., 2012) (`https://esgf-index1.ceda.ac.uk/search/cmip5-ceda/`, access date 2015/09/07). We specifically employ the first available ensemble member (see Table A.1) for each CMIP5 GCM historical simulation (1861-2005 of the Common Era (CE)) and two future climate projections under different concentration pathways (2006-2100 CE) from 32 CMIP5 GCMs (Table 2.1).

The historical experiment (Mieville et al., 2010; Schultz et al., 2008; Werf et al., 2006) allows the evaluation of the model performance against recent and present climate change. In these experiments, land use changes (Hurtt et al., 2011) are common to all modeling groups for the last two centuries, while vegetation dynamics are specific to each modeling group. Each model's historical experiment yields the initial conditions for the future projections. The CMIP5 future climate projections, Representative Concentration Pathways (RCPs), adopt four socio-economic and emission scenarios for future climate (Vuuren et al., 2011). The RCPs were developed according to the approximate magnitude of radiative forcing expected in the year 2100 CE, relative to pre-industrial conditions. The objectives of these scenarios are to provide estimates of future climate change under anthropogenic influences, to facilitate the

Table 2.1: List of the 32 GCMs used in this analysis, their employed spatial resolutions, land-surface model names, land-surface model references, atmospheric model names and references of the atmospheric models.

Model	Resolution ($lat^o \times lon^o$)	Land-Surface Model	Land-Surface Model reference	Atmospheric Model	Atmospheric Model reference
CCSM4.0	0.9×1.25	CLM4	Oleson et al., 2010	CAM4	Neale et al., 2010a
CESM1-BGC	0.9×1.25	CLM4	Oleson et al., 2010	CAM4	Neale et al., 2010a
CESM1-CAM5	0.9×1.25	CLM4	Oleson et al., 2010	CAM5	Neale et al., 2010b
CESM1-FASTCHEM	0.9×1.25	CLM4	Oleson et al., 2010	CAM4-CHEM	Lamarque et al., 2012
CESM1-WACCM	1.88×2.5	CLM4	Oleson et al., 2010	WACCM	Marsh et al., 2013
NORESM1-M	1.88×2.5	CLM4	Collins et al., 2006	CAM-OSLO	Kirkevåg et al., 2013
NORESM1-ME	1.88×2.5	CLM4	Collins et al., 2006	CAM-OSLO	Kirkevåg et al., 2013
INM-CM4	1.5×2	INM-CM4	Volodin et al., 2010	INM-CM4	Volodin et al., 2010
MIROC-ESM	2.81×2.81	MATSIRO	Takata et al., 2003	MIROC-AGCM	Watanabe et al., 2008
MIROC-ESM-CHEM	2.81×2.81	MATSIRO	Takata et al., 2003	MIROC-AGCM	Watanabe et al., 2008
MIROC5	1.4×1.4	MATSIRO	Takata et al., 2003	CCSR/NIES/FRCGC/AGCM6	Numaguti et al., 1997
GFDL-CM3	2×2.5	LM3	Dunne et al., 2012	GFDL-CM3	Donner et al., 2011
GFDL-ESM2G	2×2.5	LM3	Dunne et al., 2012	GFDL-ESM2G	Delworth et al., 2006
GFDL-ESM2M	2×2.5	LM3	Dunne et al., 2012	GFDL-ESM2M	Delworth et al., 2006
MRI-CGCM3	1.13×1.13	HAL	Yukimoto et al., 2012b	MRI-AGCM3.3	Yukimoto et al., 2012a
MRI-ESM1	1.13×1.13	HAL	Yukimoto et al., 2012b	MRI-AGCM3.3	Adachi et al., 2013
MPI-ESM-LR	1.88×1.88	JSBACH	Reick et al., 2013	ECHAM6	Stevens et al., 2013
MPI-ESM-MR	1.88×1.88	JSBACH	Reick et al., 2013	ECHAM6	Stevens et al., 2013
MPI-ESM-P	1.88×1.88	JSBACH	Reick et al., 2013	ECHAM6	Stevens et al., 2013
CMCC-CM	0.75×0.75	ECHAM5	Roeckner et al., 2003	ECHAM5	Roeckner et al., 2003
CMCC-CMS	1.88×1.88	ECHAM5	Roeckner et al., 2003	ECHAM5	Roeckner et al., 2003
CANESM2	2.81×2.81	CLASS2.7	Verseghy, 1991	CANESM2	Salzen et al., 2013
IPSL-CM5A-LR	1.88×3.75	ORCHIDEE	Krinner et al., 2005	LMDZ5	Hourdin et al., 2012
IPSL-CM5A-MR	1.25×2.5	ORCHIDEE	Krinner et al., 2005	LMDZ5	Hourdin et al., 2012
IPSL-CM5B-LR	1.88×3.75	ORCHIDEE	Krinner et al., 2005	LMDZ5B	Hourdin et al., 2012
GISS-E2-R	2×2.5	GISS-LSM	Rosenzweig et al., 1997	GISS-E2-R	Schmidt et al., 2006
GISS-E2-H	2×2.5	GISS-LSM	Rosenzweig et al., 1997	GISS-E2-H	Schmidt et al., 2006
BCC-CSM1.1	2.81×2.81	BCC-AVIM1.0	Wu et al., 2013	BCC-AGCM2.1	Wu et al., 2008
BCC-CSM1.1-M	1.13×1.13	BCC-AVIM1.0	Wu et al., 2013	BCC-AGCM2.1	Wu et al., 2008
HADCM3	2.5×3.75	MOSES2	Essery et al., 2003	HADAM3	Pope et al., 2000
HADGEM2-CC	1.25×1.88	MOSES2	Essery et al., 2003	HADGAM2	Davies et al., 2005
HADGEM2-ES	1.25×1.88	MOSES2	Essery et al., 2003	HADGAM2	Davies et al., 2005

comparison between model projections, to quantify risks associated with future climate change and to explore the impact of societal mitigation and adaptation efforts. We use the RCP4.5 and the RCP8.5 experiments as representations of moderate mitigation and business-as-usual emission scenarios, respectively (Riahi et al., 2011; Thomson et al., 2011).

The GCM simulations used in our analysis (Table 2.1) were performed by different modeling groups. Thus, each GCM differs in the character of its land-surface and atmospheric models and their configurations. We note that LSMs all adopt different subsurface thermal properties, maximum depths of the deepest soil layer (from 3 m to 43 m), the depth intervals of the soil layers and their total number (from 3 to 23); the latter three characteristics are summarized in Figure 2.1.

2.2.2 North American Regional Reanalysis (NARR)

The NARR project (Mesinger et al., 2006) is an extension of the NCEP Global Reanalysis over North America for the period 1979-2017 (`https://www.esrl.noaa.gov/psd/data/gridded/data.narr.html`, access date 2017/03/24). NARR was developed with the 2003 version of the Eta Model coupled to the Noah land surface model, and the Regional Data Assimilation System (RDAS), which assimilates temperature and precipitation observations along with other variables (Berbery et al., 2003; Ek et al., 2003; Mitchell et al., 2004). The use of an atmospheric model and a land surface model together with observational data for generating its final product makes the NARR comparable to GCMs in terms of air-ground coupling. We used the NARR variables of surface air temperature and soil temperature at 10 cm (herein referenced as Ground Surface Temperature, GST) to compare the characterization of air and ground surface temperature relationships within the CMIP5 simulations and within an observationally constrained model product.

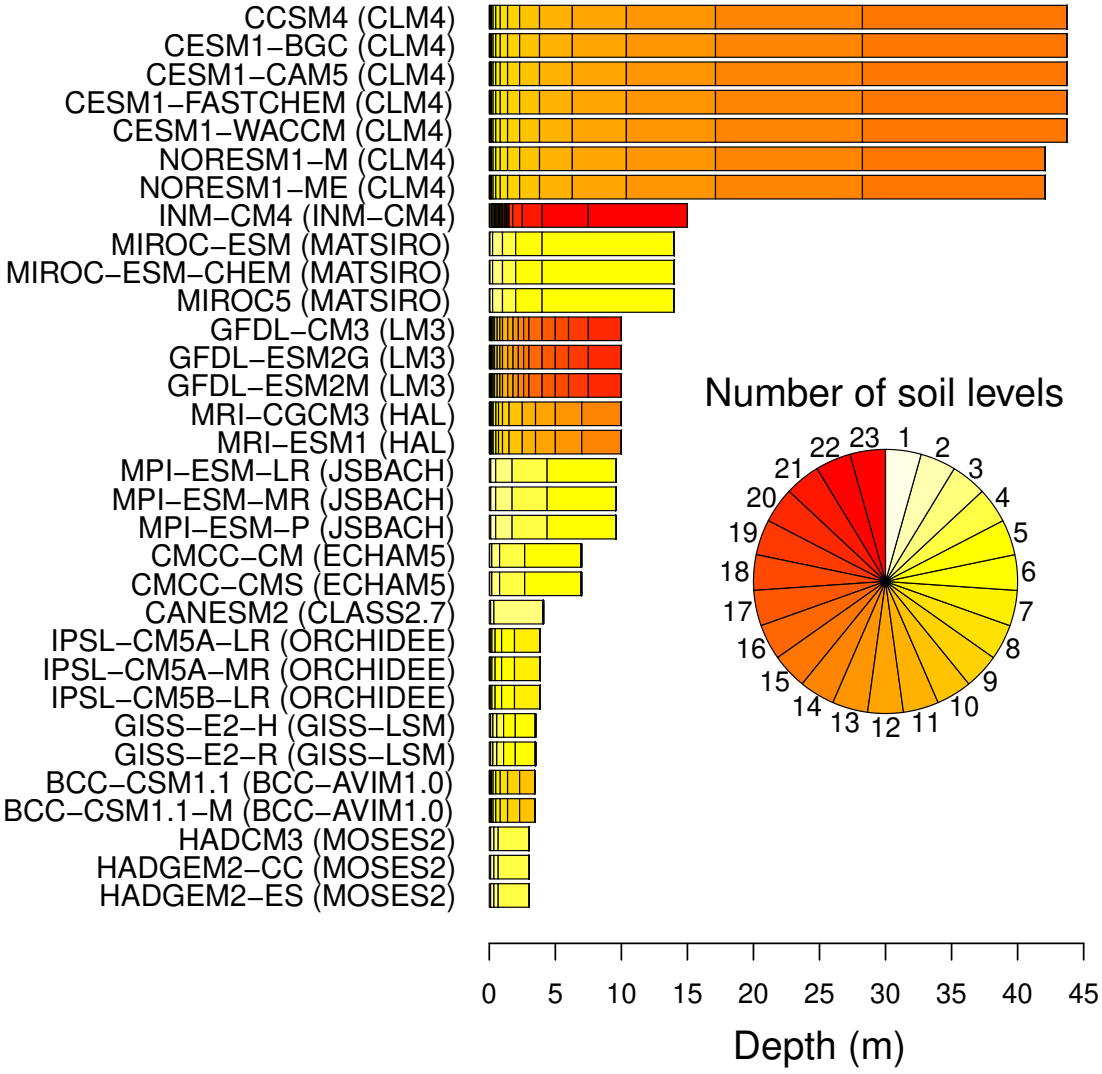

Figure 2.1: Depths and number of layers of the 12 land-surface models (in brackets), employed by the 32 CMIP5 GCMs.

2.2.3 Observational data

We employ a set of temperature observations from meteorological stations in the United States and Canada to compare the relationships between air and ground surface temperatures with those from the CMIP5 simulations and the NARR product. Observations include United States (US) measurements of air and ground surface temperatures from 1969 to 2001 and Canadian measurements from 1979 to 2005. We select the period of overlap between the historical simulation, the NARR product and observations from 1979 to 2001 for our analysis.

Monthly mean surface air temperature measurements from 292 US stations were obtained from the Monthly Summaries of the Global Historical Climatology Network (GHCN), NOAA NCEI (`https://www.ncdc.noaa.gov/`, access date 2015/02/21). The data were produced by computing simple averages of the daily maximum and minimum observations. Monthly ground surface temperature measurements were provided by Xia et al., 2013 and were taken as described and validated in the article. These soil measurements include temperature observations from 209 US stations at 10 cm depth. The annual mean values are computed for the years that have no missing values using the monthly data of both air and ground surface temperatures. The annual temperatures are additionally aggregated to a $1^\circ \times 1^\circ$ grid by averaging observations over each grid cell.

Monthly mean surface air temperature measurements at Canadian stations were obtained from the Environment and Natural Resources, Government of Canada (`http://climate.weather.gc.ca/prods_servs/cdn_climate_summary_e.html`, access date 2016/07/04). These data were provided as mean monthly values of maximum and minimum temperatures. Canadian measurements of soil temperature at 10 cm were provided by the National Office of Climate Services - Environment and Climate Change,

Canada. These data contain daily soil temperatures at 12 a.m. and 12 p.m.. Daily mean temperatures are approximated as the average of both temperatures. Monthly mean values are calculated as the mean of the daily data when they have fewer than 10 missing values and less than 5 consecutive missing values. This criterion is used for consistency with the observations from the US stations (Xia et al., 2013). Annual mean values of air and ground temperatures are calculated for years that have no missing values. Otherwise, the annual mean value is characterized as missing. Annual values of both air and ground surface temperatures are aggregated to a $1^\circ \times 1^\circ$ grid by averaging observations over each grid cell.

Monthly surface air and ground surface temperatures from the US and Canadian stations are used to calculate the differences between air and ground temperatures at each grid cell at annual and seasonal scale for the period 1979-2001. However, we do not have data from observations at all stations for the whole period. For this reason, we filter the observational database estimating the period mean only at grid cells with more than 10 annual values. Thus, our domain compromises 113 grid cells with at least one observation of SAT and GST for the mean period 1979-2001. A discussion of the uncertainty in the comparison between simulations and observations is included in Section 2.5.

2.3 Methodology

The relationships between air and ground surface temperatures depend on soil properties, surface roughness, and the energy and water exchange processes operating between the lower atmosphere and the ground surface. Because the CMIP5 simulations include a variety of LSMs, each of which involves different parameterizations of the energy and water exchanges at the land-atmosphere boundary, the air and

ground temperature relationships for each simulation may exhibit different behavior. We define an evaluation metric as the difference between mean Ground Surface Temperature at 10 cm and Surface Air Temperature at 2 m (GST-SAT) from observations, the NARR product and each CMIP5 simulation over a time interval of a calendar year, the boreal winter months (December, January and February (DJF)) and summer months (June, July and August (JJA)). This metric removes possible biases in the mean states within the models and reanalysis, thus allowing comparisons with observations. The use of GST at a depth of 10 cm allows us to evaluate both the annual and seasonal differences among models in simulating air-ground coupling. Soil temperature at 10 cm from the CMIP5 simulations are obtained using a linear interpolation between nodes of each soil layer. The difference between GST and SAT has been previously used to track the relationship between air and ground surface temperatures at daily, seasonal and annual scales (Koven et al., 2013; Melo-Aguilar et al., 2018; Smerdon et al., 2006). Smerdon et al., 2006 proposed a method to study and validate the long-term coupling between air and ground surface temperatures, which is the main assumption of paleoclimate reconstructions from geothermal data (e.g. Beltrami, 2002). Koven et al., 2013 employed the difference between GST and SAT as part of an analysis to evaluate the propagation of heat into the soil and its effect on permafrost soils within the CMIP5 simulations. Melo-Aguilar et al., 2018 most recently used the temperature difference as a metric to study the effect of radiative forcings on the coupling between air and ground temperatures within the CESM-LME ensemble.

The seasonal and annual characterization of the relationships between GST and SAT within the CMIP5 GCMs and the NARR product is compared with observations using the mean temperature difference (GST-SAT) for the period 1979-2001. We estimate spatial correlation coefficients as in Santer et al., 1995 and the Root

Mean Square Errors (RMSEs), as metrics of the agreement between simulations and observations. For the calculation of correlation coefficients and the RMSEs between models and observations, each model pattern is interpolated to the observation grid ($1^\circ \times 1^\circ$), selecting only the grid cells where observations are available. For the visual comparison between simulations and observational data, we interpolate the observations using the nearest neighbor algorithm from the Generic Mapping Tools (GMT) software (Wessel et al., 2013), which uses the weighted mean of the nearest point in each sector considering the distance to assign an average value to each node. We set the interpolation to have a search radius of 4° and divide the area centered on each point into four sectors. Average values are only computed at nodes with at least one value in each sector (Figure A.1).

After the comparison between simulations and observations, we investigate the role of near-surface processes in the model performance by studying the correlation between simulated annual and seasonal temperature differences and snow cover, vegetation cover, precipitation and soil moisture within the CMIP5 simulations and the NARR product. We compute the correlation coefficients between the absolute value of the air-ground temperature difference and the means of the monthly CMIP5 variables associated with the mentioned near-surface processes at each grid cell for the period of comparison with observations (1979-2001). We use the absolute value of the temperature differences to avoid problems in the interpretation of the correlation coefficients, when the temperature differences are negative (SAT > GST). For example, snow cover has an insulating effect (Zhang, 2005), which means that thicker snow cover leads to larger differences between air and ground temperatures (positive correlation coefficients). In cases where the ground-air temperature difference is negative, however, an increase in snow cover leads to larger differences between air and ground temperatures, which correspond to more negative GST-SAT values, yielding

negative correlation coefficients between snow cover and GST-SAT. The use of absolute values yields the correct correlation sign in those cases with negative temperature differences. The near-surface processes included in this study have a strong seasonal character, hence the computation of the seasonal correlation coefficients using the DJF and JJA means. The variables employed in this analysis are: Surface Snow Amount (SNW) -defined as the ratio of the mass of surface snow on the land portion of a grid cell and the grid cell land area (kg/m^2); Leaf Area Index (LAI) -defined as the fraction of green leaf area over the total ground area at each grid cell; Precipitation Rate (PR) -constituted by water in all phases at the surface (kg/m^2s); and Soil Moisture (SM) -defined as the mass of water in all phases in a 10 cm surface soil layer (kg/m^2). The models that do not include these variables in the CMIP5 archive are excluded from this part of the study (see Table A.1 for a detailed list of the models and their variables). For the correlation analysis, grid cells containing null values for the variables associated with each near-surface process in the 23-year period of interest are masked in grey. The areas with significant correlation coefficients at the 95% level are calculated for the CMIP5 ensemble and the NARR product using 1000 Monte Carlo runs of a phase-randomizing bootstrapping technique that preserves autocorrelation structure (Ebisuzaki, 1997). We also calculate the multimodel mean of the correlation coefficients as the mean of the correlation maps interpolated to the coarsest grid of the ensemble ($2.81° \times 2.81°$).

2.4 Results

2.4.1 Air and ground temperature relationships within the CMIP5 GCMs, the NARR and Observations

There is large variability across the CMIP5 simulations in the character of air and ground temperature relationships. The annual mean of the temperature difference (GST-SAT) from 1979 to 2001 CE varies spatially in North America among the GCMs (Figure 2.2). These results suggest a dependence of the GST-SAT differences on the LSM employed by each GCM, such that GCMs with the same LSM yield similar behavior for the temperature difference. However, the representation of air and ground temperature relationships seems to be independent of the atmospheric model. For example, the 7 GCMs that use the CLM4 LSM or the 3 GCMs that use the LM3 LSM do not show different relationship between GST and SAT despite using different versions of atmospheric models. There are small differences in the representation of air and ground temperature relationships for the simulations that use different versions of the same atmospheric model coupled to either the MOSES2 or the MATSIRO LSMs, but they are much smaller than the differences with simulations that use other LSMs. The horizontal resolution employed in each simulation is another factor expected to affect air-ground coupling (Wang et al., 2004; Xue et al., 2014), nevertheless, the differences between models in the GST-SAT metric arising from the use of different LSMs are larger than those arising from the use of different spatial resolutions (Figure 2.2). For example, the NORESM1 and the CESM1-WACCM models employ grid cells two times larger than the rest of the CLM4 simulations and show very similar values of GST-SAT. The IPSL-ESM-MR and the BCC-CSM1.1-M models use finer resolutions

than their shared-LSM simulations and also show similar relationships between GST and SAT. Otherwise, models with similar resolutions such as the GFDL and the GISS models show different results. We have tried to relate the LSM-dependency to the soil depth of each LSM and the effect of the bottom boundary condition on soil temperatures (Smerdon et al., 2006), but we have found no relationship between them, likely because we use shallow soil temperatures in our analysis. As shown in Smerdon et al., 2006, the zero-flux condition used at the bottom boundary of the soil column by all the CMIP5 LSMs affects the simulation of soil temperatures depending on the soil depth, but this effect is very weak in the first several centimeters of the soil. We also have analyzed the effect of the linear interpolation used to obtain soil temperatures at 10 cm within the models. The temperature differences using soil temperatures at the node of the soil layer containing the soil depth of 10 cm are similar to those of the interpolated GST, which indicates that the effect of the interpolation of GST on these results is negligible (Figures 2.2 and A.2).

The model discrepancies in simulating the difference between air and ground temperatures are larger at seasonal scales, showing the same LSM-dependency than in the annual analysis (Figures 2.3 and 2.4). Most of the models and the NARR product show larger temperature differences in DJF that those for the annual mean particularly at high latitudes, which is consistent with observations (Figures 2.2 and 2.3). This likely indicates a consistency across most of the models, the NARR, and the observations regarding the influence of the insulating effect of snow cover, which is the main influence on air-ground coupling in DJF and increases the difference between air and ground temperatures (e.g. Zhang, 2005). In JJA, most of the models show positive temperature differences over the western US and negative or near zero temperature differences over the rest of the domain, in agreement with the sign of the GST-SAT value at the available observations (Figure 2.4). The models showing very small GST-

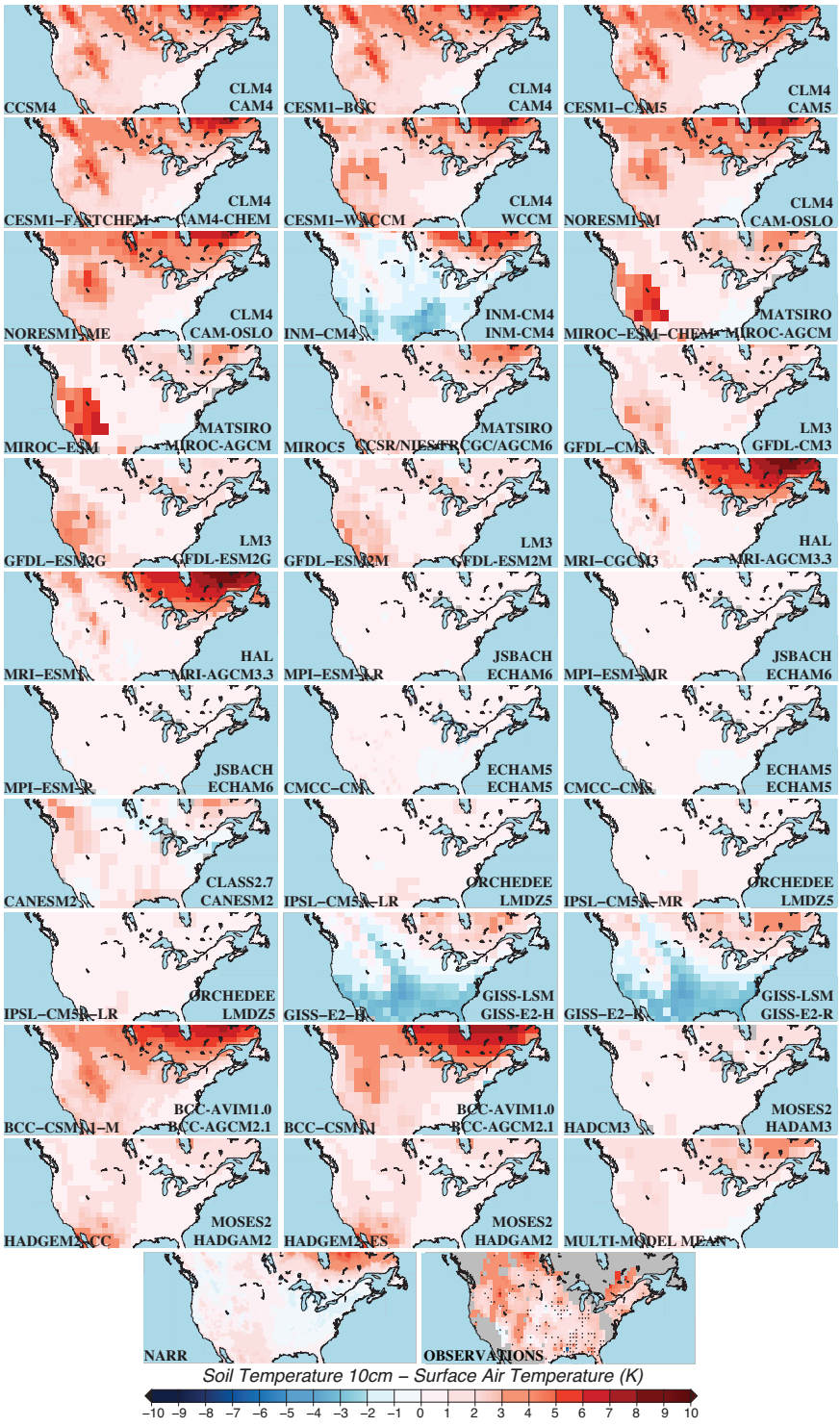

Figure 2.2: Annual mean of GST-SAT differences from 1979 to 2001 for the CMIP5 GCMs, the multimodel mean, the NARR and observations. Each map shows the GCM name on the bottom-left corner and the LSM and atmospheric model names on the bottom-right corner. The map of the observational data is interpolated using the nearest neighbor algorithm of GMT with a search radius of 4°. Black dots in the observation map show the locations of the data on a $1° \times 1°$ grid, and grey color was used to indicate missing data.

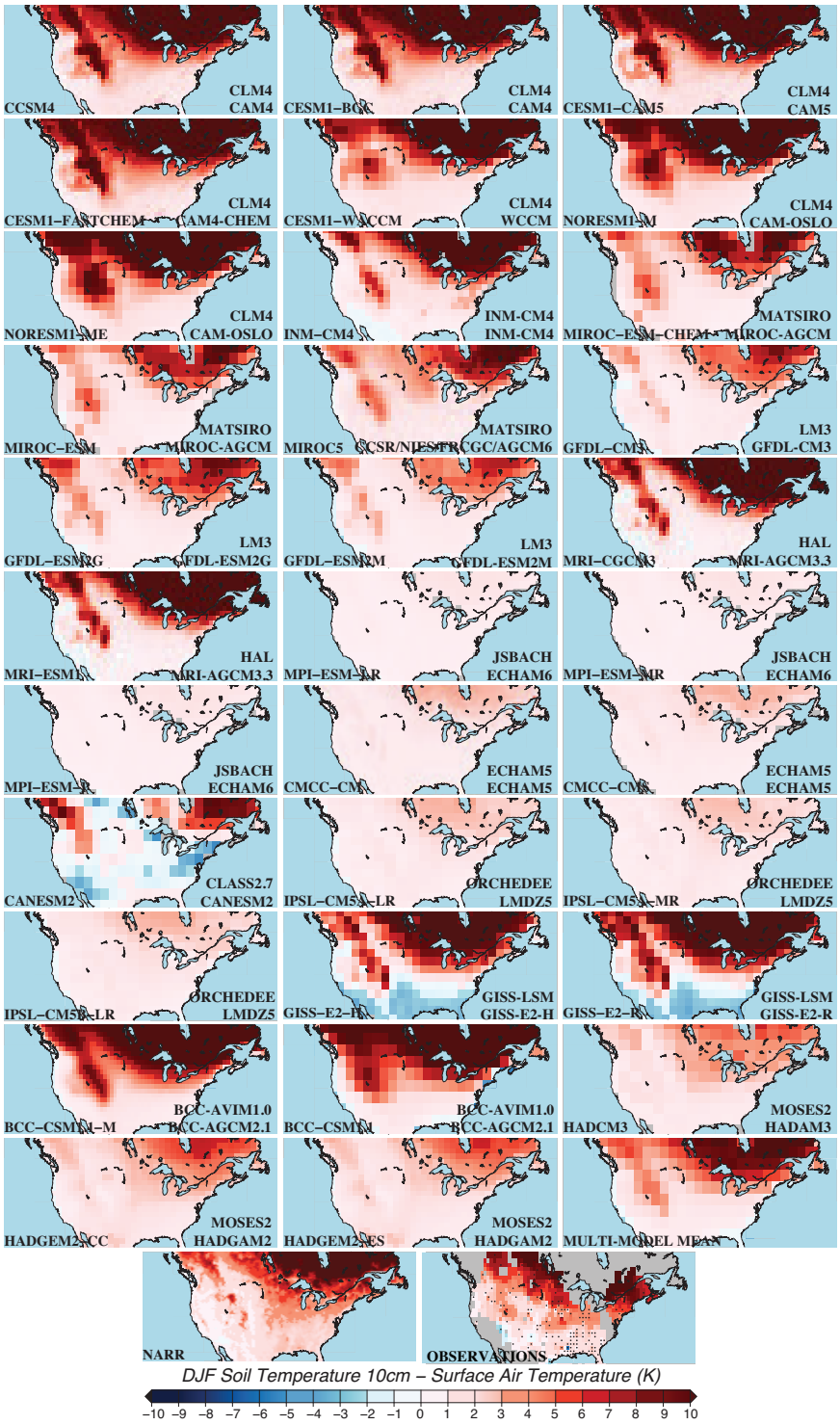

Figure 2.3: DJF mean of GST-SAT differences from 1979 to 2001 for the CMIP5 GCMs, the multimodel mean, the NARR and observations. Each map shows the GCM name on the bottom-left corner and the LSM and atmospheric model names on the bottom-right corner. The map of the observational data is interpolated using the nearest neighbor algorithm of GMT with a search radius of 4°. Black dots in the observation map show the locations of the data on a $1° \times 1°$ grid, and grey color was used to indicate missing data.

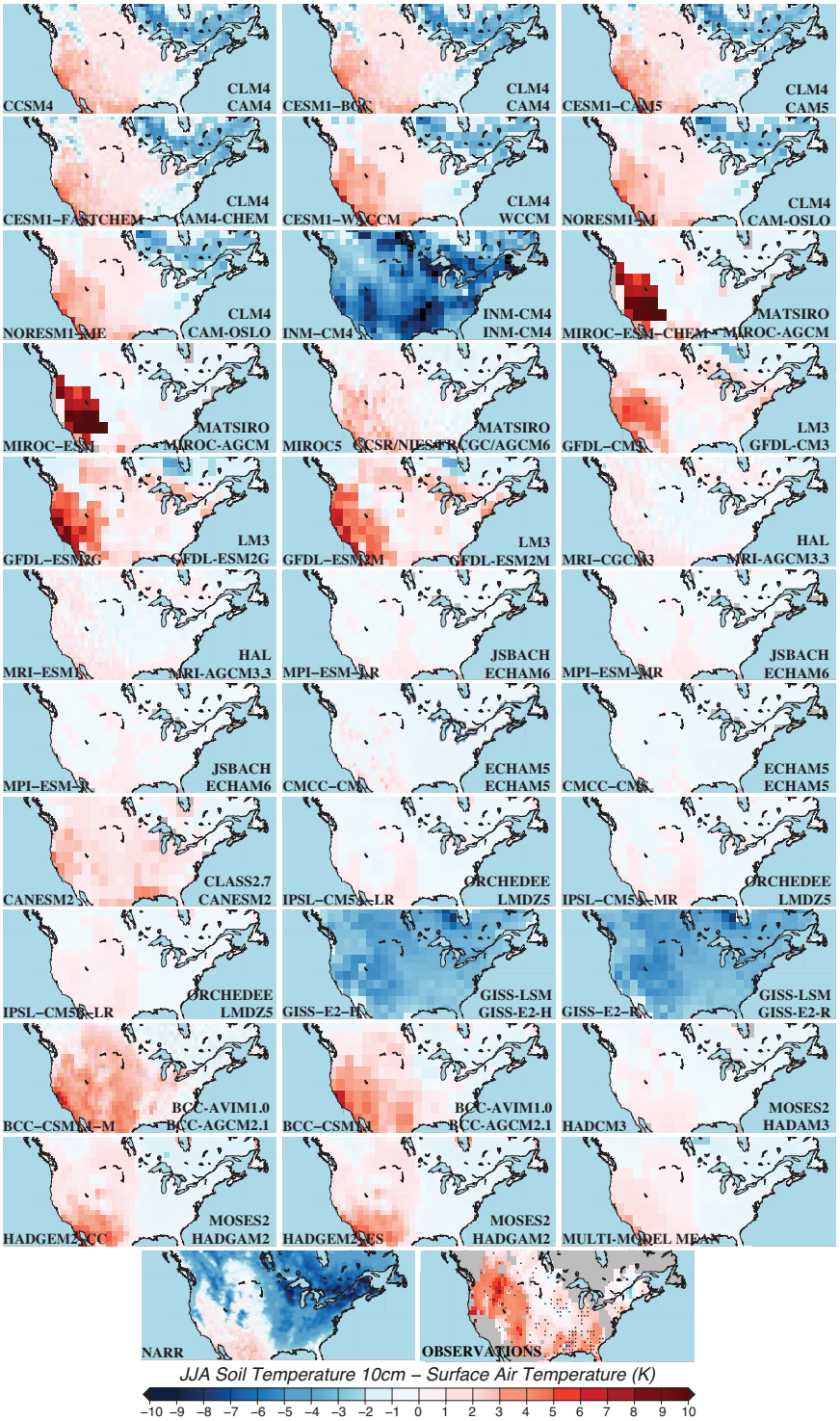

Figure 2.4: JJA mean of GST-SAT differences from 1979 to 2001 for the CMIP5 GCMs, the multimodel mean, the NARR and observations. Each map shows the GCM name on the bottom-left corner and the LSM and atmospheric model names on the bottom-right corner. The map of the observational data is interpolated using the nearest neighbor algorithm of GMT with a search radius of 4°. Black dots in the observation map show the locations of the data on a $1° \times 1°$ grid, and grey color was used to indicate missing data.

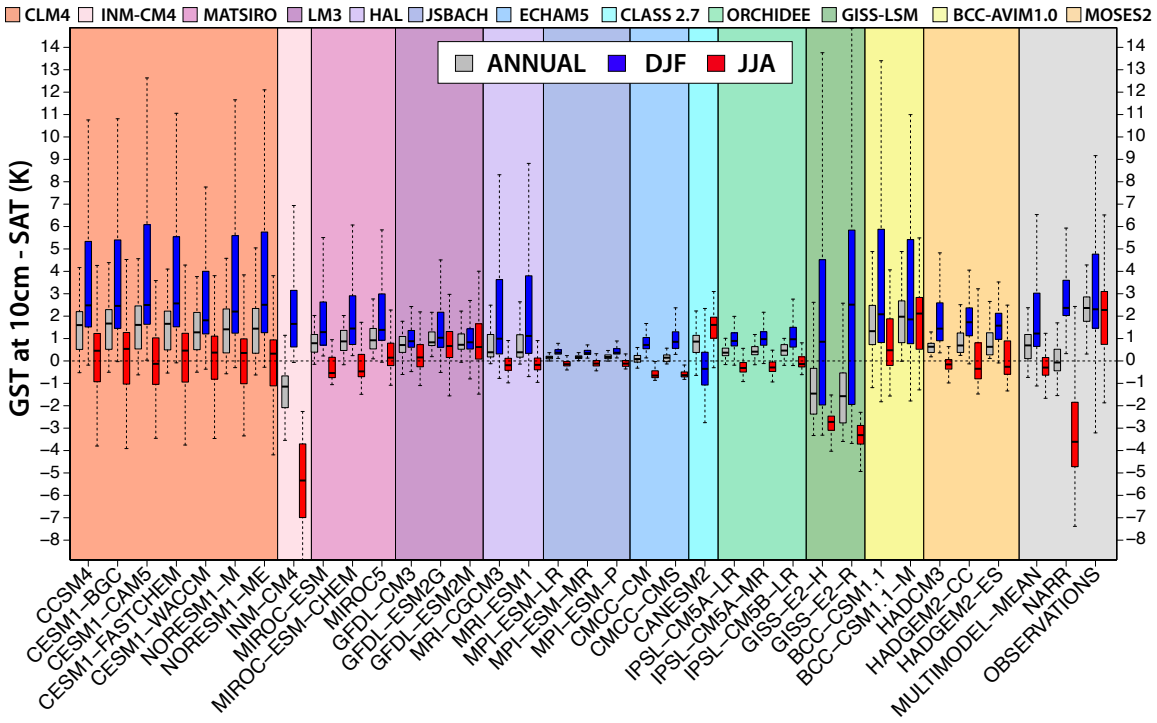

Figure 2.5: Boxplots (75th and 25th spatial percentiles (boxes), medians (center lines), maximums and minimums (extremes of dashed lines)) for the annual and seasonal temperature differences at the locations of the observations (black dots in Figure A.1). Outliers (points located 1.5 times the interquartile range above the upper quartile and bellow the lower quartile) are not included. Results are sorted from deeper to shallower LSM and each LSM is indicated using a different color. The results from the multimodel mean, the NARR product and observations are plotted on the far right.

SAT differences (the MPI, the CMCC and the IPSL models) for the annual mean also show very small values of GST-SAT in DJF and JJA in contrast to the observations. The INM-CM4 model, which shows annual negative temperature differences over most of the domain, displays positive values of the GST-SAT difference in DJF for most of the domain with large values at high latitudes. Meanwhile, the GISS and CANESM2 models, which also show negative annual temperature differences, maintain the annual spatial pattern in DJF, showing larger values of the GST-SAT metric in DJF. In JJA, the INM and the GISS models differ from observations, showing large negative temperature differences over the whole domain.

Both the coupled models and NARR do not accurately represent observations at annual and seasonal scales. While observations indicate that the difference between GST and SAT ranges from 0 K to 5 K for the annual mean, from -3 K to 9 K in DJF and from -2 K to 7 K in JJA, the temperature differences from models display values from -5 K to 5 K for the annual mean, from -3 K to 14 K in DJF and -9 K to 6 K in JJA (Figure 2.5). Results from the multimodel mean range from -1 K to 3 K for the annual mean, from -1 K to 7 K in DJF and from -2 K to 1 K in JJA, while results from the NARR range from -1 K to 2 K for the annual mean, from 0.5 K to 6 K in DJF and from -7.5 K to 3 K in JJA (Figure 2.5). Observations show that annual GST is warmer than SAT (GST-SAT > 0) at all locations, however, most simulations show locations with annually colder GSTs than SATs (Figure 2.5). In DJF, observations show more spatial variability than for the annual mean, presenting GST warmer than SAT at most locations. Most simulations agree with observations in the sign of DJF GST-SAT values, except for the CANESM2 and GISS models that show GST colder than SAT at more than the 25% of the locations. The disagreement between models and observations in the character of GST and SAT relationships is larger in JJA, when observations indicate GST higher than SAT at most locations and most of the models show areas with GST lower than SAT (Figure 2.5). The multimodel mean shows GST higher than SAT for the annual mean and in DJF at most locations in agreement with observations, in contrast to the results in JJA. The NARR product is in agreement with observations in the character of the temperature difference in DJF, but differs with the annual and JJA results.

Comparison with observations is focused on two conditions expected to be reproduced by climate models; the values of the temperature differences and the variability of the spatial pattern. We examine both features using RMSE and the spatial correlation coefficients (Table 2.2). Models using the same LSM show similar values of

Table 2.2: Spatial correlation coefficients and RMSE values of the temperature differences shown in Figure 2.2 relative to observations. The correlation coefficients and the RMSE values were calculated for each GCM, for the multimodel mean of the 32 GCMs and for the NARR product. For the comparison of simulations and observations, all maps were interpolated to the observational grid (1°×1°), selecting only the grid cells with observational data (black dots in Figure A.1).

GCM	Annual		DJF		JJA	
	Cor. Coeff.	RMSE	Cor. Coeff.	RMSE	Cor. Coeff.	RMSE
CCSM4	0.130	1.846	0.775	2.120	0.139	3.030
CESM1-BGC	0.144	1.853	0.777	2.154	0.134	3.058
CESM1-CAM5	0.180	1.835	0.800	2.260	0.135	3.092
CESM1-FASTCHEM	0.138	1.847	0.758	2.278	0.130	3.047
CESM1-WACCM	0.153	1.854	0.784	2.080	0.213	2.867
NORESM1-M	0.199	1.900	0.759	2.355	0.165	2.986
NORESM1-ME	0.209	1.909	0.742	2.501	0.172	2.997
INM-CM4	0.405	3.839	0.843	2.038	0.150	7.979
MIROC-ESM	0.100	2.149	0.684	3.192	0.241	3.115
MIROC-ESM-CHEM	0.118	2.091	0.693	3.047	0.235	3.09
MIROC5	0.160	1.904	0.727	2.756	0.252	2.532
GFDL-CM3	0.193	2.053	0.698	3.390	0.206	2.564
GFDL-ESM2G	0.105	1.940	0.689	3.126	0.208	2.380
GFDL-ESM2M	0.134	1.987	0.675	3.419	0.169	2.400
MRI-CGCM3	0.368	2.038	0.810	2.217	0.330	2.836
MRI-ESM1	0.359	2.042	0.826	2.131	0.303	2.830
MPI-ESM-LR	-0.132	2.533	0.801	4.253	-0.050	2.894
MPI-ESM-MR	-0.159	2.524	0.818	4.240	-0.021	2.866
MPI-ESM-P	-0.141	2.520	0.833	4.214	-0.102	2.889
CMCC-CM	-0.043	2.878	0.711	3.767	0.182	3.903
CMCC-CMS	0.115	2.558	0.822	3.746	0.093	3.263
CANESM2	0.019	2.108	0.275	4.979	0.365	1.788
IPSL-CM5A-LR	-0.066	2.331	0.782	3.668	-0.021	3.001
IPSL-CM5A-MR	-0.137	2.307	0.740	3.619	-0.044	3.000
IPSL-CM5B-LR	-0.032	2.279	0.762	3.569	0.032	2.840
GISS-E2-H	0.346	3.874	0.806	2.963	-0.120	5.307
GISS-E2-R	0.362	4.135	0.789	3.081	0.018	5.794
BCC-CSM1.1	0.252	1.877	0.799	2.504	0.287	2.341
BCC-CSM1.1-M	0.238	1.672	0.815	2.080	0.114	2.254
HADCM3	0.116	2.188	0.775	3.114	0.340	2.836
HADGEM2-CC	-0.017	2.089	0.743	3.033	0.115	2.913
HADGEM2-ES	-0.037	2.160	0.711	3.192	0.078	2.842
MULTIMODEL MEAN	0.232	2.146	0.811	2.436	0.259	2.918
NARR	-0.098	2.856	0.786	2.267	0.295	6.064

spatial correlation and RMSEs for the annual and seasonal temperature differences, further reinforcing the dependence of GST-SAT on the LSM employed (Figures 2.2, 2.3, 2.4 and 2.5). The CMIP5 models show high spatial correlation coefficients with observations for the difference between air and ground temperatures in DJF, displaying a decrease in correlation with the observations when using results for the JJA and annual means. The multimodel mean and the NARR product also show results in DJF in better agreement with observations than those for the JJA and annual means, again indicating their possible agreement in simulating the snow effect on the GST-SAT metric. At annual scales, the LSMs showing higher correlation coefficients than the multimodel mean are the ones used in the INM, the MRI, the GISS, and the BCC simulations. However, only the MRI and the BCC models show smaller annual RMSEs than the multimodel mean among these models. The BCC and MRI models therefore appear to yield annual temperature differences closer to observations in that they reproduce both the spatial pattern and the magnitudes of the temperature difference. In DJF, the models showing higher spatial correlation coefficients and lower RMSEs than the multimodel mean are the INM, the MRI, and the BCC-CSM1.1-M models, which differs from the BCC-CSM1.1 only in resolution. In JJA, the models showing higher spatial correlation coefficients and lower RMSEs than the multimodel mean are the MRI, the CANESM2, the HADCM3, and the BCC-CSM1.1 models. Thus, the MRI simulations appear to achieve the closest temperature differences to the observations at annual and seasonal scales. The multimodel mean of all GCMs achieves higher correlation coefficients and lower RMSEs than most of the CMIP5 models at annual and seasonal scales, consistent with the widely reported tendency for the multimodel mean of the CMIP5 GCMs to be more closely aligned to observations than most of the individual models (IPCC, 2013).

The comparison between models, the NARR and observations in reproducing the

spatial pattern of SAT and GST separately, also shows a better performance in winter than in summer (Table 2.2). The CMIP5 models and the NARR product display larger correlation coefficients and smaller RMSE values with the observations for the SAT analysis than for the GST. These results illustrate the difficulties of LSMs in simulating soil temperatures, particularly in summer when the simulation of processes related to soil moisture and vegetation cover may be affecting the evolution of soil conditions. These findings are in agreement with previous studies that have identified the simulation of soil temperatures as a factor to be improved within land surface models (Koven et al., 2013; Lytle et al., 2016; Todd-Brown et al., 2013).

2.4.2 Effect of near-surface processes on air and ground temperature relationships within the CMIP5 ensemble

From the insulating effect of snow reported in the literature (Goodrich, 1982; Pollack et al., 2005; Smerdon et al., 2004, 2006; Sokratov et al., 2002), we expect large GST-SAT values in DJF and at high latitudes, as seen in Subsection 2.4.1. Meanwhile, vegetation cover and soil moisture are expected to shift part of the net radiation absorbed by the soil from the sensible heat flux component to the latent heat flux component, decreasing air-ground temperature differences (Bonan, 2002; Lin et al., 2003; Pollack et al., 2005; Smerdon et al., 2006).

Examining the role of snow cover in the characterization of air and ground temperature relationships, we find that the annual and DJF series of the absolute values of the temperature difference appear significantly positively correlated to the series of snow amounts on the surface, indicating larger GST-SAT differences with larger snow amounts on the surface. Figure 2.6 shows significant positive correlation between snow cover and the temperature difference in the DJF and annual analyses for all the

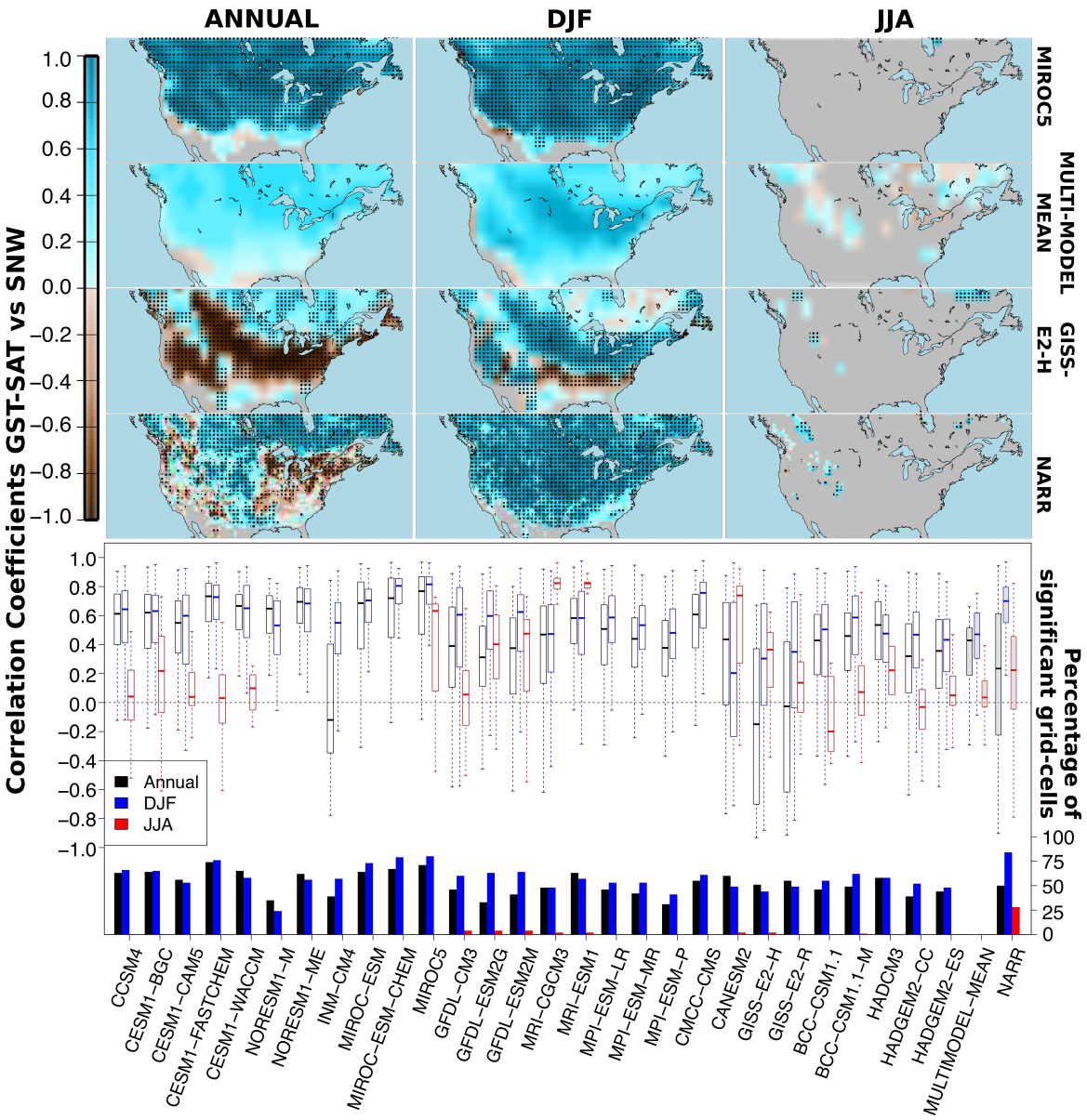

Figure 2.6: Temporal correlation, point-to-point, between monthly snow amounts (SNW) and the absolute values of the temperature differences for the annual mean (black), for mean DJF (blue) and mean JJA (red) of each model for the period 1979-2001. (bottom) Boxplots (75th and 25th spatial percentiles (boxes), medians (center line), maximums and minimums (extremes of dashed lines)) of the correlation maps. Outliers (points located 1.5 times the interquartile range above the upper quartile and bellow the lower quartile) are not included. Bars at the bottom of the boxplots indicate the percentages of land grid cells with significant correlation at the 95% level using a phase-randomizing bootstrapping technique with 1000 Monte Carlo runs (Ebisuzaki, 1997). (top) Maps correspond to the strongest (MIROC5, top) and the weakest (GISS-E2-H, second-bottom) annual mean correlations, the multimodel mean of the correlation maps (center) and the NARR product (bottom), for the annual means (left), the DJF means (center) and the JJA means (right). Dots indicate significant correlation at the 95% level and grey color indicates that the annual or seasonal mean of snow amount on surface is null in at least one of the year of the 23-year period.

models and the NARR product over most areas of the domain. The GISS models show the weakest positive correlation, displaying significant negative correlation coefficients over a large area of the domain for the annual mean (Figure 2.6), while the MIROC models show the strongest positive correlation over almost the entire domain for the annual and DJF means. The positive correlation coefficients of the ensemble attest to the strong insulating effect of snow in DJF and annually, as represented in all of the CMIP5 models and the NARR product, although not necessary represented with the same strength and over the same areas. However, some models show grid cells with significant negative correlation coefficients between the temperature difference and snow cover, that is, the difference between air and ground temperature increases when snow decreases and vice versa (Figures A.3-A.5). Over these areas, such models simulate SAT warmer than GST in opposition to the observations (Figures 2.2, 2.3 and 2.4), which means that an increase in the snow amount associated with a decrease in SAT tends to reduce the difference between air and ground temperatures. However, there are two models (the HADGEM2s) showing significant negative correlation coefficients at some grid cells with GST warmer than SAT. Over these grid cells, the simulated snow cover is thin and the air and ground temperatures are higher than 0°C. Thus, the model could be simulating the melting of snow, which leads to an increase in soil moisture and the cooling of soil by enhancing evapotranspiration, therefore rising the temperature differences at those grid cells. In JJA, few models simulate grid cells with significant correlation between snow and GST-SAT. For those models showing significant correlation between snow and the temperature difference in JJA, the correlation is positive and negative depending on the grid cell, but the snow amount at the surface is much smaller than in DJF, and the temperatures are warmer. Therefore, snow may be melting at some of these grid cells, increasing soil moisture and declining soil temperatures through evapotranspiration, reducing the

GST-SAT difference. Meanwhile, snow may be insulating GST from SAT as in DJF at some of the other grid cells at high altitude, increasing air-ground temperature differences.

The annual and seasonal series of the temperature difference and the Leaf Area Index variable are mostly inversely correlated for the majority of the CMIP5 simulations (Figure 2.7). Results from the NARR product are not included in this analysis because it does not include the LAI variable, while other variables associated with vegetation cover such as vegetation fraction are prescribed with no change in time. The correlation between vegetation cover and the absolute values of the temperature differences is negative for most of the models, showing more disagreement among models than the analysis of the snow effect (Figures A.6-A.8). In DJF, models display high spatial variability indicating few grid cells with significant positive and negative correlation coefficients without following a common pattern among models. The percentages of grid cells with significant correlation are larger in JJA and at annual scales for most of the models, although, with marked discrepancies among models. Correlation coefficients at annual scales are negative for the majority of the models over most of areas with significant correlation, which means that over these areas an increase of LAI, associated with higher evapotranspiration, leads to lower soil temperatures, and thus to smaller air-ground temperature differences when GST is higher than SAT, which occurs nearly over the whole domain for most of the models at annual scales. In JJA, areas with significant positive correlation coefficients spread over the eastern US for most of the models, but for the CANESM2 model, which shows significant positive correlation coefficients throughout the western part of the domain and significant negative correlation coefficients in the eastern part of the domain; the MIROC-ESM models show positive correlation coefficients over most areas of the domain. Except for these three models, the CMIP5 models show positive correlation

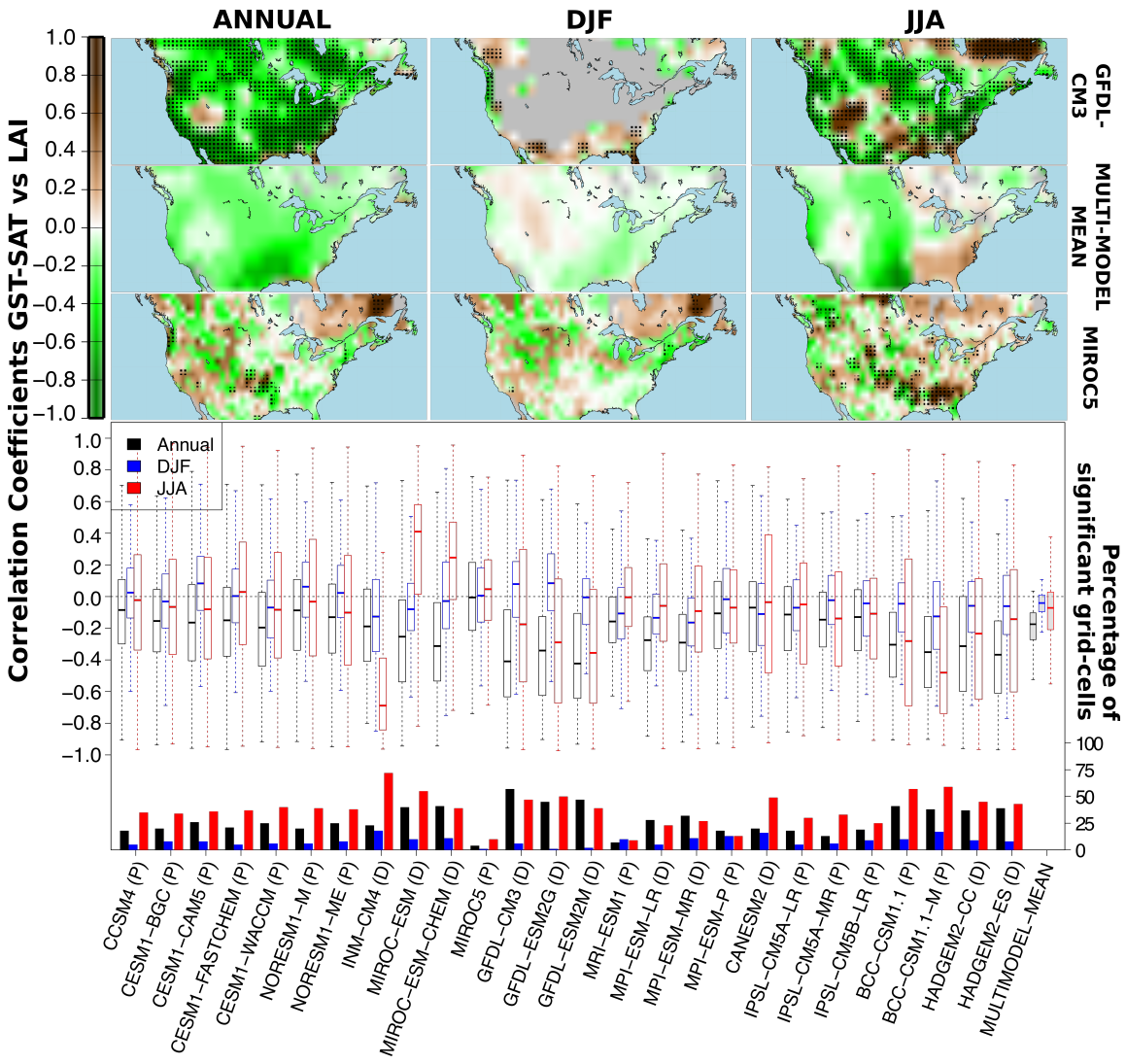

Figure 2.7: Temporal correlation, point-to-point, between monthly Leaf Area Indices (LAIs) and the absolute values of the temperature differences for the annual mean (black), for mean DJF (blue) and mean JJA (red) of each model for the period 1979-2001. (bottom) Boxplots (75th and 25th spatial percentiles (boxes), medians (center line), maximums and minimums (extremes of dashed lines)) of the correlation maps. Outliers (points located 1.5 times the interquartile range above the upper quartile and bellow the lower quartile) are not included. Bars at the bottom of the boxplots indicate the percentages of land grid cells with significant correlation at the 95% level using a phase-randomizing bootstrapping technique with 1000 Monte Carlo runs (Ebisuzaki, 1997). The capital letter next to each model name indicates the information of the vegetation mode (prescribed (P) or dynamic (D)) employed for each simulation, which was retrieved from the Earth System Documentation website (`https://search.es-doc.org`, access date 2018/03/18) as well as in the models' documentation. (top) Maps correspond to the strongest (GFDL-CM3, top) and the weakest (MIROC5, second-bottom) annual mean correlations and the multimodel mean of the correlation maps (center), for the annual means (left), the DJF means (center) and the JJA means (right). Dots indicate significant correlation at the 95% level and grey color indicates that the annual or seasonal mean of leaf area index is null in at least one of the year of the 23-year period.

coefficients over areas with SAT warmer than GST (Figure 2.4). Thus, an increase in LAI over these areas, associated with higher evapotranspiration and the induced cooling of soil, leads to SAT much higher than GST and to larger differences between air and ground temperatures. Although the CMIP5 ensemble includes models with prescribed and dynamic vegetation, these results do not show any apparent relationship with the vegetation mode employed in the simulations (Figure 2.7).

The effect of changes in soil moisture (in all phases) on the relationship between air and ground temperatures is significant over most of the domain in JJA for the majority of the models (Figure 2.8). In JJA, the significant correlation coefficients between temperature differences and soil moisture are negative for most of the models with significant positive correlation coefficients over fewer areas, in agreement with results for vegetation cover. The correlation coefficients are significantly negative throughout the western part of the domain for the models that showed large and positive GST-SAT differences in JJA over the same areas (Figure 2.4) (models using the CLM4, the MATSIRO, the LM3, the BCC, and the MOSES2 LSMs), which means that an increase (decrease) in soil moisture, related to higher (lower) evapotranspiration and the cooling (warming) of soil, reduces (increases) the gap between air and ground temperatures. Results for the rest of the models show higher spatial variability with significant positive and negative correlation coefficients over the domain (Figures A.9-A.11). There are fewer areas with significant correlation for the DJF and annual means, presenting more discrepancies among models in the correlation sign. In DJF, models show wider areas with significant positive correlation coefficients than in JJA, which may indicate the presence of freezing phenomena and the decrease of water and energy exchanges between the atmosphere and the subsurface. Meanwhile, there is a combination of significant positive and negative correlation coefficients over the domain for the annual mean, with most of the models displaying negative correlation

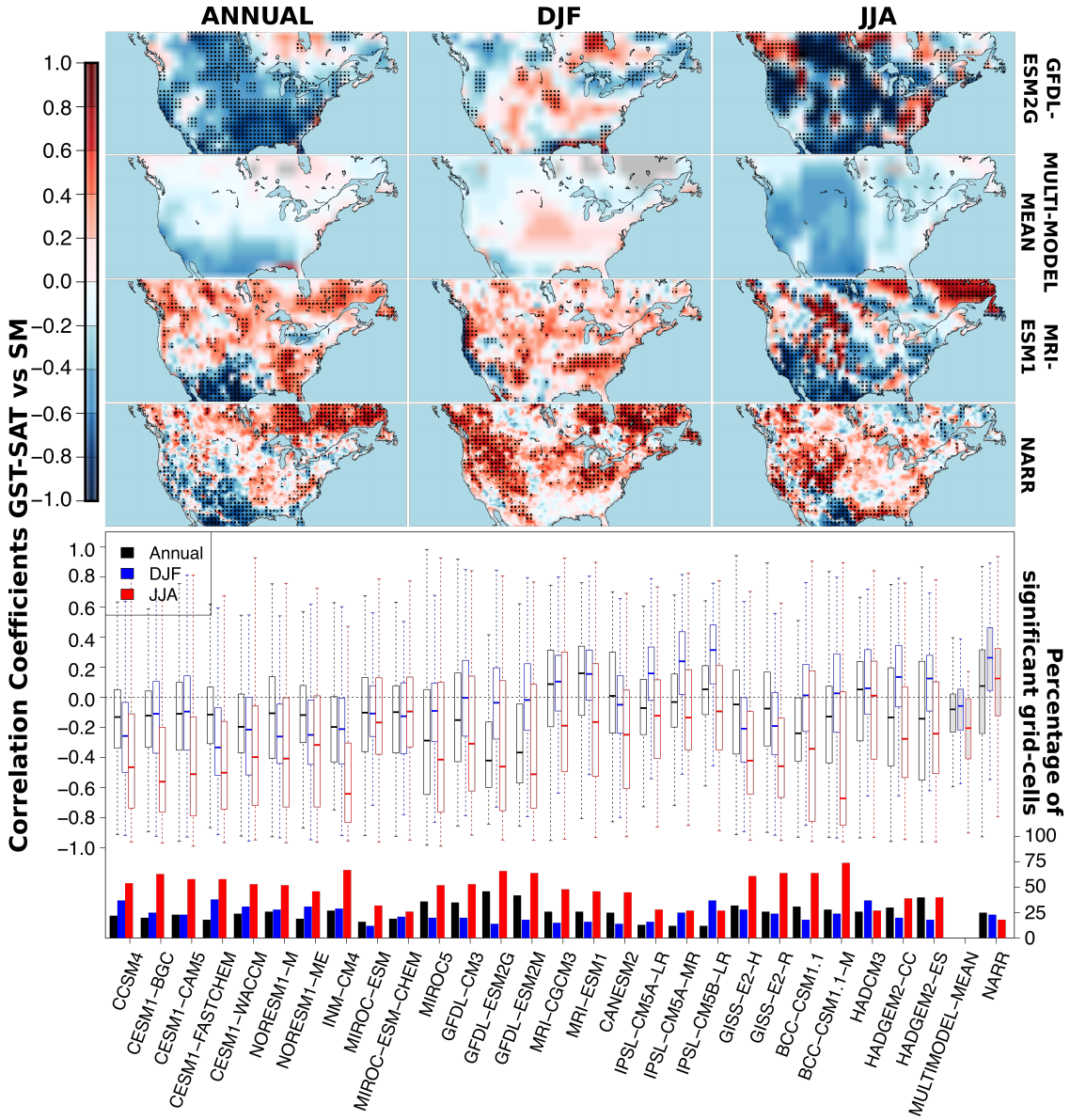

Figure 2.8: Temporal correlation, point-to-point, between monthly soil moisture in all phases at the first 10 cm (SM) and the absolute values of the temperature differences for the annual mean (black), for mean DJF (blue) and mean JJA (red) of each model for the period 1979-2001. (bottom) Boxplots (75th and 25th spatial percentiles (boxes), medians (center line), maximums and minimums (extremes of dashed lines)) of the correlation maps. Outliers (points located 1.5 times the interquartile range above the upper quartile and bellow the lower quartile) are not included. Bars at the bottom of the boxplots indicate the percentages of land grid cells with significant correlation at the 95% level using a phase-randomizing bootstrapping technique with 1000 Monte Carlo runs (Ebisuzaki, 1997). (top) Maps correspond to the strongest (GFDL-ESM2G, top) and the weakest (MRI-ESM1, second-bottom) annual mean correlations, the multimodel mean of the correlation maps (center) and the NARR product (bottom), for the annual means (left), the DJF means (center) and the JJA means (right). Dots indicate significant correlation at the 95% level and grey color indicates that the annual or seasonal mean of soil moisture is null in at least one of the year of the 23-year period.

coefficients at low latitudes. The NARR product exhibits fewer areas with significant correlation than the majority of the models, indicating positive correlation in DJF and a combination of positive correlation coefficients at high latitudes and negative correlation coefficients at low latitude for the annual mean.

The evolution of soil moisture, vegetation and snow cover directly depends on the simulation of precipitation rates (in all phases) at the surface. Within the CMIP5 models, precipitation rates are generally inversely correlated with the temperature difference, i. e. the larger the precipitation rates the smaller the differences between GST and SAT. However, results show large spatial and model variability at annual and seasonal scales (Figures 2.9 and A.12-A.14). In JJA, most of the models show significant negative correlation coefficients in the western part of the domain, in agreement with soil moisture and vegetation results, as well as a few grid cells with significant positive correlation. The MPI models show the largest area with significant positive correlation coefficients throughout the eastern part of the domain. For the annual analysis, models show fewer areas with significant correlation coefficients, being negative for most of the models at low latitudes and positive at some sporadic grid cells. In DJF, most of the models show areas with positive and negative correlation coefficients, but the significant areas are reduced in comparison with results in JJA. The significant positive correlation coefficients cover the central area of the domain, east the Rocky Mountains for most of the models, while the negative correlation coefficients are shown in eastern Canada by the majority of the models. Although the areas with significant positive correlation coefficients are in agreement with the snow analysis for most of the models, the areas with significant negative correlation coefficients over eastern Canada are similar to the soil moisture results for some of the models. The NARR product estimates a weaker relationship between precipitation rates and the GST-SAT metric than the CMIP5 models at annual and seasonal scales, reproducing

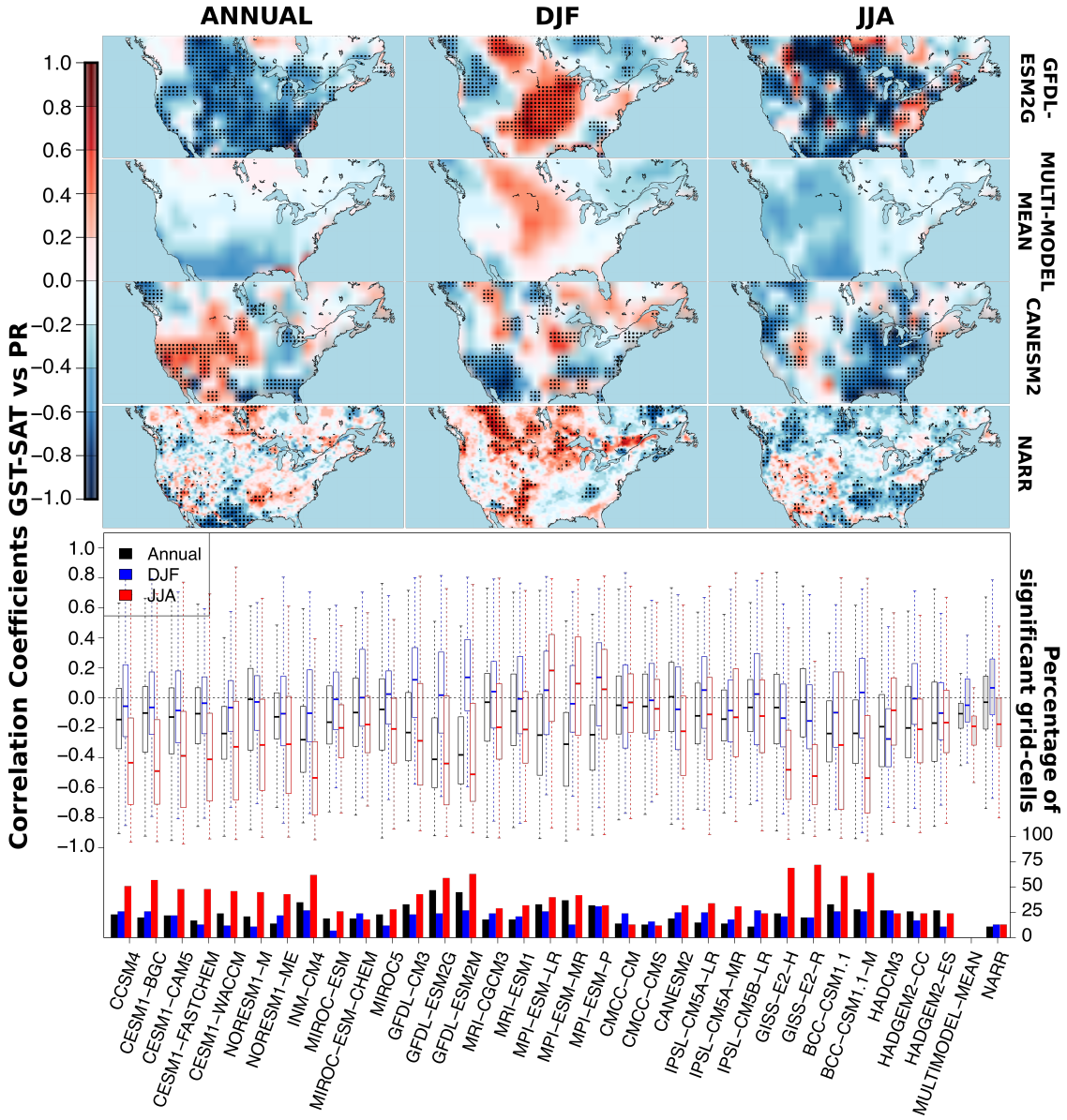

Figure 2.9: Temporal correlation, point-to-point, between monthly precipitation rates in all phases (PRs) and the absolute values of the temperature differences for the annual mean (black), for mean DJF (blue) and mean JJA (red) of each model for the period 1979-2001. (bottom) Boxplots (75th and 25th spatial percentiles (boxes), medians (center line), maximums and minimums (extremes of dashed lines)) of the correlation maps. Outliers (points located 1.5 times the interquartile range above the upper quartile and bellow the lower quartile) are not included. Bars at the bottom of the boxplots indicate the percentages of land grid cells with significant correlation at the 95% level using a phase-randomizing bootstrapping technique with 1000 Monte Carlo runs (Ebisuzaki, 1997). (top) Maps correspond to the strongest (GFDL-ESM2G, top) and the weakest (CANESM2, second-bottom) annual mean correlations, the multimodel mean of the correlation maps (center) and the NARR product (bottom), for the annual means (left), the DJF means (center) and the JJA means (right). Dots indicate significant correlation at the 95% level and grey color indicates that the annual or seasonal mean of precipitation is null in at least one of the year of the 23-year period.

the seasonality observed within the models.

2.4.3 Temporal evolution of air and ground temperature relationships

We evaluate the temporal stability of the annual relationships between GST and SAT by computing the multimodel mean of the temperature difference and its zonal average over the historical and future projection intervals (Figure 2.10). There is a small discontinuity at the end of the historical simulation, due to the annual variability and the use of a different number of models in the historical ensemble and in each RCP ensemble (See Table A.1 for a list of the ensemble members for each experiment). Such discontinuity is within the range of climate variability, thus it does not affect our results and conclusions. The multimodel mean of the annual temperature difference is temporally stable during the Historical period (1861-2005) for the entire domain, although it varies with latitude (Figure 2.10). The temperature difference is higher at northern latitudes (Figure 2.10a) than at southern latitudes (Figure 2.10b), mainly because of the insulating effect of snow cover on air and ground temperature relationships in DJF as was shown in Figure 2.6. For the future simulations (RCP4.5 and RCP8.5), the value of the temperature difference is maintained at low latitudes, while it decreases at high latitudes under both RCP scenarios, converging to the low-latitude values.

The ensemble spread of the temperature difference is large, reaching about 3.0 K (two standard deviations) for the historical simulation at high and low latitudes (Figure 2.10). At high latitudes and for the RCP4.5 and RCP8.5 simulations, the ensemble spread decreases to about 1.5 K by 2100. Examining the temporal variability of the projected temperature difference by each individual LSM reveals that not all the

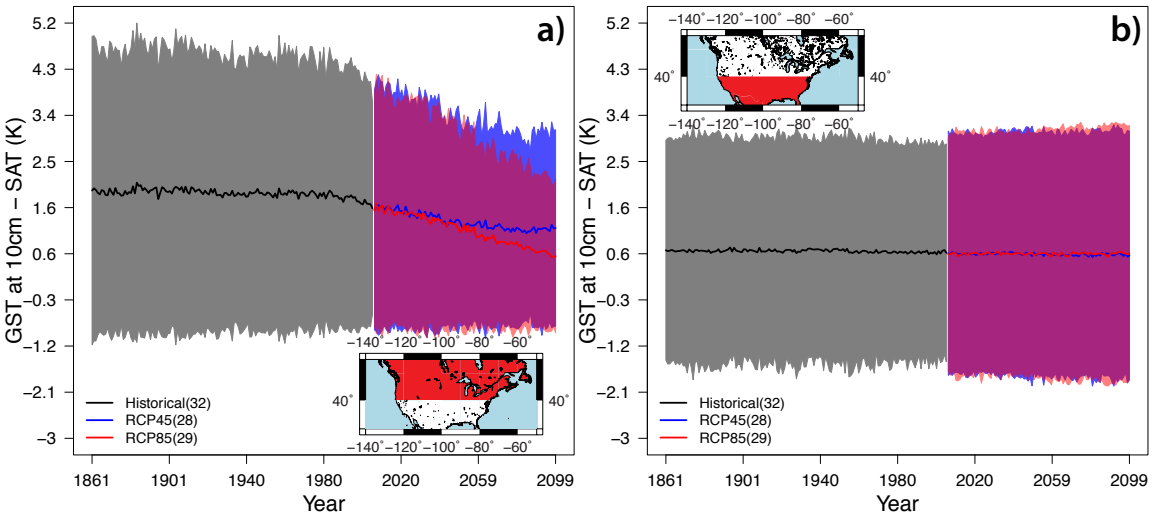

Figure 2.10: Spatial multimodel mean and two standard deviations of the difference between GST and SAT, (a) at North American high latitudes from 40°N to 55°N, and (b) at North American low latitudes from 25°N to 40°N. The number of models used in the calculations is indicated in brackets.

LSMs yield a change in the air and ground temperature relationship within the RCP simulations (Figures A.15 and A.16). For example, GCMs showing negative spatial correlation coefficients in the comparison with observations (Table 2.2) (the models using the JSBACH, and the ORCHIDEE LSMs, as well as the HADGEM2 models) do not project a decrease in the temperature difference at high latitudes and do not simulate a different value for the GST-SAT metric at low and high latitudes. Although the CMCC-CM model also shows a negative correlation coefficient with observations, this model projects a change in the temperature difference at high and low latitudes with very low spatial variability. While the CMCC-CMS model, which used the same LSM with coarser resolution than the CMCC-CM model, is spatially positively correlated with observations, but does not show a future change in the air-ground relationship and non spatial variability. The correlation coefficients between the CANESM2 model and the observations is almost zero, and this model does not include either spatial or temporal variability in the behavior of the relationship between air and ground

temperatures. The models using the LM3 LSM show similar results with a very small change in the future temperature difference at high latitudes and very low spatial variability, despite using different vertical resolutions, parameterizations (aerosols and atmospheric chemistry) and ocean components (Appendix 9.A Flato et al., 2013). The three models using the MATSIRO LSM coupled to different versions of the same atmospheric model with different horizontal and vertical resolutions display similar values and behavior of GST-SAT at high latitudes, while the MIROC5 GCM differs from the other two GCMs during the first century of the historical simulation at low latitudes. None of the models using the MATSIRO LSM shows a higher value of the temperature difference at high latitudes than at low latitudes, in opposition to the observations and the multimodel mean. The models using the CLM4 LSM, which show a slightly better performance in the comparison with observations than the models using the previously mentioned LSMs, yield similar behavior for GST-SAT, despite being coupled to different versions of atmospheric models (different parameterizations of aerosols and atmospheric chemistry) with different grid resolutions. All of them project a future change in the temperature difference and simulate a higher value of GST-SAT at high latitudes than at low latitudes. Additionally, the models using the BCC-AVIM1.0 LSM, which is based on a previous version of the CLM LSM (Wu et al., 2013), present similar results to those of the CLM4 LSM. The two BCC models show similar relationships between GST and SAT at high latitudes, but these relationships differ by about 1 K at low latitudes; with the coarsest model yielding the lower temperature difference (Figure A.16). The INM model and the GISS models, which are spatially highly correlated to observations but showing large RMSE values, include the change in the GST-SAT parameter under the RCPs at high latitudes and the spatial variability. However, these models shows negative temperature differences averaged at low latitudes in contrast to the observations and the rest of the CMIP5

models. The models using the HAL LSM, which show enhanced performance against observations in comparison with the rest of the models, project a change in the temperature difference as well as include the spatial variability. The models using the HAL LSM do not show any difference in these results despite using different atmospheric parameterizations (aerosols and atmospheric chemistry (Appendix 9.A Flato et al., 2013).

As in Subsection 2.4.2, we evaluate the long-term influence of near-surface processes on GST and SAT relationships within the CMIP5 simulations by computing the point-to-point correlation coefficients between the annual absolute values of the air-ground temperature difference and the annual means of the CMIP5 variables associated with snow cover, vegetation cover, precipitation and soil moisture at each grid cell for the historical, RCP4.5 and RCP8.5 simulations (Figures A.17-A.20). We find high positive correlation coefficients between snow cover and the temperature difference at high latitudes for the Historical (1861-2005) and RCP experiments (2006-2099), with the INM and the GISS models showing large areas with significant negative correlation coefficients where SAT is higher than GST (Figure A.17). The correlation coefficients are significant under both RCP scenarios over most areas for the CMIP5 models, indicating a strong effect of snow changes on the characterization of air and ground temperatures in the future. The high correlation coefficients of the CMIP5 models at high latitudes are indicative of the covariance between the future decrease in the temperature difference shown in Figure 2.10a and the expected decrease in snow cover due to increased SAT projected at high latitudes (IPCC, 2013; Koven et al., 2013). The relationship between vegetation cover and the temperature difference is negative for most of the models within the CMIP5 historical and future simulations, except for the MIROC5 model that shows positive correlation coefficients over a large area under the RCP8.5 scenario (Figure A.18). For the historical period, most of the

models show larger negative correlation coefficients at low latitudes and the eastern US. Meanwhile, most of the models under RCP4.5 and RCP8.5 scenarios show larger negative correlation coefficients at high latitudes and in the western US than those in the historical simulation. The increased influence of vegetation on the characterization of air and ground temperature relationships is likely related to the increasing area over which vegetation becomes dominant over snow cover in the two future experiments as well as to the increases in LAI simulated for most of the models as a response to increasing Carbon Dioxide (CO_2), regardless the vegetation model employed in the simulations (Mahowald et al., 2016). The strong correlation between LAI and the temperature difference shown by the majority of the models illustrates the important role played by vegetation in controlling air and ground temperature relationships within the historical and future simulations. The correlation results between precipitation rates and the temperature differences are negative over most areas of the domain for the majority of the models, indicating a future intensification of the precipitation effect on the characterization of air and ground temperature relationships in most of the models (23 of the 29 CMIP5 models with RCP experiments), although each shows a different increase in correlation depending on the climate scenario (Figure A.19). The multimodel mean of the correlation maps shows the agreement among models in the negative correlation between soil moisture and the temperature difference at low latitudes, and the increased number of grid cells with positive correlation coefficients at high latitudes under the RCP8.5 (Figure A.20).

2.5 Discussion

2.5.1 Uncertainty in the comparison between simulations and observations

We used the difference between SAT and GST to compare the characterization of air and ground temperature relationships within the CMIP5 simulations and the NARR product with observations. Although there are other useful variables to study air-ground coupling, such as surface energy fluxes, we used temperature because it is one of the variables with longer and broader observational data records. However, we have found several difficulties in the search and treatment of air and ground temperature measurements at US and Canadian stations. The employed observational data cover most of the domain, except north eastern Canada, but some assumptions were made to allow the comparison between models, reanalysis, and observations. These considerations include the approximation of daily means of ground temperatures at Canadian stations using soil measurements at 12 a.m. and 12 p.m., as well as the representation of the period mean from 1979 to 2001 using data at grid cells with more than 10 annual values. Even considering these caveats, the air-ground temperature difference from observations at US and Canadian stations is consistent with the expected results, showing annual ground temperatures higher than annual surface air temperatures and larger air-ground temperature differences at higher altitude and latitude, where snow and soil freezing phenomena are active (Beltrami, 1996; Goodrich, 1982; Pollack et al., 2005; Smerdon et al., 2004, 2006; Sokratov et al., 2002).

Additionally, there are other inconsistencies in making a direct comparison between simulations and observations as station data show irregularities in terms of

ground cover, elevation, soil type, station environment, instruments, observational period and time of observations. All those factors, and land cover in particular, determine the magnitude of the difference between air and ground temperatures as we have seen in Subsection 2.4.2, thus we assume that there are uncertainties in the presented comparison between models and observations arising from these factors. Spatial and temporal averages could reduce the data noise from these irregularities, hence several studies employed averages to compare simulations and observations in many studies (Robock et al., 1998, 2003; Srinivasan et al., 2000; Xia et al., 2013). We use the average of the data at all the stations contained in a $1^\circ \times 1^\circ$ grid cell ($\sim$ 110 km $\times$ 90 km) and the average from 1979 to 2001 to provide a more reliable comparison between simulations and observations. Nevertheless, increasing soil temperature measurements and enhancing the quality of observational data may provide more meaningful comparisons between simulations and observations, needed to improve the characterization of air and ground temperature relationships and associated phenomena within climate models and reanalyses.

The definition of air temperature at 2 m within the models can be another source of uncertainty in the comparison between models and observations. Air temperature at 2 m within models is defined using the displacement height as reference, which places 2 m-air temperature at approximately 2 m above 2/3 of the obstacle height. That is, in a 30 m height forest, the SAT variable would contain air temperatures at approximately 22 m height. Results of models and observations shown in Figures 2.2, 2.3 and 2.4 reveal some models with similar patterns of temperature differences to those of observations, despite using SAT at 2 m above the displacement height, suggesting that the effect of using the model's definition of SAT on our results is small. Another approach to evaluate the uncertainties arising from the SAT definition in climate models is to repeat the analysis using the differences between GST and Surface

Temperature (ST). STs in a model correspond to air, soil or canopy temperatures of a thin layer close to the surface, depending on the land cover. We obtain results similar to those shown in Figure 2.2 when SAT is replaced by ST as the air temperature variable (Figure A.21), reinforcing the use of SAT in this analysis.

2.5.2 Effect of near-surface processes on the characterization of air and ground temperature relationships

Using a simple metric defined as the difference between air and soil temperatures, we have been able to distinguish large differences among the CMIP5 models as well as their discrepancies with observations. In this study, this metric also has been employed to evaluate the influence of near-surface processes on the energy and water balances at the surface within models and reanalysis. This analysis has shown seasonal differences in the effect of the near-surface processes on the temperature differences. Snow cover has been shown to be the main driver in winter, increasing the temperature differences over most areas of the domain and for the annual mean at high latitudes. The high albedo of snow cover and its low thermal conductivity limit the net-radiation absorbed by the soil and the energy exchanges between the lower atmosphere and the surface. These properties lead to the insulating effect of snow cover yielding warmer ground temperatures in winter and increasing the difference between air and ground temperatures (e.g. Goodrich, 1982; Pollack et al., 2005; Smerdon et al., 2004, 2006; Sokratov et al., 2002). The CMIP5 models and the NARR product reproduce the effect of snow cover on the temperature difference, being the main reason for the lower model variability in DJF than in JJA, as well as for the better model performance in reproducing the DJF observations. In JJA, other near-surface processes, such as vegetation cover, soil moisture and precipitation rates, have been found to influence

temperature differences within the models, resulting in larger spatial variability and differences among models than during boreal winter. These processes are generally inversely related to the temperature differences in JJA over the western domain, indicating the influence of changes in vegetation cover, soil moisture and precipitation on the energy and water balances over this area within the CMIP5 simulations. The negative relationship between these processes and the GST-SAT metric is explained by their effect on evapotranspiration (Bonan, 2002; Lin et al., 2003; Pollack et al., 2005; Smerdon et al., 2006). When energy is not a limitation (summer), increases in vegetation cover, soil moisture, and precipitation are associated with enhanced evapotranspiration rates, which dissipate heat. Thus, the soil cools and the difference between ground and air temperatures decreases, when ground temperatures are higher than air temperatures. At annual scales, the effect of these surface processes is reduced, showing a significant effect only at low latitudes of the domain, where the effect of snow cover is weaker. In DJF, soil moisture and precipitation rates are found to be directly related to the temperature differences over some areas of the domain for most of the models, with models indicating a weaker role of these processes in the winter temperature differences than in JJA. The seasonal differences in the effect of soil moisture and precipitation likely are associated with snow cover and freezing phenomena in winter and increases in the energy and water exchanges at the surface in summer.

2.5.3 Dependence on the LSM

The CMIP5 climate models are not independent (e.g. Knutti et al., 2013). Models from different institutions may share model components or use different versions of the same model component, such as LSMs or atmospheric models. However, the LSM-dependency shown in our results appears to be robust, while the atmospheric models

apparently play a secondary role in the simulation of the difference between air and ground temperatures. To investigate this hypothesis, we calculate the Root Mean Square Errors and the spatial correlation coefficients between each pair of GCMs included in the CMIP5 ensemble, using the mean of the annual temperature difference (GST-SAT) for the period of comparison with observations (1979-2001), as well as the means of the annual GST and SAT variables separately (Figures 2.11, A.22 and A.23). To allow the comparison of the simulated GST and SAT across models, the annual temporal series of GST and SAT are normalized before estimating the period mean, by subtracting the mean of the historical period (1861-2005) and dividing by the standard deviation at each grid cell. Assuming that the GST variable is calculated by the LSM and the SAT variable is calculated by the atmospheric model (see CMIP5 metadata requirements), we can study the main source of model variability in the characterization of GST and SAT relationships. As expected, the correlation coefficients for the GST-SAT parameter are large for models using the same LSM, although there are three models (the HADCM3, the CMCC-CMS and the MIROC5) yielding results different to their shared-LSM simulations. These simulations and their shared-LSM simulations differ in the employed horizontal and vertical resolution, and two of them (the HADCM3 and the MIROC5 simulations) also use a different version of the atmosphere and ocean components than their shared-LSM simulations (Appendix 9.A Flato et al., 2013). The spatial correlation coefficients for the normalized GST and SAT variables show positive and negative values across models without a clear relationship between these results and the model components. Nevertheless, the correlation coefficients for the SAT variable appear to be larger than those for the GST variable. RSME results using the GST-SAT parameter show low values for models using the same LSM, with the rest of the RMSE values being classified according to their LSM. RMSE values among the CMIP5 ensemble for the GST are slightly

larger than those for the SAT, indicating that GCMs differs more in simulating GST than SAT. This suggests that LSMs may contribute slightly more than atmospheric components to the different representation of the GST-SAT parameter across models.

Our results show that the LSM contribution to the CMIP5 ensemble variability in representing air-ground temperature relationships could be larger than those arising from the use of different horizontal resolutions and atmospheric parameterizations. Lytle et al., 2016 also found a LSM dependence in the analysis of surface fluxes and soil conditions among reanalyses and offline land surface model simulations, reinforcing our findings. The comparison of the reanalysis product and the models employed in this study in reproducing observations has shown that the NARR product differs more from observations than most of the CMIP5 models, due to its poor performance in reproducing the spatial pattern of GST observations, and therefore due to the employed LSM to generate the NARR final product. These results agree with previous evaluations of the NARR reanalysis. For example, Kumar et al., 2011 compared the performance of the NARR reanalysis and the CLM3.5 LSM, finding a large energy balance closing error in the NARR product, and in summary a better characterization of the surface energy and water fluxes by the LSM than by the NARR.

The LSM-dependency and the heterogeneity among results is also characteristic of the temporal evolution of the temperature difference. The GST-SAT from the multimodel mean projects a future change at high latitudes under RCP4.5 and RCP8.5 conditions. However, some CMIP5 model simulations yield very small changes in GST-SAT difference in the future (Figures A.15 and A.16). Despite the statistical significance of the change in the air-ground temperature relationship, the model differences in the magnitude of these changes shown in our results may contribute to model variability in the projection of processes tied to air-ground coupling, such as weather extremes, carbon cycling and permafrost stability (Slater et al., 2013).

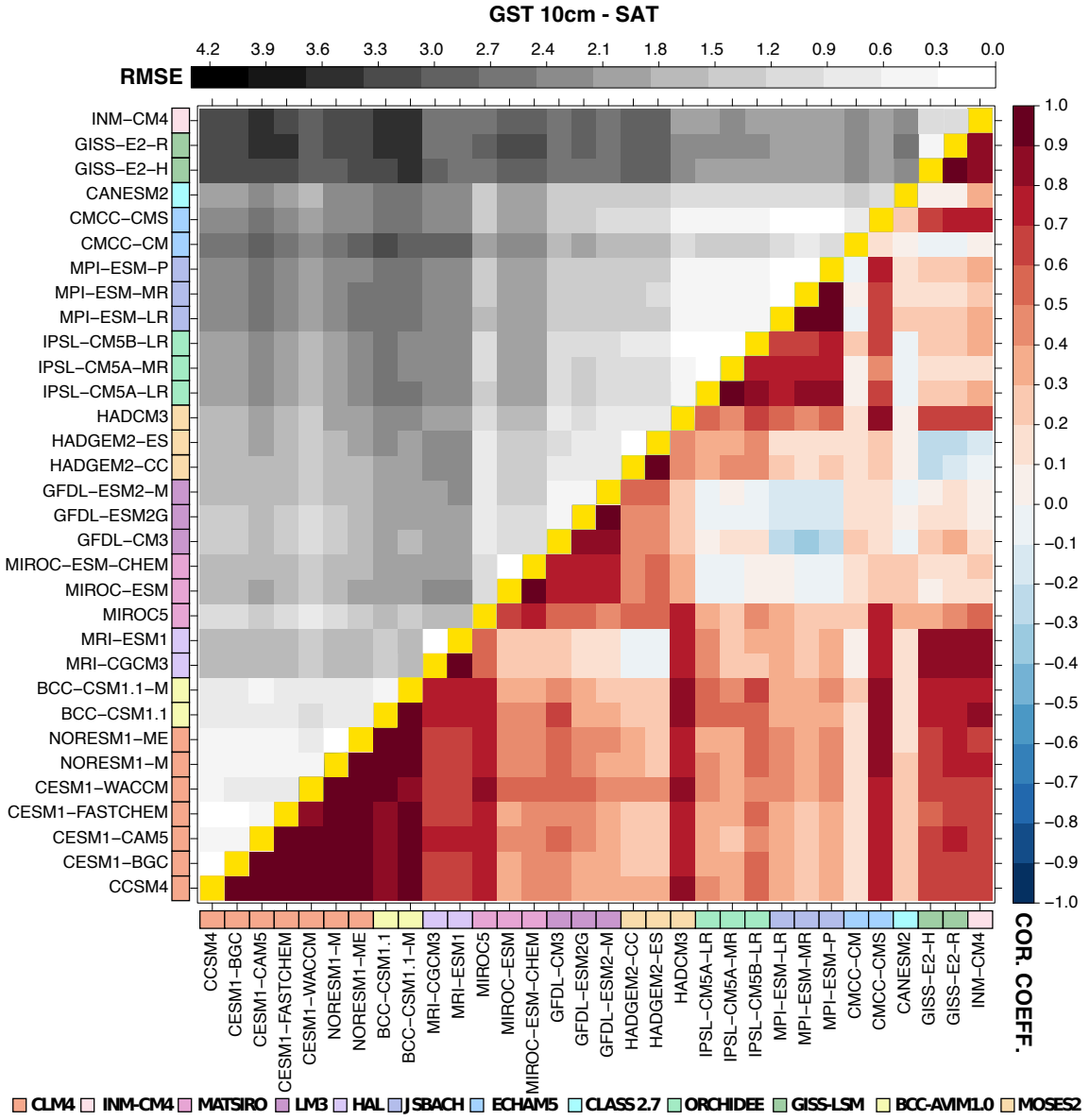

Figure 2.11: Spatial correlation coefficients and RMSE values of the annual GST-SAT differences for each pair of models within the CMIP5 ensemble for the period 1979-2001. The LSM employed by each model is indicated using a different color next to the models' name.

2.6 Conclusions

Comparison between models and observations reveals that the relationship between air and ground surface temperatures in the CMIP5 simulations displays a large range of variability and inconsistencies across GCM simulations at annual and seasonal scales. The wide range of the magnitudes of the temperature difference among GCMs, particularly in boreal summer, reveals the complexity in modelling physical processes at the land-surface boundary. Despite this large variability, the CMIP5 GCMs show different but temporally stable relationships between air and ground temperatures over the Historical simulations for North America. At low latitudes, the air-ground temperature difference is stable for the Historical and future periods under the RCP4.5 and RCP8.5 scenarios. At high latitudes, the air-ground temperature relationship changes in the future projections in response to the evolution of near-surface processes. The differences in the simulation of the energy and water balances under the influence of near-surface processes among the CMIP5 GCMs' land surface model contribute to the large variability among simulations in terms of air and ground temperature relationships. This large variability and the LSM-dependency of the results highlight the important role of LSMs in climate simulations and their possible contributions to the model variability. The heterogeneity among GCM simulations also illustrates the need to improve the treatment of the energy and water exchanges at the air-ground interface to improve the long-term simulation of the subsurface thermal state to properly assess the effect on the climate system of some potentially important positive climate feedback mechanisms such as permafrost and soil carbon stability, and high-impact phenomena like extreme events.

Bibliography

Adachi, Y., Yukimoto, S., Deushi, M., Obata, A., Nakano, H., Tanaka, T. Y., Hosaka, M., Sakami, T., Yoshimura, H., and Hirabara, M. (2013). Basic performance of a new earth system model of the Meteorological Research Institute (MRI-ESM1). *Papers in Meteorology and Geophysics* **64**, 1–19.

Beltrami, H. (1996). Active layer distortion of annual air/soil thermal orbits. *Permafrost and Periglacial Processes* **7**(2), 101–110.

— (2002). Climate from borehole data: Energy fluxes and temperatures since 1500. *Geophysical Research Letters* **29**(23), 26–1–26–4. DOI: 10.1029/2002GL015702.

Berbery, E. H., Luo, Y., Mitchell, K. E., and Betts, A. K. (2003). Eta model estimated land surface processes and the hydrologic cycle of the Mississippi basin. *Journal of Geophysical Research: Atmospheres* **108**(D22), 2156–2202. DOI: DOI:10.1029/2002JD003192.

Bonan, G. B. (2002). *Ecological climatology: concepts and applications*. Cambridge University Press, p. 678.

Broxton, P. D., Zeng, X., and Dawson, N. (2017). The Impact of a Low Bias in Snow Water Equivalent Initialization on CFS Seasonal Forecasts. *Journal of Climate* **30**(21), 8657–8671.

Christoff, P. (2016). The promissory note: COP 21 and the Paris Climate Agreement. *Environmental Politics* **25**(5), 765–787. DOI: 10.1080/09644016.2016.1191818.

Collins, W. D., Bitz, C. M., Blackmon, M. L., Bonan, G. B., Bretherton, C. S., Carton, J. A., Chang, P., Doney, S. C., Hack, J. J., Henderson, T. B., et al. (2006). The community climate system model version 3 (CCSM3). *Journal of Climate* **19**(11), 2122–2143.

Cook, B. I., Bonan, G. B., and Levis, S. (2006). Soil Moisture Feedbacks to Precipitation in Southern Africa. *Journal of Climate* **19**(17), 4198–4206. DOI: 10.1175/JCLI3856.1.

Cook, B. I., Miller, R. L., and Seager, R. (2008). Dust and sea surface temperature forcing of the 1930s "Dust Bowl" drought. *Geophysical Research Letters* **35**(8). DOI: 10.1029/2008GL033486.

Cuesta-Valero, F. J., García-García, A., Beltrami, H., and Smerdon, J. E. (2016). First Assessment of Continental Energy Storage in CMIP5 Simulations. *Geophysical Research Letters*. DOI: 10.1002/2016GL068496.

Davies, T., Cullen, M. J. P., Malcolm, A. J., Mawson, M. H., Staniforth, A., White, A. A., and Wood, N. (2005). A new dynamical core for the Met Office's global and regional modelling of the atmosphere. *Quarterly Journal of the Royal Meteorological Society* **131**(608), 1759–1782. DOI: 10.1256/qj.04.101.

Delworth, T. L., Broccoli, A. J., Rosati, A., Stouffer, R. J., Balaji, V., Beesley, J. A., Cooke, W. F., Dixon, K. W., Dunne, J., Dunne, K. A., Durachta, J. W., Findell, K. L., Ginoux, P., Gnanadesikan, A., Gordon, C. T., Griffies, S. M., Gudgel, R., Harrison, M. J., Held, I. M., Hemler, R. S., Horowitz, L. W., Klein, S. A., Knutson, T. R., Kushner, P. J., Langenhorst, A. R., Lee, H.-C., Lin, S.-J., Lu, J., Malyshev, S. L., Milly, P. C. D., Ramaswamy, V., Russell, J., Schwarzkopf, M. D., Shevliakova, E., Sirutis, J. J., Spelman, M. J., Stern, W. F., Winton, M., Wittenberg, A. T., Wyman, B., Zeng, F., and Zhang, R. (2006). GFDL's CM2 Global Coupled Climate Models. Part I: Formulation and Simulation Characteristics. *Journal of Climate* **19**(5), 643–674.

Dirmeyer, P. A., Koster, R. D., and Guo, Z. (2006). Do Global Models Properly Represent the Feedback between Land and Atmosphere? *Journal of Hydrometeorology* **7**(6), 1177–1198. DOI: 10.1175/JHM532.1.

Dirmeyer, P. A., Schlosser, C. A., and Brubaker, K. L. (2009). Precipitation, Recycling, and Land Memory: An Integrated Analysis. *Journal of Hydrometeorology* **10**(1), 278–288. DOI: 10.1175/2008JHM1016.1.

Dirmeyer, P. A., Jin, Y., Singh, B., and Yan, X. (2013). Trends in Land–Atmosphere Interactions from CMIP5 Simulations. *Journal of Hydrometeorology* **14**(3), 829–849. DOI: 10.1175/JHM-D-12-0107.1.

Donner, L. J., Wyman, B. L., Hemler, R. S., Horowitz, L. W., Ming, Y., Zhao, M., Golaz, J.-C., Ginoux, P., Lin, S.-J., Schwarzkopf, M. D., Austin, J., Alaka, G., Cooke, W. F., Delworth, T. L., Freidenreich, S. M., Gordon, C. T., Griffies, S. M., Held, I. M., Hurlin, W. J., Klein, S. A., Knutson, T. R., Langenhorst, A. R., Lee, H.-C., Lin, Y., Magi, B. I., Malyshev, S. L., Milly, P. C. D., Naik, V., Nath, M. J., Pincus, R., Ploshay, J. J., Ramaswamy, V., Seman, C. J., Shevliakova, E., Sirutis, J. J., Stern, W. F., Stouffer, R. J., Wilson, R. J., Winton, M., Wittenberg, A. T., and Zeng, F. (2011). The Dynamical Core, Physical Parameterizations, and Basic Simulation Characteristics of the Atmospheric Component AM3 of the GFDL Global Coupled Model CM3. *Journal of Climate* **24**(13), 3484–3519.

Dunne, J. P., John, J. G., Adcroft, A. J., Griffies, S. M., Hallberg, R. W., Shevliakova, E., Stouffer, R. J., Cooke, W., Dunne, K. A., Harrison, M. J., et al. (2012). GFDL's ESM2 global culled climate-carbon earth system models. Part I: Physical formulation and baseline simulation characteristics. *J. Climate* **25**, 6646–6665.

Ebisuzaki, W. (1997). A Method to Estimate the Statistical Significance of a Correlation When the Data Are Serially Correlated. *Journal of Climate* **10**(9), 2147–2153. DOI: doi:10.1175/1520-0442(1997)010<2147:AMTETS>2.0.CO;2.

Ek, M. B., Mitchell, K. E., Lin, Y., Rogers, E., Grunmann, P., Koren, V., Gayno, G., and Tarpley, J. D. (2003). Implementation of Noah land surface model advances in the National Centers for Environmental Prediction operational mesoscale Eta model. *Journal of Geophysical Research: Atmospheres* **108**(D22), 2156–2202. DOI: doi:10.1029/2002JD003296.

Essery, R., Best, M., Betts, R., Cox, P. M., and Taylor, C. M. (2003). Explicit representation of subgrid heterogeneity in a GCM land surface scheme. *Journal of Hydrometeorology* **4**(3), 530–543.

Ferguson, C. R., Wood, E. F., and Vinukollu, R. K. (2012). A Global Intercomparison of Modeled and Observed Land–Atmosphere Coupling. *Journal of Hydrometeorology* **13**(3), 749–784. DOI: 10.1175/JHM-D-11-0119.1.

Fischer, E., Seneviratne, S., Lüthi, D, and Schär, C (2007). Contribution of land-atmosphere coupling to recent European summer heat waves. *Geophysical Research Letters* **34**(6).

Flato, G., Marotzke, J., Abiodun, B., Braconnot, P., Chou, S., Collins, W., Cox, P., Driouech, F., Emori, S., Eyring, V., Forest, C., Gleckler, P., Guilyardi, E., Jakob, C., Kattsov, V., Reason, C., and Rummukainen, M. (2013). "Evaluation of Climate Models". In: *Climate Change 2013: The Physical Science Basis. Contribution of Working Group I to the Fifth Assessment Report of the Intergovernmental Panel on Climate Change*. Ed. by T. Stocker, D. Qin, G.-K. Plattner, M. Tignor, S. Allen, J. Boschung, A. Nauels, Y. Xia, V. Bex, and P. Midgley. Cambridge, United Kingdom and New York, NY, USA: Cambridge University Press. Chap. 9, pp. 741–866. DOI: 10.1017/CBO9781107415324.020.

García-García, A., Cuesta-Valero, F. J., Beltrami, H., and Smerdon, J. E. (2019). Characterization of Air and Ground Temperature Relationships within the CMIP5 Historical and Future Climate Simulations. *Journal of Geophysical Research: Atmospheres*(124), 3903–3929. DOI: https://doi.org/10.1029/2018JD030117.

Goodrich, L. (1982). The influence of snow cover on the ground thermal regime. *Canadian geotechnical journal* **19**(4), 421–432.

Guo, Z., Dirmeyer, P. A., Koster, R. D., Sud, Y. C., Bonan, G., Oleson, K. W., Chan, E., Verseghy, D., Cox, P., Gordon, C. T., McGregor, J. L., Kanae, S., Kowalczyk,

E., Lawrence, D., Liu, P., Mocko, D., Lu, C.-H., Mitchell, K., Malyshev, S., McAvaney, B., Oki, T., Yamada, T., Pitman, A., Taylor, C. M., Vasic, R., and Xue, Y. (2006). GLACE: The Global Land–Atmosphere Coupling Experiment. Part II: Analysis. *Journal of Hydrometeorology* **7**(4), 611–625. DOI: 10.1175/JHM511.1.

Hauser, M., Orth, R., and Seneviratne, S. I. (2016). Role of soil moisture versus recent climate change for the 2010 heat wave in western Russia. *Geophysical Research Letters* **43**(6), 2819–2826. DOI: 10.1002/2016GL068036.

Henderson-Sellers, A., Pitman, A. J., Love, P. K., Irannejad, P., and Chen, T. H. (1995). The Project for Intercomparison of Land Surface Parameterization Schemes (PILPS): Phases 2 and 3. *Bulletin of the American Meteorological Society* **76**(4), 489–503. DOI: 10.1175/1520-0477(1995)076<0489:TPFIOL>2.0.CO;2.

Hirsch, A. L., Pitman, A. J., Seneviratne, S. I., Evans, J. P., and Haverd, V. (2014). Summertime maximum and minimum temperature coupling asymmetry over Australia determined using WRF. *Geophysical Research Letters* **41**(5), 1546–1552. DOI: 10.1002/2013GL059055.

Hourdin, F., Foujols, M., Codron, F., Guemas, V., Dufresne, J.-L., Bony, S., Denvil, S., Guez, L., Lott, F., and Ghattas, J (2012). Climate and sensitivity of the IPSL-CM5A coupled model: impact of the LMDZ atmospheric grid configuration. *Clim. Dynam.* **10**.

Hurtt, G. C., Chini, L. P., Frolking, S., Betts, R. A., Feddema, J., Fischer, G., Fisk, J. P., Hibbard, K., Houghton, R. A., Janetos, A., Jones, C. D., Kindermann, G., Kinoshita, T., Klein Goldewijk, K., Riahi, K., Shevliakova, E., Smith, S., Stehfest, E., Thomson, A., Thornton, P., Vuuren, D. P. van, and Wang, Y. P. (2011). Harmonization of land-use scenarios for the period 1500–2100: 600 years of global gridded annual land-use transitions, wood harvest, and resulting secondary lands. *Climatic Change* **109**(1-2), 117–161. DOI: 10.1007/s10584-011-0153-2.

IPCC (2013). *Climate Change 2013: The Physical Science Basis. Contribution of Working Group I to the Fifth Assessment Report of the Intergovernmental Panel on Climate Change*. Cambridge, United Kingdom and New York, NY, USA: Cambridge University Press, p. 1535. DOI: 10.1017/CBO9781107415324.

Jaeger, E. B. and Seneviratne, S. I. (2011). Impact of soil moisture–atmosphere coupling on European climate extremes and trends in a regional climate model. *Climate Dynamics* **36**(9, 1432-0894), 1919–1939.

Kirkevåg, A., Iversen, T., Seland, Ø., Hoose, C., Kristjánsson, J. E., Struthers, H., Ekman, A. M. L., Ghan, S., Griesfeller, J., Nilsson, E. D., and Schulz, M. (2013). Aerosol–climate interactions in the Norwegian Earth System Model –NorESM1-M. *Geosci. Model Dev.* **6**(1), 207–244. DOI: 10.5194/gmd-6-207-2013.

Knist, S., Goergen, K., Buonomo, E., Christensen, O. B., Colette, A., Cardoso, R. M., Fealy, R., Fernández, J., García-Díez, M., Jacob, D., Kartsios, S., Katragkou, E., Keuler, K., Mayer, S., Meijgaard, E. van, Nikulin, G., Soares, P. M. M., Sobolowski, S., Szepszo, G., Teichmann, C., Vautard, R., Warrach-Sagi, K., Wulfmeyer, V., and Simmer, C. (2016). Land-atmosphere coupling in EURO-CORDEX evaluation experiments. *Journal of Geophysical Research: Atmospheres*. DOI: 10.1002/2016JD025476.

Knutti, R., Masson, D., and Gettelman, A. (2013). Climate model genealogy: Generation CMIP5 and how we got there. *Geophysical Research Letters* **40**(6), 1194–1199. DOI: 10.1002/grl.50256.

Koster, R. D. and Suarez, M. J. (1995). Relative contributions of land and ocean processes to precipitation variability. *Journal of Geophysical Research: Atmospheres* **100**(D7), 13775–13790. DOI: 10.1029/95JD00176.

Koster, R. D., Dirmeyer, P. A., Hahmann, A. N., Ijpelaar, R., Tyahla, L., Cox, P., and Suarez, M. J. (2002). Comparing the Degree of Land–Atmosphere Interaction in Four Atmospheric General Circulation Models. *Journal of Hydrometeorology* **3**(3), 363–375. DOI: 10.1175/1525-7541(2002)003<0363:CTDOLA>2.0.CO;2.

Koster, R. D., Dirmeyer, P. A., Guo, Z., Bonan, G., Chan, E., Cox, P., Gordon, C. T., Kanae, S., Kowalczyk, E., Lawrence, D., Liu, P., Lu, C.-H., Malyshev, S., McAvaney, B., Mitchell, K., Mocko, D., Oki, T., Oleson, K., Pitman, A., Sud, Y. C., Taylor, C. M., Verseghy, D., Vasic, R., Xue, Y., and Yamada, T. (2004). Regions of Strong Coupling Between Soil Moisture and Precipitation. *Science* **305**(5687), 1138–1140. DOI: 10.1126/science.1100217.

Koster, R. D., Suarez, M. J., and Schubert, S. D. (2006a). Distinct Hydrological Signatures in Observed Historical Temperature Fields. *Journal of Hydrometeorology* **7**(5), 1061–1075. DOI: 10.1175/JHM530.1.

Koster, R. D., Sud, Y. C., Guo, Z., Dirmeyer, P. A., Bonan, G., Oleson, K. W., Chan, E., Verseghy, D., Cox, P., Davies, H., Kowalczyk, E., Gordon, C. T., Kanae, S., Lawrence, D., Liu, P., Mocko, D., Lu, C.-H., Mitchell, K., Malyshev, S., McAvaney, B., Oki, T., Yamada, T., Pitman, A., Taylor, C. M., Vasic, R., and Xue, Y. (2006b). GLACE: The Global Land–Atmosphere Coupling Experiment. Part I: Overview. *Journal of Hydrometeorology* **7**(4), 590–610. DOI: 10.1175/JHM510.1.

Koven, C. D., Riley, W. J., and Stern, A. (2013). Analysis of Permafrost Thermal Dynamics and Response to Climate Change in the CMIP5 Earth System Models. *Journal of Climate* **26**(6), 1877–1900. DOI: 10.1175/JCLI-D-12-00228.1.

Krinner, G., Viovy, N., Noblet-Ducoudré, N. de, Ogée, J., Polcher, J., Friedlingstein, P., Ciais, P., Sitch, S., and Prentice, I. C. (2005). A dynamic global vegetation model for studies of the coupled atmosphere-biosphere system. *Global Biogeochemical Cycles* **19**(1).

Kumar, S. and Merwade, V. (2011). Evaluation of NARR and CLM3.5 outputs for surface water and energy budgets in the Mississippi River Basin. *Journal of Geophysical Research: Atmospheres* **116**(D8).

Lamarque, J., Emmons, L., Hess, P., Kinnison, D. E., Tilmes, S, Vitt, F., Heald, C., Holland, E. A., Lauritzen, P., and Neu, J (2012). CAM-chem: Description and evaluation of interactive atmospheric chemistry in the Community Earth System Model. *Geosci. Model Dev* **5**(2), 369–411.

Lin, X., Smerdon, J. E., England, A. W., and Pollack, H. N. (2003). A model study of the effects of climatic precipitation changes on ground temperatures. *Journal of Geophysical Research: Atmospheres* **108**(D7), 2156–2202. DOI: 10.1029/2002JD002878.

Lorenz, R., Argüeso, D., Donat, M. G., Pitman, A. J., Hurk, B. van den, Berg, A., Lawrence, D. M., Chéruy, F., Ducharne, A., Hagemann, S., Meier, A., Milly, P. C. D., and Seneviratne, S. I. (2016). Influence of land-atmosphere feedbacks on temperature and precipitation extremes in the GLACE-CMIP5 ensemble. *Journal of Geophysical Research: Atmospheres* **121**(2), 607–623. DOI: 10.1002/2015JD024053.

Lytle, W. and Zeng, X. (2016). Coupled Evaluation of Below- and Aboveground Energy and Water Cycle Variables from Reanalysis Products over Five Flux Tower Sites in the United States. *Journal of Hydrometeorology* **17**(7), 2105–2119. DOI: 10.1175/JHM-D-15-0224.1.

Mahowald, N., Lo, F., Zheng, Y., Harrison, L., Funk, C., Lombardozzi, D., and Goodale, C. (2016). Projections of leaf area index in earth system models. *Earth System Dynamics* **7**(1), 211–229. DOI: 10.5194/esd-7-211-2016.

Marsh, D. R., Mills, M. J., Kinnison, D. E., Lamarque, J.-F., Calvo, N., and Polvani, L. M. (2013). Climate Change from 1850 to 2005 Simulated in CESM1(WACCM). *Journal of Climate* **26**(19), 7372–7391.

Melo-Aguilar, C., González-Rouco, J. F., García-Bustamante, E., Navarro-Montesinos, J., and Steinert, N. (2018). Influence of radiative forcing factors on ground–air temperature coupling during the last millennium: implications for borehole climatology. *Climate of the Past* **14**(11), 1583–1606. DOI: 10.5194/cp-14-1583-2018.

Mesinger, F., DiMego, G., Kalnay, E., Mitchell, K., Shafran, P. C., Ebisuzaki, W., Jovic, D., Woollen, J., Rogers, E., Berbery, E. H., et al. (2006). North American regional reanalysis. *Bulletin of the American Meteorological Society* **87**(3), 343–360. DOI: https://doi.org/10.1175/BAMS-87-3-343.

Mieville, A., Granier, C., Liousse, C., Guillaume, B., Mouillot, F., Lamarque, J. F., Grégoire, J. M., and Pétron, G. (2010). Emissions of gases and particles from biomass burning during the 20th century using satellite data and an historical

reconstruction. *Atmospheric Environment* **44**(11), 1469–1477. DOI: http://dx.doi.org/10.1016/j.atmosenv.2010.01.011.

Mitchell, K. E., Lohmann, D., Houser, P. R., Wood, E. F., Schaake, J. C., Robock, A., Cosgrove, B. A., Sheffield, J., Duan, Q., Luo, L., Higgins, R. W., Pinker, R. T., Tarpley, J. D., Lettenmaier, D. P., Marshall, C. H., Entin, J. K., Pan, M., Shi, W., Koren, V., Meng, J., Ramsay, B. H., and Bailey, A. A. (2004). The multi-institution North American Land Data Assimilation System (NLDAS): Utilizing multiple GCIP products and partners in a continental distributed hydrological modeling system. *Journal of Geophysical Research: Atmospheres* **109**(D7), 2156–2202. DOI: 10.1029/2003JD003823.

Neale, R. B., Chen, C.-C., Gettelman, A., Lauritzen, P. H., Park, S., Williamson, D. L., Conley, A. J., Garcia, R., Kinnison, D., and Lamarque, J.-F. (2010a). Description of the NCAR community atmosphere model (CAM 4.0). *NCAR Tech. Note*.

— (2010b). Description of the NCAR community atmosphere model (CAM 5.0). *NCAR Tech. Note*.

Numaguti, A, Takahashi, M, Nakajima, T, and Sumi, A (1997). Description of CCSR/NIES atmospheric general circulation model. CGER's supercomputer monograph report. *Center for Global Environmental Research, National Institute for Environmental Studies* **3**, 1–48.

Oleson, K. W., Lawrence, D. M., Bonan, G. B., Flanner, M. G., Kluzek, E., Lawrence, P. J., Levis, S., Swenson, S. C., Thornton, P. E., Dai, A., Decker, M., Dickinson, R., Feddema, J., Heald, C. L., Hoffman, F., Lamarque, J.-F., Mahowald, N., Niu, G.-Y., Qian, T., Randerson, J., Running, S., Sakaguchi, K., Slater, A., Stockli, R., Wang, A., Yang, Z.-L., Zeng, X., and Zeng., X. (2010). *Technical description of version 4.0 of the Community Land Model (CLM)*. Tech. rep. NCAR, Boulder.

Pollack, H. N., Smerdon, J. E., and Keken, P. E. van (2005). Variable seasonal coupling between air and ground temperatures: A simple representation in terms of subsurface thermal diffusivity. *Geophysical Research Letters* **32**(15), 1944–8007. DOI: 10.1029/2005GL023869.

Pope, D. V., Gallani, L. M., Rowntree, R. P., and Stratton, A. R. (2000). The impact of new physical parametrizations in the Hadley Centre climate model: HadAM3. *Climate Dynamics* **16**(2/ 1432-0894), 123–146.

Reick, C. H., Raddatz, T., Brovkin, V., and Gayler, V. (2013). Representation of natural and anthropogenic land cover change in MPI-ESM. *Journal of Advances in Modeling Earth Systems* **5**(3), 459–482. DOI: 10.1002/jame.20022.

Riahi, K., Rao, S., Krey, V., Cho, C., Chirkov, V., Fischer, G., Kindermann, G., Nakicenovic, N., and Rafaj, P. (2011). RCP 8.5—A scenario of comparatively

high greenhouse gas emissions. *Climatic Change* **109**(1-2), 33–57. DOI: 10.1007/s10584-011-0149-y.

Robock, A., Schlosser, C., Vinnikov, K. Y., Speranskaya, N. A., Entin, J. K., and Qiu, S. (1998). Evaluation of the AMIP soil moisture simulations. *Global and Planetary Change* **19**(1–4), 181 –208. DOI: http://dx.doi.org/10.1016/S0921-8181(98)00047-2.

Robock, A., Luo, L., Wood, E. F., Wen, F., Mitchell, K. E., Houser, P. R., Schaake, J. C., Lohmann, D., Cosgrove, B., Sheffield, J., Duan, Q., Higgins, R. W., Pinker, R. T., Tarpley, J. D., Basara, J. B., and Crawford, K. C. (2003). Evaluation of the North American Land Data Assimilation System over the southern Great Plains during the warm season. *Journal of Geophysical Research: Atmospheres* **108**(D22), 2156–2202. DOI: 10.1029/2002JD003245.

Roeckner, E., Bäuml, G., Bonaventura, L., Brokopf, R., Giorgetta, M. E. M., Hagemann, S., Kirchner, I., Kornblueh, L., Manzini, E., Rhodin, A., Schlese, U., Schulzweida, U., and Tompkins, A. (2003). *Model description of the atmospheric general circulation model ECHAM5*. Tech. rep. Hamburg, Germany: Max-Planck-Institut für Meteorologie.

Rosenzweig, C. and Abramopoulos, F. (1997). Land-surface model development for the GISS GCM. *Journal of climate* **10**(8), 2040–2054.

Ruiz-Barradas, A. and Nigam, S. (2005). Warm Season Rainfall Variability over the U.S. Great Plains in Observations, NCEP and ERA-40 Reanalyses, and NCAR and NASA Atmospheric Model Simulations. *Journal of Climate* **18**(11), 1808–1830. DOI: 10.1175/JCLI3343.1.

Salzen, K. von, Scinocca, J. F., McFarlane, N. A., Li, J., Cole, J. N. S., Plummer, D., Verseghy, D., Reader, M. C., Ma, X., Lazare, M., and Solheim, L. (2013). The Canadian Fourth Generation Atmospheric Global Climate Model (CanAM4). Part I: Representation of Physical Processes. *Atmosphere-Ocean* **51**(1), 104–125. DOI: 10.1080/07055900.2012.755610.

Santer, B. D., Taylor, K. E., Wigley, T. M. L., Penner, J. E., Jones, P. D., and Cubasch, U. (1995). Towards the detection and attribution of an anthropogenic effect on climate. *Climate Dynamics* **12**(2), 77–100. DOI: 10.1007/BF00223722.

Schlosser, C. A. and Milly, P. C. D. (2002). A Model-Based Investigation of Soil Moisture Predictability and Associated Climate Predictability. *Journal of Hydrometeorology* **3**(4), 483–501.

Schmidt, G. A., Ruedy, R., Hansen, J. E., Aleinov, I., Bell, N., Bauer, M., Bauer, S., Cairns, B., Canuto, V., Cheng, Y., Genio, A. D., Faluvegi, G., Friend, A. D., Hall, T. M., Hu, Y., Kelley, M., Kiang, N. Y., Koch, D., Lacis, A. A., Lerner, J., Lo, K. K., Miller, R. L., Nazarenko, L., Oinas, V., Perlwitz, J., Perlwitz, J., Rind,

D., Romanou, A., Russell, G. L., Sato, M., Shindell, D. T., Stone, P. H., Sun, S., Tausnev, N., Thresher, D., and Yao, M.-S. (2006). Present-Day Atmospheric Simulations Using GISS ModelE: Comparison to In Situ, Satellite, and Reanalysis Data. *Journal of Climate* **19**(2), 153–192.

Schultz, M. G., Heil, A., Hoelzemann, J. J., Spessa, A., Thonicke, K., Goldammer, J. G., Held, A. C., Pereira, J. M. C., and Bolscher, M. van het (2008). Global wildland fire emissions from 1960 to 2000. *Global Biogeochemical Cycles* **22**(2), 1944–9224. DOI: 10.1029/2007GB003031.

Seneviratne, S. I. and Stöckli, R. (2008). "The Role of Land-Atmosphere Interactions for Climate Variability in Europe". In: *Climate Variability and Extremes during the Past 100 Years*. Ed. by S. Brönnimann, J. Luterbacher, T. Ewen, H. F. Diaz, R. S. Stolarski, and U. Neu. Dordrecht: Springer Netherlands, pp. 179–193. DOI: 10.1007/978-1-4020-6766-2{_}12.

Seneviratne, S. I., Lüthi, D., Litschi, M., and Schär, C. (2006). Land–atmosphere coupling and climate change in Europe. *Nature* **443**(7108), 205–209.

Seneviratne, S. I., Corti, T., Davin, E. L., Hirschi, M., Jaeger, E. B., Lehner, I., Orlowsky, B., and Teuling, A. J. (2010). Investigating soil moisture–climate interactions in a changing climate: A review. *Earth-Science Reviews* **99**(3–4), 125 –161. DOI: http://dx.doi.org/10.1016/j.earscirev.2010.02.004.

Seneviratne, S. I., Wilhelm, M., Stanelle, T., Hurk, B. van den, Hagemann, S., Berg, A., Cheruy, F., Higgins, M. E., Meier, A., Brovkin, V., Claussen, M., Ducharne, A., Dufresne, J.-L., Findell, K. L., Ghattas, J., Lawrence, D. M., Malyshev, S., Rummukainen, M., and Smith, B. (2013). Impact of soil moisture-climate feedbacks on CMIP5 projections: First results from the GLACE-CMIP5 experiment. *Geophysical Research Letters* **40**(19), 5212–5217. DOI: 10.1002/grl.50956.

Slater, A. G. and Lawrence, D. M. (2013). Diagnosing present and future permafrost from climate models. *Journal of Climate* **26**(15), 5608–5623.

Smerdon, J. E., Pollack, H. N., Cermak, V., Enz, J. W., Kresl, M., Safanda, J., and Wehmiller, J. F. (2004). Air-ground temperature coupling and subsurface propagation of annual temperature signals. *Journal of Geophysical Research: Atmospheres* **109**(D21), D21107. DOI: 10.1029/2004JD005056.

— (2006). Daily, seasonal, and annual relationships between air and subsurface temperatures. *Journal of Geophysical Research: Atmospheres* **111**(D7). D07101, 2156–2202. DOI: 10.1029/2004JD005578.

Sokratov, S. A. and Barry, R. G. (2002). Intraseasonal variation in the thermoinsulation effect of snow cover on soil temperatures and energy balance. *Journal of Geophysical Research: Atmospheres* **107**(D10), ACL 13–1–ACL 13–6. DOI: 10.1029/2001JD000489.

Solmon, F., Mallet, M., Elguindi, N., Giorgi, F., Zakey, A., and Konaré, A. (2008). Dust aerosol impact on regional precipitation over western Africa, mechanisms and sensitivity to absorption properties. *Geophysical Research Letters* **35**(24), 1944–8007. DOI: DOI:10.1029/2008GL035900.

Srinivasan, G, Robock, A., Entin, J. K., Luo, L., Vinnikov, K. Y., and Viterbo, P. (2000). Soil moisture simulations in revised AMIP models. *Journal of geophysical research* **105**(D21), 26,635–26,644.

Stevens, B., Giorgetta, M., Esch, M., Mauritsen, T., Crueger, T., Rast, S., Salzmann, M., Schmidt, H., Bader, J., Block, K., Brokopf, R., Fast, I., Kinne, S., Kornblueh, L., Lohmann, U., Pincus, R., Reichler, T., and Roeckner, E. (2013). Atmospheric component of the MPI-M Earth System Model: ECHAM6. *Journal of Advances in Modeling Earth Systems* **5**(2), 146–172. DOI: 10.1002/jame.20015.

Takata, K., Emori, S., and Watanabe, T. (2003). Development of the minimal advanced treatments of surface interaction and runoff. *Global and Planetary Change* **38**(1), 209–222.

Taylor, K. E., Stouffer, R. J., and Meehl, G. A. (2012). An overview of CMIP5 and the experiment design. *Bulletin of the American Meteorological Society* **93**(4), 485–498.

Thomson, A., Calvin, K., Smith, S., Kyle, G. P., Volke, A., Patel, P., Delgado-Arias, S., Bond-Lamberty, B., Wise, M., Clarke, L., and Edmonds, J. (2011). RCP4.5: a pathway for stabilization of radiative forcing by 2100. *Climatic Change* **109**(1-2), 77–94. DOI: 10.1007/s10584-011-0151-4.

Todd-Brown, K. E. O., Randerson, J. T., Post, W. M., Hoffman, F. M., Tarnocai, C., Schuur, E. A. G., and Allison, S. D. (2013). Causes of variation in soil carbon simulations from CMIP5 Earth system models and comparison with observations. *Biogeosciences* **10**(3), 1717–1736. DOI: 10.5194/bg-10-1717-2013.

Verseghy, D. L. (1991). CLASS A Canadian land surface scheme for GCMs, I. Soil Model. *International Journal of Climatology* **11**, 111–133.

Volodin, E., Dianskii, N., and Gusev, A. (2010). Simulating present-day climate with the INMCM4.0 coupled model of the atmospheric and oceanic general circulations. *Atmos. Oceanic Phys.* **46**, 141–431.

Vuuren, D. P. van, Edmonds, J., Kainuma, M., Riahi, K., Thomson, A., Hibbard, K., Hurtt, G. C., Kram, T., Krey, V., Lamarque, J.-F., Masui, T., Meinshausen, M., Nakicenovic, N., Smith, S. J., and Rose, S. K. (2011). The representative concentration pathways: an overview. *Climatic Change* **109**(1), 5. DOI: 10.1007/s10584-011-0148-z.

Wang, Y., Leung, L. R., McGREGOR, J. L., Lee, D.-K., Wang, W.-C., Ding, Y., and Kimura, F. (2004). Regional climate modeling: progress, challenges, and prospects.

Journal of the Meteorological Society of Japan. Ser. II **82**(6), 1599–1628, 0026–1165.

Watanabe, S., Miura, H., Sekiguchi, M., Nagashima, T., Sudo, K., Emori, S., and Kawamiya, M. (2008). Development of an atmospheric general circulation model for integrated Earth system modeling on the Earth Simulator. *J. Earth Simulator* **9**, 27–35.

Wei, J. and Dirmeyer, P. A. (2010). Toward understanding the large-scale land-atmosphere coupling in the models: Roles of different processes. *Geophysical Research Letters* **37**(19), 1944–8007. DOI: 10.1029/2010GL044769.

Welty, J. and Zeng, X. (2018). Does Soil Moisture Affect Warm Season Precipitation Over the Southern Great Plains? *Geophysical Research Letters* **45**(15), 7866–7873.

Werf, G. R. van der, Randerson, J. T., Giglio, L., Collatz, G. J., Kasibhatla, P. S., and Arellano Jr., A. F. (2006). Interannual variability in global biomass burning emissions from 1997 to 2004. *Atmospheric Chemistry and Physics* **6**(11), 3423–3441. DOI: 10.5194/acp-6-3423-2006.

Wessel, P., Smith, W. H. F., Scharroo, R., Luis, J., and Wobbe, F. (2013). Generic Mapping Tools: Improved Version Released. *Eos, Transactions American Geophysical Union* **94**(45), 409–410. DOI: 10.1002/2013EO450001.

Wu, T., Yu, R., and Zhang, F. (2008). A Modified Dynamic Framework for the Atmospheric Spectral Model and Its Application. *Journal of the Atmospheric Sciences* **65**(7), 2235–2253.

Wu, T., Song, L., Li, W., Wang, Z., Zhang, H., et al. (2013). An Overview of BCC Climate System Model Development and Application for Climate Change Studies. *Journal of Meteorological Research* **28**.

Xia, Y., Ek, M., Sheffield, J., Livneh, B., Huang, M., Wei, H., Feng, S., Luo, L., Meng, J., and Wood, E. (2013). Validation of NOAH-simulated soil temperature in the North American land data assimilation system phase 2. *Journal of Applied Meteorology and Climatology* **52**(2), 455–471.

Xue, Y., Juang, H. M. H., Li, W. P., Prince, S., DeFries, R., Jiao, Y., and Vasic, R. (2004). Role of land surface processes in monsoon development: East Asia and West Africa. *Journal of Geophysical Research: Atmospheres* **109**(D3), 2156–2202. DOI: DOI:10.1029/2003JD003556.

Xue, Y., Janjic, Z., Dudhia, J., Vasic, R., and Sales, F. D. (2014). A review on regional dynamical downscaling in intraseasonal to seasonal simulation/prediction and major factors that affect downscaling ability. *Atmospheric Research* **147-148**, 68 –85. DOI: https://doi.org/10.1016/j.atmosres.2014.05.001.

Yukimoto, S., Adachi, Y., Hosaka, M., Sakami, T., Yoshimura, H., Hirabara, M., Tanaka, T., Shindo, E., Tsujino, H., Deushi, M., Mizuta, R., Yabu, S., Obata, A., Nakano, H., Koshiro, T., Ose, T., and Kitoh, A. (2012a). A New Global Climate Model of the Meteorological Research Institute: MRI-CGCM3 Model Description and Basic Performance. *Journal of the Meteorological Society of Japan. Ser. II* **90A**, 23–64.

Yukimoto, S., Adachi, Y., Hosaka, M., Sakami, T., Yoshimura, H., Hirabara, M., Tanaka, T. Y., Shindo, E., Tsujino, H., Deushi, M., et al. (2012b). A new global climate model of the Meorological Research Institute: MRI-CGCM3 model description and basic performance. *J.Meteor.Soc.Japan* **90**(A), 23–64.

Zeng, X., Barlage, M., Castro, C., and Fling, K. (2010). Comparison of Land–Precipitation Coupling Strength Using Observations and Models. *Journal of Hydrometeorology* **11**(4), 979–994.

Zhang, J., Wang, W.-C., and Wei, J. (2008a). Assessing land-atmosphere coupling using soil moisture from the Global Land Data Assimilation System and observational precipitation. *Journal of Geophysical Research: Atmospheres* **113**(D17). DOI: 10.1029/2008JD009807.

Zhang, J., Wang, W.-C., and Leung, L. R. (2008b). Contribution of land-atmosphere coupling to summer climate variability over the contiguous United States. *Journal of Geophysical Research: Atmospheres* **113**(D22). DOI: 10.1029/2008JD010136.

Zhang, T. (2005). Influence of the seasonal snow cover on the ground thermal regime: An overview. *Reviews of Geophysics* **43**(4). DOI: 10.1029/2004RG000157.

Chapter 3

Land Surface Model influence on the simulated climatologies of extreme temperature and precipitation events within the WRF v.3.9 model over North America.

This chapter is based on the contents of the article submitted to *Geocientific Model Development*:

García-García, A. et al. (2020). Land Surface Model influence on the simulated climatologies of extreme temperature and precipitation events within the WRF v.3.9 model over North America. *Geocientific Model Development (In Discussion)*. DOI: https://doi.org/10.5194/gmd-2020-86

Abstract

The representation and projection of extreme temperature and precipitation events in regional and global climate models are of major importance for the study of climate change impacts. However, state-of-the-art global and regional climate model simulations yield a broad inter-model range of intensity, duration and frequency of these extremes. Here, we present a modeling experiment using the Weather Research and Forecasting (WRF) model to determine the influence of the Land Surface Model (LSM) component on uncertainties associated with extreme events. First, we analyze land-atmosphere interactions within four simulations performed by the WRF model from 1980 to 2012 over North America, using three different LSMs. Results show LSM-dependent differences at regional scales in the frequency of occurrence of events when surface conditions are altered by atmospheric forcing or land processes. The inter-model range of extreme statistics across the WRF simulations is large, particularly for indices related to the intensity and duration of temperature and precipitation extremes. Our results show that the WRF simulation of the climatology of heat extremes can be 5^oC warmer and 6 days longer depending on the employed LSM component, and similarly for cold extremes and heavy precipitation events. Areas showing large uncertainty in WRF simulated extreme events are also identified in a model ensemble from three different Regional Climate Model (RCM) simulations participating in the Coordinated Regional climate Downscaling Experiment (CORDEX) project, revealing the implications of these results for other model ensembles. Thus, studies based on multi-model ensembles and reanalyses should include a variety of LSM configurations to account for the uncertainty arising from this model component or to test the performance of the selected LSM component before running the whole simulation. This study illustrates the importance of the LSM choice in climate sim-

ulations, supporting the development of new modeling studies using different LSM components to understand inter-model differences in simulating temperature and precipitation extreme events, which in turn will help to reduce uncertainties in climate model projections.

3.1 Introduction

General Circulation Models (GCMs) and Regional Climate Models (RCMs) are currently the most useful tools for the study of processes affecting the frequency, duration and intensity of extreme temperature and precipitation events, as well as projecting their evolution under different emission scenarios at global, regional and local scales. Both observational data and climate model simulations confirm that all of these statistics respond to climate change (Jeong et al., 2016; Orlowsky et al., 2012; Seneviratne et al., 2012). However, state-of-the-art global and regional climate models differ substantially in their representation of the climatology and response to warming of various indices of temperature and precipitation extremes (Sillmann et al., 2013a,b). Climate information provided by models is currently employed by public and private institutions dedicated to the evaluation and management of risks from extreme events and associated disasters (Arneth, 2019; IPCC, 2013). It is, therefore, essential that climate models represent extreme events and their evolution as realistically as possible to aid in the design of appropriate policies to mitigate climate change and build resilience. In this study, we analyze the representation of a set of extreme indices, previously included in international reports such as the IPCC, 2013 and Seneviratne et al., 2012, as simulated by the Weather Research and Forecasting (WRF) model with different Land Surface Model (LSM) components. We focused on the climatology of these extreme indices, that is the mean of each index from 1980 to 2013.

Soil conditions are coupled to near-surface atmospheric phenomena through energy and water exchanges at the ground surface. The representation of the interactions between the land surface and the near-surface atmosphere has been identified as a key factor in the simulation of extreme events (e.g. Lorenz et al., 2016; Vogel et al., 2017). For example, changes in soil moisture and soil properties may lead to variations in energy fluxes at the land surface affecting temperature and precipitation evolution. Changes in latent heat flux affect surface temperatures in the following way: a decrease in latent heat flux likely means an increase in the energy available for sensible heat flux, which is directly related to the air-ground temperature gradient. The increase in sensible heat flux yields an increase in this temperature gradient, which may lead to changes in air temperatures (Seneviratne et al., 2010). Meanwhile, changes in latent heat flux also yield changes in the atmospheric water content, possibly affecting the formation of clouds and precipitation (Seneviratne et al., 2010). Previous observational studies have shown the impact of soil moisture deficits on hot extreme temperatures through changes in evapotranspiration over southeastern and western Europe and Russia (Hauser et al., 2016; Hirschi et al., 2011; Miralles et al., 2012). Additionally, soil moisture regimes have been found to alter the energy and water exchanges at the surface, influencing inter-annual summer temperature variability in central parts of North America (Donat et al., 2016), and precipitation events in western North America (Diro et al., 2014). Land-Atmosphere interactions, and consequently near-surface conditions, are influenced by vegetation and snow cover (Diro et al., 2018; Stieglitz et al., 2007). For example, Diro et al., 2018 showed that interactions between snow cover and atmospheric processes influence extreme events, increasing the frequency of cold events over western North America and affecting the variability in warm events over northeast Canada and the Rocky mountains.

Metrics built on the representation of land-atmosphere interactions have been

employed as a basis for evaluating extreme temperature and precipitation events in climate model simulations (Davin et al., 2016; García-García et al., 2019; Gevaert et al., 2018; Knist et al., 2016; Lorenz et al., 2016; Sippel et al., 2017). For example, Lorenz et al., 2016 evaluated outputs from six GCMs participating in the Global Land-Atmosphere Coupling Experiment (GLACE) of the 5^{th} phase of the Coupled Model Intercomparison Project (CMIP5) (GLACE-CMIP5) and concluded that ranges of intensity, frequency and duration of extreme events among climate projections are strongly related to inter-model differences in the representation land-atmosphere interactions. Gevaert et al., 2018 evaluated the representation of land-atmosphere interactions within a set of offline LSM simulations, finding similar spatial patterns of soil moisture-temperature coupling among LSM simulations, but large variability in the degree and local patterns of land-atmosphere coupling. García-García et al., 2019 employed a simple metric derived from soil and air temperatures to evaluate outputs from the CMIP5 models against observations over North America, suggesting a strong dependency of the simulated land-atmosphere interactions on the LSM component employed. The model differences in the representation of land-atmosphere interactions shown in these studies may be affecting the simulation of extreme events, and thus contributing to the uncertainty in multi-model ensembles such as those formed by the CMIP5 and the Coordinated Regional climate Downscaling Experiment (CORDEX) simulations.

The choice and complexity of the LSM component may have implications for the representation of land-atmosphere interactions in reanalysis products, since reanalysis products have shown discrepancies in the representation of land-atmosphere coupling with observations (Ferguson et al., 2012; García-García et al., 2019). However, in contrast with the variety of LSM components employed in the new generation of GCMs, reanalyses use simplified versions of LSM components, typically included as part of the

atmospheric model component. For example, all reanalysis products produced by the European Centre for Medium-range Weather Forecasts (ECMWF) model (CERA-20C, ERA-15, ERA20C, ERA-Interim, ERA-40, and ERA5 products) employed different versions of the same LSM component included in the code of the ECMWF atmospheric model (Hersbach et al., 2018). The two Modern-Era Retrospective analysis for Research and Applications (MERRA and MERRA2) global products employed similar versions of the GEOS-5 Catchment land surface model (Molod et al., 2015; Reichle et al., 2011). The Japanese Reanalysis (JRA) products employed a modified version of the Simple Biosphere (SiB) LSM (Onogi et al., 2007), while most of National Centers for Environmental Prediction (NCEP) and National Center for Atmospheric Research (NCAR) products employed the NOAH LSM (Tewari et al., 2004). The complexity and variety of these LSM components are limited in order to reduce computational costs, affecting the quality of the represented land surface processes. This has already been noted by the scientific community, and some have attempted to address the issue by incorporating updated versions of LSMs in new land reanalysis products through offline LSM simulations forced by observational data products (LDAS, MERRA-land, ERA-Iterim/Land, ERA5-land, Balsamo et al., 2015; Hersbach et al., 2018; Reichle et al., 2011; Rodell et al., 2004). Although these new products can be useful for LSM development and provide data about the soil states and fluxes (Balsamo et al., 2015), the offline character of the new land products inhibits the representation of land-atmosphere coupling and feedbacks.

Here, we perform a set of modeling experiments to examine for the first time the influence of the LSM component on the simulation of key extreme indices and land-atmosphere interactions within land-atmosphere coupled climate simulations at continental scales. For this purpose, four regional simulations are performed over North America (1979-2012) using the WRF model including three different LSM com-

ponents widely employed in model simulations and reanalysis products, as described in Section 3.2. To explore the influence of the LSM component on the simulation of extreme events in multi-model ensembles, we compare the uncertainty in the representation of extreme indices within our four WRF simulations with the uncertainty in three simulations participating in the North American component of the CORDEX project (NA-CORDEX). The methods for the analysis of land-atmosphere interactions and the representation of extreme events are described in Section 3.3. Section 3.4 presents the examination of land-atmosphere interactions, the analysis of LSM differences in the representation of temperature and precipitation extremes, and the comparison between the WRF simulations and three CORDEX simulations. A discussion about previous results and the main conclusions and implications of this study are presented in Section 3.5 and 3.6, respectively.

3.2 Description of the modeling experiment

We performed four regional simulations over North America (NA) using the version 3.9 of the Advanced Research WRF (ARW-WRF) model (Michalakes et al., 2001; Skamarock et al., 2008a) including three different land surface models: the NOAH LSM (NOAH, Tewari et al., 2004), the NOAH LSM with multiparameterizations options (NOAH-MP, Niu et al., 2011), and the Community Land Model version 4 LSM (CLM4, Oleson et al., 2010). Vegetation cover was prescribed in these three simulations (NOAH, NOAH-MP and CLM4); an additional simulation was conducted with dynamic vegetation cover in the NOAH-MP LSM (NOAH-MP-DV), allowing for the evaluation of the influence of dynamic vegetation on extremes. The use of different LSM configurations in a RCM permits the study of the influence of surface and soil processes on the simulated climate system in contrast to LSM offline simulations

(Laguë et al., 2019).

The LSM components employed have been previously included in climate model studies or in reanalysis products. The CLM4 LSM component has been coupled to several GCMs participating in the CMIP5 project (Collins et al., 2006; Vertenstein et al., 2012). The NOAH LSM has been extensively used for reanalysis products, as well as for RCM simulations such as those participating in the CORDEX project (Katragkou et al., 2015; Mesinger et al., 2006). The NOAH-MP LSM has been selected for current studies using WRF (e.g. Liu et al., 2017). The NOAH LSM is a rather basic LSM developed by the National Center for Atmospheric Research (NCAR) and the National Centers for Environmental Prediction (NCEP), based on the Oregon State University (OSU) LSM (Mitchell, 2005). This LSM component describes soils using 4 layers with thickness 10, 30, 60 and 100 cm, using a zero-flux bottom boundary condition at a depth of 2 m. The NOAH LSM estimates soil moisture and temperature at the node of each soil layer, taking into account snow cover, canopy moisture, and soil ice. The NOAH-MP LSM is based on the NOAH LSM, introducing relevant improvements, such as a dynamic vegetation option; a new separated vegetation canopy cover that improves the computation of energy, water and carbon fluxes at the surface; a separate scheme for computing energy fluxes over vegetated surfaces and bare soils; a new 3-layer snow model; a more permeable frozen soil; and an improved description of runoff and soil moisture. Although the NOAH-MP LSM is the updated version of the NOAH LSM and has been shown to improve the simulation of surface processes in comparison to the NOAH LSM (e.g. Niu et al., 2011; Yang et al., 2011), the NOAH-MP LSM has not yet been implemented in any reanalysis product. The CLM4 represents one of the most advanced LSM components, incorporating a detailed description of biogeophysics, hydrology and biogeochemistry. The CLM4 classifies vegetation cover using up to 16 different plant functional types, considering

the physiology and structure of different plants. The soil vertical structure is divided into a layer for the vegetation canopy, 5 layers for snow cover, and 10 soil layers, placing the zero-flux bottom boundary condition at approximately 4.32 m. The main characteristics of the employed LSM components are summarized in Table 3.1.

Beyond the structural differences among LSM components, the remaining options and parameters are identical for the four WRF simulations. Boundary conditions for the WRF experiments are provided by the North American Regional Reanalysis (NARR) product, which is formed by the NCEP Eta atmospheric model, the NOAH LSM and the Regional Data Assimilation System (RDAS); (Mesinger et al., 2006). NARR data are provided with a 32 km grid and three-hourly temporal resolution, available at the National Center for Environmental Information (NOAA) archive. The domain set for the WRF simulations has 50 km horizontal resolution and 27 atmospheric levels, covering North America in a Lambert projection. The land use categories employed for the four simulations (Figure B.1) are derived from the Moderate Resolution Imaging Spectroradiometer (MODIS, Barlage et al., 2005). Sea surface temperatures were prescribed using the NARR product. The four WRF simulations start on January 1st 1979, which is the first year of the NARR product, and end on December 31st 2012, using a time-step of 300 seconds for the model integrations. We use the first year of each simulation as spin-up and the other 33 years for the analysis. The selection of the first year as spin-up was done considering the initialization period previously used in WRF climate experiments, such as those in Barlage et al. (2005), Katragkou et al. (2015), and Wang et al. (2015). The comparison of the latent heat flux and surface air temperature outputs from the WRF-CLM4 simulation starting on January 1st, 1979 and a similar simulation starting on June 1st, 1979 indicates that this period is enough to initialize the simulation (Figures B.21 and B.22). The employed physics parameterizations include the WSM 6-class graupel scheme for the

Table 3.1: Characteristics of the LSM components employed for the WRF simulations performed in this analysis.

LSM	Vegetation Types	Vegetation Mode	Soil Layers	Soil Depth	Snow	Reference
NOAH	Dominant vegetation type in one grid cell	Prescribed	4	2 m	Single Layer	Tewari et al., 2004
NOAH-MP	Dominant vegetation type in one grid cell	Prescribed	4	2 m	Up to 3 Layers	Niu et al., 2011
NOAH-MP-DV	Dominant vegetation type in one grid cell	Dynamic	4	2 m	Up to 3 Layers	Niu et al., 2011
CLM4	Up to 10 vegetation types in one grid cell	Prescribed	10	4.32 m	Up to 5 Layers	Oleson et al., 2010

microphysics (Hong et al., 2006b), the Grell-Freitas ensemble scheme for cumulus description (Grell et al., 2014), the Yonsei University scheme as planetary boundary layer scheme (YSU, Hong et al., 2006a), the revised MM5 monin-Obukhov scheme for the surface layer (Jiménez et al., 2012), and the CAM scheme for the integration of radiation physics each 20 min intervals (Collins et al., 2004).

The gap in resolution from the employed boundary conditions (32 km) to the final simulations (50 km) can be counter-intuitive for a RCM experiment. The computational resources saved with this coarse resolution allow us to perform simulations long enough for the study of land-atmosphere interactions and extreme events at climatological scales and yet similar horizontal resolution and domain to those employed in the North American component of the CORDEX project (Giorgi et al., 2015) can be attained. Thus, this decrease in resolution allows us to generate a set of four WRF sensitivity experiments using different LSM configurations. Additionally, we do not apply any nudging technique, ensuring that the RCM evolves freely according to each LSM component and its representation of land-atmosphere interactions.

3.3 Methodology

Different metrics have been employed in the literature for the evaluation of land-atmosphere interactions within climate model simulations and observations. Among these metrics, we selected the Vegetation-Atmosphere Coupling (VAC) index (Zscheischler et al., 2015) as our evaluation metric for the representation of land-atmosphere interactions at monthly scales. This index has been previously employed in the literature to identify regions with episodes of strong land-atmosphere coupling within climate model simulations and observational data (Gevaert et al., 2018; Li et al., 2017; Philip et al., 2018; Sippel et al., 2017; Zscheischler et al., 2015). The VAC index is

segregated in four categories based on the simultaneous occurrence of some given extreme percentile rages of Surface Air Temperature (SAT) and Latent Heat flux (LH) (Philip et al., 2018):

$$\begin{array}{llllll} VAC_a & if & \text{SAT} < 30^{th} Pctl. & and & \text{LH} < 30^{th} Pctl. \rightarrow Atmos. & Control \\ VAC_b & if & \text{SAT} > 70^{th} Pctl. & and & \text{LH} > 70^{th} Pctl. \rightarrow Atmos. & Control \\ VAC_c & if & \text{SAT} > 70^{th} Pctl. & and & \text{LH} < 30^{th} Pctl. \rightarrow Land & Control \\ VAC_d & if & \text{SAT} < 30^{th} Pctl. & and & \text{LH} > 70^{th} Pctl. \rightarrow Land & Control \\ 0 & otherwise & & & & \end{array} \tag{3.1}$$

Extremes of SAT and LH are defined as values exceeding (below) the 70th (30th) percentile, relative to a 20-year period (1980-2000) (Eq. 3.1). We use the Vegetation-Atmosphere Coupling (VAC) metric at monthly scales as in Sippel et al., 2017, since this work proved the usefulness of the VAC metric at monthly time scales for the analysis of the climatology of extreme indices. The VAC index classifies areas depending on the soil moisture regime into energy-limited areas, where atmospheric conditions controls land-atmosphere interactions (VACa and VACb), and into water-limited areas, where soil moisture deficits control the water and energy exchanges at the air-ground interface (VACc and VACd). As explained in Zscheischler et al., 2015, the VACa category is associated with energy limitations (low SAT) caused by the presence of clouds and precipitation, which leads to a decrease in the vegetation photosynthetic activity and therefore an increase in soil moisture. The VACb category is frequent in wet areas with high SAT, usually related to clear sky and high radiation, which is associated with an increase in the vegetation photosynthetic activity inducing the depletion of soil moisture. During VACc episodes, the combination of high SAT and soil moisture deficits leads to diminished vegetation photosynthetic activity, followed by

low precipitation and consequently low soil moisture and high SAT, promoting heat waves and droughts. The VACd category is associated with high precipitation over dry soils which stimulates vegetation photosynthetic activity, increasing soil moisture and decreasing SAT. A no-coupling option also occurs when SAT and LH extremes do not coincide in time.

We calculate the frequency of occurrence for each VAC category using deseasonalized and detrended monthly SAT and LH time series following the methods employed in Sippel et al., 2017 at each grid cell from 1980 to 2012, hereafter the analysis period. The frequency of occurrence for each VAC category is calculated by counting the VAC events for the analysis period seasonally; in boreal winter (December, January, and February; DJF), in spring (March, April, and May; MAM), in summer (June, July, and August; JJA), and in fall (September, October, and November; SON). The probability of each VAC category (Figures B.2-B.5) and the probability of the no-coupling case sum 100% over the analysis period at each grid cell. The VAC probabilities of occurrence for each category are considered significant when higher than the 95th percentile of the population obtained by 100 randomly sorted 34-year time series of SAT and LH. For the study of land-atmosphere coupling within each simulation, we represent the averaged frequency of events under atmospheric control (VACa and VACb) and under land control (VACc and VACd) at grid cells with significant frequency of occurrence for at least one of the two VAC categories.

After the analysis of land-atmosphere interactions in our set of simulations, we assess the representation of extreme events across the WRF simulations coupled to different LSM components. There are several definitions of indices related to temperature and precipitation extremes, mainly using thresholds based on absolute values or statistical percentiles (e.g. Sillmann et al., 2013a). Studies based on statistical percentiles improve the comparison among models but hamper the interpretation of

Table 3.2: List of extreme indices used in this study defined by the ETCCDI (Karl et al., 1999). Percentiles are calculated over the period 1980-2000.

Index	Definition	Unit
Cold Event		
Intensity		
TXx DJF	Maximum value of daily maximum temperature (hottest day) in winter	$°C$
TNn DJF	Minimum value of daily minimum temperature (coldest nigth) in winter	$°C$
Frequency		
TN10p	Percentage of days in a year when daily minimum temperature < the calendar day 10th percentile centered on a 5-day window	%
TX10p	Percentage of days in a year when daily maximum temperature < the calendar day 10th percentile centered on a 5-day window	%
Duration		
CSDI	Cold Spell Duration Index: annual count of days with at least 6 consecutive days when daily minimum temperature < the calendar day 10th percentile centred on a 5-day window	Days
Warm Event		
Intensity		
TXx JJA	Maximum value of daily maximum temperature (hottest day) in summer	$°C$
TNn JJA	Minimum value of daily minimum temperature (coldest night) in summer	$°C$
Frequency		
TN90p	Percentage of days in a year when daily minimum temperature > the calendar day 90th percentile centered on a 5-day window	%
TX90p	Percentage of days in a year when daily maximum temperature > the calendar day 90th percentile centered on a 5-day window	%
Duration		
WSDI	Warm Spell Duration Index: annual count of days with at least 6 consecutive days when daily maximum temperature > the calendar day 90th percentile centred on a 5-day window	Days
Precipitation Event		
Intensity		
R95p	Annual total precipitation when daily accumulated precipitation on a wet day > 95th percentile of precipitation on wet days	mm
Frequency		
R10mm	Annual count of days when daily accumulated precipitation $\geq$ 10mm	Days
Duration		
CDD	Maximum length of dry spell: maximum annual number of consecutive days with daily accumulated precipitation < 1mm	Days
CWD	Maximum length of wet spell: maximum annual number of consecutive days with daily accumulated precipitation $\geq$ 1mm	Days

results by losing the physical meaning of the variable (temperature or precipitation). Although the use of extreme indices defined with absolute values facilitates the understanding of results by a general public, these indices could include model-specific biases. These biases can be corrected by bias removal techniques, however, the advantage of applying bias removal techniques is not clear for the study of future climate trends and climate variability, since these techniques have been proven to modify the spatiotemporal consistency of climate models as well as internal feedback mechanisms and conservation terms (Cannon et al., 2015; Ehret et al., 2012). Additionally, the simulation of absolute temperatures are of central importance for temperature dependent processes that may have important consequences for society and ecosystems, such as soil carbon processes (Hicks Pries et al., 2017). Since extreme indices based on both absolute values and statistical thresholds present advantages and disadvantages, we selected a set of indices including both categories from the list of 27 indices recommended by the Expert Team on Climate Change Detection and Indices (ETCCDI, Karl et al., 1999, Table 3.2). The employed intensity indices of temperature events are based on temperature values in the hottest day and coldest night in summer and winter for warm and cold events. The frequency indices of the same events indicate the percentage of hot and cold days and nights in the year. The duration of the temperature events is represented with the number of consecutive hot days and cold nights. The intensity of heavy precipitation events is characterized by the total annual precipitation in wet days, while the frequency of precipitation events is studied using the number of very wet days per year. The duration of wet and dry events is represented with the annual number of consecutive wet and dry days. For more specific definitions of the indices employed in this study, please refer to Table 3.2. Since we are interested in the climatology of extreme events, temporal averages of each annual index are computed for the analysis period at each grid cell for each WRF

experiment. Then, we compute the inter-model range of each index across the WRF simulations (i.e., the difference between the maximum and minimum values at each grid cell considering the four WRF simulations), using it as metric for the uncertainty in the WRF simulation of extreme events arising from the LSM component.

The effect of the LSM configuration on the simulation of extreme events can also be relevant for multi-model ensembles, such as those participating in the CORDEX project. Here, we compare the LSM effect on the WRF simulation of extreme temperature and precipitation events with the representation of extreme events by three different RCMs participating in the North America CORDEX (NA CORDEX) program (Mearns, 2017). For this purpose, we use the daily outputs from three NA-CORDEX simulations forced by reanalysis data (Evaluation experiments, Table 3.3). These CORDEX simulations were performed by the WRF model (Skamarock et al., 2008b), the RCA4 model (Samuelsson et al., 2011), and the CRCM-UQAM model (Martynov et al., 2013), using boundary conditions from the ERA-Interim reanalysis (Dee et al., 2011). The remaining NA-CORDEX Evaluation simulations available in the Climate Data Gateway at NCAR were not used because those simulations cover a significantly shorter period of time than our simulations. The spatial domain and resolution of the NA CORDEX simulations are similar to that of the WRF simulations, as indicated in Section 3.2. Refer to Table B.1 for information about the availability of the data employed in this work.

Table 3.3: Characteristics of the Evaluation simulations employed in this analysis from three RCMs participating in the NA-CORDEX project. The boundary conditions for these three simulations are from the ERA-Interim reanalysis.

CORDEX RCM	LSM	Vegetation Types	Spectral Nudging	Institution	Reference
WRF	NOAH	24	Yes	NCAR	Skamarock et al., 2008b
RCA4	RCA LSS	12	No	SMHI	Samuelsson et al., 2011
CRCM-UQAM	CLASS3.5+	4	No	UQAM	Martynov et al., 2013

3.4 Results

3.4.1 Evaluation of land-atmosphere interactions in WRF simulations

All WRF simulations with different LSM components display similar spatial patterns for VAC categories, agreeing in seasonality and broadly in the regional classification of energy and water limited areas (e.g. areas with high probability of episodes where atmospheric forcing or soil conditions control land-atmosphere interactions) (Figures 3.1 and 3.2). Atmospheric forcing controls surface processes at middle and high latitudes in MAM, JJA and SON, moving southward in DJF (Figure 3.1). Areas frequently driven by soil conditions are displayed over the western Mexican coast in DJF, spreading across low and middle latitudes in MAM, JJA and SON (Figure 3.2). These spatial similarities in the VAC coupling metric indicate that factors common in our four simulations, such as land cover, topography, latitudinal differences or atmospheric parameterizations produce these spatial patterns. Despite the broad agreement between LSM simulations in the spatial distribution of the VAC categories, there are regional differences in their representation of land-atmosphere coupling. These regional differences allow us to identify the NOAH LSM as the one simulating the weakest annual land control on processes at the surface, mainly due to a relatively weak land control during MAM and JJA (Figure 3.2).

The areas where LSM simulations differ in the probability of episodes under atmospheric control (VACa and VACb) vary with the season; for example the NOAH-MP LSM simulates a large area under atmospheric control over the southeastern US in DJF, while the CLM4 and NOAH LSMs identify atmospheric control areas below the Great Lakes following a northwestern direction (Figure 3.1). These differences in at-

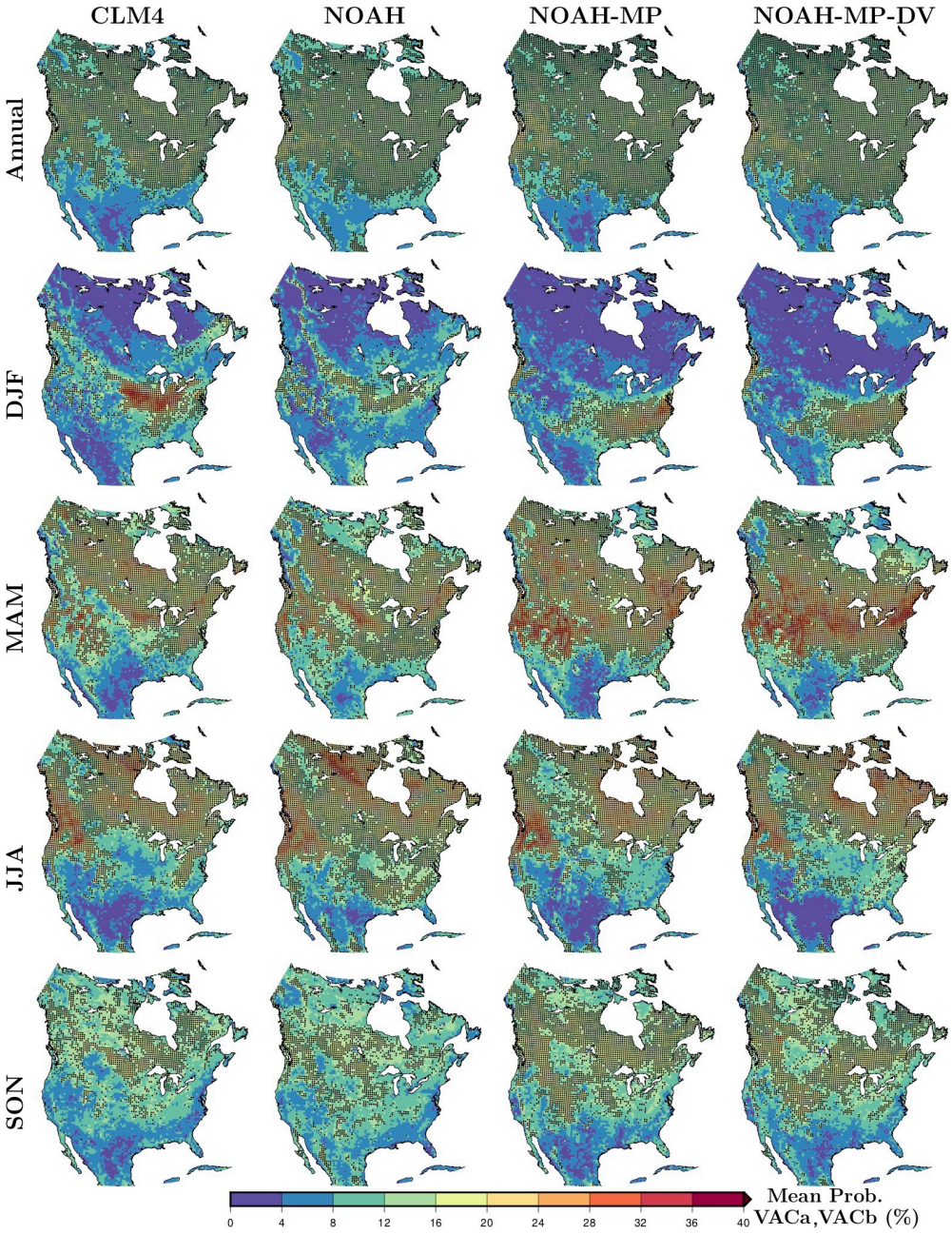

Figure 3.1: Mean frequency of occurrence for VAC categories associated with atmospheric control (VACa and VACb) for each simulation annually and seasonally; DJF, MAM, JJA and SON. Black dots in the maps indicate VAC values lower than the 95th percentile of the randomly generated series, and therefore areas with no significant probabilities.

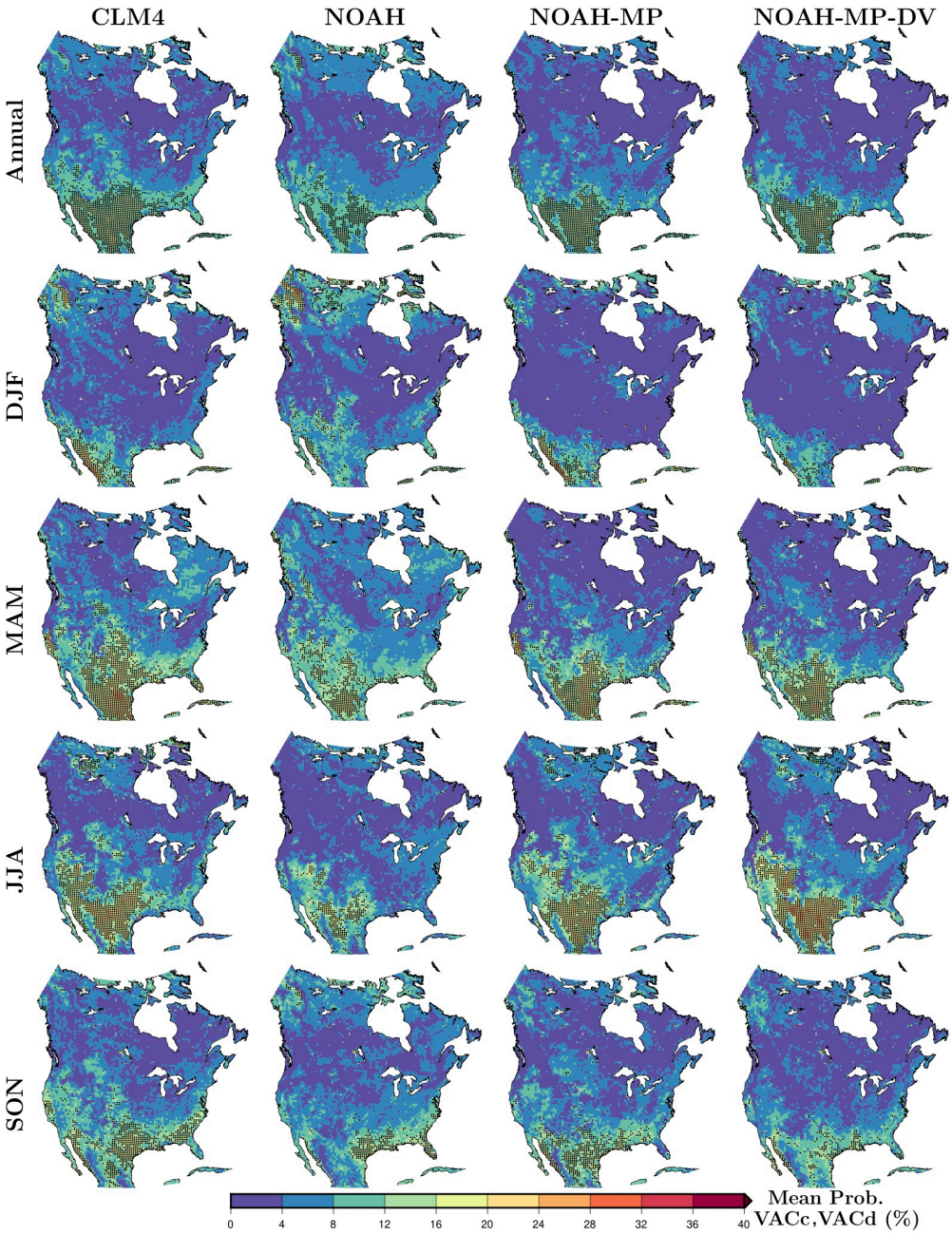

Figure 3.2: Mean frequency of occurrence for VAC categories associated with land control (VACc and VACd) for each simulation annually and seasonally; DJF, MAM, JJA and SON. Black dots in the maps indicate VAC values lower than the 95th percentile of the randomly generated series, and therefore areas with no significant probabilities.

mospheric control areas are caused by the different probability of extreme latent heat flux simulated by each LSM in DJF (Figure B.6 and B.7). In MAM, the NOAH-MP LSM represents higher probability of atmospheric control episodes over the northern US in comparison with the CLM4 and NOAH simulations (Figure 3.1). The NOAH simulation shows the strongest atmospheric control in JJA as compared with the remaining simulations, particularly over eastern and western regions of Hudson Bay, the southeastern US and small areas in Mexico (Figure 3.1). This strong JJA atmospheric control in the NOAH simulation is driven by the VACa category (Figure B.2), and likely related to the high probability of cold temperatures over these areas in this simulation (Figure B.9). During SON, the NOAH-MP LSM reaches the highest probability of episodes under atmospheric control at middle and high latitudes, caused by the high probability of extreme latent heat flux in comparison with the rest of the LSMs (Figure B.6 and B.7). The contribution of the VACa and VACb categories to these episodes is broadly similar across LSMs, with slightly higher VACa in all seasons; modest LSM-specific differences include a tendency for the NOAH simulation to show slightly higher VACa probabilities across all seasons (but especially DJF) (Figures B.2 and B.3).

Although the NOAH simulation displays the weakest land control for all seasons, it shows regions under land control over northwestern North America in DJF also indicated by the CLM4 simulation, but absent in the NOAH-MP and NOAH-MP-DV simulations (Figure 3.2). The probability of land control episodes over the western Mexican coast is higher in the CLM4 and NOAH-MP simulations than in the NOAH and NOAH-MP-DV simulations in DJF. These LSM differences are associated with the high probability of low latent heat flux over those regions in winter for the CLM4 and the NOAH-MP simulations in comparison with the remaining simulations (Figure B.7). In JJA, however, the NOAH-MP-DV simulation presents a stronger land control

at low and middle latitudes than the NOAH-MP simulation (Figure 3.2), mainly caused by the VACd category and the high probability of cold temperatures (Figures B.5 and B.9). There are also regional differences between LSM simulations in SON, particularly over the southeastern US coast where the CLM4 shows the strongest land control, followed by the NOAH-MP simulation (Figure 3.2). The NOAH-MP-DV simulation do not show this strong land control at low latitudes in SON, due to the low probability of high latent heat flux represented by the NOAH-MP LSM with dynamic vegetation (Figure B.6). The weaker land control in the NOAH simulation, however, is not explained by the probability of extreme temperature or latent heat flux, since these probabilities are similar to those in the CLM4 simulation (Figures B.6-B.9). Thus, it is associated with the absent of coincidences of extreme temperature and latent heat flux simulated by the NOAH LSM. Exploring the contribution of VACc and VACd separately, it is shown they present small differences; for example, the VACc probability in DJF is slightly higher than the VACd probability for all simulations, showing the opposite behavior in JJA for the NOAH-MP and the NOAH-MP-DV simulations (Figures B.4 and B.5).

3.4.2 Climatologies of temperature and precipitation extremes in WRF simulations

We continue this analysis comparing the representation of extreme events within the four WRF simulations by calculating the range among these four simulations. But first, we analyze the spatial features of the climatology of extreme temperature and precipitation indices as simulated by the mean of the four WRF simulations with different LSM configurations (hereafter WRF ensemble mean) and by each LSM simulation separately.

The climatologies of temperature and precipitation extreme indices as described

in Table 3.2 and represented by the mean of each index for the analysis period, show similar spatial patterns across all WRF simulations with different LSM configurations (Figures B.10, B.11 and B.12). The similarities in the spatial pattern of extreme events among our simulations indicate that other factors different from the LSM configuration, such as land cover, topography, latitudinal differences and atmospheric parameterizations, are driven these spatial features. Figure 3.3 represents the simulated climatologies of all extreme indices for the ensemble mean, formed by the four WRF simulations. The WRF ensemble mean shows the most intense cold events at high latitudes and high elevations, with cold events being more frequent and longer over northwestern North America and over Mexico (Figure 3.3a). The simulation of warm events is more intense in coastal areas of the US and Mexico and over the central US, being more frequent and longer over southern North America with a high percentage of hot nights over northeastern NA (Figure 3.3b). Precipitation events are heavier and more frequent at higher elevations and over southeastern NA (Figure 3.3c). The longest dry periods are simulated over the western Mexican and US coasts, reaching more than 80 consecutive dry days, while the longest wet periods are represented over the Rockies and the northwestern Mexican coast (Figure 3.3c)

Figure 3.4 summarizes the averaged climatology of each extreme index for each simulation. Averages are computed over six regions adapted from Giorgi et al., 2000: Central America, CAM; Western North America, WNA; Central North America, CNA; Eastern North America, ENA; Alaska, ALA; and Greenland, GRL. Although there are differences between our regions and those defined in Giorgi et al., 2000, we kept the same nomenclature for an easy comparison. That is, we label this region as GRL, although our northeastern Canadian region does not include Greenland. Colors in the figure correspond to the hottest (red) and coldest (blue) index values among the WRF simulations for the representation of cold and warm temperature extremes, and

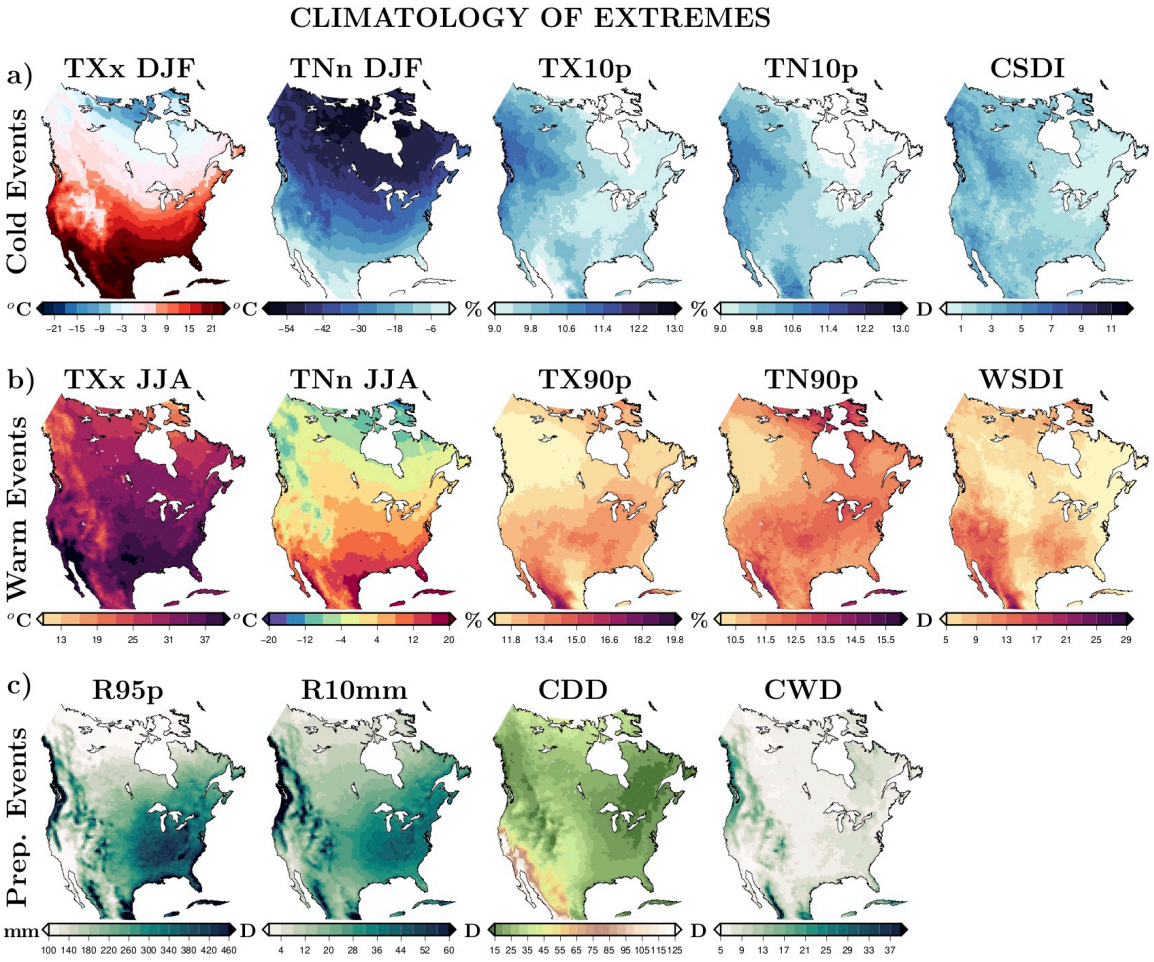

Figure 3.3: Climatology of extreme indices associated with cold temperature events (a), warm temperature events (b), and precipitation events (c) for the ensemble mean, formed by the four WRF simulations (Table 3.2: TXx/TNn, maximum/minimum value of the maximum/minimum daily temperatures; TN10p/TX10p, percentage of cold nights/days; TN90p/TX90p, percentage of hot nights/days; CSDI/WSDI, cold/warm spell duration index; R95p, total annual precipitation in wet days; R10mm, number of wet days in a year; CDD/CWD, consecutive dry/wet days). The climatology of each index is estimated as the mean of each extreme index at each grid cell for the analysis period (1980-2012).

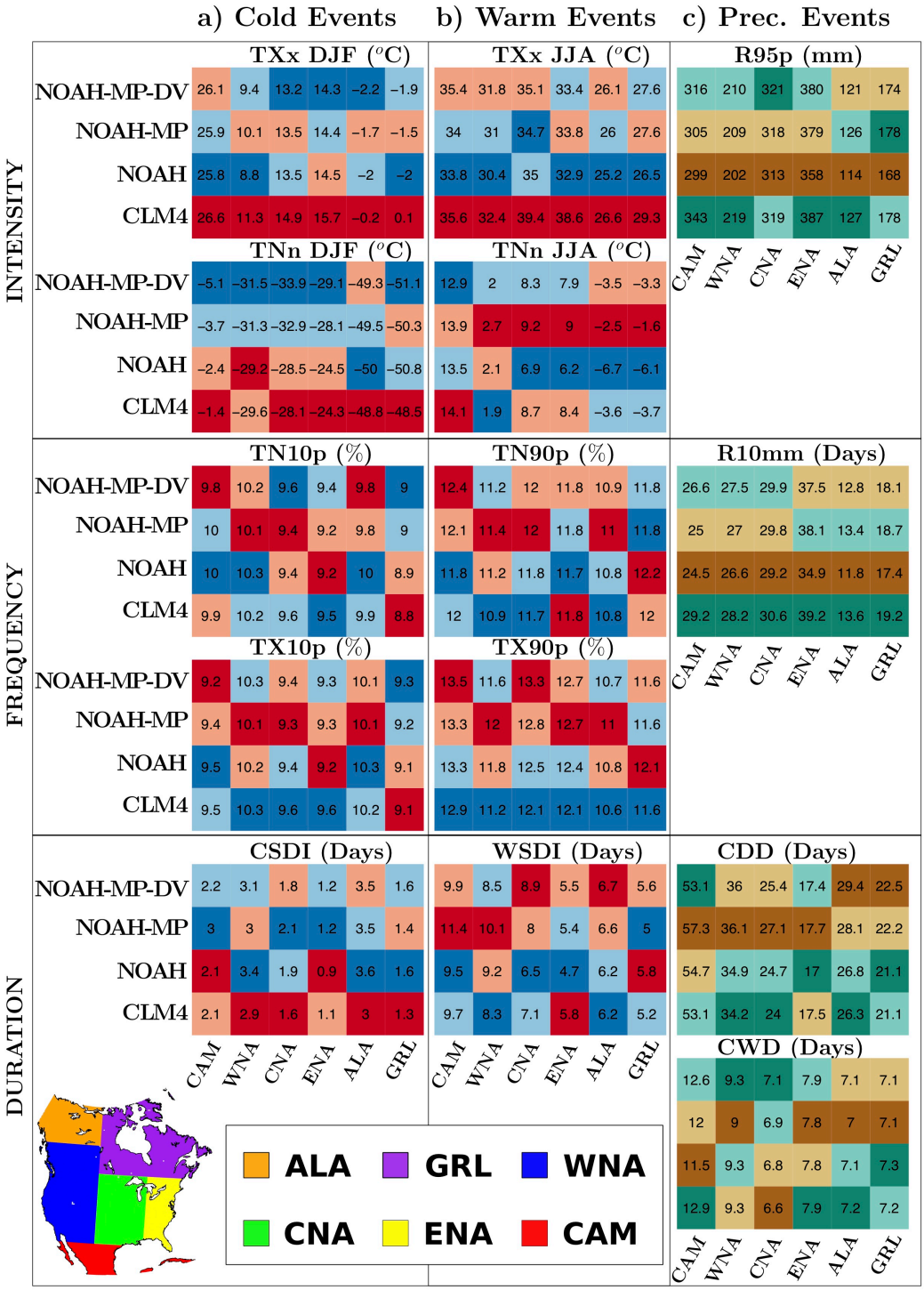

Figure 3.4: Comparison of the simulated climatologies of temperature and precipitation extreme indices included in Table 3.2 among the WRF simulations averaging over six land North American regions adapted from Giorgi et al., 2000 (Central America, CAM; Western North America, WNA; Central North America, CNA; Eastern North America, ENA; Alaska, ALA; and Greenland, GRL). Colors correspond to the hottest (red) and coldest (blue) index values among the WRF simulations for the representation of cold (a) and warm (b) temperature extremes, and to the driest (brown) and wettest (green) index values for the representation of precipitation extremes (c) over each region.

to the driest (brown) and wettest (green) index values for the representation of precipitation extremes over each region. This approach helps us to identify the CLM4 simulation as that with the weakest and shortest cold extreme events, although simulating more frequent cold events than the rest of the LSM components (Figure 3.4a). Meanwhile, the NOAH-MP-DV simulation shows more intense cold extremes during shorter periods over most of the regions (CAM, CNA, ENA and ALA) in comparison with the NOAH-MP simulation which uses prescribed vegetation (Figure 3.4a). The CLM4 simulation also corresponds to the most intense representation of warm extremes for the index based on maximum temperatures, while the intensity index based on minimum temperatures shows higher values in the NOAH-MP simulation, except for the CAM region (Figure 3.4b). The NOAH simulation is associated with the weakest and shortest warm extremes over most areas, and the NOAH-MP and NOAH-MP-DV simulations with the most frequent and longest events. The effect of dynamic vegetation seems to weaken hot extremes at nights over all regions, making them longer at middle and high latitudes (CNA, ENA, ALA and GRL), except in the western US (Figure 3.4b). That is, the NOAH-MP-DV simulation yields warm events longer but not as hot as using prescribed vegetation at most regions at middle and high latitudes. For precipitation extreme events, the CLM4 simulation shows the most intense and frequent precipitation events over most areas, while the NOAH simulation shows the weakest and the least frequent precipitation events (Figure 3.4c). The NOAH-MP simulation produces the longest dry periods over all regions except at high latitudes, where the NOAH-MP-DV simulation yields a higher number of consecutive dry days (Figure 3.4c). The simulation with dynamic vegetation yields wetter results than the simulation with prescribed vegetation at middle and low latitudes, while at high latitudes the NOAH-MP-DV simulation is generally drier than the NOAH-MP simulation (Figure 3.4c).

In summary from the results presented here and in the previous sections, we see that the spatial patterns of land-atmosphere coupling and the climatology of extreme indices are similar in our WRF simulations (Figures 3.1 and 3.2 and B.10-B.12), indicating that the LSM configuration is not influencing these spatial structures. Therefore, other factors common in our four WRF simulations, such as land cover, topography, the latitudinal gradient or atmospheric parameterizations, generate the spatial distribution of the coupling metrics and the extreme indices. Nonetheless, each LSM configuration yields different degree of land-atmosphere coupling and different values of temperature and precipitation extreme events at local scales. Thus, the CLM4 LSM is identified as the component yielding the strongest land control on surface conditions and the highest temperatures during cold and warm events over most of North America as well as the heaviest and most frequent precipitation extremes over most locations (Figures 3.1, 3.2 and 3.4). That is, the simulation with more coincidences of extreme high (low) LH and extreme low (high) SAT is also representing the most intense temperature and precipitation extremes. This suggests that the simulation of very low latent heat flux may be influencing the simulation of heat extremes by inducing an increase in the energy available for sensible heat flux, and likely increasing air temperatures. Meanwhile, the simulation of high latent heat flux may increase the representation of atmospheric water content, inducing changes in the formation of clouds and precipitation. Thus, the strong land control on the CLM4 simulation seems to enhance the intensity of warm and heavy precipitation events comparing with the rest of simulations, particularly in comparison with the NOAH simulation. The NOAH LSM produces the weakest land control on surface conditions and one of the lowest intensities for all temperature indices as well as the lowest intensity and frequency of heavy precipitation events over all regions. The comparison of the NOAH-MP simulations using prescribed and dynamic vegetation shows that the use

of dynamic vegetation yields stronger land control at low and middle latitudes in summer and more intense, frequent and longer heavy precipitation events over the same regions (Figures 3.1, 3.2 and 3.4). Thus, this comparison also supports that the simulation of strong land control leads to heavier precipitation events.

3.4.3 LSM uncertainty in the simulation of temperature and precipitation extremes

Although all WRF simulations show similar spatial patterns for temperature and precipitation extreme indices (Figures B.10, B.11 and B.12), there are large uncertainties in the climatology of each extreme index associated with the use of different LSM configurations. For the simulation of the intensity of cold events, the multi-model range across the WRF simulations for the hottest day in DJF (TXx DJF) shows large values over the boreal forest and the Rockies, where the index climatology is close to 0^oC (Figures 3.3 and 3.5a). The representation of the coldest night in DJF (TNn DJF) shows large LSM dependency, yielding ranges up to 12 $°C$ over the US and a spatial average of 4 $°C$, displaying large uncertainties over areas where the index climatology approaches to 0^oC (Figures 3.3 and 3.5a). The simulated intensity of warm temperature events, measured by the temporal average of the hottest day in summer (TXx JJA), differs up to 10 $°C$ among simulations over eastern North America, with a spatial average of 3.5 $°C$ (Figure 3.5a). The simulation of the mean coldest night in summer (TNn JJA) varies across simulations from 2 to 3 $°C$ over the whole domain, except in the Arctic where the range across simulations reaches approximately 15 $°C$ and the index value yields negative temperatures for some simulations (Figure 3.3 and 3.5a). The frequency of warm extreme temperature events varies among simulations; the range for the number of hot days (TX90p, based on maximum temperatures) is up to 4.2% over the US with a spatial average of 0.97% over the whole domain, and

the range for the number of hot nights (TN90p, based on minimum temperatures) reaches values up to 3.8% at low latitudes with a spatial average of approx. 0.7% (Figure 3.5b). Large values of the multi-model range for the number of hot days (TX90p) approximately coincide with the largest index values (Figures 3.3 and 3.5b). Note that ranges of more than 2% in the number of hot days and nights correspond to differences of more than 7 days per year in the index climatology simulated by different LSMs. Ranges of indices related to the frequency of cold events show smaller values than those for warm temperature events, displaying no clear spatial pattern with averages of $\sim$ 0.5% (i.e. 1.8 days per year) for the number of cold days and nights (TX10p and TN10p; Figure 3.5b). The duration of warm spells is greatly affected by the choice of the LSM component, while its effect is weaker on the simulated duration of cold events (Figure 3.5c). The range of the duration of warm spells across simulations yields values of more than 10 days over Mexico and over broad areas of the central and southern US, with a spatial average of 2.8 days (Figure 3.5c). Otherwise, the LSM effect on the simulated duration of cold spells is weaker, reaching differences of about 6 days among simulations in central Canada with a spatial average of 1.3 days (Figure 3.5c). For both indices, the LSM differences are larger where the duration indices display larger values (Figure 3.3 and 3.5c).

The simulated climatology of the intensity of extreme precipitation events is also strongly affected by the configuration of LSM, with the total annual precipitation in wet days (R95p) reaching LSM differences larger than 100 mm at low latitudes and over the eastern US with a spatial average of 39 mm (Figure 3.6a). The frequency of heavy precipitation events varies among simulations by about 35 days per year at some locations in Mexico and the US, with a spatially averaged range of 3.5 days per year (Figure 3.6b). The areas with the largest inter-model range of the precipitation frequency index across simulations are located in Mexico, the Rockies and at some

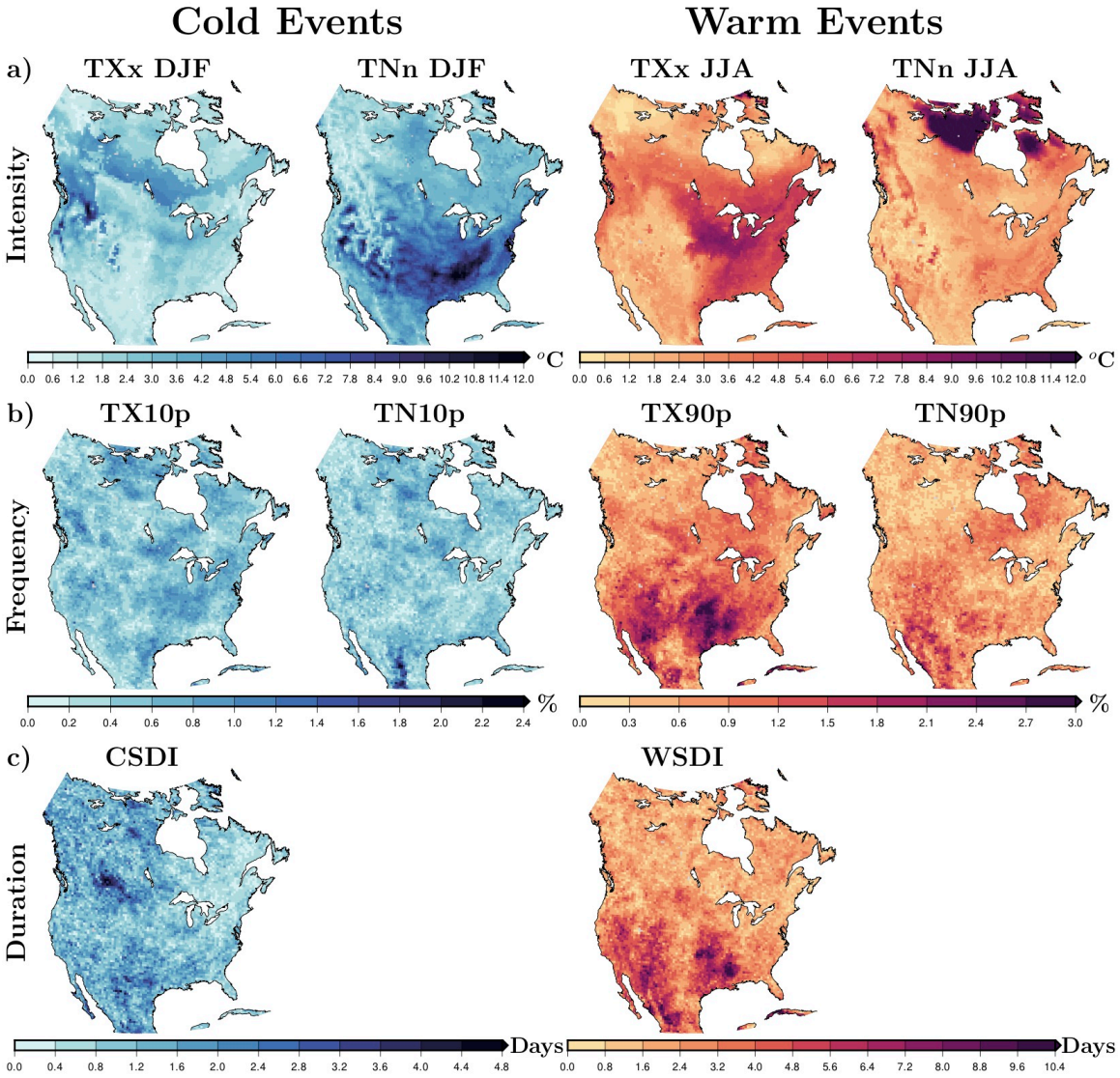

Figure 3.5: Multi-model ranges across the WRF simulations (i.e., difference between the highest value and the lowest value of the four WRF simulations at each grid cell) of extreme indices associated with the intensity (a), frequency (b), and duration (c) of cold (left) and warm (right) extreme temperature events (TXx/TNn, maximum/minimum value of the maximum/minimum daily temperatures; TN10p/TX10p, percentage of cold nights/days; TN90p/TX90p, percentage of hot nights/days; CSDI/WSDI, cold/warm spell duration index). The range among simulations is computed using the mean of each index from 1980 to 2012 for each simulation.

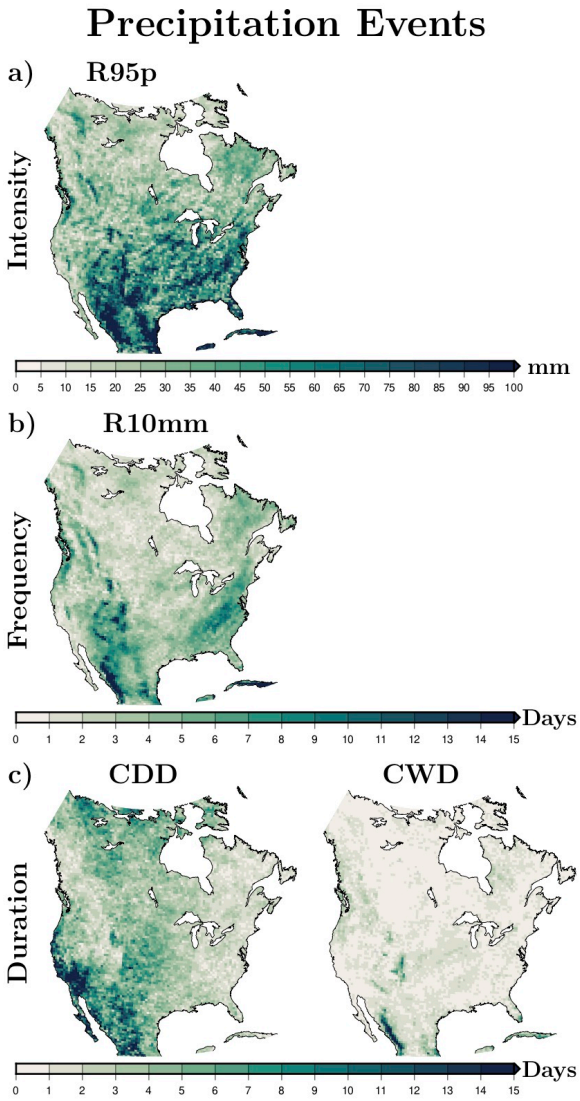

Figure 3.6: As in Figure 3.5 but for extreme precipitation events (R95p, total annual precipitation in wet days; R10mm, number of wet days in a year; CDD/CWD, consecutive dry/wet days).

grid cells over the eastern US coast (Figure 3.6b). The simulation of the number of consecutive dry and wet days also depends on the choice of the LSM component, presenting larger differences among simulations in the climatology of the consecutive dry days index than in the climatology of the consecutive wet days index (Figure 3.6c). The inter-model range across LSM simulations reaches 37 days for the number of consecutive dry days over central and southwestern North America, with a spatial average of 4 days per year (Figure 3.6c). Meanwhile, the simulated number of consecutive wet days also shows LSM differences of more than 20 days at a few grid cells, but lower values over most of the domain, yielding a spatial average of $\sim$ 1.2 days (Figure 3.6c). Large inter-model ranges of precipitation indices across WRF simulations coincide with areas where each index reaches the maximum values (Figure 3.3 and 3.6).

Results for the VAC metric present some similarities with the spatial pattern of uncertainties in the WRF simulation of temperature and precipitation extreme events, which suggest a relationship between these results. The areas showing large uncertainty in the simulation of the intensity indices of cold extremes coincide with areas where LSM simulations differ in the representation of DJF atmospheric control VAC categories (VACa and VACb; Figures 3.1 and 3.5). Particularly, the uncertainty in the hottest day in winter is larger over areas with evergreen needleleaf forest (Figure 3.5 and B.1). Thus, although all simulations include the same land use categories, the differences in the representation of vegetation by each LSM (Figure B.13) from the plant functional types used by the CLM4 LSM to the canopy cover simulated by the NOAH LSM are likely related to the differences in the simulation of land-atmosphere coupling and extreme indices. For the simulation of warm extremes, large LSM differences in the intensity indices correspond to LSM differences in the JJA VAC categories associated with the energy-limited areas (Figures 3.1 and 3.5). The

areas with large uncertainty in the hottest day in summer also correspond with areas showing a mix of vegetation from croplands to forests (Figure B.1). Thus, these results also suggest that LSM differences in the representation of vegetation cover play a role in the different representation of land-atmosphere interactions in energy-limited areas, and consequently different climatologies of the hottest day among our simulations. The uncertainty in the simulation of the coldest night in summer is larger in areas over the mixed tundra category, where LSM configurations differ in the simulation of snow cover in summer (Figures B.1 and B.13). Thus, LSM differences in the representation of snow cover from the single snow layer simulated by the NOAH LSM to the five layers simulated by the CLM4 LSM may also contribute to the uncertainty in the intensity index of warm events. The uncertainty in the number of hot days and the duration of warm spells is larger over regions under land control, particularly over open shrub-lands, suggesting the possible influence of LSM differences in the simulation of soil moisture (Figures 3.2 and B.1). The range of the intensity index of precipitation extremes displays a large JJA component over areas under land control at low latitudes and under atmospheric control at middle and high latitudes (Figures 3.1 and 3.2 and S14a). For the intensity index of heavy precipitation events, our simulations show large uncertainties in areas with mixed vegetation (Figure 3.6 and B.1), suggesting the influence of LSM differences in the representation of vegetation cover on the simulation of latent heat flux, thus leading to changes in the simulation of atmospheric water content and precipitation. The uncertainty in the intensity, frequency and duration of heavy precipitation events is high over the western Mexican coast, where the model is representing the tropical forest and the NOAH simulation showed strong atmospheric control in disagreement with the rest of our simulations (Figures 3.1 and 3.6 and B.1). These results suggest that LSM differences in the description of vegetation and snow cover (e.g the number of snow layers and the description of

the canopy) are also contributing to uncertainties in the simulations of precipitation extremes. The differences in the VAC metric and in the extreme indices are larger between different LSM components than those between simulations with prescribed and dynamic vegetation (Figures 3.1, 3.2 and 3.4). The different representation of land cover by each LSM configuration may yield different soil properties, such as albedo, evaporative resistance, and surface roughness. These soil properties play a key role in the computation of the energy and water fluxes at the land surface, and therefore in the simulation of near-surface conditions (Laguë et al., 2019).

In order to address the LSM influence on the simulation of extreme events, we compute the ranges among our four WRF simulations using the 95th percentile of the analysis period for each extreme index. The uncertainty in the WRF simulations due to the LSM component when using the 95th percentile for each extreme index leads to similar conclusions (Figures B.14 and B.15). The LSM differences using the 95th percentile of the analysis period are larger for all extreme temperature and precipitation indices than using the period mean as expected, but the marked areas are analogous (Figures 3.5, 3.6, B.14 and B.15). The agreement in the representation of areas with large uncertainty in extreme indices between results using mean and extreme climatologies suggests the LSM influence on extreme events at climatological and shorter time scales.

3.4.4 Comparison between WRF simulations and three CORDEX Evaluation simulations

The climatologies of temperature and precipitation extreme statistics as simulated by the three RCMs participating in the NA-CORDEX project (Table 3.3) show similar spatial patterns to our four WRF simulations (Figures B.10-B.12 and B.16-B.18). These similarities in the spatial pattern of extreme indices represented by WRF and

the CORDEX RCMs further support the hypothesis that the spatial features of these maps are controlled by topography, land cover and the latitudinal gradient, since the CORDEX RCMs employed atmospheric models and boundary conditions different to our WRF simulations. Although the spatial patterns are similar in both ensembles, the WRF simulations yield colder minimum temperatures in DJF (TNn DJF) and less frequent cold nights (TX10p) than the CORDEX simulations (Figures B.10 and B.16). The percentage of hot days, however, is higher and warm spells are longer in the WRF simulations than in the CORDEX simulations, particularly over southwestern NA (Figures B.11 and B.17). The intensity of heavy precipitation extremes is generally higher within the WRF ensemble than in the CORDEX ensemble, while dry periods are longer in the CORDEX simulations (Figures B.12 and B.18).

The uncertainties in the simulation of extreme statistics within the CORDEX ensemble show some similarities with the WRF uncertainties which arise from the LSM configuration. For example, the simulated climatology of DJF coldest night (TNn DJF) shows large uncertainties over the US for both ensembles, particularly over the eastern US (Figures 3.5a and 3.7a). The climatologies of DJF hottest day (TXx DJF) display large inter-model range within the WRF ensemble over areas where temperatures approximate to 0^oC, expanding southward for the CORDEX ensemble. The CORDEX inter-model ranges of the frequency indices for cold extremes do not show a clear spatial pattern in agreement with the WRF ensemble. There is, however, a region over the central US with slightly larger ranges among the CORDEX simulations than among the WRF simulations (Figures 3.5b and 3.7b and B.19). The duration of cold spells presents large uncertainties in the CORDEX ensemble over the eastern US/Mexican border and over western Canada, coinciding with a small region with large inter-model range among the WRF simulations (Figures 3.5c and 3.7c). For the simulation of warm temperature extremes, the uncertainties in the intensity

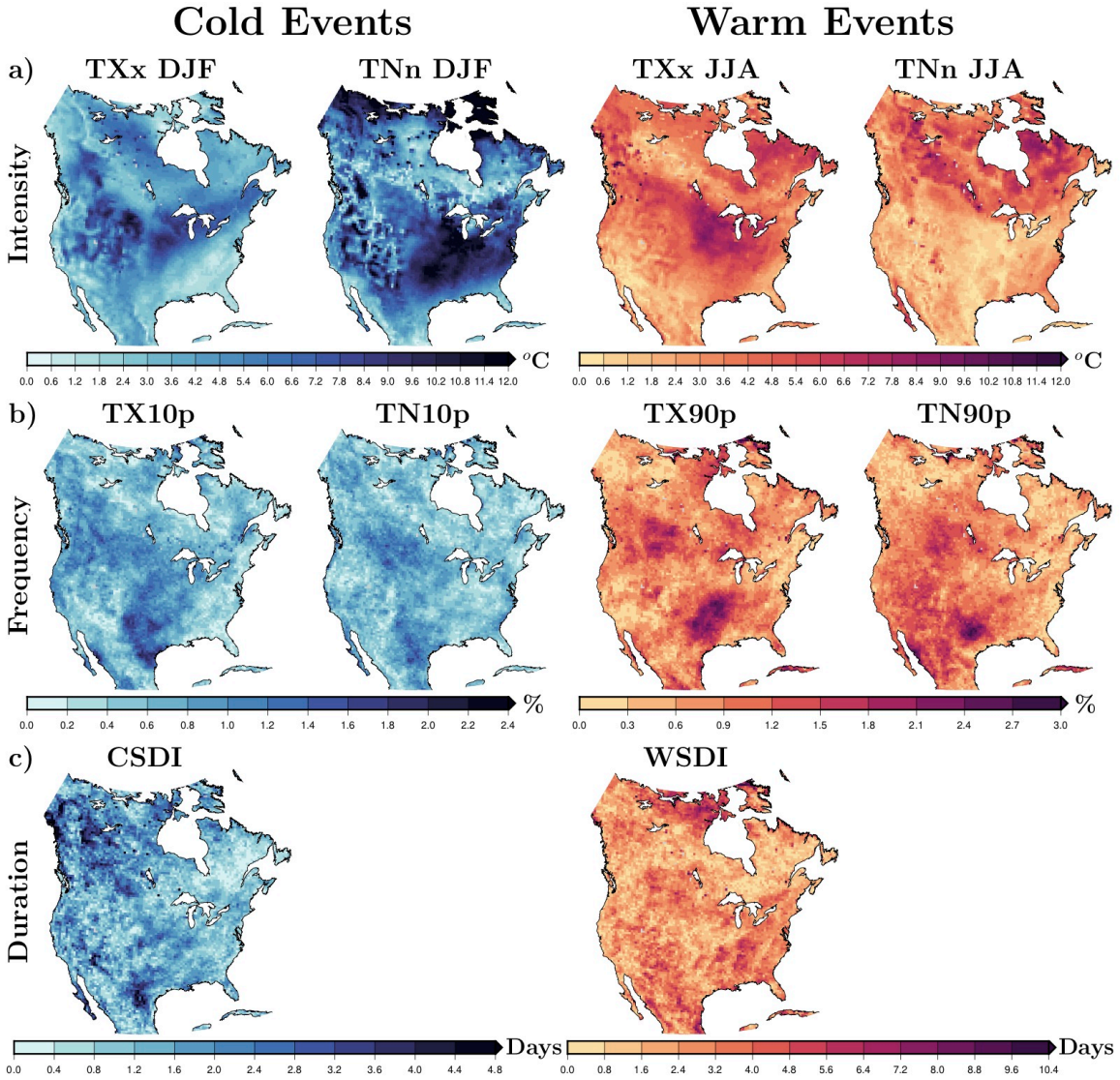

Figure 3.7: Inter-model range across three CORDEX simulations (i.e., difference between the highest value and the lowest value of the three CORDEX simulations at each grid cell) of extreme indices associated with intensity (a), frequency (b), and duration (c) of cold and warm extreme temperature events (Table 3.2). The range across simulations is computed using the mean of each index from 1980 to 2012 for each simulation.

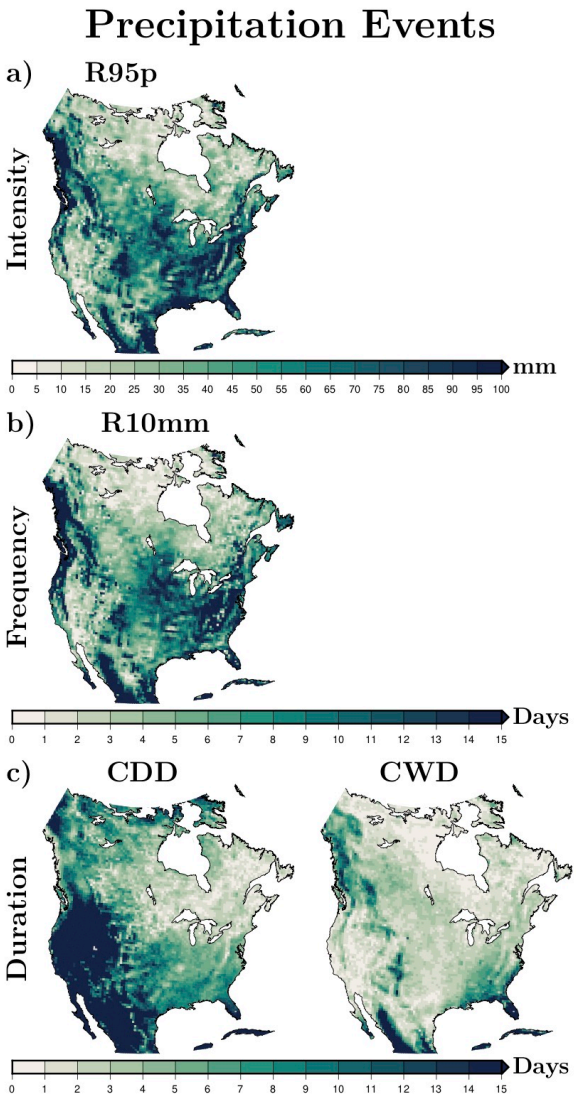

Figure 3.8: As in Figure 3.7 but for extreme precipitation events.

indices among the CORDEX simulations show large ranges over the eastern US for the JJA hottest day (TXx JJA) in agreement with the WRF simulations, and at high latitudes for the coldest night (TNn JJA), including the eastern region of Hudson Bay also marked by the WRF ensemble (Figures 3.5a and 3.7a). The frequency indices of warm events show large inter-model range across the CORDEX simulations over the central US, also shown in the WRF simulations for the TX90p index (Figures 3.5b and 3.7b). The uncertainty in the duration of warm spells among the CORDEX simulations does not show large spatial differences, although the ranges are slightly larger at low latitudes coinciding with regions marked by the WRF ensemble and at very high latitudes (Figures 3.5c and 3.7c). The simulation of precipitation extreme statistics is generally more uncertain across the CORDEX simulations than across the WRF simulations (Figures 3.6, 3.8, and B.20). Interestingly, all regions with large uncertainties in the simulation of precipitation extremes among the WRF simulations are also identified as areas with large uncertainty across the CORDEX ensemble. There are, however, additional areas with large uncertainty in the CORDEX ensemble, particularly for the consecutive dry days index and the frequency index at middle and high latitudes (Figures 3.6 and 3.8). The larger spread of the precipitation indices within the CORDEX ensemble in comparison with the spread in our WRF simulations (Figure B.20) was expected due to the use of different atmospheric models in the CORDEX ensemble. Nonetheless, the agreement between the WRF and CORDEX simulations in the placement of areas with large uncertainties suggests that results from this study may be applicable to other modelling experiments, particularly for the simulation of warm temperature and precipitation extremes.

3.5 Discussion

3.5.1 Comparison of inter-model ranges across the WRF and CORDEX ensembles

In order to provide context for the applicability of these results to other sets of simulations, we compared the range across our WRF simulations with the inter-model range across three CORDEX simulations in representing extreme events (Figures 3.5-3.8). Since CORDEX simulations were performed by three structurally different RCMs (the WRF, the RCA4, and the CRCM-UQAM models), we expected a broader inter-model range of the simulated extreme indices across CORDEX simulations. Differences in the representation of extreme events among the CORDEX simulations arise from several factors, such as different atmospheric parameterizations, land surface model components, the representation of land cover, treatment of boundary conditions, including sea surface temperatures, and the application of nudging techniques. In addition to all these factors, the sensitivity to initial conditions in models may be another important factor for the inter-model range of the simulated extreme events. The WRF sensitivity to initial conditions may also affect the interpretation of the differences among our four simulations with different LSM configurations. However, previous analyses using the WRF model (Gallus et al., 2006; Liu et al., 2019) as well as other climate models (Elía et al., 2008; Kharin et al., 2007; Sillmann et al., 2013a) have showed that the spread of extreme events among ensemble members of an individual model is generally small compared to inter-model spreads or the differences arising from different physics configurations.

Although the CORDEX simulations were performed using boundary conditions from the ERA reanalysis product, the comparison with the WRF simulations is possi-

ble because we compute the ranges across simulations as a measure of the uncertainty in each simulation ensemble. Thus, we compare the uncertainty in each set of simulations finding common areas with large ranges for the representation of cold and warm temperature extremes and precipitation extremes, despite the fact that they used different products as boundary conditions. The agreement in the placement of areas with large uncertainties in the representation of extreme events within the CORDEX ensemble and those within our WRF simulations suggests that the uncertainties in these areas may arise from similar causes. Our WRF simulations only differ in the configuration of the LSM component. Therefore, the differences between LSM components can also be an important source of uncertainty in the simulation of extreme events within the CORDEX simulations, through a different representation of land-atmosphere interactions.

One of the simulations included in the CORDEX ensemble was performed by the WRF model using the NOAH LSM component. The comparison of the extreme indices between our WRF-NOAH simulation and the one included in the CORDEX ensemble shows similar spatial patterns and regional differences in the value of each extreme index (second column in Figures B.11-B.13 and third column in Figures B.16-B.18). However, this comparison is not very different if we use another CORDEX simulation performed by a different RCM. This suggests that the spatial pattern of the extreme indices is driven by factors common in all simulations, such as land cover, topography and the latitudinal gradient. The regional differences in the value of extreme indices between our WRF-NOAH simulation and the WRF-NOAH CORDEX simulation are likely caused by the use of nudging techniques to match the ERA-Interim product in the CORDEX simulation.

Although there are more sources of uncertainty in the CORDEX simulations than across the WRF simulations, the comparison between the uncertainty within each set

of simulations (i.e. the difference between the range among the WRF simulations and the range among the CORDEX simulations) displays larger ranges across the WRF simulations than across the CORDEX ensemble over certain areas and for certain extreme indices (Figures B.19 and B.20). This suggests the possible existence of bias compensation inside the CORDEX simulations. Moreover, each RCM may have a different sensitivity to the employed LSM component as well as to other components and parameterizations. Additional sensitivity studies using the WRF model or another climate model with different settings and parameterizations may help to discern other important sources of uncertainties in the simulation of extreme events, such as horizontal resolution.

3.5.2 Climatology of extreme events as represented by the WRF simulations and by the CMIP5 simulations

Sillmann et al., 2013a presented an evaluation of the CMIP5 models in simulating some of the extreme indices defined by ETCCDI; this information was used in the Intergovernmental Panel on Climate Change (IPCC) chapter on models' evaluation (Flato et al., 2013). The analysis period employed by Sillmann et al., 2013a, 1981-2000, differs from the one used in this analysis, but a rough comparison can be done between our results and theirs for some extreme indices. For example, the spatial patterns of DJF coldest night and JJA hottest day are similar for the WRF and CMIP5 ensemble means (Figure 3.3 and Figure 2 in Sillmann et al. 2013a). The similarities in the spatial pattern of extreme indices between our WRF simulations, the CMIP5 and the CORDEX ensembles suggest that the topography, land cover and latitudinal gradient are driving these spatial features. Sillmann et al., 2013a also provides regional averages over six NA regions, adapted from Giorgi et al., 2000. These spatial averages allow identification of some regional differences between the WRF and

the CMIP5 ensembles, for example over the eastern US coast (ENA region) where the WRF simulations yield warmer JJA maximum temperatures than the CMIP5 ensemble (Figure 3.4 and Figure 3 in Sillmann et al. 2013a). The spatial patterns of the WRF and CMIP5 ensembles for CSDI and WSDI indices are also similar, although the WRF ensemble reaches longer cold and warm events (Figure 3.3 and Figures B.6-B.7 in Sillmann et al. 2013a). The representation of the intensity index for heavy precipitation events (R95p) also shows similar spatial patterns between both ensemble means, although the WRF ensemble is generally more intense over most regions (Figures 3.3 and 3.4, and Figures 6 and 7 in Sillmann et al. 2013a). Similar results are found for the simulation of consecutive dry days, showing similar spatial patterns with some regional differences especially at low latitudes (CAM region, Figures 3.3 and 3.4, and Figures 6 and 7 in Sillmann et al. 2013a). The variability across the CMIP5 ensemble for the simulation of precipitation indices seems to be particularly large at low latitudes (CAM region) similar to WRF uncertainty in the representation of precipitation extremes associated with the LSM component (Figure 3.6, and Figure 7 in Sillmann et al. 2013a). Although this is a rough comparison between results presented in this article and in Sillmann et al., 2013a, this comparison suggests that our conclusions could be also applicable to the CMIP5 ensemble as it was the case for the CORDEX ensemble.

3.5.3 Implications of these results

Increases in heat-related events have been directly and robustly associated with increases in mortality, for example in Europe during the heatwave of 2003 (Fischer et al., 2007) or in India during the heatwave of 2015 (Pattanaik et al., 2017). Heavy precipitation events often lead to floods, which also are directly associated to economic loss and death toll (Hu et al., 2018). All climate change projections point to a future

increase in temperature and precipitation extreme events (Sillmann et al., 2013b), thus developing mitigation strategies will become necessary to preserve human health. Climate model simulations are our best source of information to mitigate climate change impacts. However, the results presented here indicate that the simulation of several extreme indices varies largely depending on the employed LSM component, because of the different representation of land-atmosphere interactions. This means that a climate model may simulate the climatology of heat extremes 5^oC warmer and 6 days longer depending on the employed LSM component, and similarly for cold extremes and heavy precipitation events. Therefore, studies based on multi-model ensembles and reanalyses should include a variety of LSM configurations to account for the uncertainty arising from this model component or to test the performance of the selected LSM component before performing the whole simulation. The accuracy of climate models and the management of uncertainties in simulating extreme events will likely affect climate change policy, therefore having repercussions for society and environment.

The indices employed here to study the climatology of extreme temperature events were based on minimum and maximum temperature outputs. However, many studies have proven that the study of compound events using indices based on multiple variables, such as temperature and moisture outputs, are more representative of thermal stress in humans and ecosystems than standard indices (Zscheischler et al., 2018). The large LSM influence on the climatology of extreme temperature and precipitation events, suggests that the uncertainty arising from the LSM component could be higher on extreme indices based on multiple variables. However, the analysis of the LSM influence on compound events is beyond the scope of this work, and constitutes an interesting line for future research.

3.6 Conclusions

WRF simulations over North America coupled to different LSM components showed similar spatial patterns of land-atmosphere interactions as measured by the VAC index. The use of this metric allows the classification of our results into: energy-limited areas, where atmospheric conditions control land-atmosphere interactions (VACa and VACb); and water-limited areas, where soil moisture deficits control the energy and water exchanges between the land surface and the lower atmosphere (VACc and VACd categories). Our results indicate atmospheric control over land-atmosphere interactions at middle and high latitudes and land surface control over lower latitudes, particularly in JJA. However, the simulation of land-atmosphere coupling differs at regional scales depending on the LSM choice in two directions; by altering land control on surface processes (VACc and VACd categories) and by altering atmospheric conditions and its influence on land-atmosphere interactions (VACa and VACb categories). Thus, the NOAH LSM is associated with the weakest representation of land control on surface conditions, while the CLM4 LSM simulates one of the strongest land effects on surface conditions. The use of different LSM components leads to large ranges of represented extreme temperature and precipitation events, affecting their simulation in intensity, frequency and duration. The CLM4 LSM yields the weakest cold events, the warmest hot days, and the heaviest precipitation events, while the NOAH simulation yields the weakest warm temperature events and the weakest heavy precipitation events. Meanwhile, the NOAH-MP LSM produces the driest simulation, yielding slightly wetter conditions when using dynamic vegetation at middle and low latitudes. Although the LSM differences in our results are more marked than differences between the simulations with prescribed and dynamic vegetation, the use of dynamic vegetation yields stronger land control at low and middle latitudes in summer and more

intense, frequent and longer heavy precipitation events and reduces the duration of droughts over the same regions. Thus, our results suggest a relationship between the degree of land control on surface conditions reached by each LSM configuration and the intensity of extreme events, in agreement with the case study during the Russian 2010 heat wave (Zscheischler et al., 2015).

Previous studies using GCM simulations suggested a dependence of the simulated land-atmosphere interactions on the employed LSM component with possible consequences for the simulation of extreme events (García-García et al., 2019). Results from four WRF simulations differing only in the LSM configuration support that hypothesis, identifying LSM differences in the description of land cover as an important factor for the simulation of near-surface conditions. Additionally, areas with large uncertainties in the simulation of temperature and precipitation extremes across the WRF simulations due to different LSM components appear in the NA-CORDEX model ensemble, which indicates the possible LSM influence on the simulation of extreme events within other model ensembles. This work reinforces the important role of the LSM component in climate simulations, supporting the urgency of on-going research focused on improving this model component and their implementation in regional and global climate models as well as in reanalysis products. The strong LSM dependency of climate model simulation of extremes is also of special importance for international reports focused on land, such as the IPCC Special Report on Climate Change, Desertification, Land Degradation, Sustainable Land Management, Food Security, and Greenhouse gas fluxes in Terrestrial Ecosystems (Arneth, 2019). Future sensitivity analyses to the LSM component using different regional and global climate models would be useful to understand models' differences in simulating temperature and precipitation extremes, helping to narrow the inter-model range across reanalyses and climate model projections in simulating extreme events.

Bibliography

"Summary for Policymakers" (2019). In: *Special Report on climate change, desertification, land degradation, sustainable land management, food security, and greenhouse gas fluxes in terrestrial ecosystems. Summary for Policymakers*. Ed. by A. e. a. Arneth. Cambridge, United Kingdom and New York, NY, USA: Cambridge University Press, pp. 1–43.

Balsamo, G., Albergel, C., Beljaars, A., Boussetta, S., Brun, E., Cloke, H., Dee, D., Dutra, E., Muñoz-Sabater, J., and Pappenberger, F. (2015). ERA-Interim/Land: a global land surface reanalysis data set. *Hydrology and Earth System Sciences* **19**(1), 389–407.

Barlage, M., Zeng, X., Wei, H., and Mitchell, K. E. (2005). A global 0.05 ° maximum albedo dataset of snow-covered land based on MODIS observations. *Geophysical Research Letters* **32**(17).

Cannon, A. J., Sobie, S. R., and Murdock, T. Q. (2015). Bias Correction of GCM Precipitation by Quantile Mapping: How Well Do Methods Preserve Changes in Quantiles and Extremes? *Journal of Climate* **28**(17), 6938–6959.

Collins, W. D., Rasch, P. J., Boville, B. A., Hack, J. J., McCaa, J. R., Williamson, D. L., Kiehl, J. T., Briegleb, B., Bitz, C., and Lin, S.-J. (2004). Description of the NCAR community atmosphere model (CAM 3.0). *NCAR Tech. Note NCAR/TN-464+ STR* **226**.

Collins, W. D., Bitz, C. M., Blackmon, M. L., Bonan, G. B., Bretherton, C. S., Carton, J. A., Chang, P., Doney, S. C., Hack, J. J., Henderson, T. B., et al. (2006). The community climate system model version 3 (CCSM3). *Journal of Climate* **19**(11), 2122–2143.

Davin, E. L., Maisonnave, E., and Seneviratne, S. I. (2016). Is land surface processes representation a possible weak link in current Regional Climate Models? *Environmental Research Letters* **11**(7), 074027.

Dee, D. P., Uppala, S. M., Simmons, A. J., Berrisford, P., Poli, P., Kobayashi, S., Andrae, U., Balmaseda, M. A., Balsamo, G., Bauer, P., Bechtold, P., Beljaars, A. C. M., Berg, L. van de, Bidlot, J., Bormann, N., Delsol, C., Dragani, R., Fuentes, M., Geer, A. J., Haimberger, L., Healy, S. B., Hersbach, H., Hólm, E. V., Isaksen, L., Kållberg, P., Köhler, M., Matricardi, M., McNally, A. P., Monge-Sanz, B. M., Morcrette, J.-J., Park, B.-K., Peubey, C., Rosnay, P. de, Tavolato, C., Thépaut, J.-N., and Vitart, F. (2011). The ERA-Interim reanalysis: configuration and performance of the data assimilation system. *Quarterly Journal of the Royal Meteorological Society* **137**(656), 553–597.

Diro, G. T., Sushama, L., Martynov, A., Jeong, D. I., Verseghy, D., and Winger, K. (2014). Land-atmosphere coupling over North America in CRCM5. *Journal of Geophysical Research: Atmospheres* **119**(21), 11,955–11,972. DOI: 10.1002/2014JD021677.

Diro, G. T., Sushama, L., and Huziy, O. (2018). Snow-atmosphere coupling and its impact on temperature variability and extremes over North America. *Climate Dynamics* **50**(7), 2993–3007. DOI: 10.1007/s00382-017-3788-5.

Donat, M. G., King, A. D., Overpeck, J. T., Alexander, L. V., Durre, I., and Karoly, D. J. (2016). Extraordinary heat during the 1930s US Dust Bowl and associated large-scale conditions. *Climate Dynamics* **46**(1), 413–426.

Ehret, U., Zehe, E., Wulfmeyer, V., Warrach-Sagi, K., and Liebert, J. (2012). HESS Opinions "Should we apply bias correction to global and regional climate model data?". *Hydrol. Earth Syst. Sci.* **16**(9), 3391–3404. DOI: 10.5194/hess-16-3391-2012.

Elía, R. de, Caya, D., Côté, H., Frigon, A., Biner, S., Giguère, M., Paquin, D., Harvey, R., and Plummer, D. (2008). Evaluation of uncertainties in the CRCM-simulated North American climate. *Climate Dynamics* **30**(2), 113–132. DOI: 10.1007/s00382-007-0288-z.

Ferguson, C. R., Wood, E. F., and Vinukollu, R. K. (2012). A Global Intercomparison of Modeled and Observed Land–Atmosphere Coupling. *Journal of Hydrometeorology* **13**(3), 749–784. DOI: 10.1175/JHM-D-11-0119.1.

Fischer, E., Seneviratne, S., Lüthi, D, and Schär, C (2007). Contribution of land-atmosphere coupling to recent European summer heat waves. *Geophysical Research Letters* **34**(6).

Flato, G., Marotzke, J., Abiodun, B., Braconnot, P., Chou, S., Collins, W., Cox, P., Driouech, F., Emori, S., Eyring, V., Forest, C., Gleckler, P., Guilyardi, E., Jakob, C., Kattsov, V., Reason, C., and Rummukainen, M. (2013). "Evaluation of Climate Models". In: *Climate Change 2013: The Physical Science Basis. Contribution of Working Group I to the Fifth Assessment Report of the Intergovernmental Panel on Climate Change*. Ed. by T. Stocker, D. Qin, G.-K. Plattner, M. Tignor, S. Allen, J.

Boschung, A. Nauels, Y. Xia, V. Bex, and P. Midgley. Cambridge, United Kingdom and New York, NY, USA: Cambridge University Press. Chap. 9, pp. 741–866. DOI: 10.1017/CBO9781107415324.020.

Gallus, W. A. and Bresch, J. F. (2006). Comparison of Impacts of WRF Dynamic Core, Physics Package, and Initial Conditions on Warm Season Rainfall Forecasts. *Monthly Weather Review* **134**(9), 2632–2641. DOI: 10.1175/MWR3198.1.

García-García, A., Cuesta-Valero, F. J., Beltrami, H., and Smerdon, J. E. (2019). Characterization of Air and Ground Temperature Relationships within the CMIP5 Historical and Future Climate Simulations. *Journal of Geophysical Research: Atmospheres*(124), 3903–3929. DOI: https://doi.org/10.1029/2018JD030117.

García-García, A., Cuesta-Valero, F. J., Beltrami, H., González-Rouco, J. F., García-Bustamante, E., and Finnis, J. (2020). Land Surface Model influence on the simulated climatologies of extreme temperature and precipitation events within the WRF v.3.9 model over North America. *Geocientific Model Development (In Discussion)*. DOI: https://doi.org/10.5194/gmd-2020-86.

Gevaert, A. I., Miralles, D. G., Jeu, R. A. M., Schellekens, J., and Dolman, A. J. (2018). Soil Moisture-Temperature Coupling in a Set of Land Surface Models. *Journal of Geophysical Research: Atmospheres* **123**(3), 1481–1498. DOI: 10.1002/2017JD027346.

Giorgi, F. and Francisco, R. (2000). Uncertainties in regional climate change prediction: a regional analysis of ensemble simulations with the HADCM2 coupled AOGCM. *Climate Dynamics* **16**(2), 169–182.

Giorgi, F. and Gutowski Jr., W. J. (2015). Regional Dynamical Downscaling and the CORDEX Initiative. *Annual Review of Environment and Resources* **40**(1), 467–490. DOI: 10.1146/annurev-environ-102014-021217.

Grell, G. A. and Freitas, S. R. (2014). A scale and aerosol aware stochastic convective parameterization for weather and air quality modeling. *Atmos. Chem. Phys* **14**(10), 5233–5250. DOI: https://doi.org/10.5194/acp-14-5233-2014,2014.

Hauser, M., Orth, R., and Seneviratne, S. I. (2016). Role of soil moisture versus recent climate change for the 2010 heat wave in western Russia. *Geophysical Research Letters* **43**(6), 2819–2826. DOI: 10.1002/2016GL068036.

Hersbach, H., Rosnay, P. de, Bell, B., Schepers, D., Simmons, A., Soci, C., Abdalla, S., Alonso-Balmaseda, M., Balsamo, G., Bechtold, P., Berrisford, P., Bidlot, J.-R., Boisséson, E. de, Bonavita, M., Browne, P., Buizza, R., Dahlgren, P., Dee, D., Dragani, R., Diamantakis, M., Flemming, J., Forbes, R., Geer, A. J., Haiden, T., Hólm, E., Haimberger, L., Hogan, R., Horányi, A., Janiskova, M., Laloyaux, P., Lopez, P., Munoz-Sabater, J., Peubey, C., Radu, R., Richardson, D., Thépaut, J.-N., Vitart, F., Yang, X, Zsótér, E., and Zuo, H. (2018). *Operational global reanal-*

ysis: progress, future directions and synergies with NWP. Tech. rep. 27. European Centre for Medium Range Weather Forecasts. DOI: 10.21957/tkic6g3wm.

Hicks Pries, C. E., Castanha, C., Porras, R. C., and Torn, M. S. (2017). The whole-soil carbon flux in response to warming. *Science* **355**(6332), 1420–1423.

Hirschi, M., Seneviratne, S. I., Alexandrov, V., Boberg, F., Boroneant, C., Christensen, O. B., Formayer, H., Orlowsky, B., and Stepanek, P. (2011). Observational evidence for soil-moisture impact on hot extremes in southeastern Europe. *Nature Geosci* **4**(1), 17–21.

Hong, S.-Y., Noh, Y., and Dudhia, J. (2006a). A New Vertical Diffusion Package with an Explicit Treatment of Entrainment Processes. *Monthly Weather Review* **134**(9), 2318–2341. DOI: 10.1175/MWR3199.1.

Hong, S.-Y. and Lim, J.-O. J. (2006b). The WRF single-moment 6-class microphysics scheme (WSM6). *J. Korean Meteor. Soc* **42**(2), 129–151.

Hu, P., Zhang, Q., Shi, P., Chen, B., and Fang, J. (2018). Flood-induced mortality across the globe: Spatiotemporal pattern and influencing factors. *Science of The Total Environment* **643**, 171 –182. DOI: https://doi.org/10.1016/j.scitotenv.2018.06.197.

IPCC (2013). *Climate Change 2013: The Physical Science Basis. Contribution of Working Group I to the Fifth Assessment Report of the Intergovernmental Panel on Climate Change*. Cambridge, United Kingdom and New York, NY, USA: Cambridge University Press, p. 1535. DOI: 10.1017/CBO9781107415324.

Jeong, D. I., Sushama, L., Diro, G. T., Khaliq, M. N., Beltrami, H., and Caya, D. (2016). Projected changes to high temperature events for Canada based on a regional climate model ensemble. *Climate Dynamics* **46**(9), 3163–3180.

Jiménez, P. A., Dudhia, J., González-Rouco, J. F., Navarro, J., Montávez, J. P., and García-Bustamante, E. (2012). A Revised Scheme for the WRF Surface Layer Formulation. *Monthly Weather Review* **140**(3), 898–918.

Karl, T. R., Nicholls, N., and Ghazi, A. (1999). "CLIVAR/GCOS/WMO Workshop on Indices and Indicators for Climate Extremes Workshop Summary". In: *Weather and Climate Extremes: Changes, Variations and a Perspective from the Insurance Industry*. Ed. by T. R. Karl, N. Nicholls, and A. Ghazi. Dordrecht: Springer Netherlands, pp. 3–7.

Katragkou, E., García-Díez, M., Vautard, R., Sobolowski, S., Zanis, P., Alexandri, G., Cardoso, R. M., Colette, A., Fernandez, J., Gobiet, A., Goergen, K., Karacostas, T., Knist, S., Mayer, S., Soares, P. M. M., Pytharoulis, I., Tegoulias, I., Tsikerdekis, A., and Jacob, D. (2015). Regional climate hindcast simulations within EURO-CORDEX: evaluation of a WRF multi-physics ensemble. *Geoscientific Model Development* **8**(3), 603–618. DOI: 10.5194/gmd-8-603-2015.

Kharin, V. V., Zwiers, F. W., Zhang, X., and Hegerl, G. C. (2007). Changes in Temperature and Precipitation Extremes in the IPCC Ensemble of Global Coupled Model Simulations. *Journal of Climate* **20**(8), 1419–1444.

Knist, S., Goergen, K., Buonomo, E., Christensen, O. B., Colette, A., Cardoso, R. M., Fealy, R., Fernández, J., García-Díez, M., Jacob, D., Kartsios, S., Katragkou, E., Keuler, K., Mayer, S., Meijgaard, E. van, Nikulin, G., Soares, P. M. M., Sobolowski, S., Szepszo, G., Teichmann, C., Vautard, R., Warrach-Sagi, K., Wulfmeyer, V., and Simmer, C. (2016). Land-atmosphere coupling in EURO-CORDEX evaluation experiments. *Journal of Geophysical Research: Atmospheres*. DOI: 10.1002/2016JD025476.

Laguë, M. M., Bonan, G. B., and Swann, A. L. S. (2019). Separating the impact of individual land surface properties on the terrestrial surface energy budget in both the coupled and un-coupled land-atmosphere system. *Journal of Climate* **32**(18), 5725–5744.

Li, M., Ma, Z., Gu, H., Yang, Q., and Zheng, Z. (2017). Production of a combined land surface data set and its use to assess land-atmosphere coupling in China. *Journal of Geophysical Research: Atmospheres* **122**(2), 948–965.

Liu, C., Ikeda, K., Rasmussen, R., Barlage, M., Newman, A. J., Prein, A. F., Chen, F., Chen, L., Clark, M., Dai, A., Dudhia, J., Eidhammer, T., Gochis, D., Gutmann, E., Kurkute, S., Li, Y., Thompson, G., and Yates, D. (2017). Continental-scale convection-permitting modeling of the current and future climate of North America. *Climate Dynamics* **49**(1), 71–95.

Liu, L., Ma, Y., Menenti, M., Zhang, X., and Ma, W. (2019). Evaluation of WRF Modeling in Relation to Different Land Surface Schemes and Initial and Boundary Conditions: A Snow Event Simulation Over the Tibetan Plateau. *Journal of Geophysical Research: Atmospheres* **124**(1), 209–226. DOI: 10.1029/2018JD029208.

Lorenz, R., Argüeso, D., Donat, M. G., Pitman, A. J., Hurk, B. van den, Berg, A., Lawrence, D. M., Chéruy, F., Ducharne, A., Hagemann, S., Meier, A., Milly, P. C. D., and Seneviratne, S. I. (2016). Influence of land-atmosphere feedbacks on temperature and precipitation extremes in the GLACE-CMIP5 ensemble. *Journal of Geophysical Research: Atmospheres* **121**(2), 607–623. DOI: 10.1002/2015JD024053.

Martynov, A., Laprise, R., Sushama, L., Winger, K., Šeparović, L., and Dugas, B. (2013). Reanalysis-driven climate simulation over CORDEX North America domain using the Canadian Regional Climate Model, version 5: model performance evaluation. *Climate Dynamics* **41**(11), 2973–3005.

Mearns, L. et al. (2017). *The NA-CORDEX dataset, version 1.0. NCAR Climate Data Gateway, Boulder CO.* https://doi.org/10.5065/D6SJ1JCH accessed [December, 2018].

Mesinger, F., DiMego, G., Kalnay, E., Mitchell, K., Shafran, P. C., Ebisuzaki, W., Jovic, D., Woollen, J., Rogers, E., Berbery, E. H., et al. (2006). North American regional reanalysis. *Bulletin of the American Meteorological Society* **87**(3), 343–360. DOI: https://doi.org/10.1175/BAMS-87-3-343.

Michalakes, J, Chen, S, Dudhia, J, Hart, L, Klemp, J, Middlecoff, J, and Skamarock, W (2001). *Development of a next generation regional weather research and forecast model*. Vol. 1. World Scientific, pp. 269–276.

Miralles, D. G., Berg, M. J. den, Teuling, A. J., and Jeu, R. A. M. (2012). Soil moisture-temperature coupling: A multiscale observational analysis. *Geophysical Research Letters* **39**(21).

Mitchell, K. (2005). The community Noah land-surface model (LSM). *User's Guide* **7**.

Molod, A., Takacs, L., Suarez, M., and Bacmeister, J. (2015). Development of the GEOS-5 atmospheric general circulation model: evolution from MERRA to MERRA2. *Geosci. Model Dev.* **8**(5), 1339–1356. DOI: 10.5194/gmd-8-1339-2015.

Niu, G.-Y., Yang, Z.-L., Mitchell, K. E., Chen, F., Ek, M. B., Barlage, M., Kumar, A., Manning, K., Niyogi, D., Rosero, E., Tewari, M., and Xia, Y. (2011). The community Noah land surface model with multiparameterization options (Noah-MP): 1. Model description and evaluation with local-scale measurements. *Journal of Geophysical Research: Atmospheres* **116**(D12), 2156–2202. DOI: 10.1029/2010JD015139.

Oleson, K. W., Lawrence, D. M., Bonan, G. B., Flanner, M. G., Kluzek, E., Lawrence, P. J., Levis, S., Swenson, S. C., Thornton, P. E., Dai, A., Decker, M., Dickinson, R., Feddema, J., Heald, C. L., Hoffman, F., Lamarque, J.-F., Mahowald, N., Niu, G.-Y., Qian, T., Randerson, J., Running, S., Sakaguchi, K., Slater, A., Stockli, R., Wang, A., Yang, Z.-L., Zeng, X., and Zeng., X. (2010). *Technical description of version 4.0 of the Community Land Model (CLM)*. Tech. rep. NCAR, Boulder.

Onogi, K., Tsutsui, J., Koide, H., Sakamoto, M., Kobayashi, S., Hatsushika, H., Matsumoto, T., Yamazaki, N., Kamahori, H., and Takahashi, K. (2007). The JRA-25 reanalysis. *Journal of the Meteorological Society of Japan. Ser. II* **85**(3), 369–432.

Orlowsky, B. and Seneviratne, S. I. (2012). Global changes in extreme events: regional and seasonal dimension. *Climatic Change* **110**(3), 669–696.

Pattanaik, D., Mohapatra, M, Srivastava, A., and Kumar, A. (2017). Heat wave over India during summer 2015: an assessment of real time extended range forecast. *Meteorology and Atmospheric Physics* **129**(4), 375–393. DOI: https://doi.org/10.1007/s00703-016-0469-6.

Philip, S. Y., Kew, S. F., Hauser, M., Guillod, B. P., Teuling, A. J., Whan, K., Uhe, P., and Oldenborgh, G. J. v. (2018). Western US high June 2015 temperatures

and their relation to global warming and soil moisture. *Climate Dynamics* **50**(7), 2587–2601.

Reichle, R. H., Koster, R. D., Lannoy, G. J.M. D., Forman, B. A., Liu, Q., Mahanama, S. P. P., and Touré, A. (2011). Assessment and Enhancement of MERRA Land Surface Hydrology Estimates. *Journal of Climate* **24**(24), 6322–6338.

Rodell, M., Houser, P. R., Jambor, U., Gottschalck, J., Mitchell, K., Meng, C.-J., Arsenault, K., Cosgrove, B., Radakovich, J., Bosilovich, M., Entin, J. K., Walker, J. P., Lohmann, D., and Toll, D. (2004). The Global Land Data Assimilation System. *Bulletin of the American Meteorological Society* **85**(3), 381–394.

Samuelsson, P., Jones, C. G., Willén, U., Ullerstig, A., Gollivik, S., Hansson, U., Jansson, C., Kjellström, E., Nikulin, G., and Wyser, K. (2011). The Rossby Centre Regional Climate model RCA3: model description and performance. *Tellus A* **63**(1), 4–23.

Seneviratne, S. I., Corti, T., Davin, E. L., Hirschi, M., Jaeger, E. B., Lehner, I., Orlowsky, B., and Teuling, A. J. (2010). Investigating soil moisture–climate interactions in a changing climate: A review. *Earth-Science Reviews* **99**(3–4), 125 –161. DOI: http://dx.doi.org/10.1016/j.earscirev.2010.02.004.

Seneviratne, S. I., Nicholls, N., Easterling, D., Goodess, C. M., Kanae, S., Kossin, J., Luo, Y., Marengo, J., McInnes, K., and Rahimi, M. (2012). "Changes in climate extremes and their impacts on the natural physical environment". In: *Managing the Risks of Extreme Events and Disasters to Advance Climate Change Adaptation*. Cambridge University Press, pp. 109–203.

Sillmann, J., Kharin, V. V., Zhang, X., Zwiers, F. W., and Bronaugh, D. (2013a). Climate extremes indices in the CMIP5 multimodel ensemble: Part 1. Model evaluation in the present climate. *Journal of Geophysical Research: Atmospheres* **118**(4), 1716–1733.

Sillmann, J., Kharin, V. V., Zwiers, F. W., Zhang, X., and Bronaugh, D. (2013b). Climate extremes indices in the CMIP5 multimodel ensemble: Part 2. Future climate projections. *Journal of Geophysical Research: Atmospheres* **118**(6), 2473–2493. DOI: 10.1002/jgrd.50188.

Sippel, S., Zscheischler, J., Mahecha, M. D., Orth, R., Reichstein, M., Vogel, M., and Seneviratne, S. I. (2017). Refining multi-model projections of temperature extremes by evaluation against land–atmosphere coupling diagnostics. *Earth System Dynamics* **8**(2), 387–403. DOI: 10.5194/esd-8-387-2017.

Skamarock, W. C., Klemp, J. B., Dudhia, J., Gill, D. O., Barker, D. M., Wang, W., and Powers, J. G. (2008a). *A description of theadvanced research WRF version 3, Tech. Rep.* TN-475+STR. National Center for Atmospheric Research Boulder, Colorado,USA.

Skamarock, W. C., Klemp, J. B., Dudhia, J., Gill, D. O., Barker, D. M., Wang, W., and Powers, J. G. (2008b). *A description of theadvanced research WRF version 3, Tech. Rep.* TN-475+STR. National Center for Atmospheric Research Boulder, Colorado,USA.

Stieglitz, M. and Smerdon, J. E. (2007). Characterizing land-atmosphere coupling and the implications for subsurface thermodynamics. *Journal of climate* **20**(1), 21–37. DOI: https://doi.org/10.1175/JCLI3982.1.

Tewari, M., Chen, F, Wang, W, Dudhia, J, LeMone, M., Mitchell, K, Ek, M, Gayno, G, Wegiel, J, and Cuenca, R. (2004). *Implementation and verification of the unified NOAH land surface model in the WRF model*. 20th conference on weather analysis and forecasting/16th conference on numerical weather prediction, pp. 11-15.

Vertenstein, M., Craig, T., Middleton, A., Feddema, D., and Fischer, C. (2012). CESM1. 0.4 user's guide. *UCAR Doc.*

Vogel, M. M., Orth, R., Cheruy, F., Hagemann, S., Lorenz, R., Hurk, B. J.J. M., and Seneviratne, S. I. (2017). Regional amplification of projected changes in extreme temperatures strongly controlled by soil moisture-temperature feedbacks. *Geophysical Research Letters* **44**(3), 1511–1519. DOI: 10.1002/2016GL071235.

Wang, J. and Kotamarthi, V. R. (2015). High-resolution dynamically downscaled projections of precipitation in the mid and late 21st century over North America. *Earth's Future* **3**(7), 268–288. DOI: 10.1002/2015EF000304.

Yang, Z.-L., Niu, G.-Y., Mitchell, K. E., Chen, F., Ek, M. B., Barlage, M., Longuevergne, L., Manning, K., Niyogi, D., Tewari, M., and Xia, Y. (2011). The community Noah land surface model with multiparameterization options (Noah-MP): 2. Evaluation over global river basins. *Journal of Geophysical Research: Atmospheres* **116**(D12).

Zscheischler, J., Orth, R., and Seneviratne, S. I. (2015). A submonthly database for detecting changes in vegetation-atmosphere coupling. *Geophysical Research Letters* **42**(22). 2015GL066563, 9816–9824. DOI: 10.1002/2015GL066563.

Zscheischler, J., Westra, S., Hurk, B. J.J. M. van den, Seneviratne, S. I., Ward, P. J., Pitman, A., AghaKouchak, A., Bresch, D. N., Leonard, M., Wahl, T., and Zhang, X. (2018). Future climate risk from compound events. *Nature Climate Change* **8**(6), 469–477. DOI: 10.1038/s41558-018-0156-3.

Chapter 4

Effect of horizontal resolution on near-surface climate in the WRF v3.9 model over North America

This chapter is based on the contents of the manuscript in preparation:

García-García, A. et al. (2020a). Effect of horizontal resolution on near-surface climate in the WRF v3.9 model over North America. *In preparation*

Abstract

Understanding the origin of differences between climate models in the simulation of near-surface conditions is crucial for restricting the inter-model spread in future climate projections without losing important information. Here, we explore the effect of changing horizontal resolution on the simulation of the energy balance at the land surface and the climatology of near-surface conditions using the Weather Research and Forecasting (WRF) model. We performed an ensemble of twelve simulations using three different horizontal resolutions (25 km, 50 km and 100 km) and three different Land Surface Model (LSM) components over North America from 1980 to 2013. Our results show that increasing horizontal resolution alters the representation of shortwave radiation, affecting near-surface temperatures and consequently the partition of energy into sensible and latent heat fluxes. Thus, finer resolutions lead to higher net shortwave radiation and temperature climatologies at high latitudes and to lower net shortwave radiation and temperature climatologies at low latitudes. The use of finer resolutions also leads to an intensification of the terms associated with the surface water balance over coastal areas at low latitudes, generating higher climatologies of latent heat flux, accumulated precipitation and soil moisture. The effect of the LSM choice is larger than the effect of horizontal resolution on the representation of the surface energy balance, and consequently on near-surface temperature climatologies. By contrast, the effect of the LSM choice on the simulation of precipitation climatology is weaker than the effect of horizontal resolution, showing larger differences among LSM simulations in summer and over regions with high latent heat flux. Comparison between the Climatic Research Unit (CRU) observational data and the simulated climatology of daily maximum and minimum temperatures and accumulated precipitation indicates that enhancing horizontal resolution slightly improves the simulated

climatology of minimum and maximum temperatures in summer, while it leads to larger biases in accumulated precipitation. The larger biases in precipitation with the use of finer horizontal resolutions are likely controlled by the effect of increasing resolution on the atmospheric model component, since precipitation biases are similar using different LSM components.

4.1 Introduction

The majority of studies on climate change impacts on ecosystems, economies and communities are based on climate projections performed by Regional Climate Models (RCMs) and/or Earth System Models (ESMs) (Arneth, 2019; IPCC, 2013). Climate models are complex mathematical tools that lead to a range of possible future conditions despite simulating climate dynamics similarly and using the same future scenarios. Exploring inter-model differences in representing present climate conditions is necessary to understand the spread in future climate projections, and ultimately to reduce the uncertainty in climate projections.

The representation of land-atmosphere interactions within climate models has received considerable attention from the scientific community over the last decade due to its influence on surface conditions (e.g. Lorenz et al., 2016; Vogel et al., 2017). Energy and water exchanges between the lower atmosphere and the ground surface have proven to alter surface conditions, particularly during weather extreme events in summer (Hauser et al., 2016; Hirschi et al., 2011; Miralles et al., 2012; Seneviratne et al., 2006). Due to the influence of land-atmosphere interactions on surface conditions, several metrics defined in terms of surface energy fluxes and near-surface conditions have been employed for evaluating climate model simulations (Dirmeyer et al., 2013; García-García et al., 2019; Koven et al., 2013; Sippel et al., 2017). The representation

of land-atmosphere interactions in a climate model depends on the lower atmospheric and soil conditions as simulated by the atmospheric and soil model components respectively, and on the degree of coupling between both components implemented in the climate model (Koster et al., 2006). The simulation of energy fluxes at the surface is computed by the LSM component considering air and soil surface conditions (e.g. Oleson et al., 2010). Consequently, it is reasonable to expect an important role of the LSM component in the representation of land-atmosphere interactions (Gevaert et al., 2018). Each LSM component represents soil processes differently, generating a range of values for surface properties that yields a range of energy and water fluxes at the surface. For example, each LSM representation of surface albedo, evaporative resistance and aerodynamic roughness alters the simulation of the energy balance at the land surface and consequently affects the evolution of surface conditions (Laguë et al., 2019).

Previous studies focused on model evaluations have shown a dependence of the represented land-atmosphere interactions on the LSM component employed in both i) global climate model simulations from the Coupled Model Intercomparison Project, Phase 5 (García-García et al., 2019), and ii) regional climate model simulations performed with the WRF model (García-García et al., 2020b; Pei et al., 2014). Other studies have explored the LSM influence on the simulation of land-atmosphere interactions evaluating the surface energy fluxes over areas located in the US (Chen et al., 2014; Van Den Broeke et al., 2018), in Italy (Zhuo et al., 2019), in the Tibetan Plateau (Liu et al., 2019) and over areas of continental Europe (Davin et al., 2012; Mooney et al., 2013). Studies using the WRF model with different LSM components confirmed the dominant influence of the LSM component on the simulation of temperature and precipitation extreme events, due to the LSM influence on the representation of land-atmosphere interactions (García-García et al., 2020b; Pei et al., 2014). García-García

et al., 2020b also showed that the spread induced by different LSMs is similar or even larger than the inter-model spread using three RCM simulations from the North American component of the Coordinated Regional climate Downscaling Experiment (CORDEX) project (Giorgi et al., 2015).

Horizontal resolution used in General Circulation Models (GCMs) varies from approximately 250 to 100 km depending on the available computational resources (e.g. 5^{th} phase of the Coupled Model Intercomparison Project (CMIP5) models, Taylor et al., 2012), while RCMs allow the use of much finer resolutions, ranging from $\sim$ 50 to 4 km. The range of horizontal resolutions employed in RCMs for climate studies is usually limited to approximately 25-50 km (e.g. CORDEX models, Giorgi et al., 2015), because of the duration of the simulation and the required computational resources. This reduced range of resolutions limits the RCM ability to reproduce observations of precipitation at daily time scales, which can be greatly improved by using resolutions of $\sim$ 4 km and convection resolving RCMs (Sun et al., 2016). In the last decades, more and more studies focus on the evaluation of regional climate simulations performed including the explicit solution of convection processes in RCMs. These studies have shown some improvements in the simulation of precipitation at local and regional scales with possible implications for the simulation climate dynamics (Ban et al., 2014; Gómez-Navarro et al., 2015; Messmer et al., 2017). Still, the contrast between resolutions employed in RCMs and GCMs is expected to enhance the representation of land-atmosphere interactions in RCMs through a more adequate discretization of equations, as well as through an improved representation of small-scale processes and topographical features (Rummukainen, 2016; Xue et al., 2014). Small scale weather phenomena such as sea breezes, snowstorms induced by the presence of lakes, local winds, tropical cyclones, and mesoscale convective systems can be better represented in RCM simulations than in GCM simulations (Wehner et

al., 2010). Some studies have also suggested a resolution-induced improvement in the representation of interactions between small and large scale dynamical processes, ultimately leading to better large-scale atmospheric flow (Lucas-Picher et al., 2017). The enhanced representation of land-atmosphere interactions associated with finer resolutions is also expected to induce an improvement in the simulation of near-surface conditions, especially in the simulation of extreme events (Di Luca et al., 2015; Prein et al., 2013; Rummukainen, 2016). For example, the resolution impact on precipitation has been examined with an atmospheric general circulation model (Demory et al., 2014).

Although the literature on the impact of the LSM choice and changes in resolution on model simulations is extensive, most literature to date has focused on small domains and meteorological events, providing little information at climatological scales. Here, we evaluate and compare the influence of both factors, the LSM choice and horizontal resolution, on the representation of land-atmosphere interactions and consequently on the simulation of near-surface conditions over North America for the period 1980-2013. We explore three questions: i) how does the use of fine horizontal resolution in WRF affect the simulation of land-atmosphere interactions and near-surface conditions over North America? ii) what causes the differences between LSM components in representing land-atmosphere interactions and climatologies of near-surface conditions? finally, iii) how do the LSM choice and horizontal resolution affect the WRF ability to reproduce observations of North America climatology?

An ensemble of twelve simulations was generated to explore those points. These simulations were performed with the WRF model using different LSM components and resolutions over a pan-continental domain similar to that used by the North American component of the CORDEX project. The descriptions of the WRF experiments and the methodology applied for the analysis are included in Section 4.2 and 4.3,

respectively. Section 4.4 presents the results of the analysis, which are discussed in Section 4.5. The conclusions and importance of this work are summarized in Section 4.6.

4.2 Description of the modelling experiment

We performed three sets of regional simulations over North America from 1979 to 2013 using the version 3.9 of the Advanced Research WRF model (Michalakes et al., 2001) with initial and boundary conditions from the North American Regional Reanalysis (NARR) product (Mesinger et al., 2006). The NARR product was generated by the NCEP Eta atmospheric model, the NOAH LSM component and the Regional Data Assimilation System (RDAS) (Mesinger et al., 2006). The NARR data is available at the National Center for Environmental Information (NOAA) archive (`https://nomads.ncdc.noaa.gov/data/narr/`, accessed in August, 2017) and provides data over a 32 km grid with a three-hourly temporal resolution. The first year of all simulations performed in this study was used as spin up to minimize the effect of initial conditions on our simulations. No nudging techniques were applied to ensure the free evolution of the WRF model.

The three sets of simulations were performed using a lambert conformal projection with resolution of 25 km $\times$ 25 km, 50 km $\times$ 50 km, and 100 km $\times$ 100 km. Each set includes four simulations using three different LSM components; the NOAH LSM (NOAH, Tewari et al., 2004), the NOAH LSM with multiparameterizations options (NOAH-MP, Niu et al., 2011), and the Community Land Model version 4 LSM (CLM4, Oleson et al., 2010). The fourth simulation included in each set was performed using the NOAH-MP LSM with dynamic vegetation (NOAH-MP-DV), while vegetation was prescribed for the other simulations. The rest of WRF options remained the

Table 4.1: Summary of the regional simulations performed in this analysis and their differences.

NAME	LSM	Resolution	Vegetation Mode	Simulation Time Step	Radiation Time Step
NOAH 25 km	NOAH	25 km	Prescribed	2.5 min	6 min
NOAH 50 km		50 km	Prescribed	5.0 min	20 min
NOAH 100 km		100 km	Prescribed	10 min	30 min
NOAH-MP 25 km	NOAH-MP	25 km	Prescribed	2.5 min	6 min
NOAH-MP 50 km		50 km	Prescribed	5 min	20 min
NOAH-MP 100 km		100 km	Prescribed	10 min	30 min
NOAH-MP-DV 25 km	NOAH-MP	25 km	Dynamic	2.5 min	6 min
NOAH-MP-DV 50 km		50 km	Dynamic	5.0 min	20 min
NOAH-MP-DV 100 km		100 km	Dynamic	10 min	30 min
CLM4 25 km	CLM4	25 km	Prescribed	2.5 min	6 min
CLM4 50 km		50 km	Prescribed	5.0 min	20 min
CLM4 100 km		100 km	Prescribed	10 min	20 min

same for all simulations, employing land categories from the Moderate Resolution Imaging Spectroradiometer (MODIS, Barlage et al., 2005), the WRF Single Moment (WSM) 6-class graupel scheme for the microphysics (Hong et al., 2006b), the Grell-Freitas ensemble scheme (Grell et al., 2014), the Yonsei University scheme for the description of the planetary boundary layer (YSU, Hong et al., 2006a), the revised MM5 monin-Obukhov scheme (Jiménez et al., 2012), and the Community Atmosphere Model (CAM) scheme (Collins et al., 2004) for simulating atmospheric processes. The use of different horizontal resolutions requires the use of different time steps for performing our WRF simulations, as well as different time intervals for computing radiation physics (radt option in WRF namelist). Table 4.1 summarizes the differences between all simulations employed in this analysis. Note that the CLM4 100 km simulation employed a time step of 20 min for the radiation physics resolution in contrast to the other LSM simulations with the same horizontal resolution. This is due to model instability when using longer time steps in the CLM4 experiment. The use of different time intervals for the computation of radiation physics in the CLM4 simulation seems not to affect our results, because all LSM simulations show a similar response to increasing resolution.

4.3 Methodology

We evaluate the impact of changing horizontal resolution on the climatology of surface energy fluxes and near-surface conditions as simulated by the WRF model using different LSM components. For this purpose, we estimate the climatologies of surface energy fluxes as the temporal average of the analysis period (1980-2013) using the following energy components: Net Shortwave radiation (SNET - W/m^2), Net Longwave radiation (LNET - W/m^2), Net Radiation (RNET - W/m^2) absorbed by the soil, Latent Heat flux (LH - W/m^2), Sensible Heat flux (HFX - W/m^2) and Ground Heat Flux (GHF - W/m^2). The climatologies of near-surface conditions are estimated using outputs of: Surface Air Temperature (SAT - °C), daily maximum SAT (TASMAX - °C), daily minimum SAT (TASMIN - °C), Ground Surface Temperature at 1m depth (GST 1 m - °C), accumulated precipitation (PRE - mm/day) at the surface and Soil Moisture (SM) contained in the first soil meter (SM 1m - m^3/m^3). All climatology values are computed using the annual and seasonal (boreal winter, December, January and February (DJF); spring, March, April and May (MAM); summer, June, July and August (JJA); and fall, September, October and November (SON)) averages over the 34-year period (1980-2013) after discarding the first year of the simulation (1979) as spin up. Outputs of all WRF experiments were interpolated to a common grid with the coarsest resolution of our WRF simulations (100 km) to allow the comparison between simulations (e.g. Volosciuk et al., 2015). We also interpolate outputs from all simulations to a common grid with the finest resolution (25 km) to investigate the role of the interpolation step in our analysis. The interpolation approach is based on a bilinear algorithm included among the Climate Data Operators tools (CDO, Schulzweida et al., 2006). After the interpolation, we make sure that the same number of grid-cells are considered for all simulations to

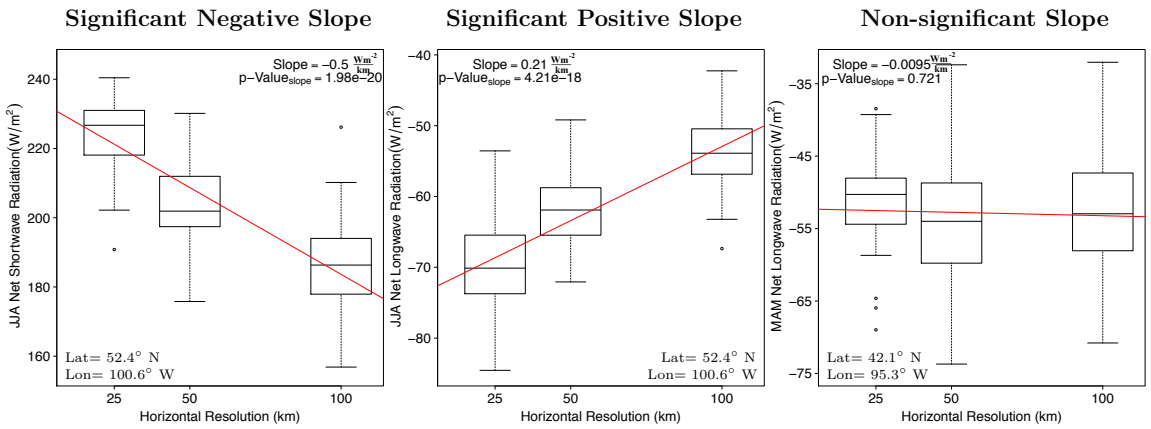

Figure 4.1: Example of the linear regression analysis performed for evaluating the impact of horizontal resolution on near-surface variables. This example represents the boxplots (75th and 25th spatial percentiles (boxes), medians (center lines), maximums and minimums (extremes of dashed lines), and outliers (points located 1.5 times the interquartile range above the upper quartile and bellow the lower quartile) for near-surface variables at one grid cell. Outputs from the 25, 50 and 100 km NOAH-MP-DV simulations were interpolated to a common 100 km grid for the analysis. The variables and grid cells indicated in the figures were selected in order to represent an example of each possible result.

avoid different results arising from coastal and lake areas.

We perform a linear regression analysis for each LSM set of simulations between the values of each variable and the employed horizontal resolution at each grid cell in order to assess the relationship between spatial discretization and simulated climatologies. The linear fit for each variable and each LSM simulation contains 34 points, one annual or seasonal value per year, for each resolution experiment (see Figure 4.1 as example). We represent the slope of the regression analysis (W/m^2 per 10 km) only at grid cells presenting significant values at the 95% confidence level after applying a t-test to the slope of the linear regression analysis.

Mean annual and seasonal climatologies of three near-surface variables (maximum and minimum air temperature and accumulated precipitation) are evaluated comparing with two observational data products, the CRU Time-Series product version 4.03 (Harris et al., 2020) and the Daily Surface Weather Data (DAYMET) version 3 (Thornton et al., 2016). The CRU product provides data of maximum and minimum

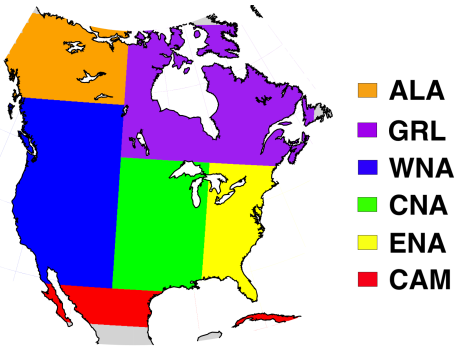

Figure 4.2: Subregions employed for the bias analysis. These regions were adapted from Giorgi et al., 2000: Central America, CAM; Western North America, WNA; Central North America, CNA; Eastern North America, ENA; Alaska, ALA; and Greenland, GRL.

air temperature and accumulated precipitation at monthly time scale over gridded fields with a resolution of 50 km. These data are based on the interpolation of monthly observational data calculated from daily or sub-daily observations obtained from National Meteorological Services and other external agents (Harris et al., 2020). The DAYMET product provides data for the same variables at daily time scale and over 1 km gridded fields. This data product is also based on the spatial interpolation of ground observations of daily maximum and minimum temperature and precipitation obtained from the NOAA National Centers and other agencies (Thornton et al., 2016). We calculate the bias in the climatology of each variable as represented by each simulation and the DAYMET product relative to the climatology of the CRU data. The estimate of the bias in the DAYMET product relative to the CRU data allows the evaluation of inconsistencies between both observational products, which is particularly important for the analysis of model simulations with different resolutions (e.g. Iles et al., 2019). The bias metric requires a grid-cell by grid-cell comparison between the WRF experiments, the DAYMET product and the CRU data; consequently, an interpolation of the experiments and data products to a common grid is required. Prior to any calculations, we interpolate all WRF experiments and observational databases to a common grid with the coarsest resolution (100 km). As done for the analysis

of the resolution impact, we also interpolate all variables to a common grid with the finest resolution (25 km) to assess the role of the interpolation step in our results. Additionally, we calculate the bias in the simulated climatologies averaging over six subregions in North America (NA) adapted from Giorgi et al., 2000: Central America, CAM; Western North America, WNA; Central North America, CNA; Eastern North America, ENA; Alaska, ALA; and Greenland, GRL (Figure 4.2).

4.4 Results

4.4.1 LSM differences in the climatologies of surface energy fluxes and near-surface conditions

The net radiation absorbed by the ground surface may enhance turbulent fluxes at the surface (latent and sensible heat fluxes) and/or warm the soil surface, which leads to an increase in the emitted longwave radiation (Bonan, 2002). The relationship between these variables is shown by the ensemble mean of LSM simulations, indicating similar latitudinal patterns in the climatologies of net radiation, turbulent fluxes and near-surface temperatures with higher fluxes and temperatures at lower latitudes (see Figure 4.3 as example for the LSMensemble mean of the 50 km experiments). Net radiation absorbed by soil results from adding net shortwave radiation and net longwave radiation, whose climatologies have similar spatial distributions but with opposite sign (Figure 4.3). Net shortwave radiation climatology is positive, which means that more shortwave radiation reaches the land surface than is reflected due to surface albedo. While net longwave radiation climatology is negative (Figure 4.3), meaning that the energy emitted from the soil due to surface temperature is higher than the longwave radiation reaching the soil surface. The energy proportion of net

radiation that is propagated through the soil is much smaller than the rest of surface energy fluxes (GHF in Figure 4.3). Areas with high latent heat flux climatology coincide with areas with high precipitation climatology, while soil moisture climatology is similar to the precipitation climatology at low latitudes except over the eastern US coast (Figure 4.3). The similarities and differences between precipitation and soil moisture climatologies illustrate the complex relationship between these two variables, which depends on the energy and water availability (Dirmeyer et al., 2009).

The relationship of surface energy fluxes with temperature and water availability at the surface is well established in the literature (e.g. Bonan, 2002), as well as the impact of land cover and soil properties on the simulation of the surface energy and water balance (e.g. Laguë et al., 2019). The use of a different LSM component in WRF affects the representation of soil properties and land cover in the simulation reaching different surface energy fluxes (Figure 4.4). In agreement with the literature (Bonan, 2002; Laguë et al., 2019), LSM differences in the WRF simulation of shortwave and longwave net radiation are related to LSM differences in temperature climatologies (Figures 4.4 and 4.5), while LSM differences in the energy partition into latent and sensible heat fluxes seems to be related to LSM differences in precipitation and soil moisture climatologies (Figures 4.4 and 4.6). That is, LSM differences in the climatology of shortwave radiation are similar to LSM differences in temperature climatologies, as well as LSM differences in latent heat flux climatology are similar to LSM differences in precipitation climatologies (Figures 4.4, 4.5 and 4.6). These results are consistent with the findings of García-García et al. (2020b) that also reported a LSM-dependency in the WRF simulation of land-atmosphere interactions, using a different metric.

LSM differences in the simulation of near-surface climatologies are consistent among the three sets of simulations with different resolutions (Figures 4.4, 4.5, 4.6,

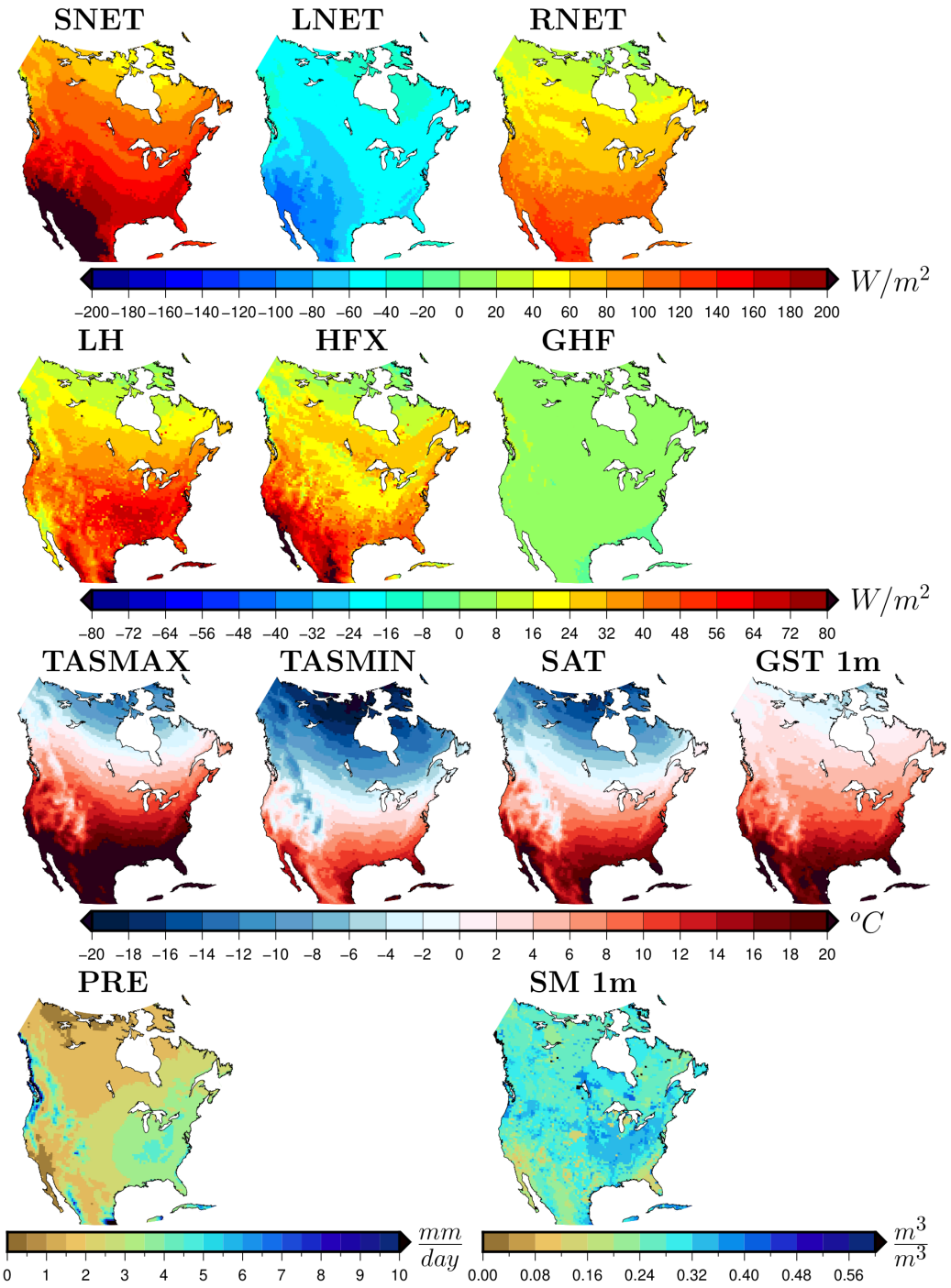

Figure 4.3: Climatology of surface energy balance terms and conditions (net shortwave radiation SNET; net longwave radiation LNET; soil net radiation RNET; latent heat flux LH; sensible heat flux HFX; ground heat flux GHF; maximum temperature TASMAX; minimum temperature TASMIN; surface air temperature SAT; soil temperature at 1m depth GST 1m; accumulated precipitation PRE; and soil moisture contained in the first soil meter SM 1m) for the WRF ensemble mean. Climatologies are estimated as the temporal average for the period 1980-2013 using simulations performed with 50 km resolution.

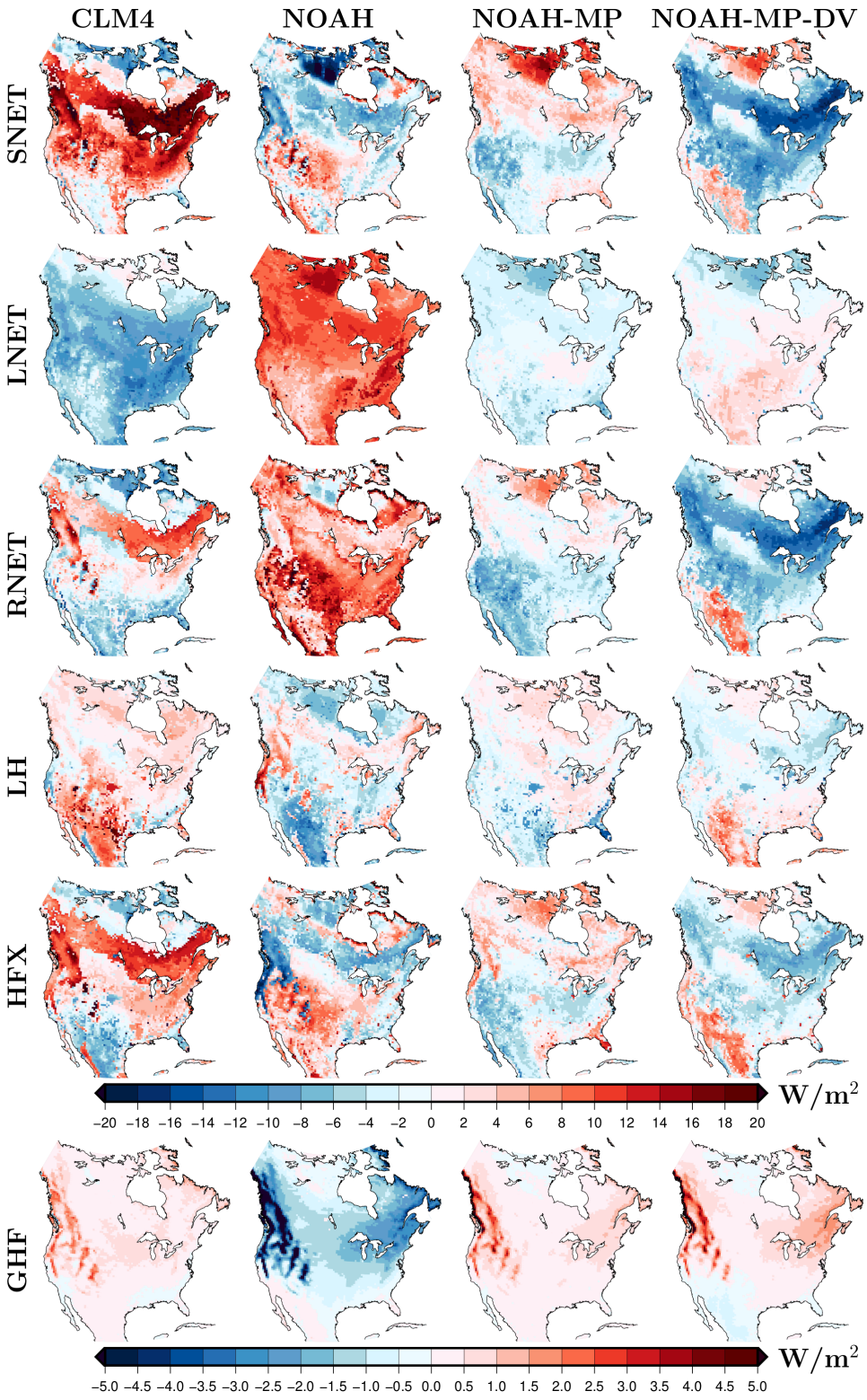

Figure 4.4: Climatology of energy fluxes at the surface (net shortwave radiation SNET; net longwave radiation LNET; soil net radiation RNET; latent heat flux LH; sensible heat flux HFX; and ground heat flux GHF) for each LSM simulation relative to the multi-model mean. Climatologies are estimated as the temporal average for the period 1980-2013 using simulations performed with 50 km resolution.

C.1, C.2 and C.3). For example, based on the differences between each LSM simulation with 50 km resolution and the 50 km ensemble mean (Figure 4.3), we can identify the CLM4 as the LSM component simulating the highest net shortwave radiation over most of North America. Meanwhile, the NOAH-MP-DV simulation reaches the lowest net shortwave radiation over the same areas (Figure 4.4). At high latitudes and over the southwestern NA coast, however, the NOAH-MP-DV simulation yields the highest net shortwave radiation and the CLM4 component simulates one of the lowest radiation values (Figure 4.4). The WRF simulation of net longwave radiation reaches negative climatologies (Figure 4.3) with the maximum values simulated by the NOAH LSM and the minimum values simulated by the CLM4 LSM (Figure 4.4). The upward (negative) component of the net longwave radiation is based on surface temperatures, following the Stefan-Boltzmann equation ($L\uparrow \propto \sigma T_s^4$, where T_s is surface temperature and σ is the Stefan-Boltzmann constant). Thus, the CLM4 simulation generates the lowest values of net longwave radiation, that correspond with the highest values of upward longwave radiation (Figure C.4), and therefore with the highest temperature climatology at the surface (Figures 4.4 and 4.5). The opposite behaviour is observed in the NOAH LSM, yielding the highest net longwave radiation absorbed by soil, the lowest upward longwave radiation (Figure C.4), and one of the coldest temperature climatologies relative to the ensemble mean (Figures 4.4 and 4.5). The relationship between the simulation of net longwave radiation and minimum temperatures is strong, while maximum temperatures are more influenced by net shortwave radiation, particularly over the boreal forest (Figures 4.4 and 4.5). Over the boreal forest, the CLM4 LSM generates the highest net shortwave radiation and the warmest maximum temperatures, while the NOAH and NOAH-MP-DV simulations reach the lowest net shortwave radiation values and the coldest maximum temperatures (Figures 4.4 and 4.5). The total radiation absorbed by soil yields the highest values in

the NOAH simulation and the lowest values in the NOAH-MP-DV simulation at most locations, except at very high latitudes and over the southwestern NA coast (Figure 4.4).

The CLM4 simulation reaches the highest latent heat flux climatology, particularly over southwestern NA, followed by the NOAH-MP-DV simulation, while the NOAH and NOAH-MP simulations provide the lowest latent heat flux climatology over southwestern NA (Figures 4.4). Over southwestern NA, the CLM4 simulation also generates the highest values of accumulated precipitation, while the NOAH simulation displays the lowest precipitation values (Figure 4.6), indicating the relationship between climatologies of latent heat flux and precipitation over water limited areas in agreement with the literature (e.g. Mueller et al., 2014). At mid- and high latitudes, the CLM4 LSM reaches one of the highest climatologies of latent heat flux among LSM simulations and the driest soil moisture climatology (Figures 4.4 and 4.6). The NOAH-MP-DV simulation shows higher latent heat flux climatology than the NOAH-MP simulation at low latitudes, also yielding higher values of accumulated precipitation and lower values of soil moisture than the NOAH-MP simulation (Figures 4.4 and 4.6). The simulated climatology of sensible heat flux reaches the highest values using the CLM4 LSM over the boreal forest, while the NOAH and NOAH-MP-DV simulations reach the lowest sensible heat flux climatologies in agreement with results for the net shortwave radiation and daily maximum temperatures (Figures 4.4 and 4.5). LSM differences in the ground heat flux climatology are smaller than for the rest of the energy fluxes due to the small magnitude of the GHF climatology in comparison with the rest of energy components (Figure 4.3). The NOAH LSM reaches the lowest ground heat flux climatology and the coldest soil temperatures over most of the domain except over the southwestern NA coast, where the NOAH-MP-DV simulation yields the lowest ground heat flux and the coldest climatology of

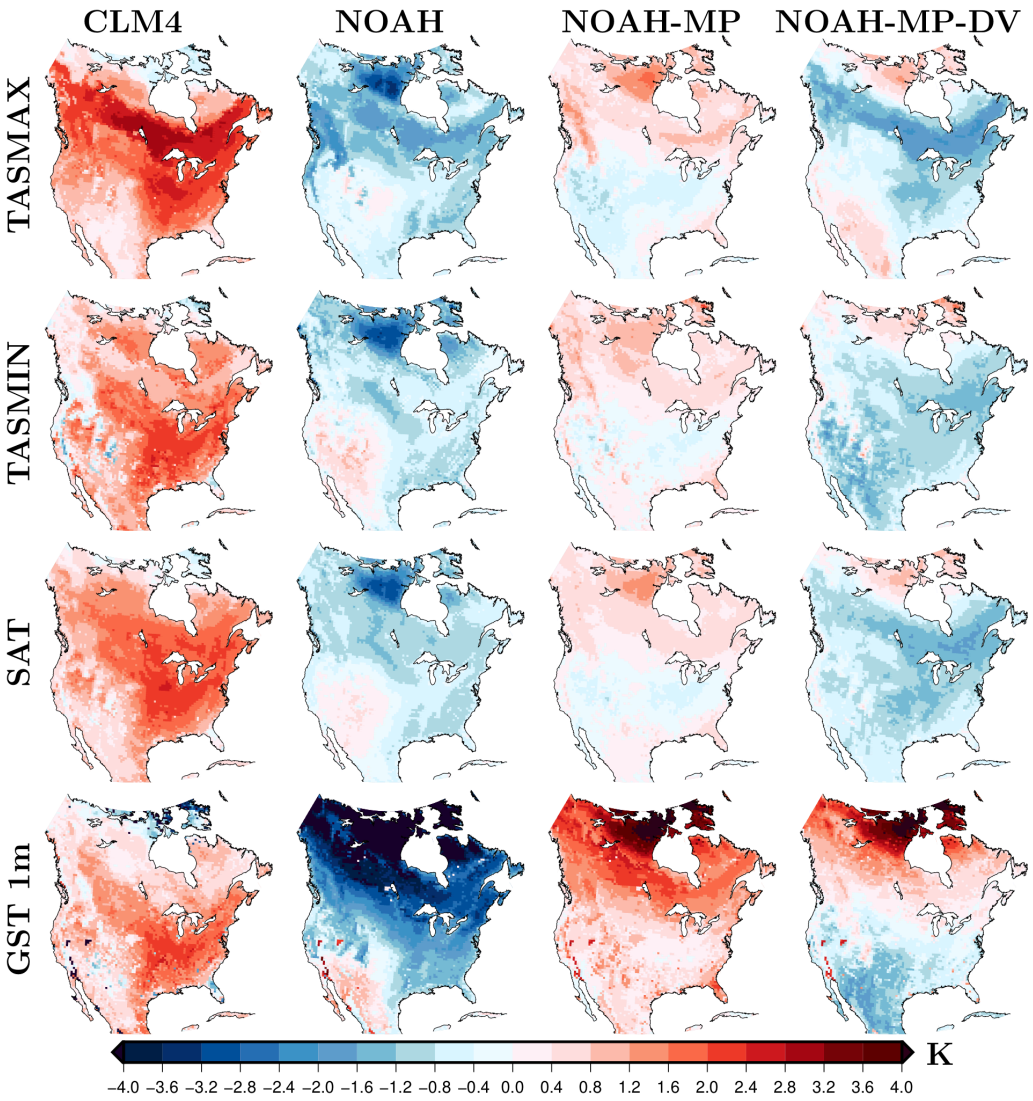

Figure 4.5: Climatology of near-surface temperature conditions (daily maximum temperature TASMAX; daily minimum temperature TASMIN; surface air temperature SAT; and soil temperature at 1m depth GST 1m) for each LSM simulation relative to the multi-model mean. Climatologies are estimated as the temporal average for the period 1980-2013 using simulations performed with 50 km resolution.

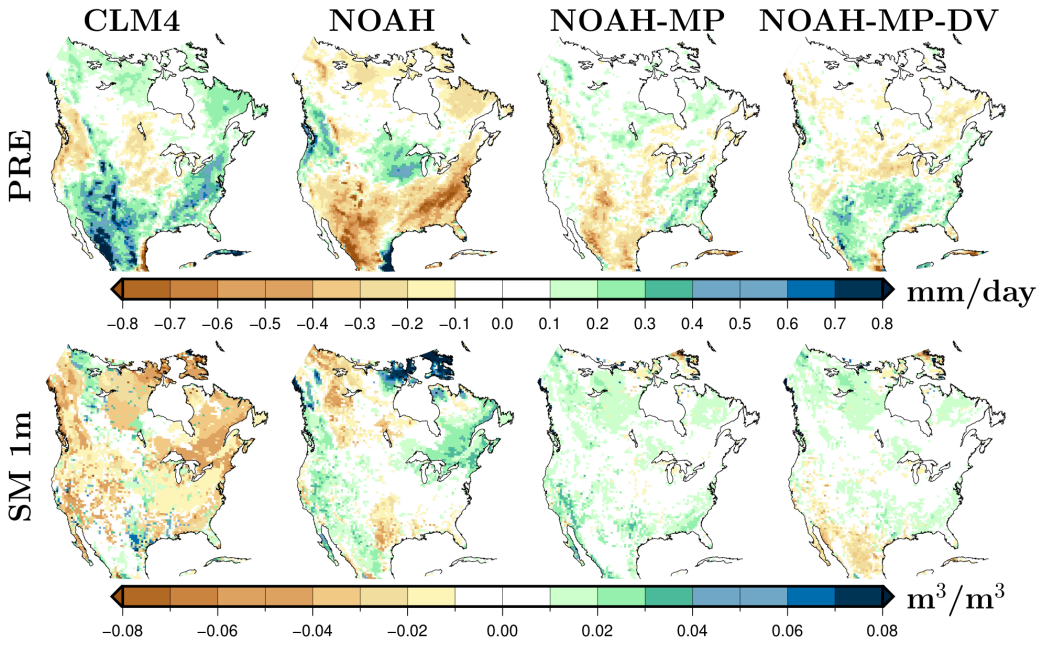

Figure 4.6: Climatology of variables involved in the surface water balance (accumulated precipitation PRE; and soil moisture contained in the first soil meter SM 1m) for each LSM simulation relative to the multi-model mean. Climatologies are estimated as the temporal average for the period 1980-2013 using simulations performed with 50 km resolution.

soil temperatures. LSM differences are larger for the simulation of soil temperatures than for the simulation of air temperatures especially at high latitudes where LSM differs largely in the simulation of shortwave net radiation climatology, probably due to different estimates of surface albedo (Figures 4.3 and 4.5).

4.4.2 Resolution impact on the climatologies of surface energy fluxes and near-surface conditions

The analysis of the resolution influence on the simulation of energy fluxes and near-surface conditions requires the interpolation of all simulations (25 km, 50 km and 100 km) to a common grid in order to be compared. Results from model outputs interpolated to the 25 and 100 km grids yield small differences, showing slightly larger areas with significant response of the energy fluxes and near-surface conditions to the

reduction in resolution interpolating into a 25 km grid than into a 100 km grid, especially for soil moisture outputs (Figures 4.8, 4.7 and 4.9, C.8, C.9 and C.10). However conclusions drawn from outputs mapped onto a 25 or 100 km grid are similar. This suggests that the changes in surface energy fluxes and near-surface conditions arising from increasing horizontal resolutions result from the ability of the WRF model to represent physical properties and processes rather than from the grid cell averaging (i.e. not an artifact of the mapping). Additionally, the effect of horizontal resolution on the WRF simulation of annual surface climatologies is similar for all LSM components, displaying a large seasonality (Figures 4.8, 4.7, 4.9, C.5, C.6 and C.7). This section includes results derived from the NOAH-MP-DV outputs interpolated to the common 100 km grid, since the resolution impact on simulations with different LSM components is similar and in order to reduce the number of figures included in the manuscript.

The response of surface energy fluxes to horizontal resolution varies considerably with the season (Figure 4.7). In DJF, changing resolution alters the climatology of surface energy fluxes mainly over regions of complex topography and coastal areas, while in JJA the simulation of energy fluxes is affected by resolution over the whole domain except over a region in the central US and northern areas of Hudson Bay (Figure 4.7). Overall, the use of coarser horizontal resolutions induces a decrease in the net radiation absorbed by soil over high latitudes, mainly caused by a decrease in net shortwave radiation (Figure 4.7). The decrease in net radiation induced by coarser resolutions limits the energy available for turbulent energy fluxes at high latitudes. Thus, climatologies of latent and sensible heat fluxes also decrease with the use of coarser resolutions at high latitudes. At low latitudes, however, coarser resolutions lead to higher shortwave radiation values that is mostly dissipated by larger negative values of longwave radiation (Figure 4.7). The use of coarser resolutions also induces

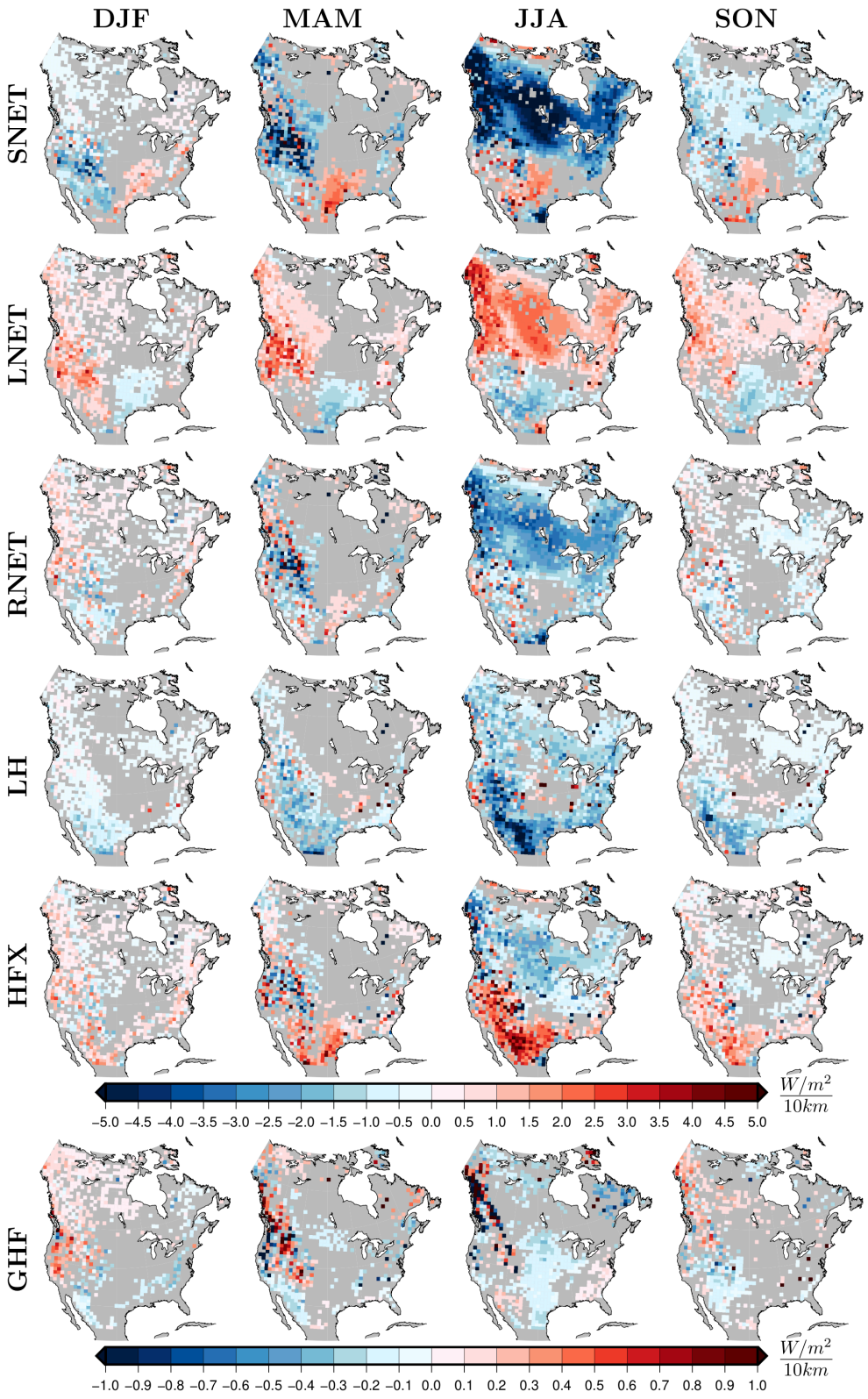

Figure 4.7: Seasonal mean change in surface energy fluxes for a reduction of 10 km in horizontal resolution, using the NOAH-MP-DV simulations for the period 1980-2013. Only grid cells where the response to changing resolution is significant at the 95% level are plotted. All outputs from the 25, 50 and 100 km simulations were mapped to a common 100 km grid.

higher sensible heat flux at low latitudes, which is balanced by lower latent heat flux in all seasons (Figure 4.7).

The solar energy absorbed by soil during daytime (shortwave) is employed in warming the land surface until reaching daily maximum temperatures, while at night soil surface temperature decreases due to longwave radiative cooling and the absence of shortwave radiation (Wang et al., 2013). Thus, we expect a relationship between the resolution impact on the two radiative components and daily minimum and maximum temperature climatologies. Consistent with the literature (e.g. Wang et al., 2013) and the effect of LSM differences on near-surface conditions (Section 4.4.1), the spatial pattern of the resolution impact on net shortwave radiation is similar to the resolution-induced changes in daily maximum temperatures (Figure 4.8). The response of minimum temperature climatology to reducing resolution is, however, smaller than for maximum temperatures, contrary to the effect on shortwave and longwave radiation. Over eastern North America, JJA minimum temperature climatology increases with the use of coarser resolutions, while it decreases over western North America (Figure 4.8). The response of mean temperature climatology to resolution is mainly driven by the resolution impact on maximum temperatures, since both variables show similar spatial patterns (Figure 4.8). Air and soil temperatures are similarly affected by changing resolution in summer, yielding different responses to resolution in MAM and SON at high latitudes and in DJF over most locations (Figure 4.8). The resolution impact on soil temperature climatology is stronger than on air temperature climatology in JJA and SON, while soil temperature response to resolution is weaker than the air temperature response in DJF and MAM (Figure 4.8). This indicates that soil temperatures are more sensitive to JJA and SON changes in the energy budget induced by reducing resolution, while in DJF and MAM soil temperature climatology remains insulated from resolution-induced changes in surface conditions.

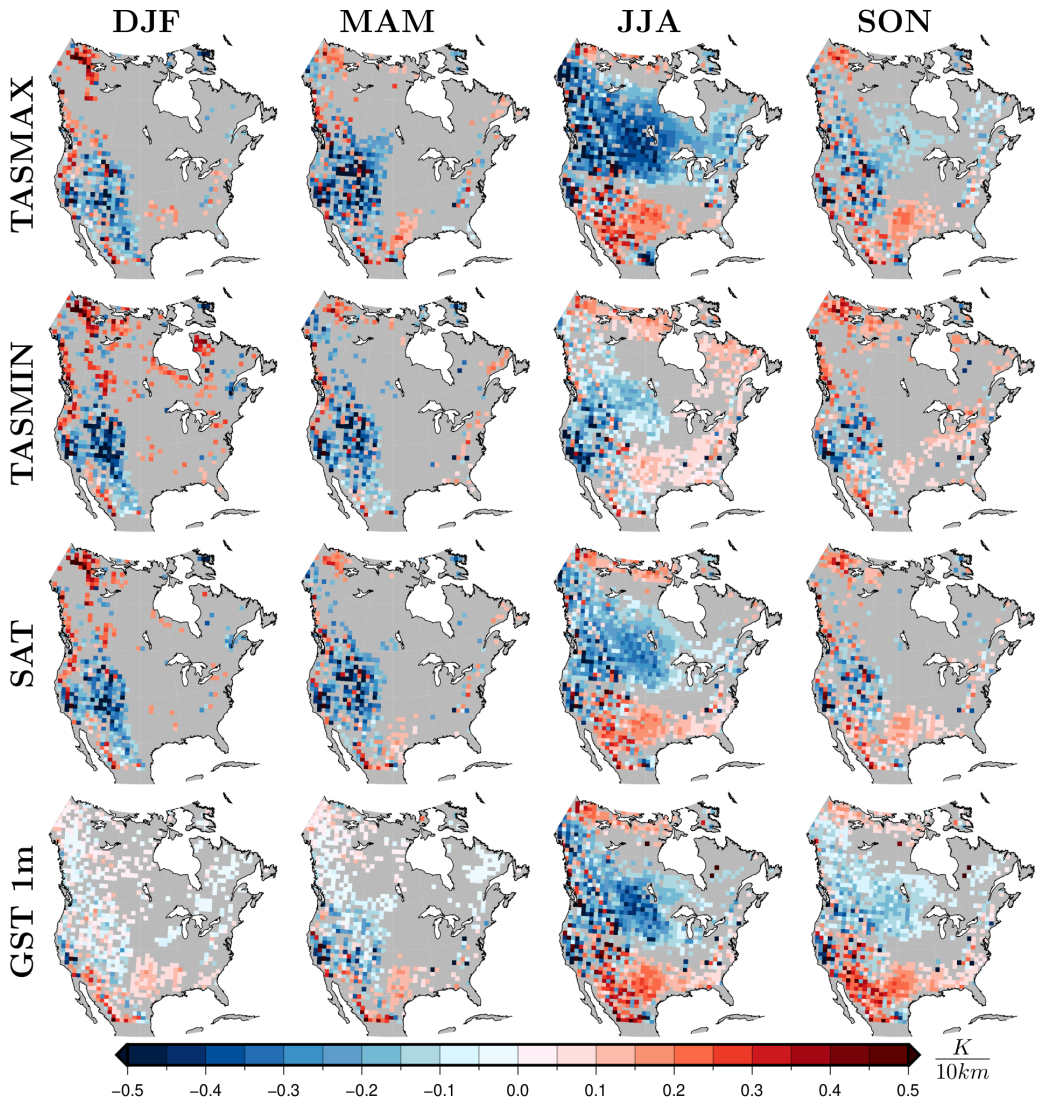

Figure 4.8: Seasonal mean change in near-surface temperature conditions for a reduction of 10 km in horizontal resolution, using the NOAH-MP-DV simulations for the period 1980-2013. Only grid cells where the response to changing resolution changing resolution is significant at the 95% level are plotted. All outputs from the 25, 50 and 100 km simulations were mapped to a common 100 km grid.

The response of precipitation to reducing horizontal resolution is similar to the response of latent heat flux climatology, particularly in summer (Figures 4.7 and 4.9). The use of coarser resolutions leads to a marked reduction in JJA precipitation and latent heat flux climatologies over southern NA coastal areas, generating smaller changes in these variables at higher latitudes (Figures 4.7 and 4.9). Soil moisture climatology also decreases with the use of coarser resolutions at low latitudes, particularly in summer (Figure 4.9). At mid-latitudes, however, the use of larger grid cells leads to an increase in soil moisture climatology during the year (Figure 4.9). Results on the response of soil moisture climatology to reducing horizontal resolution are more dependent on the LSM component than the rest of analyzed outputs, while the effect of including dynamic vegetation (NOAH-MP-DV) or prescribed vegetation (NOAAH-MP) in the simulation is small (Figure C.7). The NOAH simulation reaches the strongest response of soil moisture to changing resolution, in opposition to results of latent heat flux, for which the NOAH simulation generates the weakest response of LH to resolution in comparison with the other LSM simulations (Figures C.5 and C.7). The weakest soil moisture response to resolution is performed by the CLM4 LSM, differing from the rest of simulations particularly at mid- and high latitudes (Figure C.7).

At low latitudes, the climatologies of the three variables associated with the surface water balance (LH, PRE and SM 1m) decrease with the use of coarser horizontal resolutions (Figures 4.7 and 4.9). This is probably related to the resolution-induced increase in net shortwave radiation and temperature, and its effect on the surface energy partition into sensible and latent heat flux. Due to the relationship between surface temperatures and sensible heat flux (Bonan, 2002), the resolution-induced increase in temperature is probably related to the increase in sensible heat flux climatology, reducing the available energy for latent heat flux and leading to a decrease in latent heat

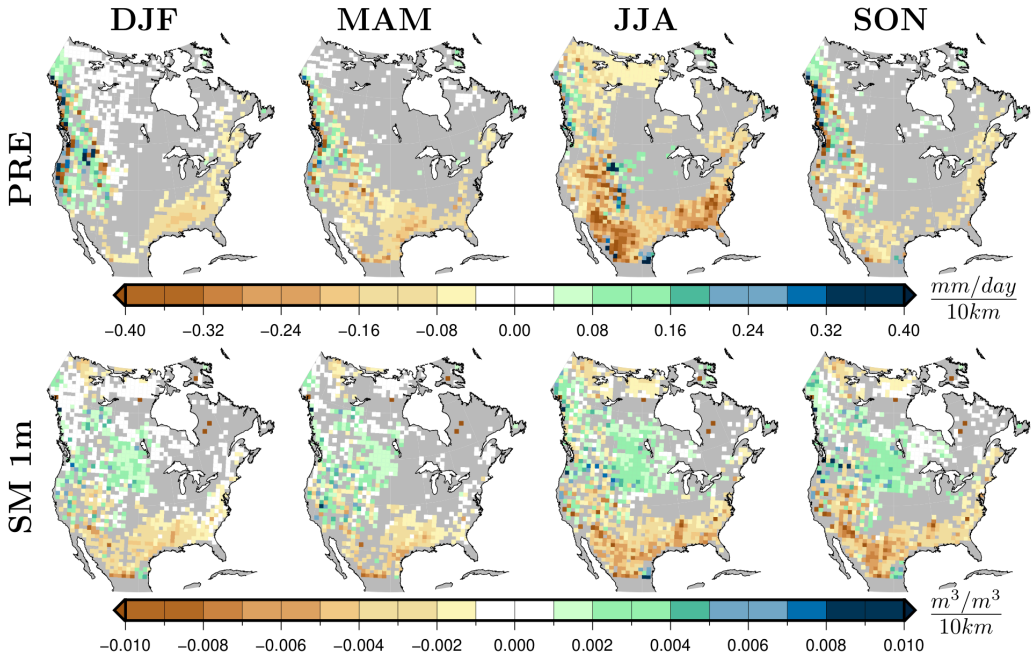

Figure 4.9: Seasonal mean change in accumulated precipitation and soil moisture for a reduction of 10 km in horizontal resolution, using the NOAH-MP-DV simulations for the period 1980-2013. Only grid cells where the response to changing resolution is significant at the 95% level are plotted. All outputs from the 25, 50 and 100 km simulations were mapped to a common 100 km grid.

flux climatology with the use of coarser resolutions at low latitudes (Figures 4.7, 4.8 and 4.9). At mid- and high latitudes, there are differences in the response of the water balance variables to the use of coarser resolutions. For example focusing on the JJA results, soil moisture climatology increases with coarser resolutions over a large area at mid-latitudes, while precipitation climatology increases just over a few grid cells, decreasing over most western areas (Figure 4.9). Latent heat flux decreases with the use of coarser resolutions over most regions at high and mid-latitudes, increasing just over a few grid cells at mid-latitudes (Figure 4.7). This decrease in latent heat flux climatology at mid- and high latitudes is driven by the resolution-induced decrease in net radiation absorbed by soil, which also leads to a decrease in sensible heat flux at these latitudes (Figure 4.7). The differences in the spatial patterns of the response of the water balance variables to reducing resolution seems to be interrelated. For example, the resolution-induced decrease in latent heat flux climatology over central NA can be caused by the increase in soil moisture (Figures 4.7 and 4.9).

4.4.3 Evaluation of temperature and precipitation climatologies against observations

For the comparison of the effect of changing the LSM component and horizontal resolution on climate simulations, we estimate the bias in all WRF simulations and the DAYMET product relative to the CRU observational product (Harris et al., 2014). The comparison of model outputs and observational databases requires the interpolation of all outputs to a common grid. The comparison between our WRF simulations, DAYMET product and the CRU data interpolating to a common grid with 25 or 100 km resolution yields similar results for minimum and maximum temperatures (Figures 4.10, 4.11, C.13 and C.14) and for the precipitation climatology (Figures 4.12 and C.16). As a measure of the possible uncertainties in the CRU product, we also

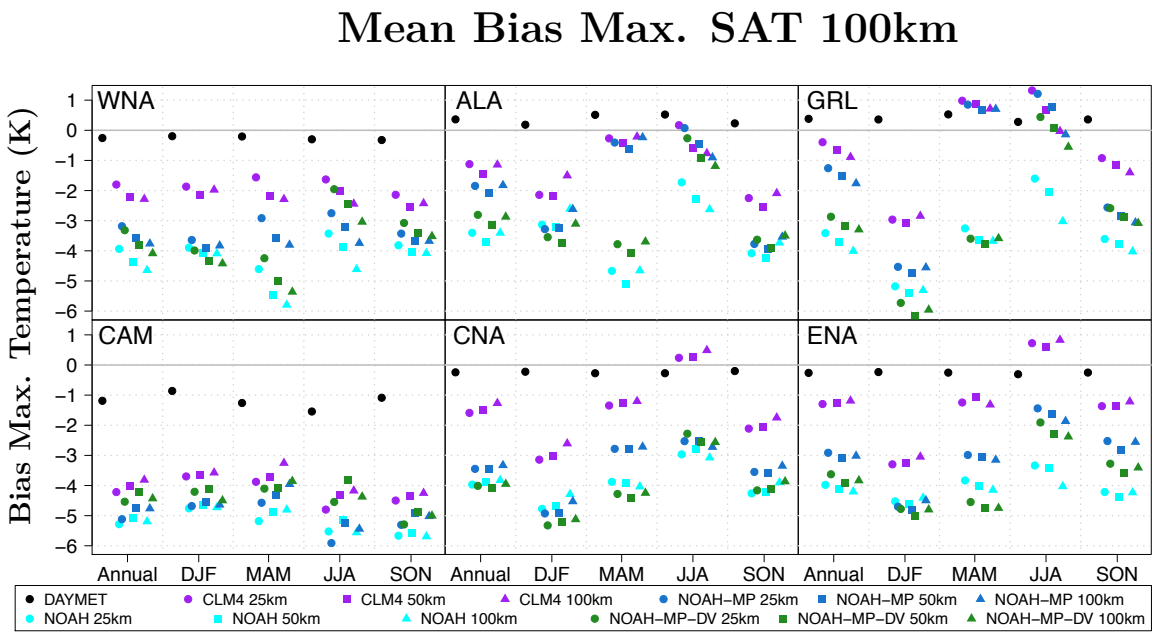

Figure 4.10: Mean annual and seasonal bias in maximum temperature climatology (^oC) for all experiments and the DAYMET data product relative to the CRU database from 1980 to 2013. All experiments and databases are interpolated to a 100 km grid before any calculation. Biases are estimated over six subregions (Figure 1) adapted from Giorgi et al., 2000: Central America, CAM; Western North America, WNA; Central North America, CNA; Eastern North America, ENA; Alaska, ALA; and Greenland, GRL.

estimate the bias in the DAYMET product relative to the CRU data. The inconsistencies between both observational data are noticeably smaller than the biases in the WRF experiments for all variables in all regions except for minimum temperatures in the CAM region and for precipitation in the ALA region (Figures 4.10, 4.11 and 4.12).

The WRF model underestimates annual climatologies of daily maximum temperatures over most of North America at all resolutions, comparing grid-cell by grid-cell (Figure C.11) and on average over subdomains (Figure 4.10). These biases are generally less pronounced for the experiments using the CLM4 LSM at most locations and in all seasons. The impact of horizontal resolution on these climatologies is weaker than the LSM-dependency over the whole domain and in all seasons, showing a larger

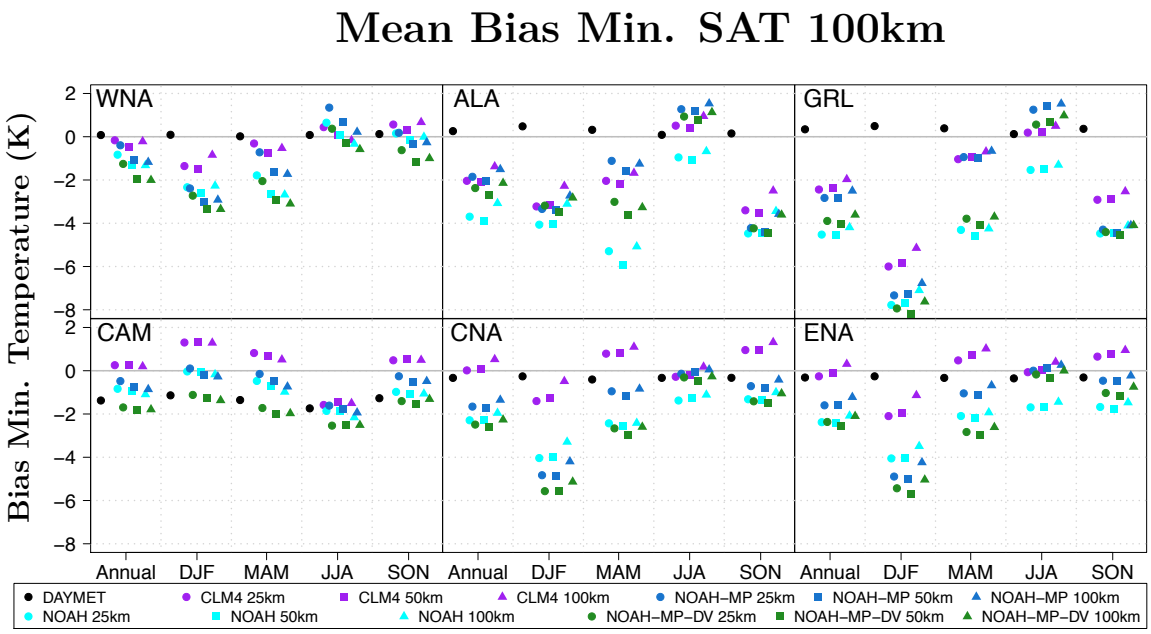

Figure 4.11: Mean annual and seasonal bias in minimum temperature climatology (^oC) for all experiments and the DAYMET data product relative to the CRU database from 1980 to 2013. All experiments and databases are interpolated to a 100 km grid before any calculation. Biases are estimated over six subregions (Figure 1) adapted from Giorgi et al., 2000: Central America, CAM; Western North America, WNA; Central North America, CNA; Eastern North America, ENA; Alaska, ALA; and Greenland, GRL.

resolution impact on maximum temperatures in summer over western North America and at high latitudes (WNA, ALA and GRL in Figure 4.10). Over these areas, finer horizontal resolutions are associated with warmer JJA maximum temperatures, reducing the bias relative to the CRU dataset except in northeastern NA (GRL). In the GRL region, the WRF model with the CLM4 and the NOAH-MP LSM components overestimates JJA maximum temperatures, increasing the bias in these simulations with the use of finer resolution (Figure 4.10).

The performance of the WRF model in reproducing the climatology of daily minimum temperatures from the CRU observations is generally better than reproducing the maximum temperature climatology at mid- and low latitudes, but it is worse at high latitudes especially in DJF (Figures 4.10 and 4.11). Experiments using the

CLM4 LSM yield a warmer climatology over most areas and for all seasons than the experiments with the other LSM components, implying smaller biases in the CLM4 simulations for most of regions (Figure 4.11). The WRF bias in minimum temperature climatology is large in winter over the central and eastern areas of North America and at mid- and high latitudes (subdomains ALA, GRL, CNA and ENA in Figure 4.11). Enhancing horizontal resolution generally reduces the bias in minimum temperatures at high latitudes in JJA, except for the NOAH simulations, but these improvements are small relative to the impact of the LSM choice. Finer resolutions are associated with larger biases in minimum temperatures at mid- and high latitudes in DJF (Figure 4.11).

The effect of horizontal resolution on the temperature biases in our simulations is similar using different LSM components and vegetation mode (Figures 4.10 and 4.11), in agreement with results presented in subsection 4.4.2. Thus, LSM differences in maximum and minimum temperature biases remain the same for the different resolution experiments. The effect of dynamic vegetation on temperature biases also remains constant with resolution, reaching larger biases and colder temperature climatologies with dynamic vegetation than with prescribed vegetation (Figures 4.10 and 4.11). The vegetation mode affects temperature biases particularly in spring (Figures 4.10 and 4.11) and over the boreal forest (Figures C.11 and C.12).

The WRF model simulates large positive biases in daily accumulated precipitation over most of North America during all seasons, with larger biases in summer (Figures 4.12 and C.15). A negative bias is also present in all experiments over the southeastern US and the eastern coast of North America for all seasons (Figure C.15). Dry biases are reduced when using finer horizontal resolutions, while wet biases are larger when using smaller scales, because of the increase in precipitation induced by finer resolutions (Figure 4.12). The impact of resolution on the climatology of sur-

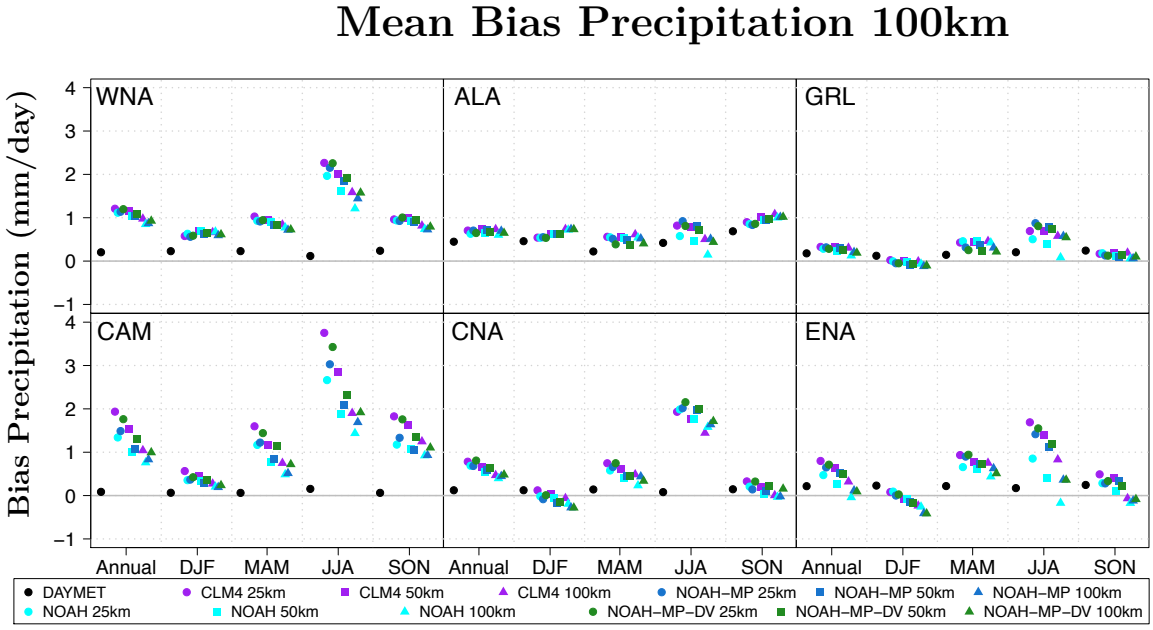

Figure 4.12: Mean annual and seasonal bias in precipitation climatology (mm/day) for all experiments and the DAYMET data product relative to the CRU database from 1980 to 2013. All experiments and databases are interpolated to a 100 km grid before any calculation. Biases are estimated over six subregions (Figure 1) adapted from Giorgi et al., 2000: Central America, CAM; Western North America, WNA; Central North America, CNA; Eastern North America, ENA; Alaska, ALA; and Greenland, GRL.

face precipitation is stronger than the effect of the LSM component, which affects precipitation climatology mainly in summer at low and mid-latitudes (Figure 4.12).

The impact of horizontal resolution is expected to be larger on the simulation of extreme events than on surface climatologies (Di Luca et al., 2015; Prein et al., 2013; Rummukainen, 2016). We examined this by repeating figures included in Section 4.4.3 using the 5th and 95th percentiles of daily temperature and precipitation outputs for the analysis period. For the evaluation of extremes, we compare all simulations with the DAYMET product, because it provides daily data (Figure C.17, C.18 and C.19). The values of the bias relative to the DAYMET dataset are larger when using the 5th and 95th percentiles of the analysis period than when using mean climatologies (Figures 4.10, 4.11, 4.12, C.17, C.18 and C.19). However, results from extreme and mean climatologies yield similar conclusions; the influence of the LSM component is stronger for extreme temperatures than for extreme precipitation, while the simulation of precipitation extremes is greatly affected by changes in resolution.

In summary, the LSM impact on temperature climatologies is larger than the resolution effect (Figures 4.10 and 4.11), while the opposite is true for precipitation climatologies (Figure 4.12). The influence of both the LSM choice and resolution intensifies in summer comparing with the rest of seasons, probably because of the intensification of land-atmosphere coupling in summer (Mei et al., 2012; Zhang et al., 2008). The CLM4 LSM generates the smallest biases in the WRF simulation of maximum and minimum temperature climatologies. Nonetheless, the NOAH LSM yields slightly smaller biases in JJA precipitation climatologies in comparison with the rest of LSM components. The use of finer resolutions leads to slightly larger or smaller biases in the simulation of maximum and minimum temperatures depending on the LSM component. For the WRF simulation of precipitation climatology, the increase in resolution implies larger precipitation biases at low and mid-latitudes for all

LSM components, particularly in summer. Biases in the WRF simulation of extreme temperature and precipitation behave similar to biases in mean climatologies.

4.5 Discussion

The effect of horizontal resolution on the WRF simulation of near-surface climate is similar for all LSM components. All LSM simulations yielded a larger effect of horizontal resolution in summer than in the remaining seasons, as well as at low latitudes, over complex terrain and coastal areas (Figures 4.7, 4.8 and 4.9). Although the increase in resolution greatly affects the performance of the atmospheric model component and therefore precipitation outputs, our results also suggest a relationship between the effect of changing resolution on climatologies of precipitation and surface energy fluxes. For example at low latitudes, the resolution-induced increase in shortwave radiation may lead to higher surface temperatures and sensible heat flux, resulting in lower energy available for latent heat flux, and therefore leading to a decrease in precipitation at coarser resolutions. At high latitudes, the resolution-induced decrease in precipitation climatology probably is associated with the decrease in latent heat flux climatology driven by the decrease in the net radiation absorbed by soil. The relationship between precipitation climatology and shortwave radiation is in agreement with results from the HadGEM atmospheric GCM (Demory et al., 2014), that showed high values of the variables associated with the hydrological cycle resulting from excess surface shortwave radiation. However, they did not find an effect of resolution on shortwave radiation, probably due to the tuning of GCMs to balance top-of-the atmosphere radiation (Demory et al., 2014).

The shown dependence of climate simulations on the LSM component agrees with conclusions drawn from previous analyses at different temporal and spatial scales

(Chen et al., 2014; Davin et al., 2012; García-García et al., 2020b; Laguë et al., 2019; Liu et al., 2019; Mooney et al., 2013; Van Den Broeke et al., 2018; Zhuo et al., 2019). For example, using the Consortium for Small-scale Modeling (COSMO) and WRF RCMs, Davin et al. (2012) and Mooney et al. (2013) identified a LSM sensitivity of temperature and precipitation conditions over Europe, which intensifies in summer. Additionally, our analysis has shown that the impact of the LSM choice on the WRF simulation of precipitation climatology is weaker than its impact on temperature climatology in agreement with studies over a small region in Italy (Zhuo et al., 2019), over Europe (Mooney et al., 2013) and over the western and central US at seasonal scales (Chen et al., 2014; Jin et al., 2010; Van Den Broeke et al., 2018).

Previous evaluations of LSM components over different domains reached the conclusion that the most complex LSM components, that is, the LSM components representing more physical phenomena, outperform others (Chen et al., 2014; Liu et al., 2019; Van Den Broeke et al., 2018). Over North America, our results indicate that the WRF simulation of temperature climatology using the CLM4 LSM outperforms the simulations generated by the NOAH and NOAH-MP LSMs (Figures 4.10 and 4.11). The simulation of precipitation climatology in summer is, however, slightly better represented by the NOAH LSM than by the other LSM components (Figure 4.12). Nonetheless, all our WRF simulations overestimate precipitation over most of North America in agreement with other studies using WRF over the western US (Chen et al., 2014; Jin et al., 2010) and over Europe (Pieri et al., 2015). Atmospheric parameterizations were not tested in this study; however, other WRF sensitivity experiments using several microphysics schemes over Europe found a positive bias in precipitation for all simulations, which was considerably reduced in summer within a convective permitting simulation (Pieri et al., 2015). That is, the positive bias in precipitation has been reported in WRF simulations over different domains using several LSM components,

horizontal resolutions, microphysics parameterizations, and reanalysis products as initial and boundary conditions (Figures 4.12 in this manuscript, Chen et al., 2014; Jin et al., 2010; Pieri et al., 2015). Therefore, the results included in this study together with the results reported in the literature suggest that the use of finer resolutions may raise precipitation biases in WRF simulations over North America, without using the proper atmospheric configuration or resolutions finer enough to simulate convective processes explicitly.

Although the positive bias in precipitation shown in these results agrees with the literature (e.g. Chen et al., 2014; Jin et al., 2010; Pieri et al., 2015), uncertainties in observational data products may be affecting our results. The accuracy of precipitation over mountain areas is strongly reduced. Strong wind conditions at meteorological stations affect the measurement of gauges with documented under-catch of precipitation of up to 40% (Frei et al., 1998, 2003). Thus, the bias in our simulations over the Rocky mountains may arise from uncertainties in observations. Improving the accuracy of precipitation data is crucial for the evaluation of climate model simulations and sensitivity tests.

4.6 Conclusions

This study has showed the effect of horizontal resolution and LSM choice on the climatology of surface energy fluxes and near-surface conditions, which intensifies in summer. Enhancing horizontal resolution leads to higher precipitation climatologies at low latitudes, mainly due to an increase in latent heat flux, which is driven by resolution-induced changes in net shortwave radiation absorbed by soil. Our results highlights the important role of the LSM component in the WRF representation of the energy partition at the surface, which mainly affects the simulation of temperature

climatologies over North America.

The evaluation of the WRF simulations against observations supports the use of the CLM4 LSM as the best choice within the options available for WRF simulations over North America. The use of finer resolutions slightly improves the representation of temperature climatologies within WRF. Nonetheless, the use of finer resolutions should be implemented with caution since it may increase the WRF bias in precipitation. These results are similar for the mean and extreme climatologies of maximum and minimum temperatures and accumulated precipitation. However, the use of other atmospheric parameterizations or resolutions fine enough for convective-permitting simulations may reach other conclusions about the final outcome of increasing resolution. Further studies using WRF with different resolutions are required to identify the best atmospheric configuration for downscaling climate simulations over North America.

Information provided by downscaling studies are used for building climate change policies, thus understanding and restricting uncertainties and inaccuracies in climate simulations may have direct benefits to society and environment. The results presented here should be considered for downscaling studies over North America aimed at projecting future conditions and informing policy-makers.

Bibliography

"Summary for Policymakers" (2019). In: *Special Report on climate change, desertification, land degradation, sustainable land management, food security, and greenhouse gas fluxes in terrestrial ecosystems. Summary for Policymakers*. Ed. by A. e. a. Arneth. Cambridge, United Kingdom and New York, NY, USA: Cambridge University Press, pp. 1–43.

Ban, N., Schmidli, J., and Schär, C. (2014). Evaluation of the convection-resolving regional climate modeling approach in decade-long simulations. *Journal of Geophysical Research: Atmospheres* **119**(13), 7889–7907. DOI: 10.1002/2014JD021478.

Barlage, M., Zeng, X., Wei, H., and Mitchell, K. E. (2005). A global 0.05 ° maximum albedo dataset of snow-covered land based on MODIS observations. *Geophysical Research Letters* **32**(17).

Bonan, G. B. (2002). *Ecological climatology: concepts and applications*. Cambridge University Press, p. 678.

Chen, F., Liu, C., Dudhia, J., and Chen, M. (2014). A sensitivity study of high-resolution regional climate simulations to three land surface models over the western United States. *Journal of Geophysical Research: Atmospheres* **119**(12), 7271–7291. DOI: 10.1002/2014JD021827.

Collins, W. D., Rasch, P. J., Boville, B. A., Hack, J. J., McCaa, J. R., Williamson, D. L., Kiehl, J. T., Briegleb, B., Bitz, C., and Lin, S.-J. (2004). Description of the NCAR community atmosphere model (CAM 3.0). *NCAR Tech. Note NCAR/TN-464+ STR* **226**.

Davin, E. L. and Seneviratne, S. I. (2012). Role of land surface processes and diffuse/direct radiation partitioning in simulating the European climate. *Biogeosciences* **9**(5), 1695–1707. DOI: 10.5194/bg-9-1695-2012.

Demory, M.-E., Vidale, P. L., Roberts, M. J., Berrisford, P., Strachan, J., Schiemann, R., and Mizielinski, M. S. (2014). The role of horizontal resolution in simulating

drivers of the global hydrological cycle. *Climate Dynamics* **42**(7), 2201–2225. DOI: 10.1007/s00382-013-1924-4.

Di Luca, A., Elía, R. de, and Laprise, R. (2015). Challenges in the Quest for Added Value of Regional Climate Dynamical Downscaling. *Current Climate Change Reports* **1**(1), 10–21. DOI: 10.1007/s40641-015-0003-9.

Dirmeyer, P. A., Schlosser, C. A., and Brubaker, K. L. (2009). Precipitation, Recycling, and Land Memory: An Integrated Analysis. *Journal of Hydrometeorology* **10**(1), 278–288. DOI: 10.1175/2008JHM1016.1.

Dirmeyer, P. A., Jin, Y., Singh, B., and Yan, X. (2013). Trends in Land–Atmosphere Interactions from CMIP5 Simulations. *Journal of Hydrometeorology* **14**(3), 829–849. DOI: 10.1175/JHM-D-12-0107.1.

Frei, C. and Schär, C. (1998). A precipitation climatology of the Alps from high-resolution rain-gauge observations. *International Journal of Climatology* **18**(0899-8418), 873–900. DOI: doi:10.1002/(SICI)1097-0088(19980630)18:8<873::AID-JOC255>3.0.CO;2-9.

Frei, C., Christensen, J. H., Déqué, M., Jacob, D., Jones, R. G., and Vidale, P. L. (2003). Daily precipitation statistics in regional climate models: Evaluation and intercomparison for the European Alps. *Journal of Geophysical Research: Atmospheres* **108**(0148-0227). DOI: 10.1029/2002JD002287.

García-García, A., Cuesta-Valero, F. J., Beltrami, H., and Smerdon, J. E. (2019). Characterization of Air and Ground Temperature Relationships within the CMIP5 Historical and Future Climate Simulations. *Journal of Geophysical Research: Atmospheres*(124), 3903–3929. DOI: https://doi.org/10.1029/2018JD030117.

García-García, A., Cuesta-Valero, F. J., and Beltrami, H. (2020a). Effect of horizontal resolution on near-surface climate in the WRF v3.9 model over North America. *In preparation.*

García-García, A., Cuesta-Valero, F. J., Beltrami, H., González-Rouco, J. F., García-Bustamante, E., and Finnis, J. (2020b). Land Surface Model influence on the simulated climatologies of extreme temperature and precipitation events within the WRF v.3.9 model over North America. *Geocientific Model Development (In Discussion)*. DOI: https://doi.org/10.5194/gmd-2020-86.

Gevaert, A. I., Miralles, D. G., Jeu, R. A. M., Schellekens, J., and Dolman, A. J. (2018). Soil Moisture-Temperature Coupling in a Set of Land Surface Models. *Journal of Geophysical Research: Atmospheres* **123**(3), 1481–1498. DOI: 10.1002/2017JD027346.

Giorgi, F. and Francisco, R. (2000). Uncertainties in regional climate change prediction: a regional analysis of ensemble simulations with the HADCM2 coupled AOGCM. *Climate Dynamics* **16**(2), 169–182.

Giorgi, F. and Gutowski Jr., W. J. (2015). Regional Dynamical Downscaling and the CORDEX Initiative. *Annual Review of Environment and Resources* **40**(1), 467–490. DOI: 10.1146/annurev-environ-102014-021217.

Gómez-Navarro, J. J., Raible, C. C., and Dierer, S. (2015). Sensitivity of the WRF model to PBL parametrisations and nesting techniques: evaluation of wind storms over complex terrain. *Geoscientific Model Development* **8**(10), 3349–3363. DOI: 10.5194/gmd-8-3349-2015.

Grell, G. A. and Freitas, S. R. (2014). A scale and aerosol aware stochastic convective parameterization for weather and air quality modeling. *Atmos. Chem. Phys* **14**(10), 5233–5250. DOI: https://doi.org/10.5194/acp-14-5233-2014,2014.

Harris, I., Jones, P., Osborn, T., and Lister, D. (2014). Updated high-resolution grids of monthly climatic observations – the CRU TS3.10 Dataset. *International Journal of Climatology* **34**(3), 623–642.

Harris, I., Osborn, T. J., Jones, P., and Lister, D. (2020). Version 4 of the CRU TS monthly high-resolution gridded multivariate climate dataset. *Scientific Data* **7**(1), 109, 2052–4463. DOI: 10.1038/s41597-020-0453-3.

Hauser, M., Orth, R., and Seneviratne, S. I. (2016). Role of soil moisture versus recent climate change for the 2010 heat wave in western Russia. *Geophysical Research Letters* **43**(6), 2819–2826. DOI: 10.1002/2016GL068036.

Hirschi, M., Seneviratne, S. I., Alexandrov, V., Boberg, F., Boroneant, C., Christensen, O. B., Formayer, H., Orlowsky, B., and Stepanek, P. (2011). Observational evidence for soil-moisture impact on hot extremes in southeastern Europe. *Nature Geosci* **4**(1), 17–21.

Hong, S.-Y., Noh, Y., and Dudhia, J. (2006a). A New Vertical Diffusion Package with an Explicit Treatment of Entrainment Processes. *Monthly Weather Review* **134**(9), 2318–2341. DOI: 10.1175/MWR3199.1.

Hong, S.-Y. and Lim, J.-O. J. (2006b). The WRF single-moment 6-class microphysics scheme (WSM6). *J. Korean Meteor. Soc* **42**(2), 129–151.

Iles, C. E., Vautard, R., Strachan, J., Joussaume, S., Eggen, B. R., and Hewitt, C. D. (2019). The benefits of increasing resolution in global and regional climate simulations for European climate extremes. *Geosci. Model Dev. Discuss.* **2019**, 1–39. DOI: 10.5194/gmd-2019-253.

IPCC (2013). *Climate Change 2013: The Physical Science Basis. Contribution of Working Group I to the Fifth Assessment Report of the Intergovernmental Panel on Climate Change*. Cambridge, United Kingdom and New York, NY, USA: Cambridge University Press, p. 1535. DOI: 10.1017/CBO9781107415324.

Jiménez, P. A., Dudhia, J., González-Rouco, J. F., Navarro, J., Montávez, J. P., and García-Bustamante, E. (2012). A Revised Scheme for the WRF Surface Layer Formulation. *Monthly Weather Review* **140**(3), 898–918.

Jin, J., Miller, N. L., and Schlegel, N. (2010). Sensitivity Study of Four Land Surface Schemes in the WRF Model. *Advances in Meteorology*(167436), 11. DOI: https://doi.org/10.1155/2010/167436.

Koster, R. D., Sud, Y. C., Guo, Z., Dirmeyer, P. A., Bonan, G., Oleson, K. W., Chan, E., Verseghy, D., Cox, P., Davies, H., Kowalczyk, E., Gordon, C. T., Kanae, S., Lawrence, D., Liu, P., Mocko, D., Lu, C.-H., Mitchell, K., Malyshev, S., McAvaney, B., Oki, T., Yamada, T., Pitman, A., Taylor, C. M., Vasic, R., and Xue, Y. (2006). GLACE: The Global Land–Atmosphere Coupling Experiment. Part I: Overview. *Journal of Hydrometeorology* **7**(4), 590–610. DOI: 10.1175/JHM510.1.

Koven, C. D., Riley, W. J., and Stern, A. (2013). Analysis of Permafrost Thermal Dynamics and Response to Climate Change in the CMIP5 Earth System Models. *Journal of Climate* **26**(6), 1877–1900. DOI: 10.1175/JCLI-D-12-00228.1.

Laguë, M. M., Bonan, G. B., and Swann, A. L. S. (2019). Separating the impact of individual land surface properties on the terrestrial surface energy budget in both the coupled and un-coupled land-atmosphere system. *Journal of Climate* **32**(18), 5725–5744.

Liu, L., Ma, Y., Menenti, M., Zhang, X., and Ma, W. (2019). Evaluation of WRF Modeling in Relation to Different Land Surface Schemes and Initial and Boundary Conditions: A Snow Event Simulation Over the Tibetan Plateau. *Journal of Geophysical Research: Atmospheres* **124**(1), 209–226. DOI: 10.1029/2018JD029208.

Lorenz, R., Argüeso, D., Donat, M. G., Pitman, A. J., Hurk, B. van den, Berg, A., Lawrence, D. M., Chéruy, F., Ducharne, A., Hagemann, S., Meier, A., Milly, P. C. D., and Seneviratne, S. I. (2016). Influence of land-atmosphere feedbacks on temperature and precipitation extremes in the GLACE-CMIP5 ensemble. *Journal of Geophysical Research: Atmospheres* **121**(2), 607–623. DOI: 10.1002/2015JD024053.

Lucas-Picher, P., Laprise, R., and Winger, K. (2017). Evidence of added value in North American regional climate model hindcast simulations using ever-increasing horizontal resolutions. *Climate Dynamics* **48**(7), 2611–2633.

Mei, R. and Wang, G. (2012). Summer Land–Atmosphere Coupling Strength in the United States: Comparison among Observations, Reanalysis Data, and Numerical Models. *Journal of Hydrometeorology* **13**(3), 1010–1022. DOI: 10.1175/JHM-D-11-075.1.

Mesinger, F., DiMego, G., Kalnay, E., Mitchell, K., Shafran, P. C., Ebisuzaki, W., Jovic, D., Woollen, J., Rogers, E., Berbery, E. H., et al. (2006). North American

regional reanalysis. *Bulletin of the American Meteorological Society* **87**(3), 343–360. DOI: https://doi.org/10.1175/BAMS-87-3-343.

Messmer, M., Gómez-Navarro, J. J., and Raible, C. C. (2017). Sensitivity experiments on the response of Vb cyclones to sea surface temperature and soil moisture changes. *Earth System Dynamics* **8**(3), 477–493. DOI: 10.5194/esd-8-477-2017.

Michalakes, J, Chen, S, Dudhia, J, Hart, L, Klemp, J, Middlecoff, J, and Skamarock, W (2001). *Development of a next generation regional weather research and forecast model*. Vol. 1. World Scientific, pp. 269–276.

Miralles, D. G., Berg, M. J. den, Teuling, A. J., and Jeu, R. A. M. (2012). Soil moisture-temperature coupling: A multiscale observational analysis. *Geophysical Research Letters* **39**(21).

Mooney, P. A., Mulligan, F. J., and Fealy, R. (2013). Evaluation of the Sensitivity of the Weather Research and Forecasting Model to Parameterization Schemes for Regional Climates of Europe over the Period 1990–95. *Journal of Climate* **26**(3), 1002–1017. DOI: 10.1175/JCLI-D-11-00676.1.

Mueller, B. and Seneviratne, S. I. (2014). Systematic land climate and evapotranspiration biases in CMIP5 simulations. *Geophysical Research Letters* **41**(1), 128–134. DOI: 10.1002/2013GL058055.

Niu, G.-Y., Yang, Z.-L., Mitchell, K. E., Chen, F., Ek, M. B., Barlage, M., Kumar, A., Manning, K., Niyogi, D., Rosero, E., Tewari, M., and Xia, Y. (2011). The community Noah land surface model with multiparameterization options (Noah-MP): 1. Model description and evaluation with local-scale measurements. *Journal of Geophysical Research: Atmospheres* **116**(D12), 2156–2202. DOI: 10.1029/2010JD015139.

Oleson, K. W., Lawrence, D. M., Bonan, G. B., Flanner, M. G., Kluzek, E., Lawrence, P. J., Levis, S., Swenson, S. C., Thornton, P. E., Dai, A., Decker, M., Dickinson, R., Feddema, J., Heald, C. L., Hoffman, F., Lamarque, J.-F., Mahowald, N., Niu, G.-Y., Qian, T., Randerson, J., Running, S., Sakaguchi, K., Slater, A., Stockli, R., Wang, A., Yang, Z.-L., Zeng, X., and Zeng., X. (2010). *Technical description of version 4.0 of the Community Land Model (CLM)*. Tech. rep. NCAR, Boulder.

Pei, L., Moore, N., Zhong, S., Luo, L., Hyndman, D. W., Heilman, W. E., and Gao, Z. (2014). WRF Model Sensitivity to Land Surface Model and Cumulus Parameterization under Short-Term Climate Extremes over the Southern Great Plains of the United States. *Journal of Climate* **27**(20), 7703–7724.

Pieri, A. B., Hardenberg, J. von, Parodi, A., and Provenzale, A. (2015). Sensitivity of Precipitation Statistics to Resolution, Microphysics, and Convective Parameterization: A Case Study with the High-Resolution WRF Climate Model over Europe. *Journal of Hydrometeorology* **16**(4), 1857–1872. DOI: 10.1175/JHM-D-14-0221.1.

Prein, A. F., Gobiet, A., Suklitsch, M., Truhetz, H., Awan, N. K., Keuler, K., and Georgievski, G. (2013). Added value of convection permitting seasonal simulations. *Climate Dynamics* **41**(9), 2655–2677. DOI: 10.1007/s00382-013-1744-6.

Rummukainen, M. (2016). Added value in regional climate modeling. *Wiley Interdisciplinary Reviews: Climate Change* **7**(1), 145–159. DOI: 10.1002/wcc.378.

Schulzweida, U., Kornblueh, L., and Quast, R. (2006). CDO User's Guide. *Climate Data Operators, Version 1. 9. 5* **1**(6). DOI: https://code.mpimet.mpg.de/projects/cdo/embedded/index.html(accessedOct.2019).

Seneviratne, S. I., Lüthi, D., Litschi, M., and Schär, C. (2006). Land–atmosphere coupling and climate change in Europe. *Nature* **443**(7108), 205–209.

Sippel, S., Zscheischler, J., Mahecha, M. D., Orth, R., Reichstein, M., Vogel, M., and Seneviratne, S. I. (2017). Refining multi-model projections of temperature extremes by evaluation against land–atmosphere coupling diagnostics. *Earth System Dynamics* **8**(2), 387–403. DOI: 10.5194/esd-8-387-2017.

Sun, X., Xue, M., Brotzge, J., McPherson, R. A., Hu, X.-M., and Yang, X.-Q. (2016). An evaluation of dynamical downscaling of Central Plains summer precipitation using a WRF-based regional climate model at a convection-permitting 4 km resolution. *Journal of Geophysical Research: Atmospheres* **121**(23), 13,801–13,825. DOI: 10.1002/2016JD024796.

Taylor, K. E., Stouffer, R. J., and Meehl, G. A. (2012). An overview of CMIP5 and the experiment design. *Bulletin of the American Meteorological Society* **93**(4), 485–498.

Tewari, M., Chen, F, Wang, W, Dudhia, J, LeMone, M., Mitchell, K, Ek, M, Gayno, G, Wegiel, J, and Cuenca, R. (2004). *Implementation and verification of the unified NOAH land surface model in the WRF model*. 20th conference on weather analysis and forecasting/16th conference on numerical weather prediction, pp. 11-15.

Thornton, P., Thornton, M., Mayer, B., Wei, Y., Devarakonda, R., Vose, R., and Cook, R. (2016). Daymet: Daily Surface Weather Data on a 1-km Grid for North America, Version 3. *ORNL DAAC, Oak Ridge, Tennessee, USA*. DOI: https://doi.org/10.3334/ORNLDAAC/1328.

Van Den Broeke, M. S., Kalin, A., Alavez, J. A. T., Oglesby, R., and Hu, Q. (2018). A warm-season comparison of WRF coupled to the CLM4.0, Noah-MP, and Bucket hydrology land surface schemes over the central USA. *Theoretical and Applied Climatology* **134**(3), 801–816. DOI: 10.1007/s00704-017-2301-8.

Vogel, M. M., Orth, R., Cheruy, F., Hagemann, S., Lorenz, R., Hurk, B. J.J. M., and Seneviratne, S. I. (2017). Regional amplification of projected changes in extreme temperatures strongly controlled by soil moisture-temperature feedbacks. *Geophysical Research Letters* **44**(3), 1511–1519. DOI: 10.1002/2016GL071235.

Volosciuk, C., Maraun, D., Semenov, V. A., and Park, W. (2015). Extreme Precipitation in an Atmosphere General Circulation Model: Impact of Horizontal and Vertical Model Resolutions. *Journal of Climate* **28**(3), 1184–1205.

Wang, K. and Dickinson, R. E. (2013). Contribution of solar radiation to decadal temperature variability over land. *Proceedings of the National Academy of Sciences* **110**(37), 14877–14882. DOI: 10.1073/pnas.1311433110.

Wehner, M. F., Smith, R. L., Bala, G., and Duffy, P. (2010). The effect of horizontal resolution on simulation of very extreme US precipitation events in a global atmosphere model. *Climate Dynamics* **34**(2), 241–247.

Xue, Y., Janjic, Z., Dudhia, J., Vasic, R., and Sales, F. D. (2014). A review on regional dynamical downscaling in intraseasonal to seasonal simulation/prediction and major factors that affect downscaling ability. *Atmospheric Research* **147-148**, 68 –85. DOI: https://doi.org/10.1016/j.atmosres.2014.05.001.

Zhang, J., Wang, W.-C., and Leung, L. R. (2008). Contribution of land-atmosphere coupling to summer climate variability over the contiguous United States. *Journal of Geophysical Research: Atmospheres* **113**(D22). DOI: 10.1029/2008JD010136.

Zhuo, L., Dai, Q., Han, D., Chen, N., and Zhao, B. (2019). Assessment of simulated soil moisture from WRF Noah, Noah-MP, and CLM land surface schemes for landslide hazard application. *Hydrology and Earth System Sciences* **23**(10), 4199–4218.

.

Chapter 5

Summary and Global Conclusions

5.1 Global Conclusions

The three studies included in Chapter 2, 3 and 4 have contributed to the research goal of this thesis, providing information on the research questions presented in Chapter 1. Thus, these articles provide information about how climate models simulate land-atmosphere interactions, identifying the factors leading to inter-model differences. This research also addressed questions about the consequences of the different representation of land-atmosphere interactions in climate models for the simulation of near-surface conditions, especially for the simulation of temperature and precipitation extremes.

Chapter 2 addressed the first research question raised in the Introduction of this dissertation; are land-atmosphere interactions properly represented within the global climate models used by the fifth assessment report of the Intergovernmental Panel on Climate Change (IPCC)? The IPCC report is the most comprehensive report to date about climate change and its impact on society and ecosystems at global scales. Hence, the importance of evaluating one of its sources of climate information, that is the 5^{th} phase of the Coupled Model Intercomparison Project (CMIP5) General Circulation

Model (GCM) simulations. The evaluation of climate simulations requires observations; however, measuring land-atmosphere interactions can be challenging because of the need for observations of both air and soil. In this study, my co-authors and I proposed the use of a simple metric based on soil and air temperatures to overcome the scarcity of observations of land-atmosphere interactions, since temperature is the most frequent variable measured in meteorological stations. This study concluded that most of the CMIP5 GCMs are not able to reproduce observations of the thermal component of land-atmosphere interactions, and suggests that the Land Surface Model (LSM) component is primarily responsible for inter-model differences in the representation of these interactions. In this article, we were also able to identify the simulation of land cover as one of the main processes affecting the thermal component of land-atmosphere interactions. Most notably, snow cover was found to control the relationship between air and ground temperatures in winter due to its insulating effect. Thus, the different representation of land cover by each LSM may result in a different simulation of the surface energy balance, and then a different representation of the thermal component of land-atmosphere interactions.

Results presented in the first article suggest the LSM component as as important factor for the simulation of land-atmosphere interactions. Thus, these results also contribute to address the second research question of this thesis; what factors lead to model differences in the representation of land-atmosphere interactions? Are they also contributing to uncertainties in near-surface conditions? However, this first study employed climate simulations from GCMs composed by several model components, which share parts of the code. Therefore, the attribution of inter-model differences in representing land-atmosphere interactions to the LSM component can only be hypothesized using these results. In the second article included in this thesis, I designed a modeling experiment using a regional climate model to perform a set of

simulations which only differ in the LSM component, allowing this hypothesis to be explored further. Using this set of regional climate simulations, my co-authors and I confirm that the LSM component plays a key role in simulating land-atmosphere interactions, as well as the LSM contribution to model uncertainty in the simulation of temperature and precipitation extremes. This study also explored the implications of these results for other sets of regional simulations, using three regional simulations from different Regional Climate Models (RCMs), participating in the North American component of the Coordinated Regional climate Downscaling Experiment (CORDEX) program. These RCM simulations differ in several aspects beyond the use of different LSM components, however the comparison between the uncertainty in the simulation of extreme events within the CORDEX ensemble and in our set of simulations showed similar spatial patterns. The agreement between both model ensembles indicates that the LSM component can be an important source of uncertainty in the simulation of extreme events within other model ensembles.

The last of the research questions posed in the Introduction was undertaken in Chapter 4; how does horizontal resolution affect the representation of land-atmosphere interactions within climate models? Are land-atmosphere interactions better represented within RCMs than within GCMs due to the use of finer horizontal resolution? This third study presents results on the influence of horizontal resolution on the representation of land-atmosphere interactions, by evaluating the simulation of the energy partition at the air-ground interface. For this purpose, I designed another modeling experiment consisting of a larger set of simulations, using different LSM components and different horizontal resolutions. The analysis of this set of simulations provided information to understand LSM differences in the representation of land-atmosphere interactions as well as information on how a more detailed description of topography affects the simulation of soil properties and consequently the surface energy and water

balance. The effect of horizontal resolution on the surface energy balance and near-surface conditions in simulations with different LSM components is similar. However, simulations using different LSM components showed large discrepancies in the representation of surface energy fluxes. Thus, the effect of the LSM choice was found to be primarily determinant for the representation of temperature climatologies, while horizontal resolution was found to affect the simulation of precipitation climatology. The comparison of the simulated climatologies with observations of near-surface conditions also yielded interesting results; an increase in horizontal resolution may increase the bias in the simulation of precipitation climatology. However, these results should be interpreted with caution, since model tuning (the adjustment of parameter in each climate model to fit observations) may be influencing our conclusions and the use of different atmospheric parameterizations in our simulations may yield contradictory results.

Although the three studies included in this dissertation provide information about the representation of land-atmosphere interactions in RCMs and GCMs, the comparison of results from regional and global climate simulations presents some challenges. In the second and third manuscripts, I was able to evaluate the impact of the LSM choice and horizontal resolution on the simulation of land-atmosphere interactions because I performed my own simulations using the Weather Research and Forecasting (WRF) model. However, I was not able to determine the effect of the LSM choice and horizontal resolution on the representation of land-atmosphere interactions within the GCM simulations employed in Chapter 2, because of several differences between GCMs beyond the LSM component. Nonetheless, results from the three manuscripts support the dependence of land-atmosphere interactions on the LSM component within GCM and RCM simulations. The effect of horizontal resolution on land-atmosphere interactions, meanwhile, was not apparent in the analysis of GCM simulations (Chapter 2)

and was found to be weaker than the effect of the LSM choice on the WRF simulation of the surface energy balance (Chapter 4). Therefore, it cannot be determined from these results whether land-atmosphere interactions are better represented in RCMs than in GCMs, although they suggest that the representation of land-atmosphere interactions in both regional and global climate models is mainly influenced by the choice of LSM component. In order to continue exploring this question, a comparison between GCM and RCM simulations should be pursued using various metrics and observations of land-atmosphere interactions. Additionally, a sensitivity study to horizontal resolution using GCMs could shed light on the impact of increasing resolution on the representation of land-atmosphere interactions in climate simulations.

5.2 Significance of the Research

Although LSM components have received little attention by the modeling community in comparison with the rest of model components, this thesis highlights the role of the LSM component in climate simulations performed by GCMs and RCMs. These results are particularly relevant for RCM simulations and reanalysis products, which include very simple LSM components in order to save computational resources to improve the performance of the atmospheric model component. Due to the large effect of the LSM component on the simulation of near-surface conditions shown in this dissertation, the use of simple version of LSM component in RCMs and reanalyses can be an important limitation in regional simulations and reanalysis products. Thus, this research supports the ongoing work on developing LSM components as well as the implementation of new versions of these components in current and future RCMs and reanalyses in order to improve the models' representation of land-atmosphere interactions and therefore near-surface conditions.

This work also provides information about the role of horizontal resolution on the simulation of land-atmosphere interactions, showing the intensification of the variables related to the water cycle with the use of finer resolutions at low latitudes of North America. These results, however, raise doubts about the benefit of increasing resolution to the WRF simulation of land-atmosphere interactions, since the LSM choice was shown to be the determinant factor for the simulation of the surface energy balance. Additionally, the use of finer resolution in our WRF simulations was associated with larger biases in precipitation climatology. However, this result should be tested using different atmospheric parameterizations and convective-permitting simulations in order to clarify the impact of increasing resolution on WRF climate simulations over North America. Thus, this thesis emphasizes the importance of selecting the model configuration, particularly the LSM component, that best works for North America, before performing a dynamical downscaling simulation. Also, scientists interested in downscaling experiments over North America using the WRF model should consider the use of the Community Land Model version 4 (CLM4) LSM over the rest of LSM components available to improve the simulation of temperature climatologies.

Inter-model differences in representing land-atmosphere interactions due to the employed LSM component have also been shown to affect the representation of statistics of temperature and precipitation extremes, thus likely contributing to model uncertainties in the projection of extreme indices. The information provided in this dissertation has helped to understand these inter-model differences in representing land-atmosphere interactions, which in turn may help to restrict uncertainties in climate model simulations, particularly those associated with the simulation of temperature and precipitation extremes. This is very important for the wellbeing and sustainability of society and environment, since reducing uncertainties in climate model simulations will improve climate information employed for developing climate change

adaptation and mitigation measures. The implementation of more adequate adaptation and mitigation strategies may reduce economic and biodiversity losses and death toll.

5.3 Future Directions

There are several lines of future work arising from this thesis that are of scientific interest. One of these lines is to perform and analyze a set of WRF simulations with different atmospheric parameterizations, maintaining the same LSM component. Although there are many studies analyzing the sensitivity of the WRF model to atmospheric parameterizations (e.g. Sun et al., 2020), the use of different atmospheric parameterizations with the configuration used for our simulations would allow the comparison of the effect of the LSM choice, horizontal resolution and atmospheric parameterizations on the WRF simulation of land-atmosphere interactions and near-surface conditions. Furthermore, performing an additional simulation with much finer horizontal resolution (4 km) would allow the simulation of convective-permitting processes and its comparison with the rest of our simulations, providing information of the WRF configuration best suited to North America.

As discussed in Chapter 3, the consequences of compound extreme events for society and environment are much more dangerous than consequences of temperature or precipitation extremes separately. This thesis has demonstrated the impact of the LSM choice and increasing resolution on the simulation of land-atmosphere interactions and consequently on the representation of extreme events; however, the LSM component and horizontal resolution may also affect the simulation of compound extreme events. Although the large LSM differences in the representation of near-surface conditions suggest a large LSM influence on the simulation of compound

extreme events, the uncertainties in temperature and precipitation arising from the LSM component are interrelated in the simulation. Thus, a future study evaluating the LSM and resolution impact on the uncertainty in the simulation of compound extreme events (e.g. events with concurrent drought and heat waves) would be of major interest.

Another interesting line for continuing this research is the analysis of the impact of the LSM choice and horizontal resolution on the simulation of temporal anomalies of land-atmosphere interactions and near-surface conditions, in contrast to the climatologies examined in this dissertation. However, the temporal analysis of these impacts would require longer simulations, likely including future climate projections, which require large amounts of computational resources and time. Nevertheless, this constitutes a very interesting line of work since, theoretically, the different representation of climatologies due to the LSM component should affect the simulation of temperature-dependent processes, such as carbon and permafrost stabilities, which are positive climate feedbacks and therefore should affect the climate simulation progressively. This progressive effect of the LSM component can be small in RCMs because RCMs do not represent the global carbon cycle. Thus, the study of the LSM impact on temperature-dependent processes and consequently on climate evolution should probably be accomplished using a Earth System Model.

A new generation of GCMs is currently being used for updated simulations to inform the sixth assessment report of the IPCC. Outputs from this new set of models will be available soon, allowing the evaluation of land-atmosphere interactions in this generation of models, as well as comparison with their predecessors. Thus, the proposed inter-model comparison might provide information on the improvement in the new generation of models associated with the representation of land-atmosphere interactions. This comparison would benefit from including new observations of land-

atmosphere interactions in the evaluation of climate models. As mentioned in this thesis, measuring land-atmosphere interactions presents some difficulties, but there are a few projects providing observational data of surface energy fluxes, such as the FluxNet project (Baldocchi et al., 2001). However, the temporal and spatial coverage of this database is still insufficient for model evaluations at climatological scales. Nonetheless, the use of the FluxNet database might also be interesting for the evaluation of the surface energy balance in WRF simulations at shorter time scales.

Bibliography

Adachi, Y., Yukimoto, S., Deushi, M., Obata, A., Nakano, H., Tanaka, T. Y., Hosaka, M., Sakami, T., Yoshimura, H., and Hirabara, M. (2013). Basic performance of a new earth system model of the Meteorological Research Institute (MRI-ESM1). *Papers in Meteorology and Geophysics* **64**, 1–19.

Alessandri, A. and Navarra, A. (2008). On the coupling between vegetation and rainfall inter-annual anomalies: Possible contributions to seasonal rainfall predictability over land areas. *Geophysical Research Letters* **35**(2), 1944–8007. DOI: 10.1029/2007GL032415.

"Summary for Policymakers" (2019). In: *Special Report on climate change, desertification, land degradation, sustainable land management, food security, and greenhouse gas fluxes in terrestrial ecosystems. Summary for Policymakers*. Ed. by A. e. a. Arneth. Cambridge, United Kingdom and New York, NY, USA: Cambridge University Press, pp. 1–43.

Baldocchi, D., Falge, E., Gu, L., Olson, R., Hollinger, D., Running, S., Anthoni, P., Bernhofer, C., Davis, K., Evans, R., Fuentes, J., Goldstein, A., Katul, G., Law, B., Lee, X., Malhi, Y., Meyers, T., Munger, W., Oechel, W., U, K. T. P., Pilegaard, K., Schmid, H. P., Valentini, R., Verma, S., Vesala, T., Wilson, K., and Wofsy, S. (2001). FLUXNET: A New Tool to Study the Temporal and Spatial Variability of Ecosystem-Scale Carbon Dioxide, Water Vapor, and Energy Flux Densities. *Bulletin of the American Meteorological Society* **82**(11), 2415–2434.

Balsamo, G., Albergel, C., Beljaars, A., Boussetta, S., Brun, E., Cloke, H., Dee, D., Dutra, E., Muñoz-Sabater, J., and Pappenberger, F. (2015). ERA-Interim/Land: a global land surface reanalysis data set. *Hydrology and Earth System Sciences* **19**(1), 389–407.

Ban, N., Schmidli, J., and Schär, C. (2014). Evaluation of the convection-resolving regional climate modeling approach in decade-long simulations. *Journal of Geophysical Research: Atmospheres* **119**(13), 7889–7907. DOI: 10.1002/2014JD021478.

Ban-Weiss, G. A., Bala, G., Cao, L., Pongratz, J., and Caldeira, K. (2011). Climate forcing and response to idealized changes in surface latent and sensible heat. *Environmental Research Letters* **6**(3), 034032.

Barlage, M., Zeng, X., Wei, H., and Mitchell, K. E. (2005). A global 0.05 ° maximum albedo dataset of snow-covered land based on MODIS observations. *Geophysical Research Letters* **32**(17).

Beltrami, H. (1996). Active layer distortion of annual air/soil thermal orbits. *Permafrost and Periglacial Processes* **7**(2), 101–110.

— (2002). Climate from borehole data: Energy fluxes and temperatures since 1500. *Geophysical Research Letters* **29**(23), 26–1–26–4. DOI: 10.1029/2002GL015702.

Berbery, E. H., Luo, Y., Mitchell, K. E., and Betts, A. K. (2003). Eta model estimated land surface processes and the hydrologic cycle of the Mississippi basin. *Journal of Geophysical Research: Atmospheres* **108**(D22), 2156–2202. DOI: DOI:10.1029/2002JD003192.

Berg, A., Lintner, B. R., Findell, K., Seneviratne, S. I., Hurk, B. van den, Ducharne, A., Chéruy, F., Hagemann, S., Lawrence, D. M., Malyshev, S., Meier, A., and Gentine, P. (2015). Interannual Coupling between Summertime Surface Temperature and Precipitation over Land: Processes and Implications for Climate Change. *Journal of Climate* **28**(3), 1308–1328. DOI: 10.1175/JCLI-D-14-00324.1.

Bonan, G. B. (1995). Land-Atmosphere interactions for climate system Models: coupling biophysical, biogeochemical, and ecosystem dynamical processes. *Remote Sensing of Environment* **51**(1), 57 –73. DOI: http://dx.doi.org/10.1016/0034-4257(94)00065-U.

Bonan, G. B. (2002). *Ecological climatology: concepts and applications*. Cambridge University Press, p. 678.

Broxton, P. D., Zeng, X., and Dawson, N. (2017). The Impact of a Low Bias in Snow Water Equivalent Initialization on CFS Seasonal Forecasts. *Journal of Climate* **30**(21), 8657–8671.

Cannon, A. J., Sobie, S. R., and Murdock, T. Q. (2015). Bias Correction of GCM Precipitation by Quantile Mapping: How Well Do Methods Preserve Changes in Quantiles and Extremes? *Journal of Climate* **28**(17), 6938–6959.

Chen, F., Liu, C., Dudhia, J., and Chen, M. (2014). A sensitivity study of high-resolution regional climate simulations to three land surface models over the western United States. *Journal of Geophysical Research: Atmospheres* **119**(12), 7271–7291. DOI: 10.1002/2014JD021827.

Christoff, P. (2016). The promissory note: COP 21 and the Paris Climate Agreement. *Environmental Politics* **25**(5), 765–787. DOI: 10.1080/09644016.2016.1191818.

Collins, W. D., Rasch, P. J., Boville, B. A., Hack, J. J., McCaa, J. R., Williamson, D. L., Kiehl, J. T., Briegleb, B., Bitz, C., and Lin, S.-J. (2004). Description of the NCAR community atmosphere model (CAM 3.0). *NCAR Tech. Note NCAR/TN-464+ STR* **226**.

Collins, W. D., Bitz, C. M., Blackmon, M. L., Bonan, G. B., Bretherton, C. S., Carton, J. A., Chang, P., Doney, S. C., Hack, J. J., Henderson, T. B., et al. (2006). The community climate system model version 3 (CCSM3). *Journal of Climate* **19**(11), 2122–2143.

Cook, B. I., Bonan, G. B., and Levis, S. (2006). Soil Moisture Feedbacks to Precipitation in Southern Africa. *Journal of Climate* **19**(17), 4198–4206. DOI: 10.1175/JCLI3856.1.

Cook, B. I., Miller, R. L., and Seager, R. (2008). Dust and sea surface temperature forcing of the 1930s "Dust Bowl" drought. *Geophysical Research Letters* **35**(8). DOI: 10.1029/2008GL033486.

Cubasch, U., Wuebbles, D., Chen, D., Facchini, M., Frame, D., Mahowald, N., and Winther, J.-G. (2013). "Introduction". In: *Climate Change 2013: The Physical Science Basis. Contribution of Working Group I to the Fifth Assessment Report of the Intergovernmental Panel on Climate Change*. Ed. by T. Stocker, D. Qin, G.-K. Plattner, M. Tignor, S. Allen, J. Boschung, A. Nauels, Y. Xia, V. Bex, and P. Midgley. Cambridge, United Kingdom and New York, NY, USA: Cambridge University Press. Chap. 1, pp. 119–158. DOI: 10.1017/CBO9781107415324.007.

Cuesta-Valero, F. J., García-García, A., Beltrami, H., and Smerdon, J. E. (2016). First Assessment of Continental Energy Storage in CMIP5 Simulations. *Geophysical Research Letters*. DOI: 10.1002/2016GL068496.

Davies, T., Cullen, M. J. P., Malcolm, A. J., Mawson, M. H., Staniforth, A., White, A. A., and Wood, N. (2005). A new dynamical core for the Met Office's global and regional modelling of the atmosphere. *Quarterly Journal of the Royal Meteorological Society* **131**(608), 1759–1782. DOI: 10.1256/qj.04.101.

Davin, E. L. and Seneviratne, S. I. (2012). Role of land surface processes and diffuse/direct radiation partitioning in simulating the European climate. *Biogeosciences* **9**(5), 1695–1707. DOI: 10.5194/bg-9-1695-2012.

Davin, E. L., Maisonnave, E., and Seneviratne, S. I. (2016). Is land surface processes representation a possible weak link in current Regional Climate Models? *Environmental Research Letters* **11**(7), 074027.

Decker, M, Pitman, A, and Evans, J (2015). Diagnosing the seasonal land–atmosphere correspondence over northern Australia: dependence on soil moisture state and correspondence strength definition. *Hydrology and Earth System Sciences* **19**(8), 3433–3447.

Dee, D. P., Uppala, S. M., Simmons, A. J., Berrisford, P., Poli, P., Kobayashi, S., Andrae, U., Balmaseda, M. A., Balsamo, G., Bauer, P., Bechtold, P., Beljaars, A. C. M., Berg, L. van de, Bidlot, J., Bormann, N., Delsol, C., Dragani, R., Fuentes, M., Geer, A. J., Haimberger, L., Healy, S. B., Hersbach, H., Hólm, E. V., Isaksen, L., Kållberg, P., Köhler, M., Matricardi, M., McNally, A. P., Monge-Sanz, B. M., Morcrette, J.-J., Park, B.-K., Peubey, C., Rosnay, P. de, Tavolato, C., Thépaut, J.-N., and Vitart, F. (2011). The ERA-Interim reanalysis: configuration and performance of the data assimilation system. *Quarterly Journal of the Royal Meteorological Society* **137**(656), 553–597.

Delworth, T. L., Broccoli, A. J., Rosati, A., Stouffer, R. J., Balaji, V., Beesley, J. A., Cooke, W. F., Dixon, K. W., Dunne, J., Dunne, K. A., Durachta, J. W., Findell, K. L., Ginoux, P., Gnanadesikan, A., Gordon, C. T., Griffies, S. M., Gudgel, R., Harrison, M. J., Held, I. M., Hemler, R. S., Horowitz, L. W., Klein, S. A., Knutson, T. R., Kushner, P. J., Langenhorst, A. R., Lee, H.-C., Lin, S.-J., Lu, J., Malyshev, S. L., Milly, P. C. D., Ramaswamy, V., Russell, J., Schwarzkopf, M. D., Shevliakova, E., Sirutis, J. J., Spelman, M. J., Stern, W. F., Winton, M., Wittenberg, A. T., Wyman, B., Zeng, F., and Zhang, R. (2006). GFDL's CM2 Global Coupled Climate Models. Part I: Formulation and Simulation Characteristics. *Journal of Climate* **19**(5), 643–674.

Demory, M.-E., Vidale, P. L., Roberts, M. J., Berrisford, P., Strachan, J., Schiemann, R., and Mizielinski, M. S. (2014). The role of horizontal resolution in simulating drivers of the global hydrological cycle. *Climate Dynamics* **42**(7), 2201–2225. DOI: 10.1007/s00382-013-1924-4.

Di Luca, A., Elía, R. de, and Laprise, R. (2015). Challenges in the Quest for Added Value of Regional Climate Dynamical Downscaling. *Current Climate Change Reports* **1**(1), 10–21. DOI: 10.1007/s40641-015-0003-9.

Dirmeyer, P. A., Koster, R. D., and Guo, Z. (2006a). Do Global Models Properly Represent the Feedback between Land and Atmosphere? *Journal of Hydrometeorology* **7**(6), 1177–1198. DOI: 10.1175/JHM532.1.

Dirmeyer, P. A., Gao, X., Zhao, M., Guo, Z., Oki, T., and Hanasaki, N. (2006b). GSWP-2: Multimodel Analysis and Implications for Our Perception of the Land Surface. *Bulletin of the American Meteorological Society* **87**(10), 1381–1397. DOI: 10.1175/BAMS-87-10-1381.

Dirmeyer, P. A., Schlosser, C. A., and Brubaker, K. L. (2009). Precipitation, Recycling, and Land Memory: An Integrated Analysis. *Journal of Hydrometeorology* **10**(1), 278–288. DOI: 10.1175/2008JHM1016.1.

Dirmeyer, P. A., Cash, B. A., III, J. L. K., Stan, C., Jung, T., Marx, L., Towers, P., Wedi, N., Adams, J. M., Altshuler, E. L., Huang, B., Jin, E. K., and Manganello, J.

(2012). Evidence for Enhanced Land–Atmosphere Feedback in a Warming Climate. *Journal of Hydrometeorology* **13**(3), 981–995. DOI: 10.1175/JHM-D-11-0104.1.

Dirmeyer, P. A., Jin, Y., Singh, B., and Yan, X. (2013c). Trends in Land–Atmosphere Interactions from CMIP5 Simulations. *Journal of Hydrometeorology* **14**(3), 829–849. DOI: 10.1175/JHM-D-12-0107.1.

Dirmeyer, P. A., Wang, Z., Mbuh, M. J., and Norton, H. E. (2014). Intensified land surface control on boundary layer growth in a changing climate. *Geophysical Research Letters* **41**(4), 1290–1294. DOI: 10.1002/2013GL058826.

Diro, G. T., Sushama, L., Martynov, A., Jeong, D. I., Verseghy, D., and Winger, K. (2014). Land-atmosphere coupling over North America in CRCM5. *Journal of Geophysical Research: Atmospheres* **119**(21), 11,955–11,972. DOI: 10.1002/2014JD021677.

Diro, G. T., Sushama, L., and Huziy, O. (2018). Snow-atmosphere coupling and its impact on temperature variability and extremes over North America. *Climate Dynamics* **50**(7), 2993–3007. DOI: 10.1007/s00382-017-3788-5.

Donat, M. G., King, A. D., Overpeck, J. T., Alexander, L. V., Durre, I., and Karoly, D. J. (2016). Extraordinary heat during the 1930s US Dust Bowl and associated large-scale conditions. *Climate Dynamics* **46**(1), 413–426.

Donner, L. J., Wyman, B. L., Hemler, R. S., Horowitz, L. W., Ming, Y., Zhao, M., Golaz, J.-C., Ginoux, P., Lin, S.-J., Schwarzkopf, M. D., Austin, J., Alaka, G., Cooke, W. F., Delworth, T. L., Freidenreich, S. M., Gordon, C. T., Griffies, S. M., Held, I. M., Hurlin, W. J., Klein, S. A., Knutson, T. R., Langenhorst, A. R., Lee, H.-C., Lin, Y., Magi, B. I., Malyshev, S. L., Milly, P. C. D., Naik, V., Nath, M. J., Pincus, R., Ploshay, J. J., Ramaswamy, V., Seman, C. J., Shevliakova, E., Sirutis, J. J., Stern, W. F., Stouffer, R. J., Wilson, R. J., Winton, M., Wittenberg, A. T., and Zeng, F. (2011). The Dynamical Core, Physical Parameterizations, and Basic Simulation Characteristics of the Atmospheric Component AM3 of the GFDL Global Coupled Model CM3. *Journal of Climate* **24**(13), 3484–3519.

Dunne, J. P., John, J. G., Adcroft, A. J., Griffies, S. M., Hallberg, R. W., Shevliakova, E., Stouffer, R. J., Cooke, W., Dunne, K. A., Harrison, M. J., et al. (2012). GFDL's ESM2 global culled climate-carbon earth system models. Part I: Physical formulation and baseline simulation characteristics. *J. Climate* **25**, 6646–6665.

Ebisuzaki, W. (1997). A Method to Estimate the Statistical Significance of a Correlation When the Data Are Serially Correlated. *Journal of Climate* **10**(9), 2147–2153. DOI: doi:10.1175/1520-0442(1997)010<2147:AMTETS>2.0.CO;2.

Ehret, U., Zehe, E., Wulfmeyer, V., Warrach-Sagi, K., and Liebert, J. (2012). HESS Opinions "Should we apply bias correction to global and regional climate model

data?". *Hydrol. Earth Syst. Sci.* **16**(9), 3391–3404. DOI: 10.5194/hess-16-3391-2012.

Ek, M. B., Mitchell, K. E., Lin, Y., Rogers, E., Grunmann, P., Koren, V., Gayno, G., and Tarpley, J. D. (2003). Implementation of Noah land surface model advances in the National Centers for Environmental Prediction operational mesoscale Eta model. *Journal of Geophysical Research: Atmospheres* **108**(D22), 2156–2202. DOI: doi:10.1029/2002JD003296.

Ek, M. B. and Holtslag, A. A. M. (2004). Influence of Soil Moisture on Boundary Layer Cloud Development. *Journal of Hydrometeorology* **5**(1), 86–99.

Elía, R. de, Caya, D., Côté, H., Frigon, A., Biner, S., Giguère, M., Paquin, D., Harvey, R., and Plummer, D. (2008). Evaluation of uncertainties in the CRCM-simulated North American climate. *Climate Dynamics* **30**(2), 113–132. DOI: 10.1007/s00382-007-0288-z.

Essery, R., Best, M., Betts, R., Cox, P. M., and Taylor, C. M. (2003). Explicit representation of subgrid heterogeneity in a GCM land surface scheme. *Journal of Hydrometeorology* **4**(3), 530–543.

Ferguson, C. R., Wood, E. F., and Vinukollu, R. K. (2012). A Global Intercomparison of Modeled and Observed Land–Atmosphere Coupling. *Journal of Hydrometeorology* **13**(3), 749–784. DOI: 10.1175/JHM-D-11-0119.1.

Fischer, E., Seneviratne, S., Lüthi, D, and Schär, C (2007). Contribution of land-atmosphere coupling to recent European summer heat waves. *Geophysical Research Letters* **34**(6).

Flato, G., Marotzke, J., Abiodun, B., Braconnot, P., Chou, S., Collins, W., Cox, P., Driouech, F., Emori, S., Eyring, V., Forest, C., Gleckler, P., Guilyardi, E., Jakob, C., Kattsov, V., Reason, C., and Rummukainen, M. (2013). "Evaluation of Climate Models". In: *Climate Change 2013: The Physical Science Basis. Contribution of Working Group I to the Fifth Assessment Report of the Intergovernmental Panel on Climate Change*. Ed. by T. Stocker, D. Qin, G.-K. Plattner, M. Tignor, S. Allen, J. Boschung, A. Nauels, Y. Xia, V. Bex, and P. Midgley. Cambridge, United Kingdom and New York, NY, USA: Cambridge University Press. Chap. 9, pp. 741–866. DOI: 10.1017/CBO9781107415324.020.

Frei, C. and Schär, C. (1998). A precipitation climatology of the Alps from high-resolution rain-gauge observations. *International Journal of Climatology* **18**(0899-8418), 873–900. DOI: doi:10.1002/(SICI)1097-0088(19980630)18:8<873::AID-JOC255>3.0.CO;2-9.

Frei, C., Christensen, J. H., Déqué, M., Jacob, D., Jones, R. G., and Vidale, P. L. (2003). Daily precipitation statistics in regional climate models: Evaluation and

intercomparison for the European Alps. *Journal of Geophysical Research: Atmospheres* **108**(0148-0227). DOI: 10.1029/2002JD002287.

Gallus, W. A. and Bresch, J. F. (2006). Comparison of Impacts of WRF Dynamic Core, Physics Package, and Initial Conditions on Warm Season Rainfall Forecasts. *Monthly Weather Review* **134**(9), 2632–2641. DOI: 10.1175/MWR3198.1.

García-García, A., Cuesta-Valero, F. J., Beltrami, H., and Smerdon, J. E. (2019). Characterization of Air and Ground Temperature Relationships within the CMIP5 Historical and Future Climate Simulations. *Journal of Geophysical Research: Atmospheres*(124), 3903–3929. DOI: https://doi.org/10.1029/2018JD030117.

García-García, A., Cuesta-Valero, F. J., and Beltrami, H. (2020b). Effect of horizontal resolution on near-surface climate in the WRF v3.9 model over North America. *In preparation.*

García-García, A., Cuesta-Valero, F. J., Beltrami, H., González-Rouco, J. F., García-Bustamante, E., and Finnis, J. (2020c). Land Surface Model influence on the simulated climatologies of extreme temperature and precipitation events within the WRF v.3.9 model over North America. *Geocientific Model Development (In Discussion)*. DOI: https://doi.org/10.5194/gmd-2020-86.

Garnaud, C. and Sushama, L. (2015). Biosphere-climate interactions in a changing climate over North America. *Journal of Geophysical Research: Atmospheres* **120**(3). 2014JD022055, 1091–1108. DOI: 10.1002/2014JD022055.

Gevaert, A. I., Miralles, D. G., Jeu, R. A. M., Schellekens, J., and Dolman, A. J. (2018). Soil Moisture-Temperature Coupling in a Set of Land Surface Models. *Journal of Geophysical Research: Atmospheres* **123**(3), 1481–1498. DOI: 10.1002/2017JD027346.

Giorgi, F. and Francisco, R. (2000). Uncertainties in regional climate change prediction: a regional analysis of ensemble simulations with the HADCM2 coupled AOGCM. *Climate Dynamics* **16**(2), 169–182.

Giorgi, F. and Gutowski Jr., W. J. (2015). Regional Dynamical Downscaling and the CORDEX Initiative. *Annual Review of Environment and Resources* **40**(1), 467–490. DOI: 10.1146/annurev-environ-102014-021217.

Gómez-Navarro, J. J., Raible, C. C., and Dierer, S. (2015). Sensitivity of the WRF model to PBL parametrisations and nesting techniques: evaluation of wind storms over complex terrain. *Geoscientific Model Development* **8**(10), 3349–3363. DOI: 10.5194/gmd-8-3349-2015.

Goodrich, L. (1982b). The influence of snow cover on the ground thermal regime. *Canadian geotechnical journal* **19**(4), 421–432.

Gouttevin, I., Menegoz, M., Dominé, F., Krinner, G., Koven, C., Ciais, P., Tarnocai, C., and Boike, J. (2012). How the insulating properties of snow affect soil carbon distribution in the continental pan-Arctic area. *Journal of Geophysical Research: Biogeosciences* **117**(G2), 2156–2202. DOI: 10.1029/2011JG001916.

Grell, G. A. and Freitas, S. R. (2014). A scale and aerosol aware stochastic convective parameterization for weather and air quality modeling. *Atmos. Chem. Phys* **14**(10), 5233–5250. DOI: https://doi.org/10.5194/acp-14-5233-2014,2014.

Guo, Z., Dirmeyer, P. A., Koster, R. D., Sud, Y. C., Bonan, G., Oleson, K. W., Chan, E., Verseghy, D., Cox, P., Gordon, C. T., McGregor, J. L., Kanae, S., Kowalczyk, E., Lawrence, D., Liu, P., Mocko, D., Lu, C.-H., Mitchell, K., Malyshev, S., McAvaney, B., Oki, T., Yamada, T., Pitman, A., Taylor, C. M., Vasic, R., and Xue, Y. (2006). GLACE: The Global Land–Atmosphere Coupling Experiment. Part II: Analysis. *Journal of Hydrometeorology* **7**(4), 611–625. DOI: 10.1175/JHM511.1.

Guo, Z. and Dirmeyer, P. A. (2013). Interannual Variability of Land–Atmosphere Coupling Strength. *Journal of Hydrometeorology* **14**(5), 1636–1646. DOI: 10.1175/JHM-D-12-0171.1.

Hansen, J., Nazarenko, L., Ruedy, R., Sato, M., Willis, J., Del Genio, A., Koch, D., Lacis, A., Lo, K., Menon, S., Novakov, T., Perlwitz, J., Russell, G., Schmidt, G. A., and Tausnev, N. (2005). Earth's Energy Imbalance: Confirmation and Implications. *Science* **308**(5727), 1431–1435.

Hansen, J., Sato, M., Kharecha, P., and Schuckmann, K. v. (2011). Earth's energy imbalance and implications. *Atmospheric Chemistry and Physics* **11**(24), 13421–13449.

Harris, I., Jones, P., Osborn, T., and Lister, D. (2014). Updated high-resolution grids of monthly climatic observations – the CRU TS3.10 Dataset. *International Journal of Climatology* **34**(3), 623–642.

Harris, I., Osborn, T. J., Jones, P., and Lister, D. (2020). Version 4 of the CRU TS monthly high-resolution gridded multivariate climate dataset. *Scientific Data* **7**(1), 109, 2052–4463. DOI: 10.1038/s41597-020-0453-3.

Hartmann, D., Klein Tank, A., Rusticucci, M., Alexander, L., Brönnimann, S., Charabi, Y., Dentener, F., Dlugokencky, E., Easterling, D., Kaplan, A., Soden, B., Thorne, P., Wild, M., and Zhai, P. (2013). "Observations: Atmosphere and Surface". In: *Climate Change 2013: The Physical Science Basis. Contribution of Working Group I to the Fifth Assessment Report of the Intergovernmental Panel on Climate Change*. Ed. by T. Stocker, D. Qin, G.-K. Plattner, M. Tignor, S. Allen, J. Boschung, A. Nauels, Y. Xia, V. Bex, and P. Midgley. Cambridge, United Kingdom and New York, NY, USA: Cambridge University Press. Chap. 2, pp. 159–254. DOI: 10.1017/CBO9781107415324.008.

Hauser, M., Orth, R., and Seneviratne, S. I. (2016). Role of soil moisture versus recent climate change for the 2010 heat wave in western Russia. *Geophysical Research Letters* **43**(6), 2819–2826. DOI: 10.1002/2016GL068036.

Henderson-Sellers, A., Pitman, A. J., Love, P. K., Irannejad, P., and Chen, T. H. (1995). The Project for Intercomparison of Land Surface Parameterization Schemes (PILPS): Phases 2 and 3. *Bulletin of the American Meteorological Society* **76**(4), 489–503. DOI: 10.1175/1520-0477(1995)076<0489:TPFIOL>2.0.CO;2.

Henderson-Sellers, A., McGuffie, K., and Pitman, J. A. (1996). The Project for Intercomparison of Land-surface Parametrization Schemes (PILPS): 1992 to 1995. *Climate Dynamics* **12**(12), 849–859. DOI: 10.1007/s003820050147.

Herold, N, Kala, J, and Alexander, L. V. (2016). The influence of soil moisture deficits on Australian heatwaves. *Environmental Research Letters* **11**(6), 064003.

Hersbach, H., Rosnay, P. de, Bell, B., Schepers, D., Simmons, A., Soci, C., Abdalla, S., Alonso-Balmaseda, M., Balsamo, G., Bechtold, P., Berrisford, P., Bidlot, J.-R., Boisséson, E. de, Bonavita, M., Browne, P., Buizza, R., Dahlgren, P., Dee, D., Dragani, R., Diamantakis, M., Flemming, J., Forbes, R., Geer, A. J., Haiden, T., Hólm, E., Haimberger, L., Hogan, R., Horányi, A., Janiskova, M., Laloyaux, P., Lopez, P., Munoz-Sabater, J., Peubey, C., Radu, R., Richardson, D., Thépaut, J.-N., Vitart, F., Yang, X, Zsótér, E., and Zuo, H. (2018). *Operational global reanalysis: progress, future directions and synergies with NWP*. Tech. rep. 27. European Centre for Medium Range Weather Forecasts. DOI: 10.21957/tkic6g3wm.

Hicks Pries, C. E., Castanha, C., Porras, R. C., and Torn, M. S. (2017). The whole-soil carbon flux in response to warming. *Science* **355**(6332), 1420–1423.

Hirsch, A. L., Pitman, A. J., Seneviratne, S. I., Evans, J. P., and Haverd, V. (2014a). Summertime maximum and minimum temperature coupling asymmetry over Australia determined using WRF. *Geophysical Research Letters* **41**(5), 1546–1552. DOI: 10.1002/2013GL059055.

Hirsch, A. L., Pitman, A. J., and Kala, J. (2014b). The role of land cover change in modulating the soil moisture-temperature land-atmosphere coupling strength over Australia. *Geophysical Research Letters* **41**(16), 5883–5890. DOI: 10.1002/2014GL061179.

Hirschi, M., Mueller, B., Dorigo, W., and Seneviratne, S. (2014). Using remotely sensed soil moisture for land–atmosphere coupling diagnostics: The role of surface vs. root-zone soil moisture variability. *Remote Sensing of Environment* **154**, 246–252. DOI: https://doi.org/10.1016/j.rse.2014.08.030.

Hirschi, M., Seneviratne, S. I., Alexandrov, V., Boberg, F., Boroneant, C., Christensen, O. B., Formayer, H., Orlowsky, B., and Stepanek, P. (2011). Observational

evidence for soil-moisture impact on hot extremes in southeastern Europe. *Nature Geosci* **4**(1), 17–21.

Hobbins, M. T., Ramírez, J. A., Brown, T. C., and Claessens, L. H.J. M. (2001). The complementary relationship in estimation of regional evapotranspiration: The complementary relationship areal evapotranspiration and advection-aridity models. *Water Resources Research* **37**(5), 1367–1387. DOI: 10.1029/2000WR900358.

Hohenegger, C., Brockhaus, P., Bretherton, C. S., and Schär, C. (2009). The Soil Moisture–Precipitation Feedback in Simulations with Explicit and Parameterized Convection. *Journal of Climate* **22**(19), 5003–5020. DOI: 10.1175/2009JCLI2604.1.

Hong, S.-Y., Noh, Y., and Dudhia, J. (2006a). A New Vertical Diffusion Package with an Explicit Treatment of Entrainment Processes. *Monthly Weather Review* **134**(9), 2318–2341. DOI: 10.1175/MWR3199.1.

Hong, S.-Y. and Lim, J.-O. J. (2006b). The WRF single-moment 6-class microphysics scheme (WSM6). *J. Korean Meteor. Soc* **42**(2), 129–151.

Hourdin, F., Foujols, M., Codron, F., Guemas, V., Dufresne, J.-L., Bony, S., Denvil, S., Guez, L., Lott, F., and Ghattas, J (2012). Climate and sensitivity of the IPSL-CM5A coupled model: impact of the LMDZ atmospheric grid configuration. *Clim. Dynam.* **10**.

Hu, P., Zhang, Q., Shi, P., Chen, B., and Fang, J. (2018a). Flood-induced mortality across the globe: Spatiotemporal pattern and influencing factors. *Science of The Total Environment* **643**, 171 –182. DOI: https://doi.org/10.1016/j.scitotenv.2018.06.197.

Hu, Q., Torres-Alavez, J. A., and Broeke, M. S.V. D. (2018b). Land-Cover Change and the "Dust Bowl" Drought in the U.S. Great Plains. *Journal of Climate* **31**(12), 4657–4667. DOI: https://doi.org/10.1175/JCLI-D-17-0515.1.

Hurk, B. van den, Kim, H., Krinner, G., Seneviratne, S. I., Derksen, C., Oki, T., Douville, H., Colin, J., Ducharne, A., Cheruy, F., Viovy, N., Puma, M. J., Wada, Y., Li, W., Jia, B., Alessandri, A., Lawrence, D. M., Weedon, G. P., Ellis, R., Hagemann, S., Mao, J., Flanner, M. G., Zampieri, M., Materia, S., Law, R. M., and Sheffield, J. (2016). LS3MIP (v1.0) contribution to CMIP6: the Land Surface, Snow and Soil moisture Model Intercomparison Project – aims, setup and expected outcome. *Geoscientific Model Development* **9**(8), 2809–2832. DOI: 10.5194/gmd-9-2809-2016.

Hurtt, G. C., Chini, L. P., Frolking, S., Betts, R. A., Feddema, J., Fischer, G., Fisk, J. P., Hibbard, K., Houghton, R. A., Janetos, A., Jones, C. D., Kindermann, G., Kinoshita, T., Klein Goldewijk, K., Riahi, K., Shevliakova, E., Smith, S., Stehfest, E., Thomson, A., Thornton, P., Vuuren, D. P. van, and Wang, Y. P. (2011). Har-

monization of land-use scenarios for the period 1500–2100: 600 years of global gridded annual land-use transitions, wood harvest, and resulting secondary lands. *Climatic Change* **109**(1-2), 117–161. DOI: 10.1007/s10584-011-0153-2.

Iles, C. E., Vautard, R., Strachan, J., Joussaume, S., Eggen, B. R., and Hewitt, C. D. (2019). The benefits of increasing resolution in global and regional climate simulations for European climate extremes. *Geosci. Model Dev. Discuss.* **2019**, 1–39. DOI: 10.5194/gmd-2019-253.

IPCC (2013g). *Climate Change 2013: The Physical Science Basis. Contribution of Working Group I to the Fifth Assessment Report of the Intergovernmental Panel on Climate Change*. Cambridge, United Kingdom and New York, NY, USA: Cambridge University Press, p. 1535. DOI: 10.1017/CBO9781107415324.

Jaeger, E. B. and Seneviratne, S. I. (2011). Impact of soil moisture–atmosphere coupling on European climate extremes and trends in a regional climate model. *Climate Dynamics* **36**(9, 1432-0894), 1919–1939.

Jeong, D. I., Sushama, L., and Naveed Khaliq, M. (2014). The role of temperature in drought projections over North America. *Climatic Change* **127**(2), 289–303. DOI: 10.1007/s10584-014-1248-3.

Jeong, D. I., Sushama, L., Diro, G. T., Khaliq, M. N., Beltrami, H., and Caya, D. (2016). Projected changes to high temperature events for Canada based on a regional climate model ensemble. *Climate Dynamics* **46**(9), 3163–3180.

Jiménez, P. A., Dudhia, J., González-Rouco, J. F., Navarro, J., Montávez, J. P., and García-Bustamante, E. (2012). A Revised Scheme for the WRF Surface Layer Formulation. *Monthly Weather Review* **140**(3), 898–918.

Jin, J., Miller, N. L., and Schlegel, N. (2010). Sensitivity Study of Four Land Surface Schemes in the WRF Model. *Advances in Meteorology*(167436), 11. DOI: https://doi.org/10.1155/2010/167436.

Karl, T. R., Nicholls, N., and Ghazi, A. (1999). "CLIVAR/GCOS/WMO Workshop on Indices and Indicators for Climate Extremes Workshop Summary". In: *Weather and Climate Extremes: Changes, Variations and a Perspective from the Insurance Industry*. Ed. by T. R. Karl, N. Nicholls, and A. Ghazi. Dordrecht: Springer Netherlands, pp. 3–7.

Katragkou, E., García-Díez, M., Vautard, R., Sobolowski, S., Zanis, P., Alexandri, G., Cardoso, R. M., Colette, A., Fernandez, J., Gobiet, A., Goergen, K., Karacostas, T., Knist, S., Mayer, S., Soares, P. M. M., Pytharoulis, I., Tegoulias, I., Tsikerdekis, A., and Jacob, D. (2015). Regional climate hindcast simulations within EURO-CORDEX: evaluation of a WRF multi-physics ensemble. *Geoscientific Model Development* **8**(3), 603–618. DOI: 10.5194/gmd-8-603-2015.

Kharin, V. V., Zwiers, F. W., Zhang, X., and Hegerl, G. C. (2007). Changes in Temperature and Precipitation Extremes in the IPCC Ensemble of Global Coupled Model Simulations. *Journal of Climate* **20**(8), 1419–1444.

Kirkevåg, A., Iversen, T., Seland, Ø., Hoose, C., Kristjánsson, J. E., Struthers, H., Ekman, A. M. L., Ghan, S., Griesfeller, J., Nilsson, E. D., and Schulz, M. (2013). Aerosol–climate interactions in the Norwegian Earth System Model –NorESM1-M. *Geosci. Model Dev.* **6**(1), 207–244. DOI: 10.5194/gmd-6-207-2013.

Knist, S., Goergen, K., Buonomo, E., Christensen, O. B., Colette, A., Cardoso, R. M., Fealy, R., Fernández, J., García-Díez, M., Jacob, D., Kartsios, S., Katragkou, E., Keuler, K., Mayer, S., Meijgaard, E. van, Nikulin, G., Soares, P. M. M., Sobolowski, S., Szepszo, G., Teichmann, C., Vautard, R., Warrach-Sagi, K., Wulfmeyer, V., and Simmer, C. (2016). Land-atmosphere coupling in EURO-CORDEX evaluation experiments. *Journal of Geophysical Research: Atmospheres*. DOI: 10.1002/2016JD025476.

Knutti, R., Masson, D., and Gettelman, A. (2013). Climate model genealogy: Generation CMIP5 and how we got there. *Geophysical Research Letters* **40**(6), 1194–1199. DOI: 10.1002/grl.50256.

Koster, R. D. and Suarez, M. J. (1995). Relative contributions of land and ocean processes to precipitation variability. *Journal of Geophysical Research: Atmospheres* **100**(D7), 13775–13790. DOI: 10.1029/95JD00176.

Koster, R. D., Dirmeyer, P. A., Hahmann, A. N., Ijpelaar, R., Tyahla, L., Cox, P., and Suarez, M. J. (2002). Comparing the Degree of Land–Atmosphere Interaction in Four Atmospheric General Circulation Models. *Journal of Hydrometeorology* **3**(3), 363–375. DOI: 10.1175/1525-7541(2002)003<0363:CTDOLA>2.0.CO;2.

Koster, R. D., Suarez, M. J., Higgins, R. W., and Dool, H. M. Van den (2003). Observational evidence that soil moisture variations affect precipitation. *Geophysical Research Letters* **30**(5), 1241. DOI: 10.1029/2002GL016571.

Koster, R. D., Dirmeyer, P. A., Guo, Z., Bonan, G., Chan, E., Cox, P., Gordon, C. T., Kanae, S., Kowalczyk, E., Lawrence, D., Liu, P., Lu, C.-H., Malyshev, S., McAvaney, B., Mitchell, K., Mocko, D., Oki, T., Oleson, K., Pitman, A., Sud, Y. C., Taylor, C. M., Verseghy, D., Vasic, R., Xue, Y., and Yamada, T. (2004a). Regions of Strong Coupling Between Soil Moisture and Precipitation. *Science* **305**(5687), 1138–1140. DOI: 10.1126/science.1100217.

— (2004b). Regions of Strong Coupling Between Soil Moisture and Precipitation. *Science* **305**(5687), 1138–1140. DOI: 10.1126/science.1100217.

Koster, R. D., Suarez, M. J., and Schubert, S. D. (2006a). Distinct Hydrological Signatures in Observed Historical Temperature Fields. *Journal of Hydrometeorology* **7**(5), 1061–1075. DOI: 10.1175/JHM530.1.

Koster, R. D., Sud, Y. C., Guo, Z., Dirmeyer, P. A., Bonan, G., Oleson, K. W., Chan, E., Verseghy, D., Cox, P., Davies, H., Kowalczyk, E., Gordon, C. T., Kanae, S., Lawrence, D., Liu, P., Mocko, D., Lu, C.-H., Mitchell, K., Malyshev, S., McAvaney, B., Oki, T., Yamada, T., Pitman, A., Taylor, C. M., Vasic, R., and Xue, Y. (2006b). GLACE: The Global Land–Atmosphere Coupling Experiment. Part I: Overview. *Journal of Hydrometeorology* **7**(4), 590–610. DOI: 10.1175/JHM510.1.

Koven, C. D., Riley, W. J., and Stern, A. (2013). Analysis of Permafrost Thermal Dynamics and Response to Climate Change in the CMIP5 Earth System Models. *Journal of Climate* **26**(6), 1877–1900. DOI: 10.1175/JCLI-D-12-00228.1.

Krinner, G., Viovy, N., Noblet-Ducoudré, N. de, Ogée, J., Polcher, J., Friedlingstein, P., Ciais, P., Sitch, S., and Prentice, I. C. (2005). A dynamic global vegetation model for studies of the coupled atmosphere-biosphere system. *Global Biogeochemical Cycles* **19**(1).

Kumar, S. and Merwade, V. (2011). Evaluation of NARR and CLM3.5 outputs for surface water and energy budgets in the Mississippi River Basin. *Journal of Geophysical Research: Atmospheres* **116**(D8).

Laguë, M. M., Bonan, G. B., and Swann, A. L. S. (2019). Separating the impact of individual land surface properties on the terrestrial surface energy budget in both the coupled and un-coupled land-atmosphere system. *Journal of Climate* **32**(18), 5725–5744.

Lamarque, J., Emmons, L., Hess, P., Kinnison, D. E., Tilmes, S, Vitt, F., Heald, C., Holland, E. A., Lauritzen, P., and Neu, J (2012). CAM-chem: Description and evaluation of interactive atmospheric chemistry in the Community Earth System Model. *Geosci. Model Dev* **5**(2), 369–411.

Lawrence, D. M., Thornton, P. E., Oleson, K. W., and Bonan, G. B. (2007). The Partitioning of Evapotranspiration into Transpiration, Soil Evaporation, and Canopy Evaporation in a GCM: Impacts on Land–Atmosphere Interaction. *Journal of Hydrometeorology* **8**(4), 862–880. DOI: 10.1175/JHM596.1.

Lejeune, Q., Davin, E. L., Guillod, B. P., and Seneviratne, S. I. (2015). Influence of Amazonian deforestation on the future evolution of regional surface fluxes, circulation, surface temperature and precipitation. *Climate Dynamics* **44**(9), 2769–2786. DOI: 10.1007/s00382-014-2203-8.

Lejeune, Q., Seneviratne, S. I., and Davin, E. L. (2017). Historical Land-Cover Change Impacts on Climate: Comparative Assessment of LUCID and CMIP5 Multimodel Experiments. *Journal of Climate* **30**(4), 1439–1459. DOI: 10.1175/JCLI-D-16-0213.1.

Li, M., Ma, Z., Gu, H., Yang, Q., and Zheng, Z. (2017). Production of a combined land surface data set and its use to assess land-atmosphere coupling in China. *Journal of Geophysical Research: Atmospheres* **122**(2), 948–965.

Li, Y., Zhao, M., Mildrexler, D. J., Motesharrei, S., Mu, Q., Kalnay, E., Zhao, F., Li, S., and Wang, K. (2016). Potential and Actual impacts of deforestation and afforestation on land surface temperature. *Journal of Geophysical Research: Atmospheres* **121**(24). 2016JD024969, 14,372–14,386. DOI: 10.1002/2016JD024969.

Lin, X., Smerdon, J. E., England, A. W., and Pollack, H. N. (2003). A model study of the effects of climatic precipitation changes on ground temperatures. *Journal of Geophysical Research: Atmospheres* **108**(D7), 2156–2202. DOI: 10.1029/2002JD002878.

Liu, C., Ikeda, K., Rasmussen, R., Barlage, M., Newman, A. J., Prein, A. F., Chen, F., Chen, L., Clark, M., Dai, A., Dudhia, J., Eidhammer, T., Gochis, D., Gutmann, E., Kurkute, S., Li, Y., Thompson, G., and Yates, D. (2017). Continental-scale convection-permitting modeling of the current and future climate of North America. *Climate Dynamics* **49**(1), 71–95.

Liu, L., Ma, Y., Menenti, M., Zhang, X., and Ma, W. (2019). Evaluation of WRF Modeling in Relation to Different Land Surface Schemes and Initial and Boundary Conditions: A Snow Event Simulation Over the Tibetan Plateau. *Journal of Geophysical Research: Atmospheres* **124**(1), 209–226. DOI: 10.1029/2018JD029208.

Lorenz, R. and Pitman, A. J. (2014). Effect of land-atmosphere coupling strength on impacts from Amazonian deforestation. *Geophysical Research Letters* **41**(16). 2014GL061017, 5987–5995. DOI: 10.1002/2014GL061017.

Lorenz, R., Pitman, A. J., Hirsch, A. L., and Srbinovsky, J. (2015). Intraseasonal versus Interannual Measures of Land–Atmosphere Coupling Strength in a Global Climate Model: GLACE-1 versus GLACE-CMIP5 Experiments in ACCESS1.3b. *Journal of Hydrometeorology* **16**(5), 2276–2295. DOI: 10.1175/JHM-D-14-0206.1.

Lorenz, R., Argüeso, D., Donat, M. G., Pitman, A. J., Hurk, B. van den, Berg, A., Lawrence, D. M., Chéruy, F., Ducharne, A., Hagemann, S., Meier, A., Milly, P. C. D., and Seneviratne, S. I. (2016). Influence of land-atmosphere feedbacks on temperature and precipitation extremes in the GLACE-CMIP5 ensemble. *Journal of Geophysical Research: Atmospheres* **121**(2), 607–623. DOI: 10.1002/2015JD024053.

Lucas-Picher, P., Laprise, R., and Winger, K. (2017). Evidence of added value in North American regional climate model hindcast simulations using ever-increasing horizontal resolutions. *Climate Dynamics* **48**(7), 2611–2633.

Lytle, W. and Zeng, X. (2016). Coupled Evaluation of Below- and Aboveground Energy and Water Cycle Variables from Reanalysis Products over Five Flux Tower

Sites in the United States. *Journal of Hydrometeorology* **17**(7), 2105–2119. DOI: 10.1175/JHM-D-15-0224.1.

Mahowald, N., Lo, F., Zheng, Y., Harrison, L., Funk, C., Lombardozzi, D., and Goodale, C. (2016). Projections of leaf area index in earth system models. *Earth System Dynamics* **7**(1), 211–229. DOI: 10.5194/esd-7-211-2016.

Mao, J., Fu, W., Shi, X., Ricciuto, D. M., Fisher, J. B., Dickinson, R. E., Wei, Y., Shem, W., Piao, S., Wang, K., Schwalm, C. R., Tian, H., Mu, M., Arain, A., Ciais, P., Cook, R., Dai, Y., Hayes, D., Hoffman, F. M., Huang, M., Huang, S., Huntzinger, D. N., Ito, A., Jain, A., King, A. W., Lei, H., Lu, C., Michalak, A. M., Parazoo, N., Peng, C., Peng, S., Poulter, B., Schaefer, K., Jafarov, E., Thornton, P. E., Wang, W., Zeng, N., Zeng, Z., Zhao, F., Zhu, Q., and Zhu, Z. (2015). Disentangling climatic and anthropogenic controls on global terrestrial evapotranspiration trends. *Environmental Research Letters* **10**(9), 094008.

Marsh, D. R., Mills, M. J., Kinnison, D. E., Lamarque, J.-F., Calvo, N., and Polvani, L. M. (2013). Climate Change from 1850 to 2005 Simulated in CESM1(WACCM). *Journal of Climate* **26**(19), 7372–7391.

Martynov, A., Laprise, R., Sushama, L., Winger, K., Šeparović, L., and Dugas, B. (2013b). Reanalysis-driven climate simulation over CORDEX North America domain using the Canadian Regional Climate Model, version 5: model performance evaluation. *Climate Dynamics* **41**(11), 2973–3005.

Mearns, L. et al. (2017). *The NA-CORDEX dataset, version 1.0. NCAR Climate Data Gateway, Boulder CO.* https://doi.org/10.5065/D6SJ1JCH accessed [December, 2018].

Mei, R. and Wang, G. (2012). Summer Land–Atmosphere Coupling Strength in the United States: Comparison among Observations, Reanalysis Data, and Numerical Models. *Journal of Hydrometeorology* **13**(3), 1010–1022. DOI: 10.1175/JHM-D-11-075.1.

Melo-Aguilar, C., González-Rouco, J. F., García-Bustamante, E., Navarro-Montesinos, J., and Steinert, N. (2018). Influence of radiative forcing factors on ground–air temperature coupling during the last millennium: implications for borehole climatology. *Climate of the Past* **14**(11), 1583–1606. DOI: 10.5194/cp-14-1583-2018.

Meng, X. H., Evans, J. P., and McCabe, M. F. (2014). The Impact of Observed Vegetation Changes on Land–Atmosphere Feedbacks During Drought. *Journal of Hydrometeorology* **15**(2), 759–776. DOI: 10.1175/JHM-D-13-0130.1.

Mesinger, F., DiMego, G., Kalnay, E., Mitchell, K., Shafran, P. C., Ebisuzaki, W., Jovic, D., Woollen, J., Rogers, E., Berbery, E. H., et al. (2006). North American regional reanalysis. *Bulletin of the American Meteorological Society* **87**(3), 343–360. DOI: https://doi.org/10.1175/BAMS-87-3-343.

Messmer, M., Gómez-Navarro, J. J., and Raible, C. C. (2017). Sensitivity experiments on the response of Vb cyclones to sea surface temperature and soil moisture changes. *Earth System Dynamics* **8**(3), 477–493. DOI: 10.5194/esd-8-477-2017.

Michalakes, J, Chen, S, Dudhia, J, Hart, L, Klemp, J, Middlecoff, J, and Skamarock, W (2001). *Development of a next generation regional weather research and forecast model*. Vol. 1. World Scientific, pp. 269–276.

Mieville, A., Granier, C., Liousse, C., Guillaume, B., Mouillot, F., Lamarque, J. F., Grégoire, J. M., and Pétron, G. (2010). Emissions of gases and particles from biomass burning during the 20th century using satellite data and an historical reconstruction. *Atmospheric Environment* **44**(11), 1469–1477. DOI: http://dx.doi.org/10.1016/j.atmosenv.2010.01.011.

Miralles, D. G., Berg, M. J. den, Teuling, A. J., and Jeu, R. A. M. (2012). Soil moisture-temperature coupling: A multiscale observational analysis. *Geophysical Research Letters* **39**(21).

Mitchell, K. (2005). The community Noah land-surface model (LSM). *User's Guide* **7**.

Mitchell, K. E., Lohmann, D., Houser, P. R., Wood, E. F., Schaake, J. C., Robock, A., Cosgrove, B. A., Sheffield, J., Duan, Q., Luo, L., Higgins, R. W., Pinker, R. T., Tarpley, J. D., Lettenmaier, D. P., Marshall, C. H., Entin, J. K., Pan, M., Shi, W., Koren, V., Meng, J., Ramsay, B. H., and Bailey, A. A. (2004). The multi-institution North American Land Data Assimilation System (NLDAS): Utilizing multiple GCIP products and partners in a continental distributed hydrological modeling system. *Journal of Geophysical Research: Atmospheres* **109**(D7), 2156–2202. DOI: 10.1029/2003JD003823.

Molod, A., Takacs, L., Suarez, M., and Bacmeister, J. (2015). Development of the GEOS-5 atmospheric general circulation model: evolution from MERRA to MERRA2. *Geosci. Model Dev.* **8**(5), 1339–1356. DOI: 10.5194/gmd-8-1339-2015.

Mooney, P. A., Mulligan, F. J., and Fealy, R. (2013). Evaluation of the Sensitivity of the Weather Research and Forecasting Model to Parameterization Schemes for Regional Climates of Europe over the Period 1990–95. *Journal of Climate* **26**(3), 1002–1017. DOI: 10.1175/JCLI-D-11-00676.1.

Mueller, B. and Seneviratne, S. I. (2014). Systematic land climate and evapotranspiration biases in CMIP5 simulations. *Geophysical Research Letters* **41**(1), 128–134. DOI: 10.1002/2013GL058055.

Mueller, B. and Seneviratne, S. I. (2012). Hot days induced by precipitation deficits at the global scale. *Proceedings of the National Academy of Sciences* **109**(31), 12398–12403.

Neale, R. B., Chen, C.-C., Gettelman, A., Lauritzen, P. H., Park, S., Williamson, D. L., Conley, A. J., Garcia, R., Kinnison, D., and Lamarque, J.-F. (2010a). Description of the NCAR community atmosphere model (CAM 4.0). *NCAR Tech. Note*.

— (2010b). Description of the NCAR community atmosphere model (CAM 5.0). *NCAR Tech. Note*.

Niu, G.-Y., Yang, Z.-L., Mitchell, K. E., Chen, F., Ek, M. B., Barlage, M., Kumar, A., Manning, K., Niyogi, D., Rosero, E., Tewari, M., and Xia, Y. (2011). The community Noah land surface model with multiparameterization options (Noah-MP): 1. Model description and evaluation with local-scale measurements. *Journal of Geophysical Research: Atmospheres* **116**(D12), 2156–2202. DOI: 10.1029/2010JD015139.

Numaguti, A, Takahashi, M, Nakajima, T, and Sumi, A (1997). Description of CCSR/NIES atmospheric general circulation model. CGER's supercomputer monograph report. *Center for Global Environmental Research, National Institute for Environmental Studies* **3**, 1–48.

Oleson, K. W., Lawrence, D. M., Bonan, G. B., Flanner, M. G., Kluzek, E., Lawrence, P. J., Levis, S., Swenson, S. C., Thornton, P. E., Dai, A., Decker, M., Dickinson, R., Feddema, J., Heald, C. L., Hoffman, F., Lamarque, J.-F., Mahowald, N., Niu, G.-Y., Qian, T., Randerson, J., Running, S., Sakaguchi, K., Slater, A., Stockli, R., Wang, A., Yang, Z.-L., Zeng, X., and Zeng., X. (2010). *Technical description of version 4.0 of the Community Land Model (CLM)*. Tech. rep. NCAR, Boulder.

Onogi, K., Tsutsui, J., Koide, H., Sakamoto, M., Kobayashi, S., Hatsushika, H., Matsumoto, T., Yamazaki, N., Kamahori, H., and Takahashi, K. (2007). The JRA-25 reanalysis. *Journal of the Meteorological Society of Japan. Ser. II* **85**(3), 369–432.

Orlowsky, B. and Seneviratne, S. I. (2010). Statistical Analyses of Land–Atmosphere Feedbacks and Their Possible Pitfalls. *Journal of Climate* **23**(14), 3918–3932. DOI: 10.1175/2010JCLI3366.1.

— (2012). Global changes in extreme events: regional and seasonal dimension. *Climatic Change* **110**(3), 669–696.

Pattanaik, D., Mohapatra, M, Srivastava, A., and Kumar, A. (2017). Heat wave over India during summer 2015: an assessment of real time extended range forecast. *Meteorology and Atmospheric Physics* **129**(4), 375–393. DOI: https://doi.org/10.1007/s00703-016-0469-6.

Pei, L., Moore, N., Zhong, S., Luo, L., Hyndman, D. W., Heilman, W. E., and Gao, Z. (2014). WRF Model Sensitivity to Land Surface Model and Cumulus Parameterization under Short-Term Climate Extremes over the Southern Great Plains of the United States. *Journal of Climate* **27**(20), 7703–7724.

Philip, S. Y., Kew, S. F., Hauser, M., Guillod, B. P., Teuling, A. J., Whan, K., Uhe, P., and Oldenborgh, G. J. v. (2018). Western US high June 2015 temperatures and their relation to global warming and soil moisture. *Climate Dynamics* **50**(7), 2587–2601.

Phillips, T. J. and Klein, S. A. (2014). Land-atmosphere coupling manifested in warm-season observations on the U.S. southern great plains. *Journal of Geophysical Research: Atmospheres* **119**(2). 2013JD020492, 509–528. DOI: 10.1002/2013JD020492.

Pieri, A. B., Hardenberg, J. von, Parodi, A., and Provenzale, A. (2015). Sensitivity of Precipitation Statistics to Resolution, Microphysics, and Convective Parameterization: A Case Study with the High-Resolution WRF Climate Model over Europe. *Journal of Hydrometeorology* **16**(4), 1857–1872. DOI: 10.1175/JHM-D-14-0221.1.

Pollack, H. N., Smerdon, J. E., and Keken, P. E. van (2005). Variable seasonal coupling between air and ground temperatures: A simple representation in terms of subsurface thermal diffusivity. *Geophysical Research Letters* **32**(15), 1944–8007. DOI: 10.1029/2005GL023869.

Pope, D. V., Gallani, L. M., Rowntree, R. P., and Stratton, A. R. (2000). The impact of new physical parametrizations in the Hadley Centre climate model: HadAM3. *Climate Dynamics* **16**(2/ 1432-0894), 123–146.

Prein, A. F., Gobiet, A., Suklitsch, M., Truhetz, H., Awan, N. K., Keuler, K., and Georgievski, G. (2013). Added value of convection permitting seasonal simulations. *Climate Dynamics* **41**(9), 2655–2677. DOI: 10.1007/s00382-013-1744-6.

Pu, B. and Dickinson, R. E. (2012). Examining vegetation feedbacks on global warming in the Community Earth System Model. *Journal of Geophysical Research: Atmospheres* **117**(D20). D20110, 2156–2202. DOI: 10.1029/2012JD017623.

Reichle, R. H., Koster, R. D., Lannoy, G. J.M. D., Forman, B. A., Liu, Q., Mahanama, S. P. P., and Touré, A. (2011). Assessment and Enhancement of MERRA Land Surface Hydrology Estimates. *Journal of Climate* **24**(24), 6322–6338.

Reick, C. H., Raddatz, T., Brovkin, V., and Gayler, V. (2013). Representation of natural and anthropogenic land cover change in MPI-ESM. *Journal of Advances in Modeling Earth Systems* **5**(3), 459–482. DOI: 10.1002/jame.20022.

Riahi, K., Rao, S., Krey, V., Cho, C., Chirkov, V., Fischer, G., Kindermann, G., Nakicenovic, N., and Rafaj, P. (2011). RCP 8.5—A scenario of comparatively high greenhouse gas emissions. *Climatic Change* **109**(1-2), 33–57. DOI: 10.1007/s10584-011-0149-y.

Robock, A., Schlosser, C., Vinnikov, K. Y., Speranskaya, N. A., Entin, J. K., and Qiu, S. (1998). Evaluation of the AMIP soil moisture simulations. *Global and*

Planetary Change **19**(1–4), 181 –208. DOI: http://dx.doi.org/10.1016/S0921-8181(98)00047-2.

Robock, A., Luo, L., Wood, E. F., Wen, F., Mitchell, K. E., Houser, P. R., Schaake, J. C., Lohmann, D., Cosgrove, B., Sheffield, J., Duan, Q., Higgins, R. W., Pinker, R. T., Tarpley, J. D., Basara, J. B., and Crawford, K. C. (2003). Evaluation of the North American Land Data Assimilation System over the southern Great Plains during the warm season. *Journal of Geophysical Research: Atmospheres* **108**(D22), 2156–2202. DOI: 10.1029/2002JD003245.

Rodell, M., Houser, P. R., Jambor, U., Gottschalck, J., Mitchell, K., Meng, C.-J., Arsenault, K., Cosgrove, B., Radakovich, J., Bosilovich, M., Entin, J. K., Walker, J. P., Lohmann, D., and Toll, D. (2004). The Global Land Data Assimilation System. *Bulletin of the American Meteorological Society* **85**(3), 381–394.

Roeckner, E., Bäuml, G., Bonaventura, L., Brokopf, R., Giorgetta, M. E. M., Hagemann, S., Kirchner, I., Kornblueh, L., Manzini, E., Rhodin, A., Schlese, U., Schulzweida, U., and Tompkins, A. (2003a). *Model description of the atmospheric general circulation model ECHAM5*. Tech. rep. Hamburg, Germany: Max-Planck-Institut für Meteorologie.

Rosenzweig, C. and Abramopoulos, F. (1997). Land-surface model development for the GISS GCM. *Journal of climate* **10**(8), 2040–2054.

Ruiz-Barradas, A. and Nigam, S. (2005). Warm Season Rainfall Variability over the U.S. Great Plains in Observations, NCEP and ERA-40 Reanalyses, and NCAR and NASA Atmospheric Model Simulations. *Journal of Climate* **18**(11), 1808–1830. DOI: 10.1175/JCLI3343.1.

Rummukainen, M. (2016). Added value in regional climate modeling. *Wiley Interdisciplinary Reviews: Climate Change* **7**(1), 145–159. DOI: 10.1002/wcc.378.

Salzen, K. von, Scinocca, J. F., McFarlane, N. A., Li, J., Cole, J. N. S., Plummer, D., Verseghy, D., Reader, M. C., Ma, X., Lazare, M., and Solheim, L. (2013). The Canadian Fourth Generation Atmospheric Global Climate Model (CanAM4). Part I: Representation of Physical Processes. *Atmosphere-Ocean* **51**(1), 104–125. DOI: 10.1080/07055900.2012.755610.

Samuelsson, P., Jones, C. G., Willén, U., Ullerstig, A., Gollivik, S., Hansson, U., Jansson, C., Kjellström, E., Nikulin, G., and Wyser, K. (2011). The Rossby Centre Regional Climate model RCA3: model description and performance. *Tellus A* **63**(1), 4–23.

Santanello-Jr., J. A., Friedl, M. A., and Ek, M. B. (2007). Convective Planetary Boundary Layer Interactions with the Land Surface at Diurnal Time Scales: Diagnostics and Feedbacks. *Journal of Hydrometeorology* **8**(5), 1082–1097. DOI: 10.1175/JHM614.1.

Santanello-Jr., J. A., Peters-Lidard, C. D., and Kumar, S. V. (2011). Diagnosing the Sensitivity of Local Land–Atmosphere Coupling via the Soil Moisture–Boundary Layer Interaction. *Journal of Hydrometeorology* **12**(5), 766–786. DOI: 10.1175/JHM-D-10-05014.1.

Santer, B. D., Taylor, K. E., Wigley, T. M. L., Penner, J. E., Jones, P. D., and Cubasch, U. (1995). Towards the detection and attribution of an anthropogenic effect on climate. *Climate Dynamics* **12**(2), 77–100. DOI: 10.1007/BF00223722.

Schlosser, C. A. and Milly, P. C. D. (2002). A Model-Based Investigation of Soil Moisture Predictability and Associated Climate Predictability. *Journal of Hydrometeorology* **3**(4), 483–501.

Schmidt, G. A., Ruedy, R., Hansen, J. E., Aleinov, I., Bell, N., Bauer, M., Bauer, S., Cairns, B., Canuto, V., Cheng, Y., Genio, A. D., Faluvegi, G., Friend, A. D., Hall, T. M., Hu, Y., Kelley, M., Kiang, N. Y., Koch, D., Lacis, A. A., Lerner, J., Lo, K. K., Miller, R. L., Nazarenko, L., Oinas, V., Perlwitz, J., Perlwitz, J., Rind, D., Romanou, A., Russell, G. L., Sato, M., Shindell, D. T., Stone, P. H., Sun, S., Tausnev, N., Thresher, D., and Yao, M.-S. (2006). Present-Day Atmospheric Simulations Using GISS ModelE: Comparison to In Situ, Satellite, and Reanalysis Data. *Journal of Climate* **19**(2), 153–192.

Schultz, M. G., Heil, A., Hoelzemann, J. J., Spessa, A., Thonicke, K., Goldammer, J. G., Held, A. C., Pereira, J. M. C., and Bolscher, M. van het (2008). Global wildland fire emissions from 1960 to 2000. *Global Biogeochemical Cycles* **22**(2), 1944–9224. DOI: 10.1029/2007GB003031.

Schulzweida, U., Kornblueh, L., and Quast, R. (2006). CDO User's Guide. *Climate Data Operators, Version 1. 9. 5* **1**(6). DOI: https://code.mpimet.mpg.de/projects/cdo/embedded/index.html(accessedOct.2019).

Schuur, E. A. G., Chadwick, O. A., and Matson, P. A. (2001). Carbon Cycling and Soil Carbon Storage in Mesic to Wet Hawaiian Montane Forests. *Ecology* **82**, 3182–3196. DOI: 10.1890/0012-9658(2001)082[3182:CCASCS]2.0.CO;2.

Seneviratne, S. I. and Stöckli, R. (2008). "The Role of Land-Atmosphere Interactions for Climate Variability in Europe". In: *Climate Variability and Extremes during the Past 100 Years*. Ed. by S. Brönnimann, J. Luterbacher, T. Ewen, H. F. Diaz, R. S. Stolarski, and U. Neu. Dordrecht: Springer Netherlands, pp. 179–193. DOI: 10.1007/978-1-4020-6766-2{_}12.

Seneviratne, S. I., Lüthi, D., Litschi, M., and Schär, C. (2006). Land–atmosphere coupling and climate change in Europe. *Nature* **443**(7108), 205–209.

Seneviratne, S. I., Corti, T., Davin, E. L., Hirschi, M., Jaeger, E. B., Lehner, I., Orlowsky, B., and Teuling, A. J. (2010). Investigating soil moisture–climate inter-

actions in a changing climate: A review. *Earth-Science Reviews* **99**(3–4), 125 –161. DOI: http://dx.doi.org/10.1016/j.earscirev.2010.02.004.

Seneviratne, S. I., Nicholls, N., Easterling, D., Goodess, C. M., Kanae, S., Kossin, J., Luo, Y., Marengo, J., McInnes, K., and Rahimi, M. (2012). "Changes in climate extremes and their impacts on the natural physical environment". In: *Managing the Risks of Extreme Events and Disasters to Advance Climate Change Adaptation*. Cambridge University Press, pp. 109–203.

Seneviratne, S. I., Wilhelm, M., Stanelle, T., Hurk, B. van den, Hagemann, S., Berg, A., Cheruy, F., Higgins, M. E., Meier, A., Brovkin, V., Claussen, M., Ducharne, A., Dufresne, J.-L., Findell, K. L., Ghattas, J., Lawrence, D. M., Malyshev, S., Rummukainen, M., and Smith, B. (2013). Impact of soil moisture-climate feedbacks on CMIP5 projections: First results from the GLACE-CMIP5 experiment. *Geophysical Research Letters* **40**(19), 5212–5217. DOI: 10.1002/grl.50956.

Sillmann, J., Kharin, V. V., Zhang, X., Zwiers, F. W., and Bronaugh, D. (2013a). Climate extremes indices in the CMIP5 multimodel ensemble: Part 1. Model evaluation in the present climate. *Journal of Geophysical Research: Atmospheres* **118**(4), 1716–1733.

Sillmann, J., Kharin, V. V., Zwiers, F. W., Zhang, X., and Bronaugh, D. (2013b). Climate extremes indices in the CMIP5 multimodel ensemble: Part 2. Future climate projections. *Journal of Geophysical Research: Atmospheres* **118**(6), 2473–2493. DOI: 10.1002/jgrd.50188.

Sippel, S., Zscheischler, J., Mahecha, M. D., Orth, R., Reichstein, M., Vogel, M., and Seneviratne, S. I. (2017). Refining multi-model projections of temperature extremes by evaluation against land–atmosphere coupling diagnostics. *Earth System Dynamics* **8**(2), 387–403. DOI: 10.5194/esd-8-387-2017.

Skamarock, W. C., Klemp, J. B., Dudhia, J., Gill, D. O., Barker, D. M., Wang, W., and Powers, J. G. (2008a). *A description of theadvanced research WRF version 3, Tech. Rep.* TN-475+STR. National Center for Atmospheric Research Boulder, Colorado,USA.

— (2008b). *A description of theadvanced research WRF version 3, Tech. Rep.* TN-475+STR. National Center for Atmospheric Research Boulder, Colorado,USA.

Skopp, J., Jawson, M. D., and Doran, J. W. (1990). Steady-State Aerobic Microbial Activity as a Function of Soil Water Content. *Soil Science Society of America Journal* **54**(6), 1619–1625. DOI: 10.2136/sssaj1990.03615995005400060018x.

Slater, A. G. and Lawrence, D. M. (2013). Diagnosing present and future permafrost from climate models. *Journal of Climate* **26**(15), 5608–5623.

Smerdon, J. E., Pollack, H. N., Cermak, V., Enz, J. W., Kresl, M., Safanda, J., and Wehmiller, J. F. (2004). Air-ground temperature coupling and subsurface propaga-

tion of annual temperature signals. *Journal of Geophysical Research: Atmospheres* **109**(D21), D21107. DOI: 10.1029/2004JD005056.

Smerdon, J. E., Pollack, H. N., Cermak, V., Enz, J. W., Kresl, M., Safanda, J., and Wehmiller, J. F. (2006a). Daily, seasonal, and annual relationships between air and subsurface temperatures. *Journal of Geophysical Research: Atmospheres* **111**(D7). D07101, 2156–2202. DOI: 10.1029/2004JD005578.

Sokratov, S. A. and Barry, R. G. (2002). Intraseasonal variation in the thermoinsulation effect of snow cover on soil temperatures and energy balance. *Journal of Geophysical Research: Atmospheres* **107**(D10), ACL 13–1–ACL 13–6. DOI: 10.1029/2001JD000489.

Solmon, F., Mallet, M., Elguindi, N., Giorgi, F., Zakey, A., and Konaré, A. (2008). Dust aerosol impact on regional precipitation over western Africa, mechanisms and sensitivity to absorption properties. *Geophysical Research Letters* **35**(24), 1944–8007. DOI: DOI:10.1029/2008GL035900.

Srinivasan, G, Robock, A., Entin, J. K., Luo, L., Vinnikov, K. Y., and Viterbo, P. (2000). Soil moisture simulations in revised AMIP models. *Journal of geophysical research* **105**(D21), 26,635–26,644.

Stark, J. M. and Firestone, M. K. (1995). Mechanisms for soil moisture effects on activity of nitrifying bacteria. *Applied and Environmental Microbiology* **61**(1), 218–221.

Stevens, B., Giorgetta, M., Esch, M., Mauritsen, T., Crueger, T., Rast, S., Salzmann, M., Schmidt, H., Bader, J., Block, K., Brokopf, R., Fast, I., Kinne, S., Kornblueh, L., Lohmann, U., Pincus, R., Reichler, T., and Roeckner, E. (2013). Atmospheric component of the MPI-M Earth System Model: ECHAM6. *Journal of Advances in Modeling Earth Systems* **5**(2), 146–172. DOI: 10.1002/jame.20015.

Stieglitz, M. and Smerdon, J. E. (2007). Characterizing land-atmosphere coupling and the implications for subsurface thermodynamics. *Journal of climate* **20**(1), 21–37. DOI: https://doi.org/10.1175/JCLI3982.1.

Sun, C. and Liang, X.-Z. (2020). Improving US extreme precipitation simulation: sensitivity to physics parameterizations. *Climate Dynamics*, 1432–0894. DOI: 10.1007/s00382-020-05267-6.

Sun, X., Xue, M., Brotzge, J., McPherson, R. A., Hu, X.-M., and Yang, X.-Q. (2016). An evaluation of dynamical downscaling of Central Plains summer precipitation using a WRF-based regional climate model at a convection-permitting 4 km resolution. *Journal of Geophysical Research: Atmospheres* **121**(23), 13,801–13,825. DOI: 10.1002/2016JD024796.

Takata, K., Emori, S., and Watanabe, T. (2003). Development of the minimal advanced treatments of surface interaction and runoff. *Global and Planetary Change* **38**(1), 209–222.

Taylor, K. E., Stouffer, R. J., and Meehl, G. A. (2012). An overview of CMIP5 and the experiment design. *Bulletin of the American Meteorological Society* **93**(4), 485–498.

Teuling, A. J., Hirschi, M., Ohmura, A., Wild, M., Reichstein, M., Ciais, P., Buchmann, N., Ammann, C., Montagnani, L., Richardson, A. D., Wohlfahrt, G., and Seneviratne, S. I. (2009). A regional perspective on trends in continental evaporation. *Geophysical Research Letters* **36**(2). L02404, 1944–8007. DOI: 10.1029/2008GL036584.

Tewari, M., Chen, F, Wang, W, Dudhia, J, LeMone, M., Mitchell, K, Ek, M, Gayno, G, Wegiel, J, and Cuenca, R. (2004). *Implementation and verification of the unified NOAH land surface model in the WRF model*. 20th conference on weather analysis and forecasting/16th conference on numerical weather prediction, pp. 11-15.

Thomas, J. A., Berg, A. A., and Merryfield, W. J. (2016). Influence of snow and soil moisture initialization on sub-seasonal predictability and forecast skill in boreal spring. *Climate Dynamics* **47**(1), 49–65. DOI: 10.1007/s00382-015-2821-9.

Thomson, A., Calvin, K., Smith, S., Kyle, G. P., Volke, A., Patel, P., Delgado-Arias, S., Bond-Lamberty, B., Wise, M., Clarke, L., and Edmonds, J. (2011). RCP4.5: a pathway for stabilization of radiative forcing by 2100. *Climatic Change* **109**(1-2), 77–94. DOI: 10.1007/s10584-011-0151-4.

Thornton, P., Thornton, M., Mayer, B., Wei, Y., Devarakonda, R., Vose, R., and Cook, R. (2016). Daymet: Daily Surface Weather Data on a 1-km Grid for North America, Version 3. *ORNL DAAC, Oak Ridge, Tennessee, USA*. DOI: https://doi.org/10.3334/ORNLDAAC/1328.

Todd-Brown, K. E. O., Randerson, J. T., Post, W. M., Hoffman, F. M., Tarnocai, C., Schuur, E. A. G., and Allison, S. D. (2013). Causes of variation in soil carbon simulations from CMIP5 Earth system models and comparison with observations. *Biogeosciences* **10**(3), 1717–1736. DOI: 10.5194/bg-10-1717-2013.

Trenberth, K. E., Fasullo, J. T., and Balmaseda, M. A. (2014). Earth's Energy Imbalance. *Journal of Climate* **27**(9), 3129–3144. DOI: 10.1175/JCLI-D-13-00294.1.

Van Den Broeke, M. S., Kalin, A., Alavez, J. A. T., Oglesby, R., and Hu, Q. (2018). A warm-season comparison of WRF coupled to the CLM4.0, Noah-MP, and Bucket hydrology land surface schemes over the central USA. *Theoretical and Applied Climatology* **134**(3), 801–816. DOI: 10.1007/s00704-017-2301-8.

Verseghy, D. L. (1991). CLASS A Canadian land surface scheme for GCMs, I. Soil Model. *International Journal of Climatology* **11**, 111–133.

Vertenstein, M., Craig, T., Middleton, A., Feddema, D., and Fischer, C. (2012). CESM1. 0.4 user's guide. *UCAR Doc.*

Vogel, M. M., Orth, R., Cheruy, F., Hagemann, S., Lorenz, R., Hurk, B. J.J. M., and Seneviratne, S. I. (2017). Regional amplification of projected changes in extreme temperatures strongly controlled by soil moisture-temperature feedbacks. *Geophysical Research Letters* **44**(3), 1511–1519. DOI: 10.1002/2016GL071235.

Volodin, E., Dianskii, N., and Gusev, A. (2010). Simulating present-day climate with the INMCM4.0 coupled model of the atmospheric and oceanic general circulations. *Atmos. Oceanic Phys.* **46**, 141–431.

Volosciuk, C., Maraun, D., Semenov, V. A., and Park, W. (2015). Extreme Precipitation in an Atmosphere General Circulation Model: Impact of Horizontal and Vertical Model Resolutions. *Journal of Climate* **28**(3), 1184–1205.

Vuuren, D. P. van, Edmonds, J., Kainuma, M., Riahi, K., Thomson, A., Hibbard, K., Hurtt, G. C., Kram, T., Krey, V., Lamarque, J.-F., Masui, T., Meinshausen, M., Nakicenovic, N., Smith, S. J., and Rose, S. K. (2011). The representative concentration pathways: an overview. *Climatic Change* **109**(1), 5. DOI: 10.1007/s10584-011-0148-z.

Wang, G., Huang, J., Guo, W., Zuo, J., Wang, J., Bi, J., Huang, Z., and Shi, J. (2010a). Observation analysis of land-atmosphere interactions over the Loess Plateau of northwest China. *Journal of Geophysical Research: Atmospheres* **115**(D7). D00K17, 2156–2202. DOI: 10.1029/2009JD013372.

Wang, J. and Kotamarthi, V. R. (2015). High-resolution dynamically downscaled projections of precipitation in the mid and late 21st century over North America. *Earth's Future* **3**(7), 268–288. DOI: 10.1002/2015EF000304.

Wang, K. and Dickinson, R. E. (2012a). A review of global terrestrial evapotranspiration: Observation, modeling, climatology, and climatic variability. *Reviews of Geophysics* **50**(2). RG2005, 1944–9208. DOI: 10.1029/2011RG000373.

— (2013b). Contribution of solar radiation to decadal temperature variability over land. *Proceedings of the National Academy of Sciences* **110**(37), 14877–14882. DOI: 10.1073/pnas.1311433110.

Wang, Y., Leung, L. R., McGREGOR, J. L., Lee, D.-K., Wang, W.-C., Ding, Y., and Kimura, F. (2004). Regional climate modeling: progress, challenges, and prospects. *Journal of the Meteorological Society of Japan. Ser. II* **82**(6), 1599–1628, 0026–1165.

Watanabe, S., Miura, H., Sekiguchi, M., Nagashima, T., Sudo, K., Emori, S., and Kawamiya, M. (2008). Development of an atmospheric general circulation model for integrated Earth system modeling on the Earth Simulator. *J. Earth Simulator* **9**, 27–35.

Wehner, M. F., Smith, R. L., Bala, G., and Duffy, P. (2010). The effect of horizontal resolution on simulation of very extreme US precipitation events in a global atmosphere model. *Climate Dynamics* **34**(2), 241–247.

Wei, J. and Dirmeyer, P. A. (2010). Toward understanding the large-scale land-atmosphere coupling in the models: Roles of different processes. *Geophysical Research Letters* **37**(19), 1944–8007. DOI: 10.1029/2010GL044769.

Welty, J. and Zeng, X. (2018). Does Soil Moisture Affect Warm Season Precipitation Over the Southern Great Plains? *Geophysical Research Letters* **45**(15), 7866–7873.

Werf, G. R. van der, Randerson, J. T., Giglio, L., Collatz, G. J., Kasibhatla, P. S., and Arellano Jr., A. F. (2006). Interannual variability in global biomass burning emissions from 1997 to 2004. *Atmospheric Chemistry and Physics* **6**(11), 3423–3441. DOI: 10.5194/acp-6-3423-2006.

Wessel, P., Smith, W. H. F., Scharroo, R., Luis, J., and Wobbe, F. (2013). Generic Mapping Tools: Improved Version Released. *Eos, Transactions American Geophysical Union* **94**(45), 409–410. DOI: 10.1002/2013EO450001.

Wild, M. and Liepert, B. (2010). The Earth radiation balance as driver of the global hydrological cycle. *Environmental Research Letters* **5**(2), 025203.

Wild, M., Folini, D., Hakuba, M. Z., Schär, C., Seneviratne, S. I., Kato, S., Rutan, D., Ammann, C., Wood, E. F., and König-Langlo, G. (2015). The energy balance over land and oceans: an assessment based on direct observations and CMIP5 climate models. *Climate Dynamics* **44**(11), 3393–3429. DOI: 10.1007/s00382-014-2430-z.

Wilhelm, M., Davin, E. L., and Seneviratne, S. I. (2015). Climate engineering of vegetated land for hot extremes mitigation: An Earth system model sensitivity study. *Journal of Geophysical Research: Atmospheres* **120**(7). 2014JD022293, 2612–2623. DOI: 10.1002/2014JD022293.

Wu, T., Yu, R., and Zhang, F. (2008). A Modified Dynamic Framework for the Atmospheric Spectral Model and Its Application. *Journal of the Atmospheric Sciences* **65**(7), 2235–2253.

Wu, T., Song, L., Li, W., Wang, Z., Zhang, H., et al. (2013). An Overview of BCC Climate System Model Development and Application for Climate Change Studies. *Journal of Meteorological Research* **28**.

Xia, Y., Ek, M., Sheffield, J., Livneh, B., Huang, M., Wei, H., Feng, S., Luo, L., Meng, J., and Wood, E. (2013). Validation of NOAH-simulated soil temperature in the North American land data assimilation system phase 2. *Journal of Applied Meteorology and Climatology* **52**(2), 455–471.

Xue, Y., Juang, H. M. H., Li, W. P., Prince, S., DeFries, R., Jiao, Y., and Vasic, R. (2004). Role of land surface processes in monsoon development: East Asia and West Africa. *Journal of Geophysical Research: Atmospheres* **109**(D3), 2156–2202. DOI: DOI:10.1029/2003JD003556.

Xue, Y., Janjic, Z., Dudhia, J., Vasic, R., and Sales, F. D. (2014). A review on regional dynamical downscaling in intraseasonal to seasonal simulation/prediction and major factors that affect downscaling ability. *Atmospheric Research* **147-148**, 68 –85. DOI: https://doi.org/10.1016/j.atmosres.2014.05.001.

Yang, Z.-L., Niu, G.-Y., Mitchell, K. E., Chen, F., Ek, M. B., Barlage, M., Longuevergne, L., Manning, K., Niyogi, D., Tewari, M., and Xia, Y. (2011). The community Noah land surface model with multiparameterization options (Noah-MP): 2. Evaluation over global river basins. *Journal of Geophysical Research: Atmospheres* **116**(D12).

Yukimoto, S., Adachi, Y., Hosaka, M., Sakami, T., Yoshimura, H., Hirabara, M., Tanaka, T., Shindo, E., Tsujino, H., Deushi, M., Mizuta, R., Yabu, S., Obata, A., Nakano, H., Koshiro, T., Ose, T., and Kitoh, A. (2012a). A New Global Climate Model of the Meteorological Research Institute: MRI-CGCM3 Model Description and Basic Performance. *Journal of the Meteorological Society of Japan. Ser. II* **90A**, 23–64.

Yukimoto, S., Adachi, Y., Hosaka, M., Sakami, T., Yoshimura, H., Hirabara, M., Tanaka, T. Y., Shindo, E., Tsujino, H., Deushi, M., et al. (2012b). A new global climate model of the Meorological Research Institute: MRI-CGCM3 model description and basic performance. *J.Meteor.Soc.Japan* **90**(A), 23–64.

Zeng, X., Barlage, M., Castro, C., and Fling, K. (2010). Comparison of Land–Precipitation Coupling Strength Using Observations and Models. *Journal of Hydrometeorology* **11**(4), 979–994.

Zhang, J., Wang, W.-C., and Wei, J. (2008a). Assessing land-atmosphere coupling using soil moisture from the Global Land Data Assimilation System and observational precipitation. *Journal of Geophysical Research: Atmospheres* **113**(D17). DOI: 10.1029/2008JD009807.

Zhang, J., Wang, W.-C., and Leung, L. R. (2008b). Contribution of land-atmosphere coupling to summer climate variability over the contiguous United States. *Journal of Geophysical Research: Atmospheres* **113**(D22). DOI: 10.1029/2008JD010136.

Zhang, T. (2005). Influence of the seasonal snow cover on the ground thermal regime: An overview. *Reviews of Geophysics* **43**(4). DOI: 10.1029/2004RG000157.

Zhou, C. and Wang, K. (2016a). Biological and Environmental Controls on Evaporative Fractions at AmeriFlux Sites. *Journal of Applied Meteorology and Climatology* **55**(1), 145–161. DOI: 10.1175/JAMC-D-15-0126.1.

Zhuo, L., Dai, Q., Han, D., Chen, N., and Zhao, B. (2019). Assessment of simulated soil moisture from WRF Noah, Noah-MP, and CLM land surface schemes for landslide hazard application. *Hydrology and Earth System Sciences* **23**(10), 4199–4218.

Zscheischler, J., Orth, R., and Seneviratne, S. I. (2015). A submonthly database for detecting changes in vegetation-atmosphere coupling. *Geophysical Research Letters* **42**(22). 2015GL066563, 9816–9824. DOI: 10.1002/2015GL066563.

Zscheischler, J., Westra, S., Hurk, B. J.J. M. van den, Seneviratne, S. I., Ward, P. J., Pitman, A., AghaKouchak, A., Bresch, D. N., Leonard, M., Wahl, T., and Zhang, X. (2018). Future climate risk from compound events. *Nature Climate Change* **8**(6), 469–477. DOI: 10.1038/s41558-018-0156-3.

Appendices

Appendix A

Supporting Information for Chapter 2

Table A.1: List of ensemble members for each experiment, and variables employed in this article.

GCM	Experiments			Variables			
	Historical	RCP4.5	RCP8.5	SNW	LAI	SM	PR
CCSM4	r1i1p1	r1i1p1	r1i1p1	✓	✓	✓	✓
CESM1-BGC	r1i1p1	r1i1p1	r1i1p1	✓	✓	✓	✓
CESM1-CAM5	r1i1p1	r1i1p1	r1i1p1	✓	✓	✓	✓
CESM1-FASTCHEM	r1i1p1	–	–	✓	✓	✓	✓
CESM1-WACCM	r1i1p1	r2i1p1	r2i1p1	✓	✓	✓	✓
NORESM1-M	r1i1p1	r1i1p1	r1i1p1	✓	✓	✓	✓
NORESM1-ME	r1i1p1	r1i1p1	r1i1p1	✓	✓	✓	✓
INM-CM4	r1i1p1	r1i1p1	r1i1p1	✓	✓	✓	✓
MIROC-ESM	r1i1p1	r1i1p1	r1i1p1	✓	✓	✓	✓
MIROC-ESM-CHEM	r1i1p1	r1i1p1	r1i1p1	✓	✓	✓	✓
MIROC5	r1i1p1	r1i1p1	r1i1p1	✓	✓	✓	✓
GFDL-CM3	r1i1p1	r1i1p1	r1i1p1	✓	✓	✓	✓
GFDL-ESM2G	r1i1p1	r1i1p1	r1i1p1	✓	✓	✓	✓
GFDL-ESM2M	r1i1p1	r1i1p1	r1i1p1	✓	✓	✓	✓
MRI-CGCM3	r1i1p1	r1i1p1	r1i1p1	✓	χ	✓	✓
MRI-ESM1	r1i1p1	–	r1i1p1	✓	✓	✓	✓
MPI-ESM-LR	r1i1p1	r1i1p1	r1i1p1	✓	✓	χ	✓
MPI-ESM-MR	r1i1p1	r1i1p1	r1i1p1	✓	✓	χ	✓
MPI-ESM-P	r1i1p1	–	–	✓	✓	χ	✓
CMCC-CM	r1i1p1	r1i1p1	r1i1p1	χ	χ	χ	✓
CMCC-CMS	r1i1p1	r1i1p1	r1i1p1	✓	χ	χ	✓
CANESM2	r1i1p1	r1i1p1	r1i1p1	✓	✓	✓	✓
IPSL-CM5A-LR	r1i1p1	r1i1p1	r1i1p1	χ	✓	✓	✓
IPSL-CM5A-MR	r1i1p1	r1i1p1	r1i1p1	χ	✓	✓	✓
IPSL-CM5B-LR	r1i1p1	r1i1p1	r1i1p1	χ	✓	✓	✓
GISS-E2-H	r1i1p1	r1i1p1	r1i1p1	✓	χ	✓	✓
GISS-E2-R	r1i1p1	r1i1p1	r1i1p1	✓	χ	✓	✓
BCC-CSM1.1	r1i1p1	r1i1p1	r1i1p1	✓	✓	✓	✓
BCC-CSM1.1-M	r1i1p1	r1i1p1	r1i1p1	✓	✓	✓	✓
HADCM3	r1i1p1	–	–	✓	χ	✓	✓
HADGEM2-CC	r1i1p1	r1i1p1	r1i1p1	✓	✓	✓	✓
HADGEM2-ES	r1i1p1	r1i1p1	r1i1p1	✓	✓	✓	✓

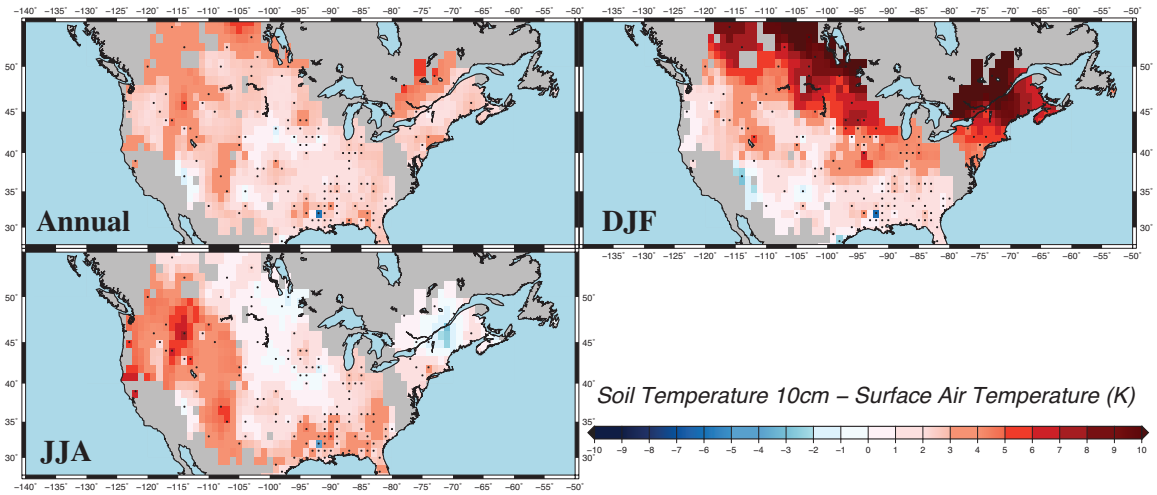

Figure A.1: Annual mean difference, DJF mean difference, and JJA mean difference between GST at 10 cm and SAT from 1979 to 2001 for the observations. Observational data are interpolated using the nearest neighbor algorithm of GMT with a search radius of 4°. Black dots show the locations of the data on a $1° \times 1°$ grid and grey color indicates missing data.

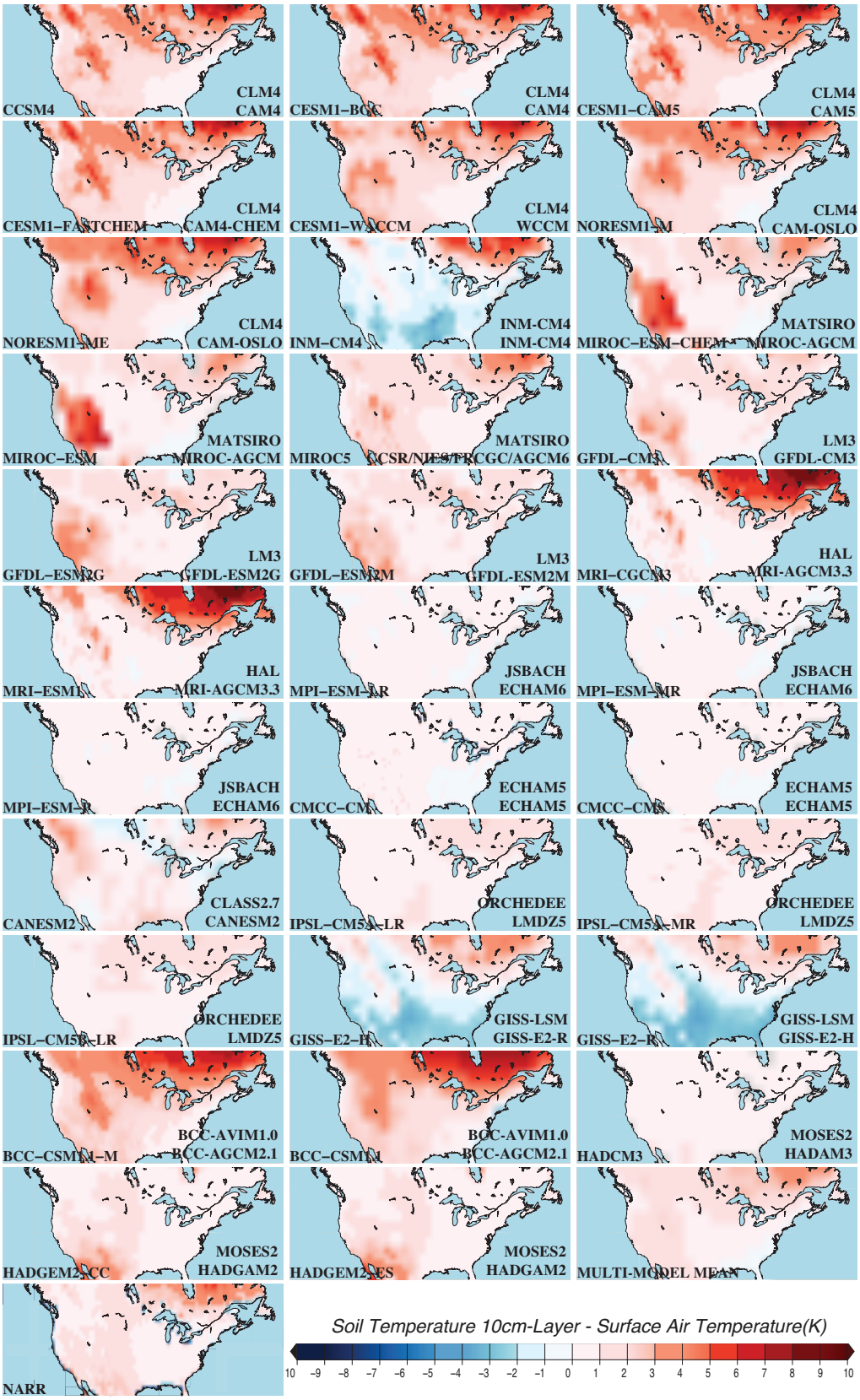

Figure A.2: Annual mean difference between GST at the layer containing the depth of 10cm and SAT from 1979 to 2001 for the CMIP5 GCMs, the multimodel mean and the NARR.

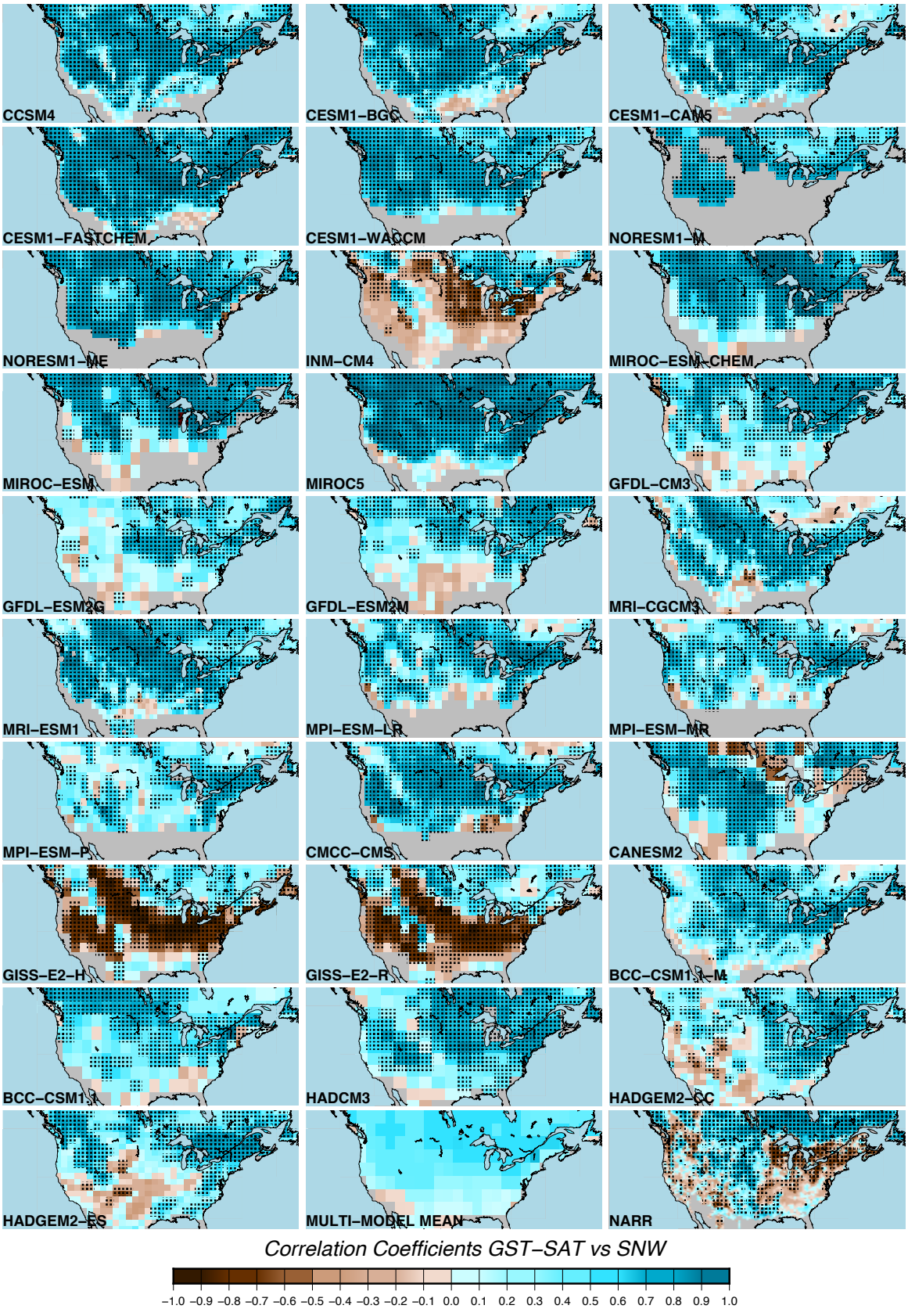

Figure A.3: Temporal correlation, point to point, between the annual mean of snow amounts (SNW) and the absolute values of the annual temperature difference of each model, GST-SAT. Dots indicate significant correlation at the 95% level.

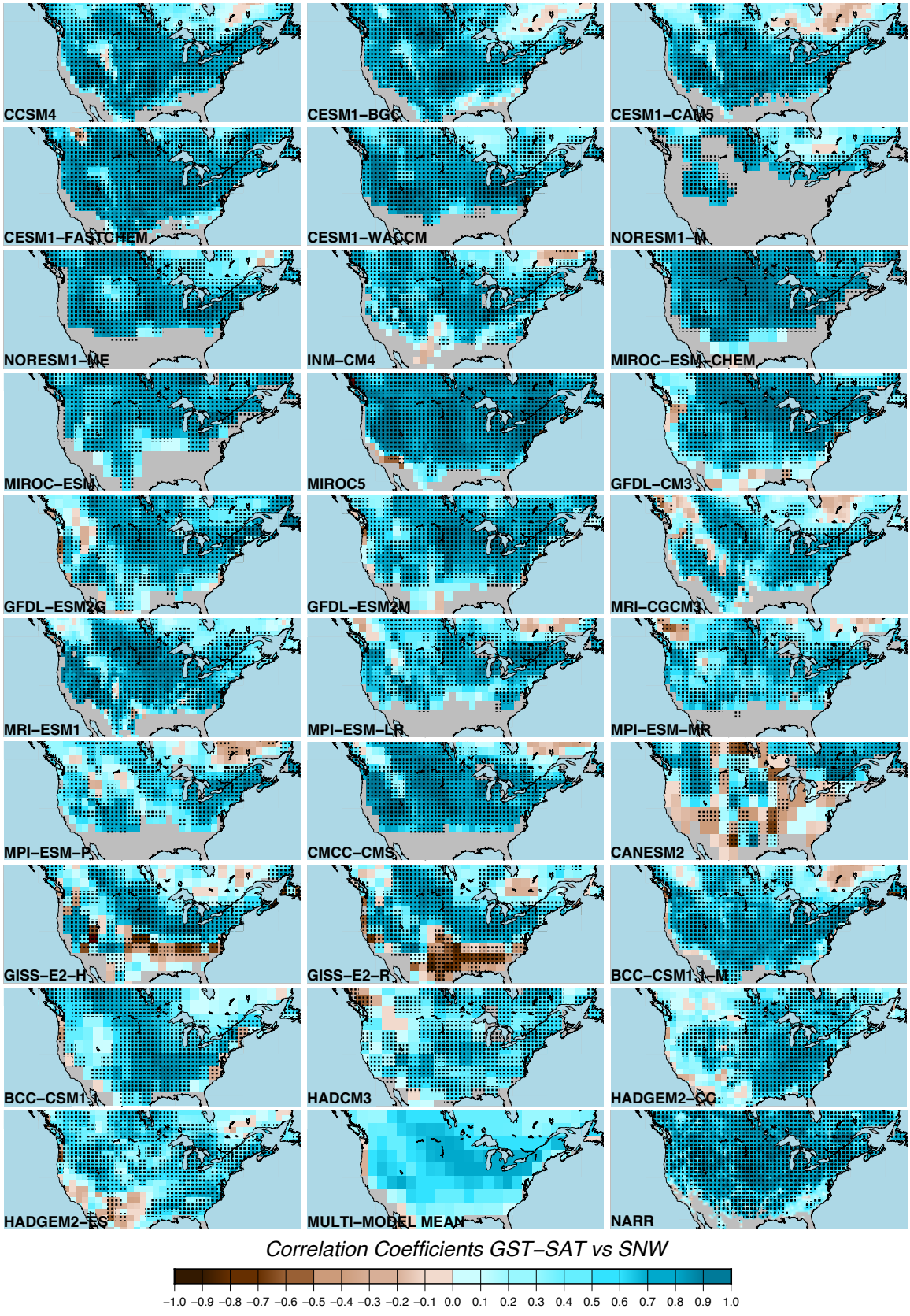

Figure A.4: Temporal correlation, point to point, between the DJF mean of snow amounts (SNW) and the absolute values of the winter temperature difference of each model, GST-SAT. Dots indicate significant correlation at the 95% level.

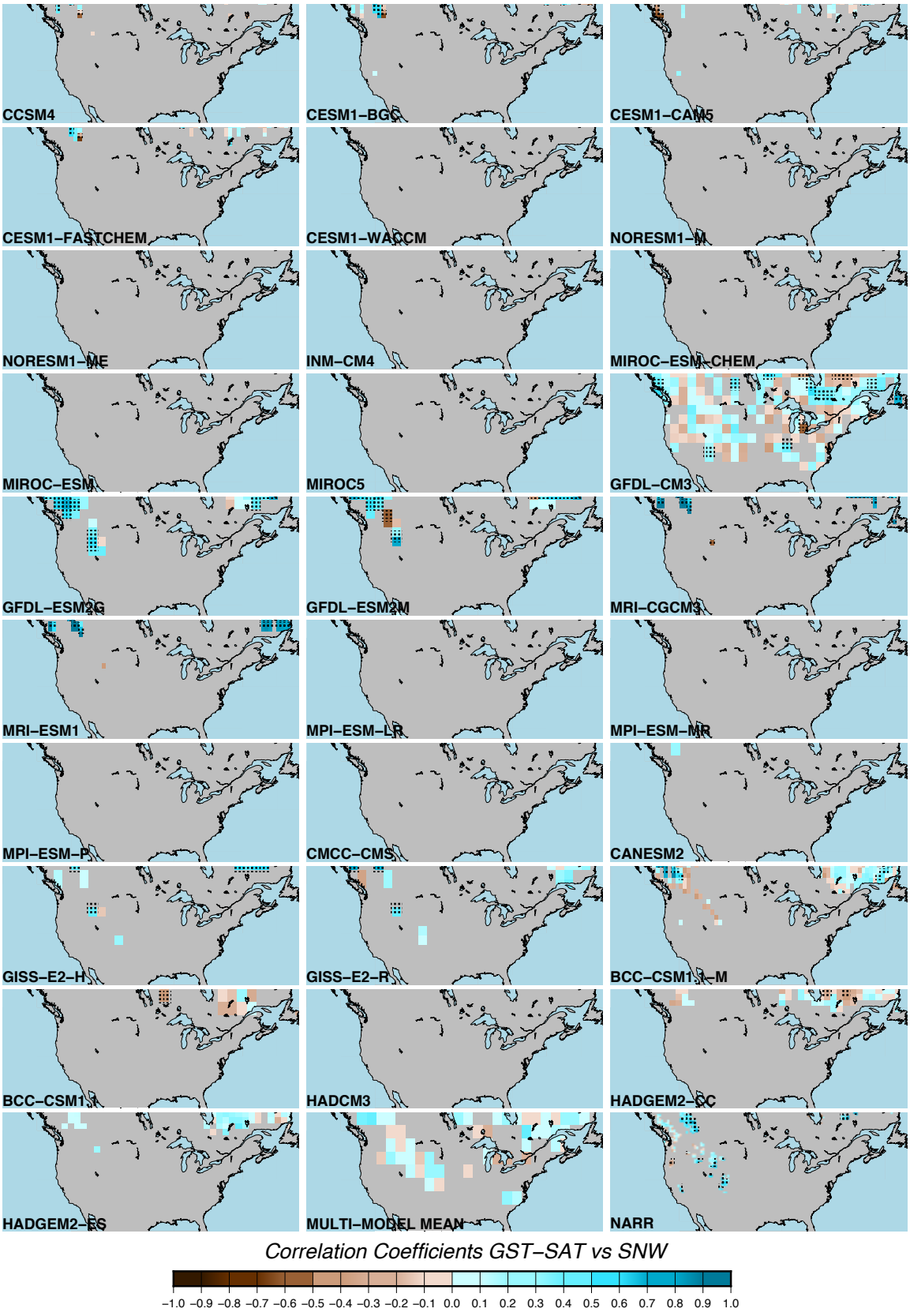

Figure A.5: Temporal correlation, point to point, between the JJA mean of snow amounts (SNW) and the absolute values of the summer temperature difference of each model, GST-SAT. Dots indicate significant correlation at the 95% level.

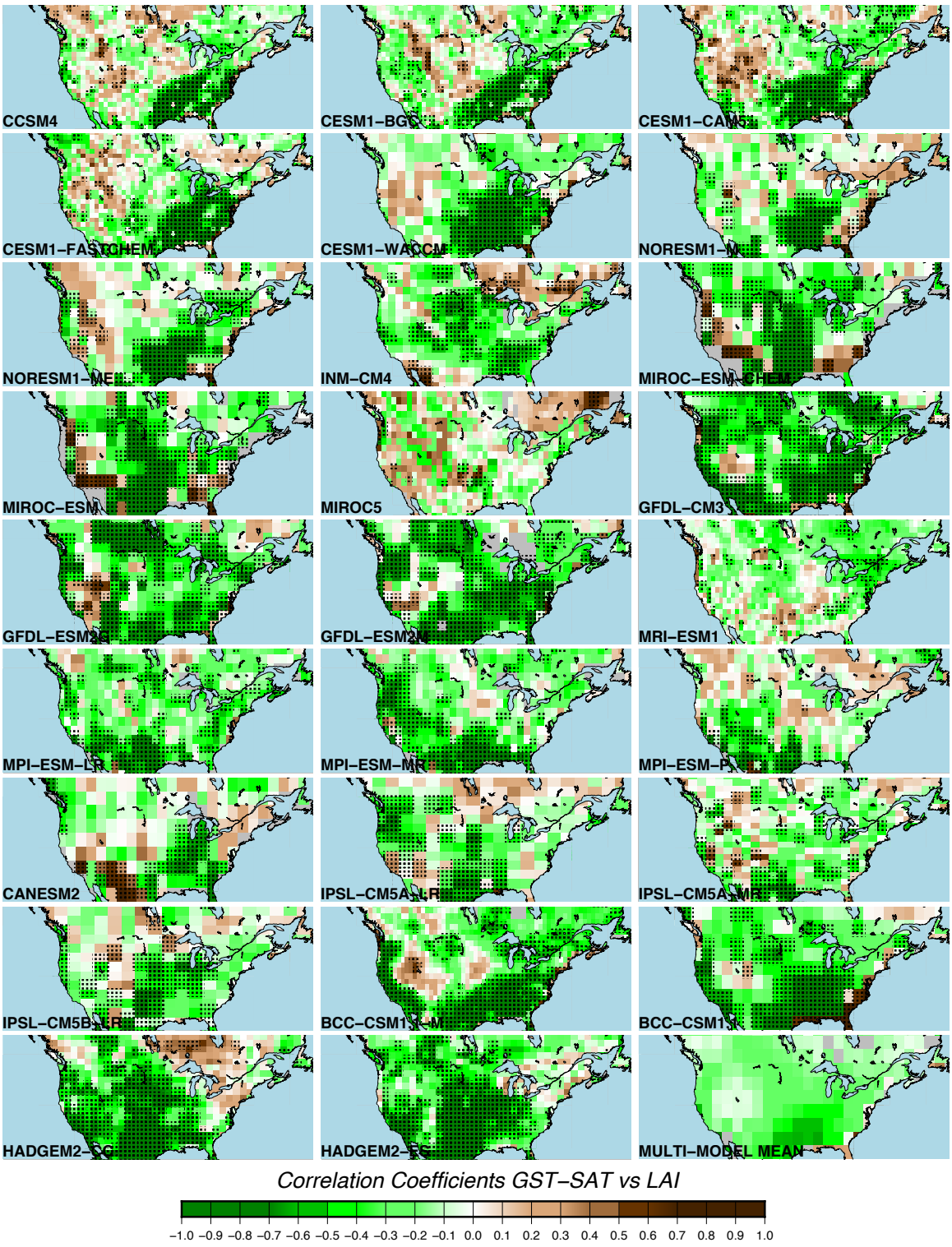

Figure A.6: Temporal correlation, point to point, between the annual mean of Leaf Area Index values (LAI) and the absolute values of the annual temperature difference of each model, GST-SAT. Dots indicate significant correlation at the 95% level.

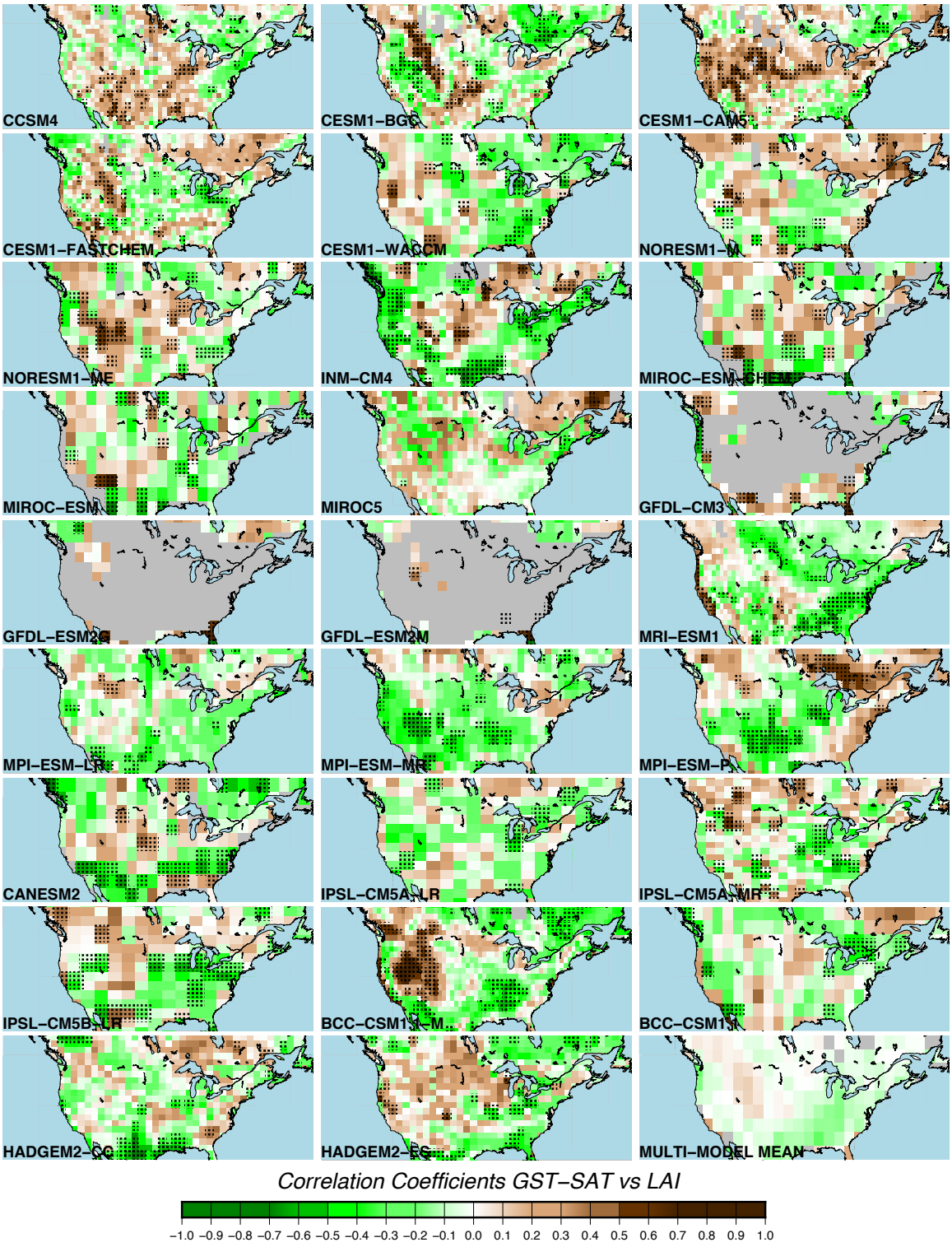

Figure A.7: Temporal correlation, point to point, between the DJF mean of Leaf Area Index values (LAI) and the absolute values of the winter temperature difference of each model, GST-SAT. Dots indicate significant correlation at the 95% level.

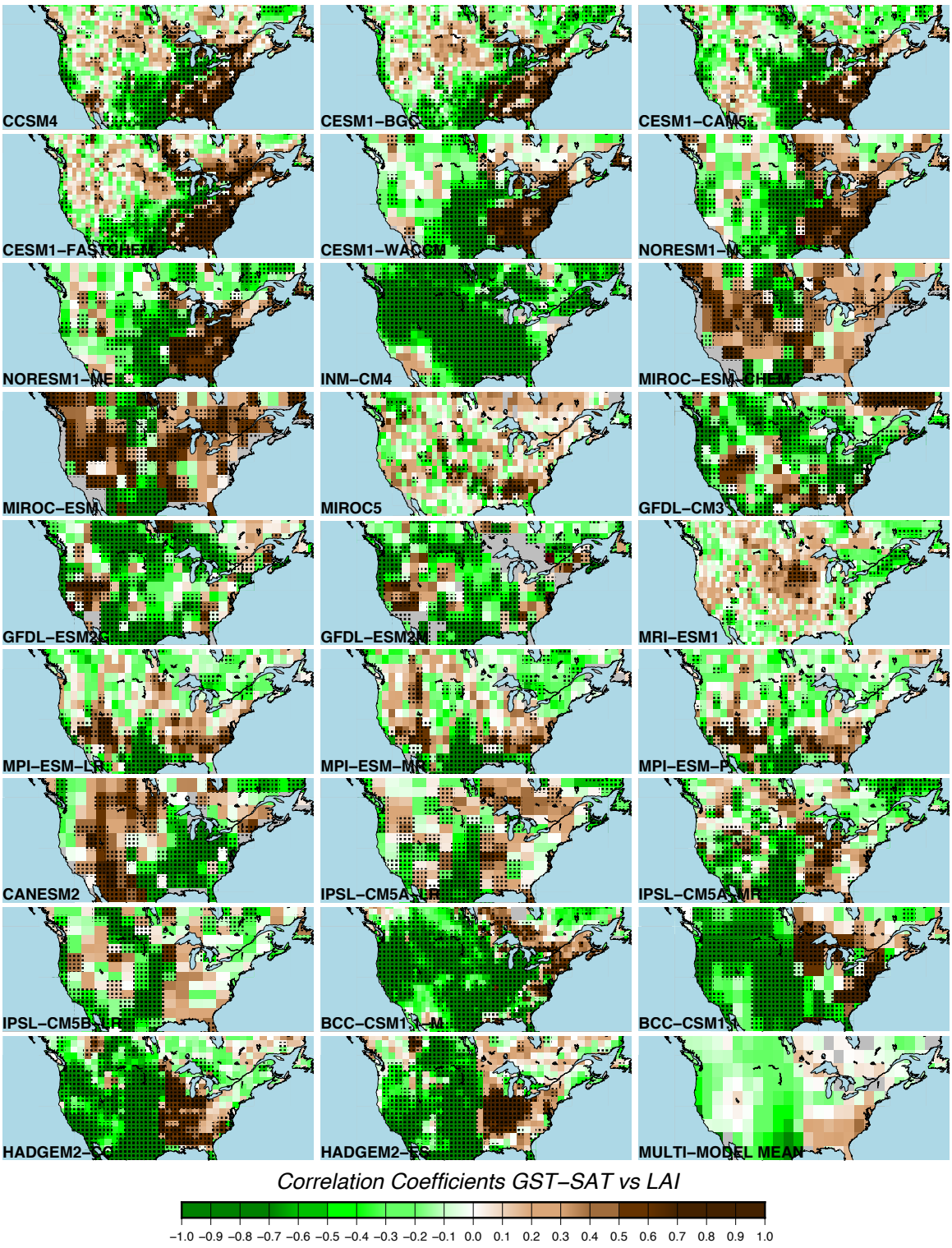

Figure A.8: Temporal correlation, point to point, between the JJA mean of Leaf Area Index values (LAI) and the absolute values of the summer temperature difference of each model, GST-SAT. Dots indicate significant correlation at the 95% level.

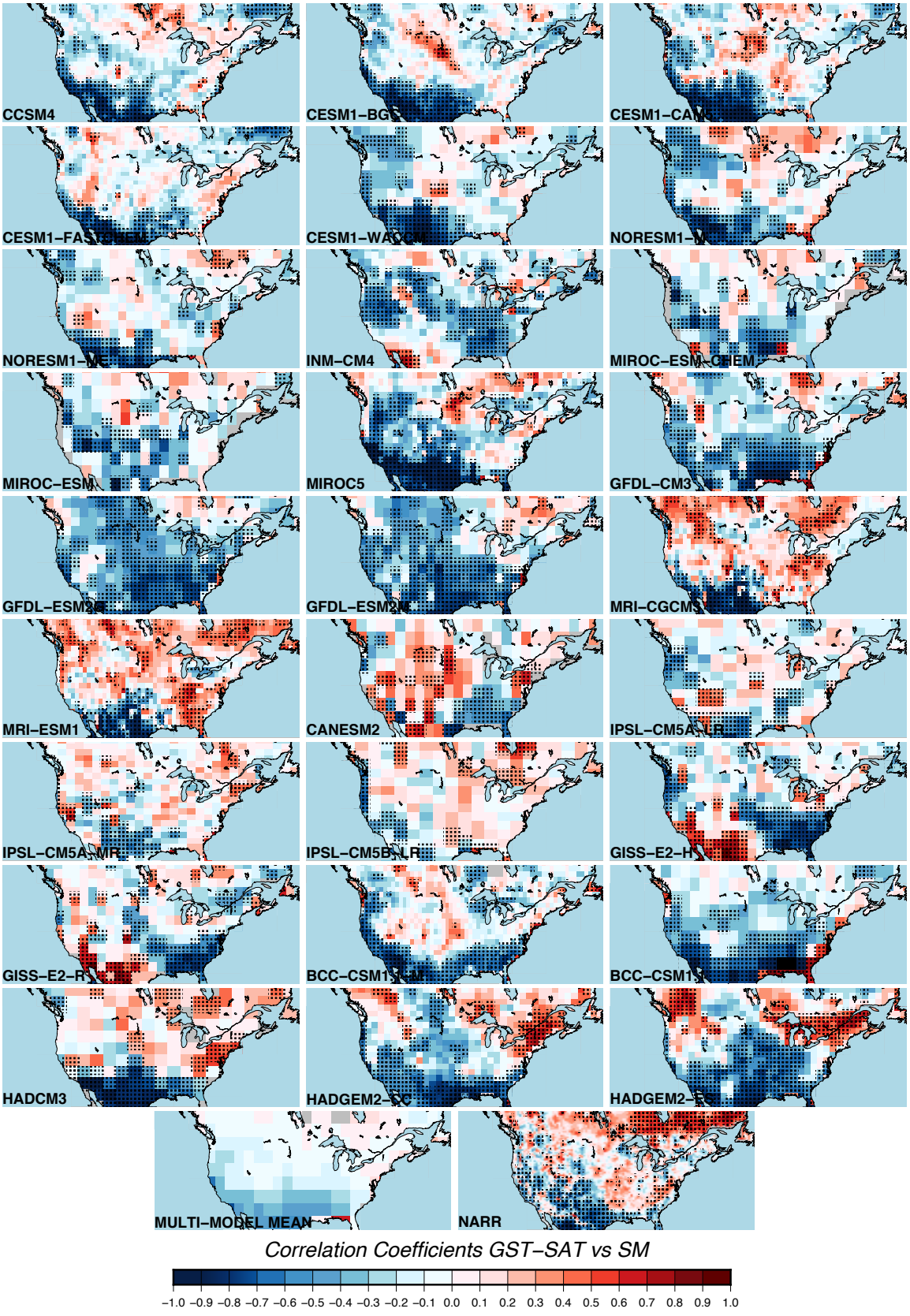

Figure A.9: Temporal correlation, point to point, between the annual mean of Soil Moisture values (SM) and the absolute values of the annual temperature difference of each model, GST-SAT. Dots indicate significant correlation at the 95% level.

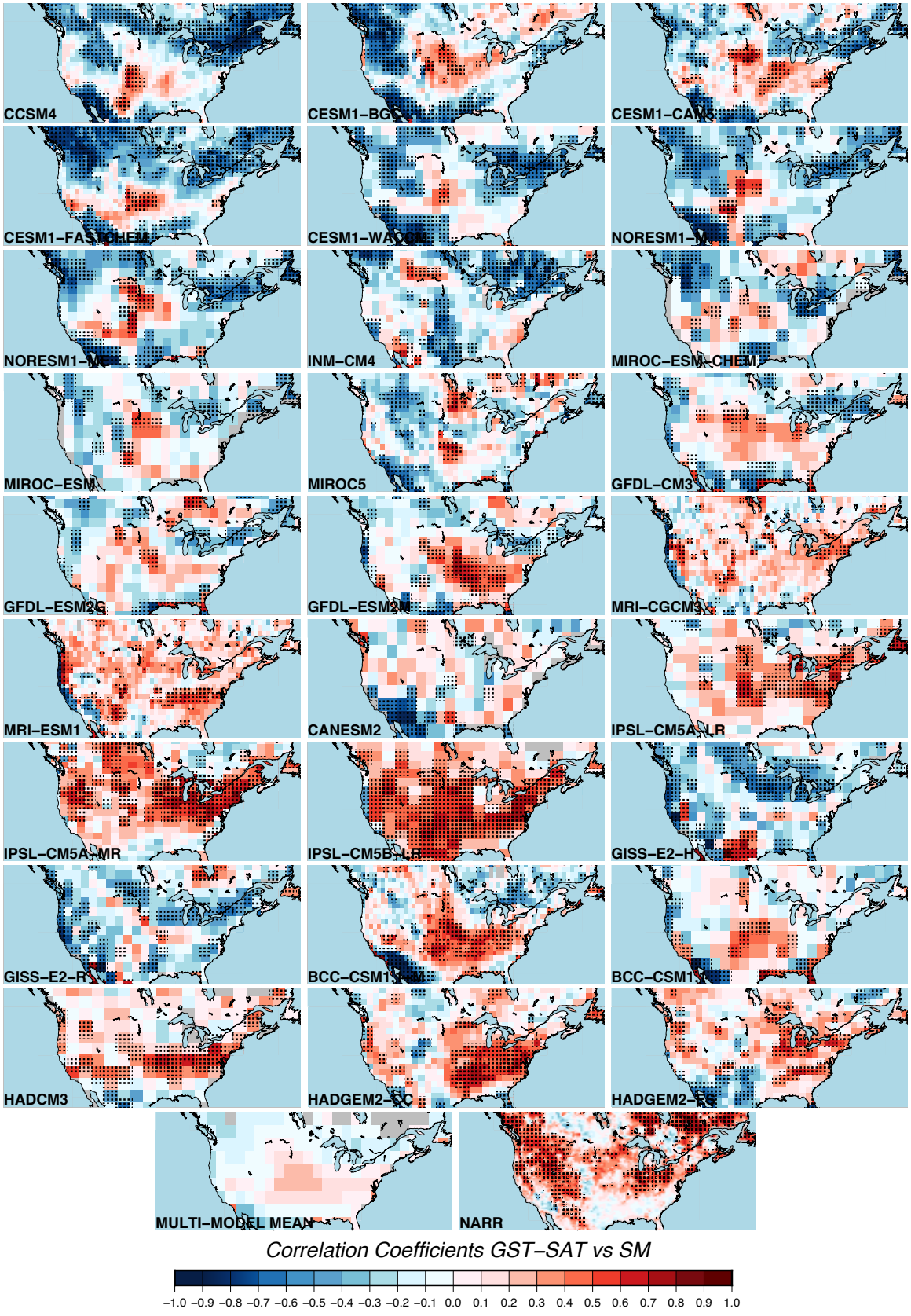

Figure A.10: Temporal correlation, point to point, between the DJF mean of Soil Moisture values (SM) and the absolute values of the winter temperature difference of each model, GST-SAT. Dots indicate significant correlation at the 95% level.

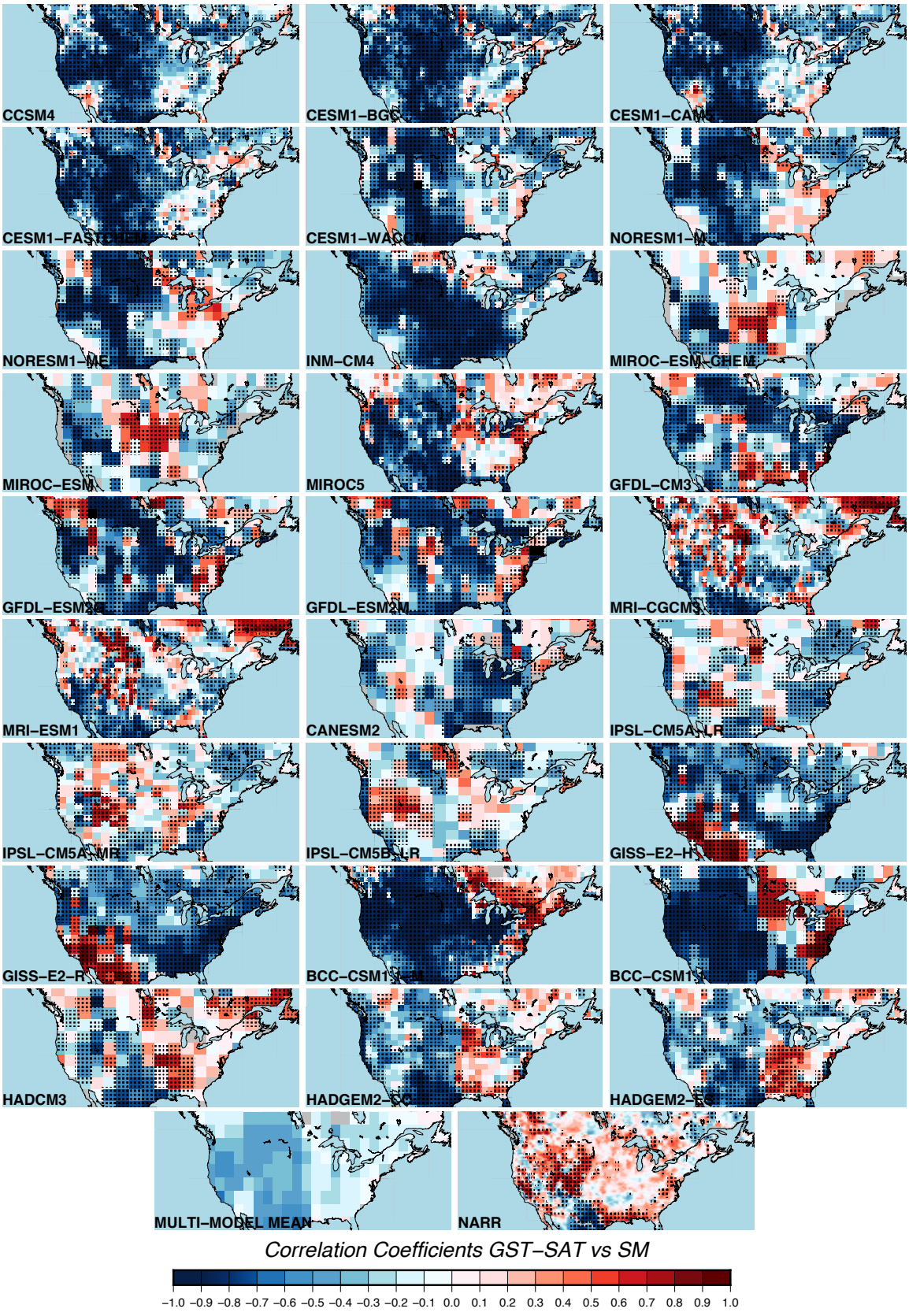

Figure A.11: Temporal correlation, point to point, between the JJA mean of Soil Moisture values (SM) and the absolute values of the summer temperature difference of each model, GST-SAT. Dots indicate significant correlation at the 95% level.

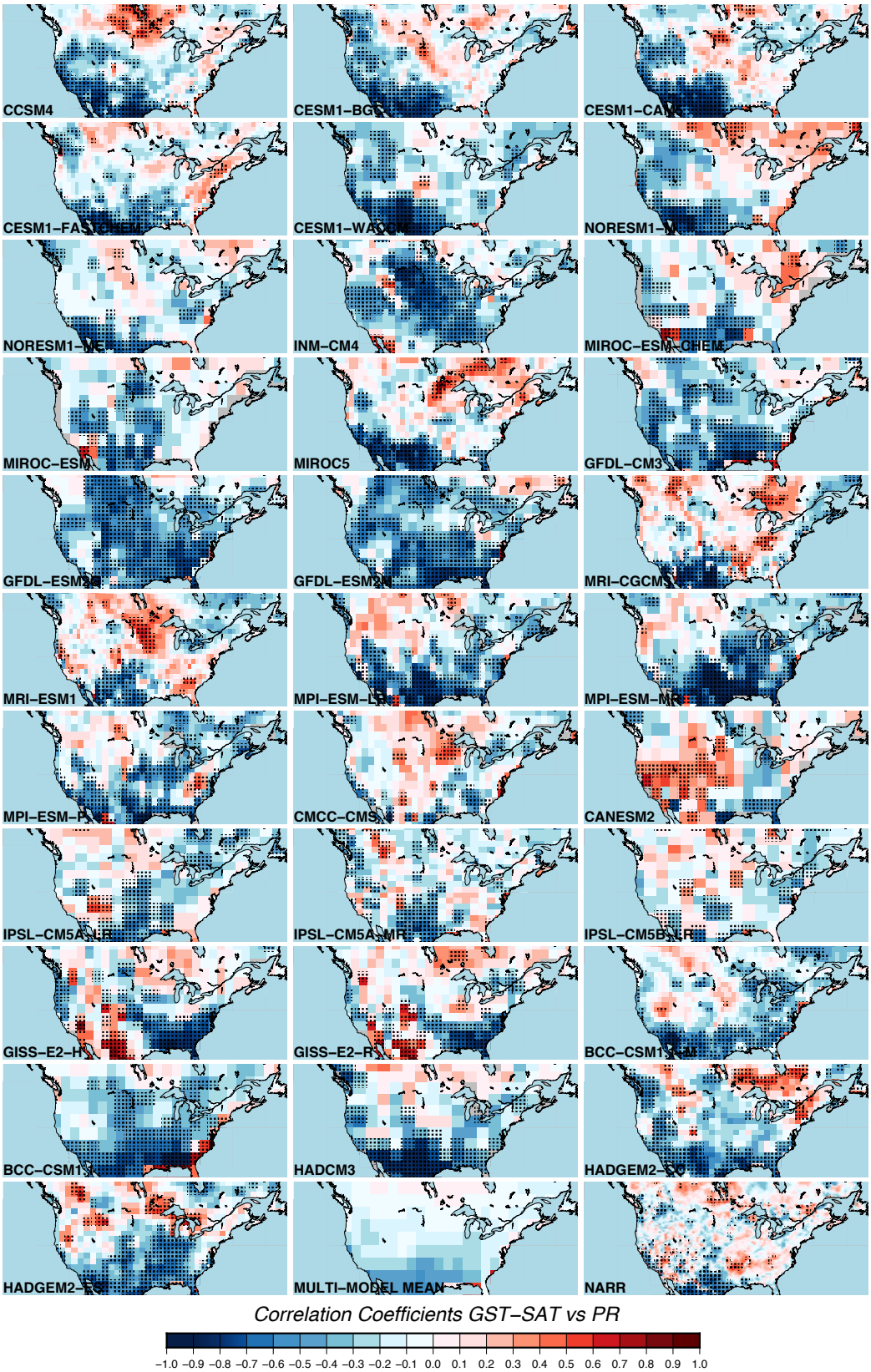

Figure A.12: Temporal correlation, point to point, between the annual mean of Precipitation Rates (PR) and the absolute values of the annual temperature difference of each model, GST-SAT. Dots indicate significant correlation at the 95% level.

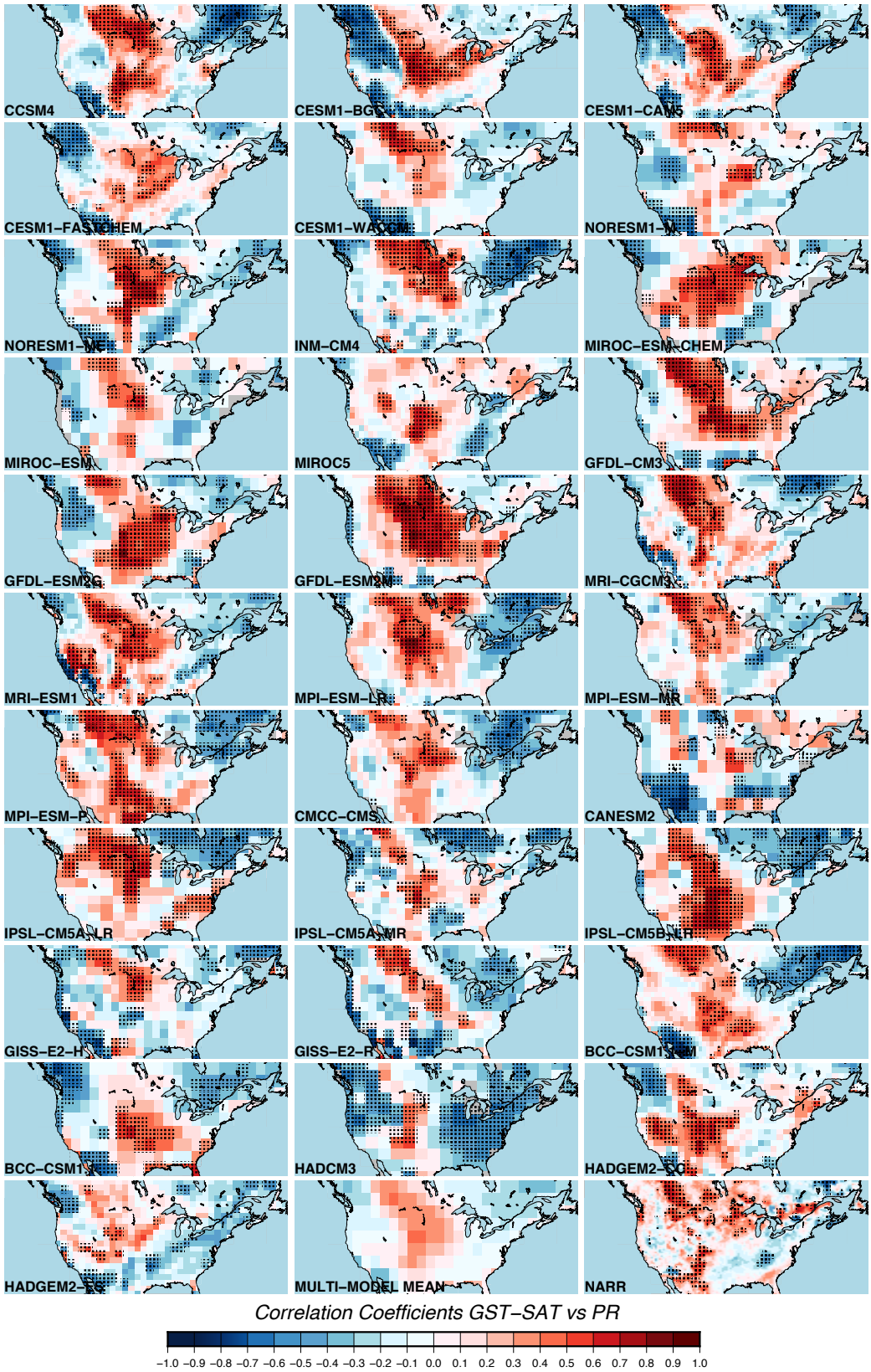

Figure A.13: Temporal correlation, point to point, between the DJF mean of Precipitation Rates (PR) and the absolute values of the winter temperature difference of each model, GST-SAT. Dots indicate significant correlation at the 95% level.

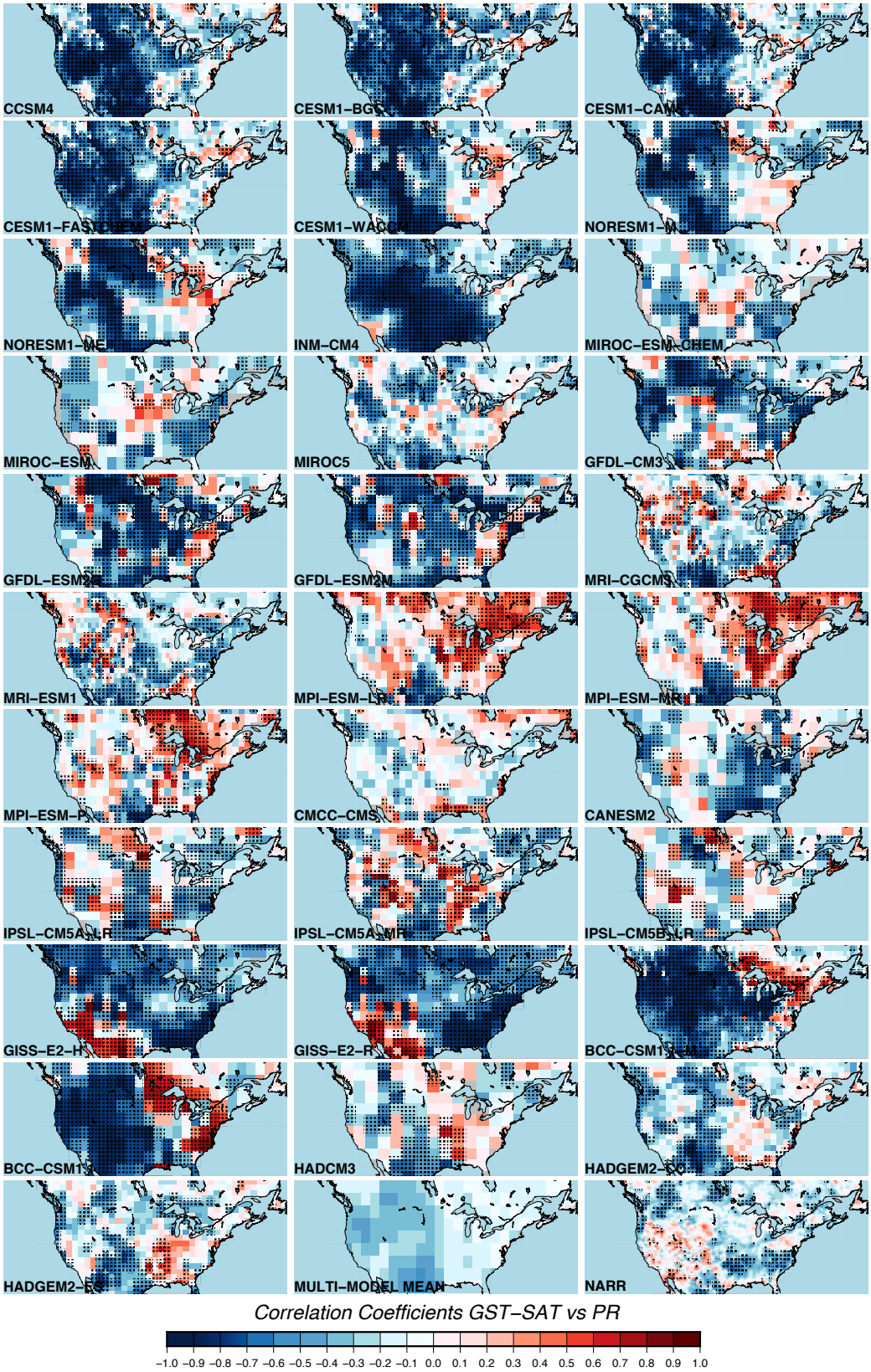

Figure A.14: Temporal correlation, point to point, between the JJA mean of Precipitation Rates (PR) and the absolute values of the summer temperature difference of each model, GST-SAT. Dots indicate significant correlation at the 95% level.

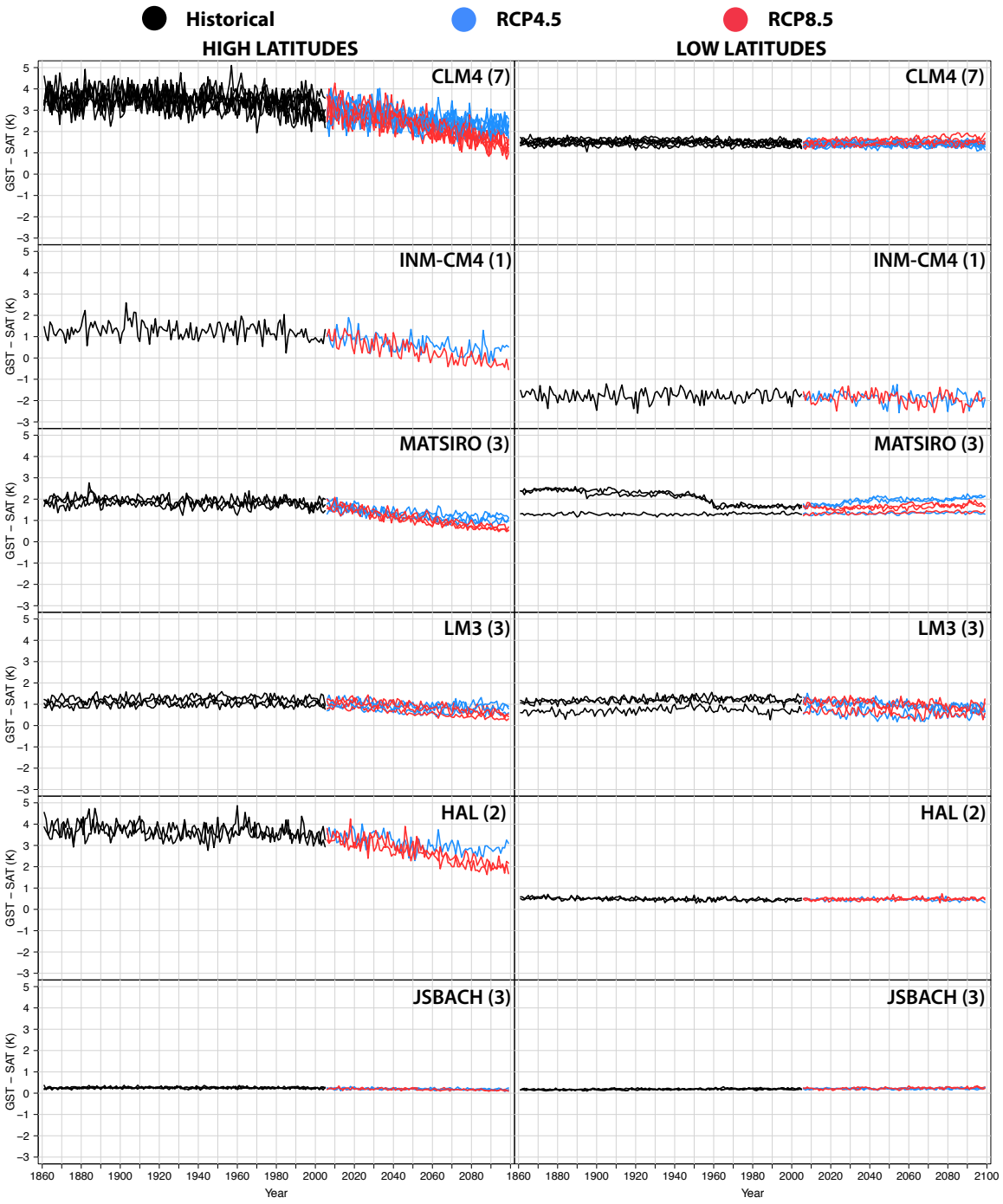

Figure A.15: Temporal evolution of the annual difference between GST and SAT for each LSM at North American high latitudes from 40°N to 55°N (left column), and at North American low latitudes from 25°N to 40°N (right column). The numbers in bracket indicate the number of GCMs employing each LSM.

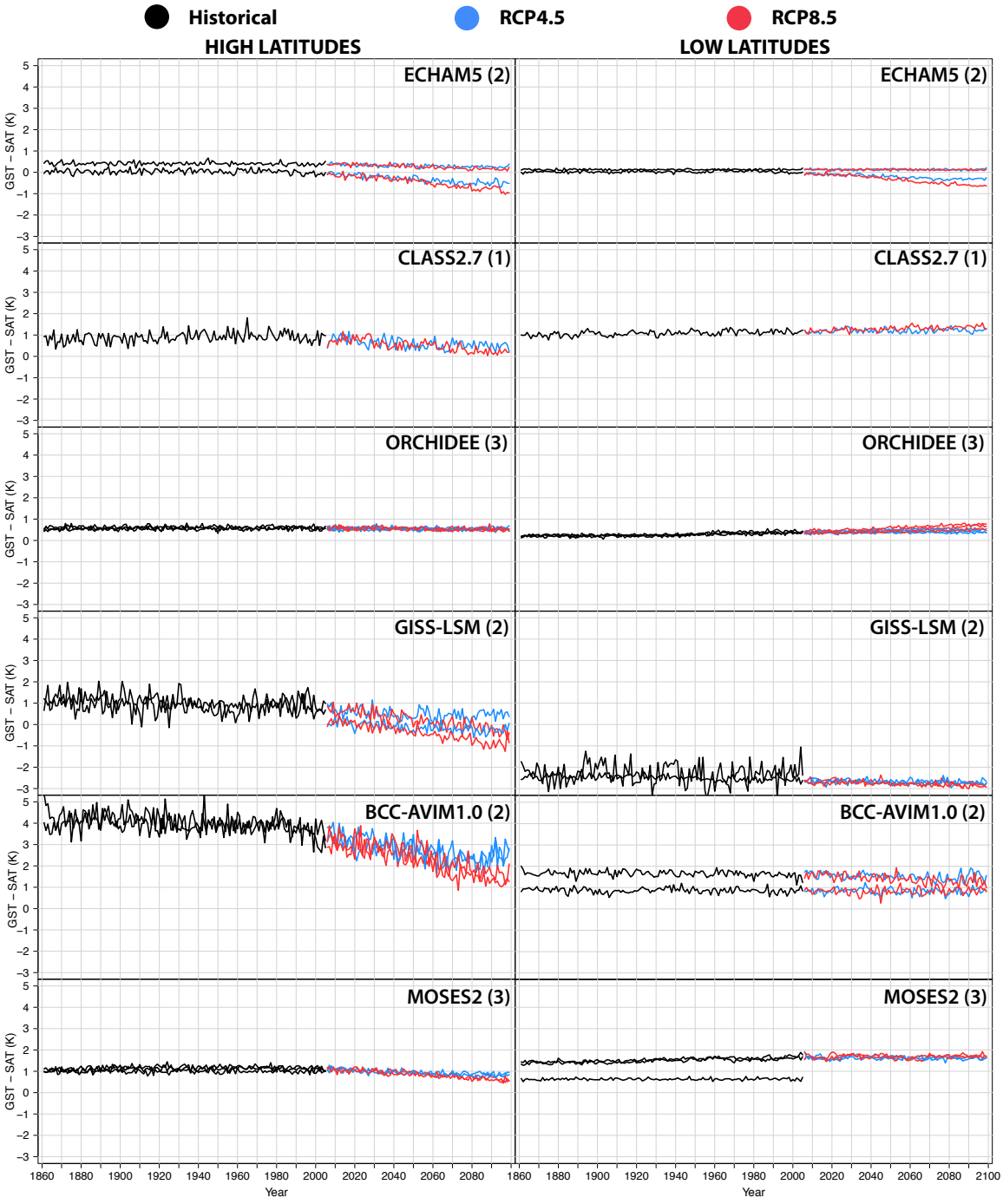

Figure A.16: As in Fig. A.15, for the rest of the LSMs.

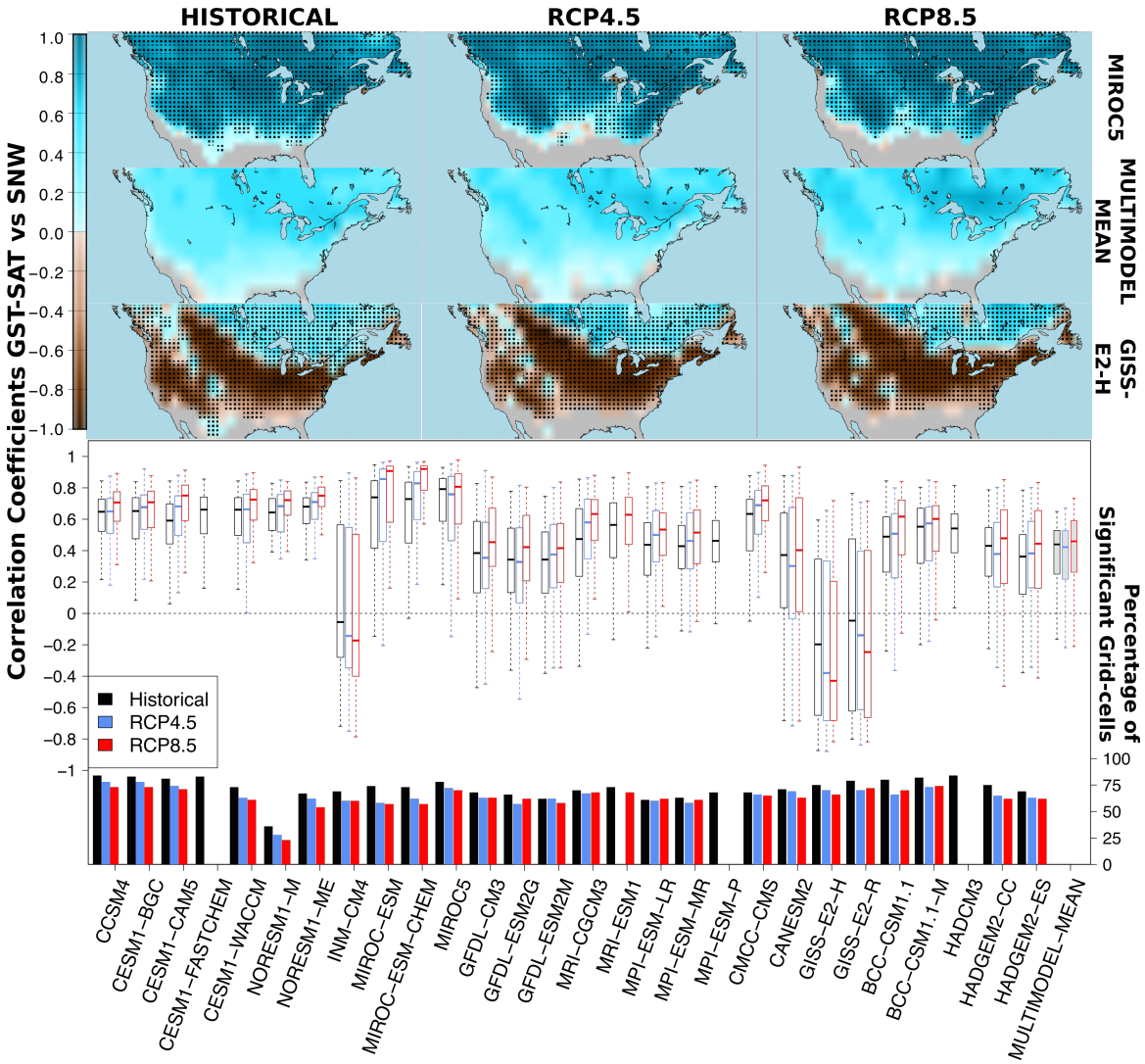

Figure A.17: Temporal correlation, point to point, between the annual mean of monthly snow amounts (SNW) and the absolute values of the annual temperature difference of each model, GST-SAT. (bottom) Boxplots (75th and 25th spatial percentiles (boxes), medians (center line), maximums and minimums (extremes of dashed lines)) of the correlation maps, using Historical (1860-2005) (black), RCP4.5 (blue) and RCP8.5 (2006-2099) (red) simulations. Outliers (points located 1.5 times the interquartile range above the upper quartile and bellow the lower quartile) are not included. Bars at the bottom of the boxplots indicate the percentages of grid-cells with significant correlation at the 95% level using a phase-randomizing bootstrapping technique with 1000 Monte Carlo runs (Ebisuzaki, 1997). (top) Maps correspond to the strongest (MIROC5, top) and the weakest (GISS-E2-H, bottom) mean correlations and the multimodel mean of the correlation coefficients (center), for the Historical simulation (left), the RCP4.5 (center) and the RCP8.5 (right). Dots indicate significant correlation at the 95% level.

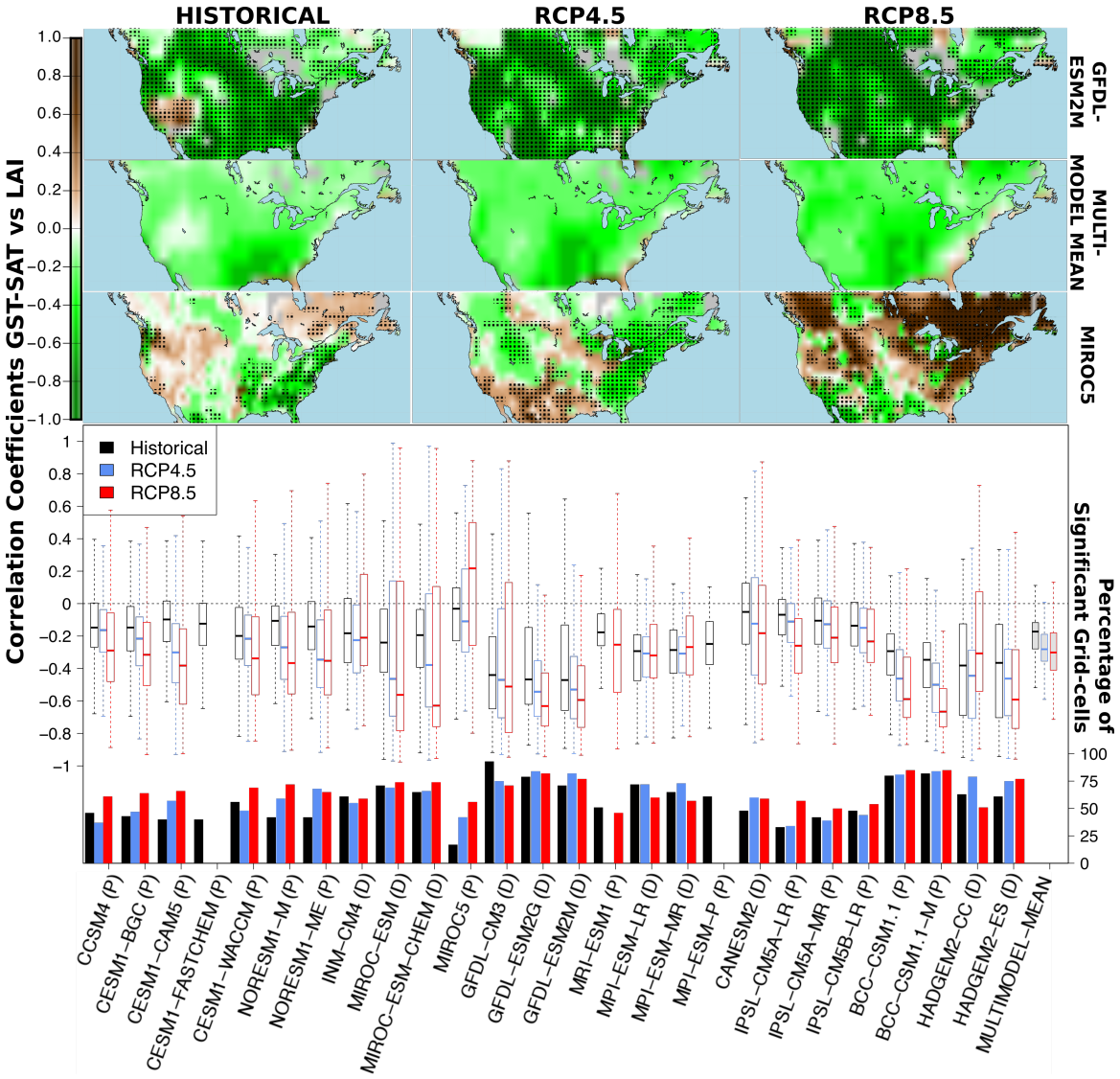

Figure A.18: Temporal correlation, point to point, between the annual mean of monthly Leaf Area Index (LAI) and the absolute values of the annual temperature difference of each model, GST-SAT. (bottom) Boxplots (75th and 25th spatial percentiles (boxes), medians (center line), maximums and minimums (extremes of dashed lines)) of the correlation maps, using Historical (1860-2005) (black), RCP4.5 (blue) and RCP8.5 (2006-2099) (red) simulations. Outliers (points located 1.5 times the interquartile range above the upper quartile and bellow the lower quartile) are not included. Bars at the bottom of the boxplots indicate the percentages of grid-cells with significant correlation at the 95% level using a phase-randomizing bootstrapping technique with 1000 Monte Carlo runs (Ebisuzaki, 1997). The capital letter next to each model name indicates the information of the vegetation mode (prescribed (P) or dynamic (D)) employed for each simulation, which was retrieved from the Earth System Documentation website (`https://search.es-doc.org`, access date 2018/03/18) as well as in the models' documentation. (top) Maps correspond to the strongest (GFDL-ESM2G, top) and the weakest (CANESM2, bottom) mean correlations and the multimodel mean of the correlation coefficients (center), for the Historical simulation (left), the RCP4.5 (center) and the RCP8.5 (right). Dots indicate significant correlation at the 95% level.

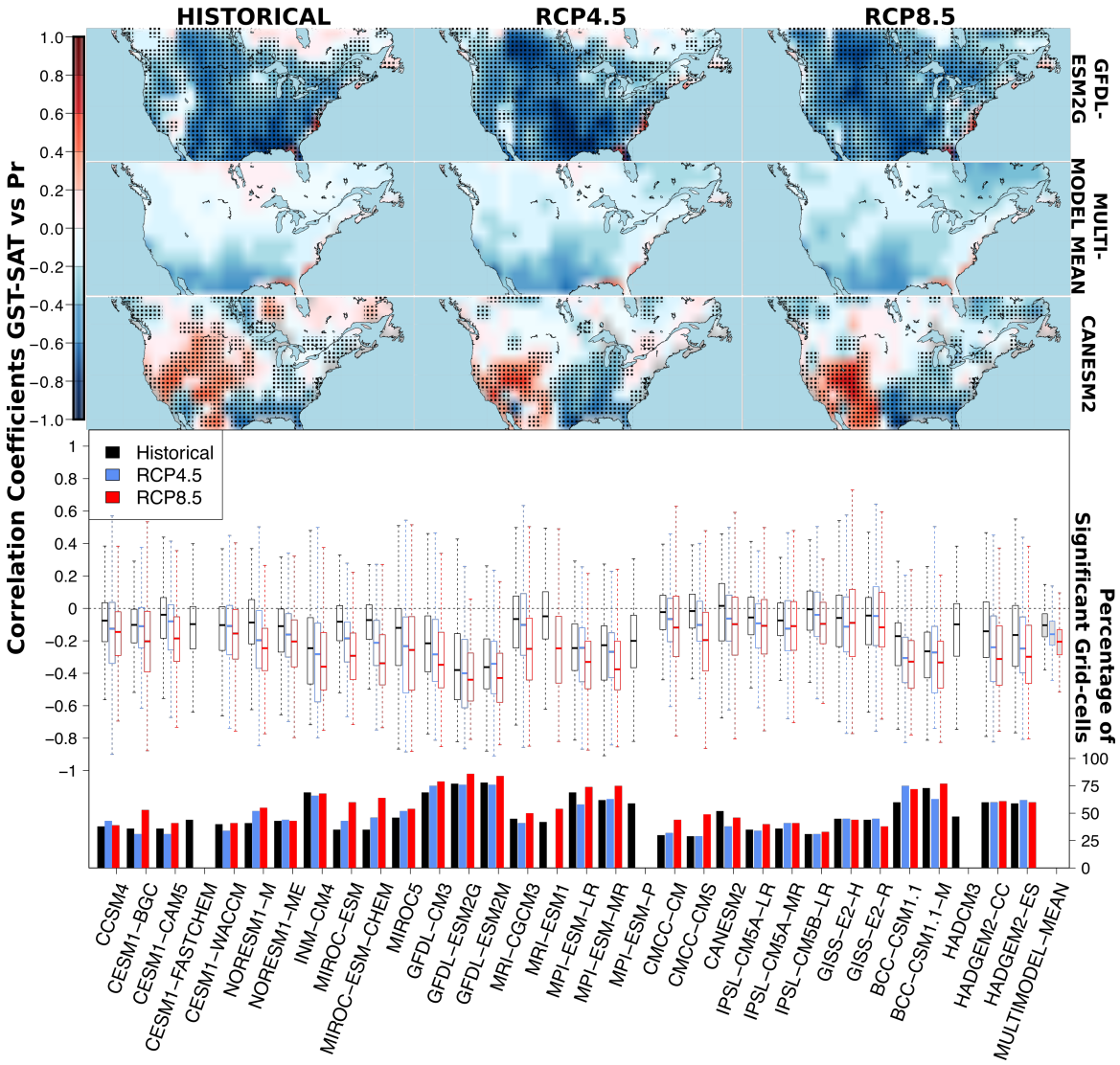

Figure A.19: Temporal correlation, point to point, between the annual mean of monthly precipitation rates at the surface (PR) and the absolute values of the annual temperature difference of each model, GST-SAT. (bottom) Boxplots (75th and 25th spatial percentiles (boxes), medians (center line), maximums and minimums (extremes of dashed lines)) of the correlation maps, using Historical (1860-2005) (black), RCP4.5 (blue) and RCP8.5 (2006-2099) (red) simulations. Outliers (points located 1.5 times the interquartile range above the upper quartile and bellow the lower quartile) are not included. Bars at the bottom of the boxplots indicate the percentages of grid-cells with significant correlation at the 95% level using a phase-randomizing bootstrapping technique with 1000 Monte Carlo runs (Ebisuzaki, 1997). (top) Maps correspond to the strongest (GFDL-ESM2G, top) and the weakest (MRI-CGCM3, bottom) mean correlations and the multimodel mean of the correlation coefficients (center), for the Historical simulation (left), the RCP4.5 (center) and the RCP8.5 (right). Dots indicate significant correlation at the 95% level.

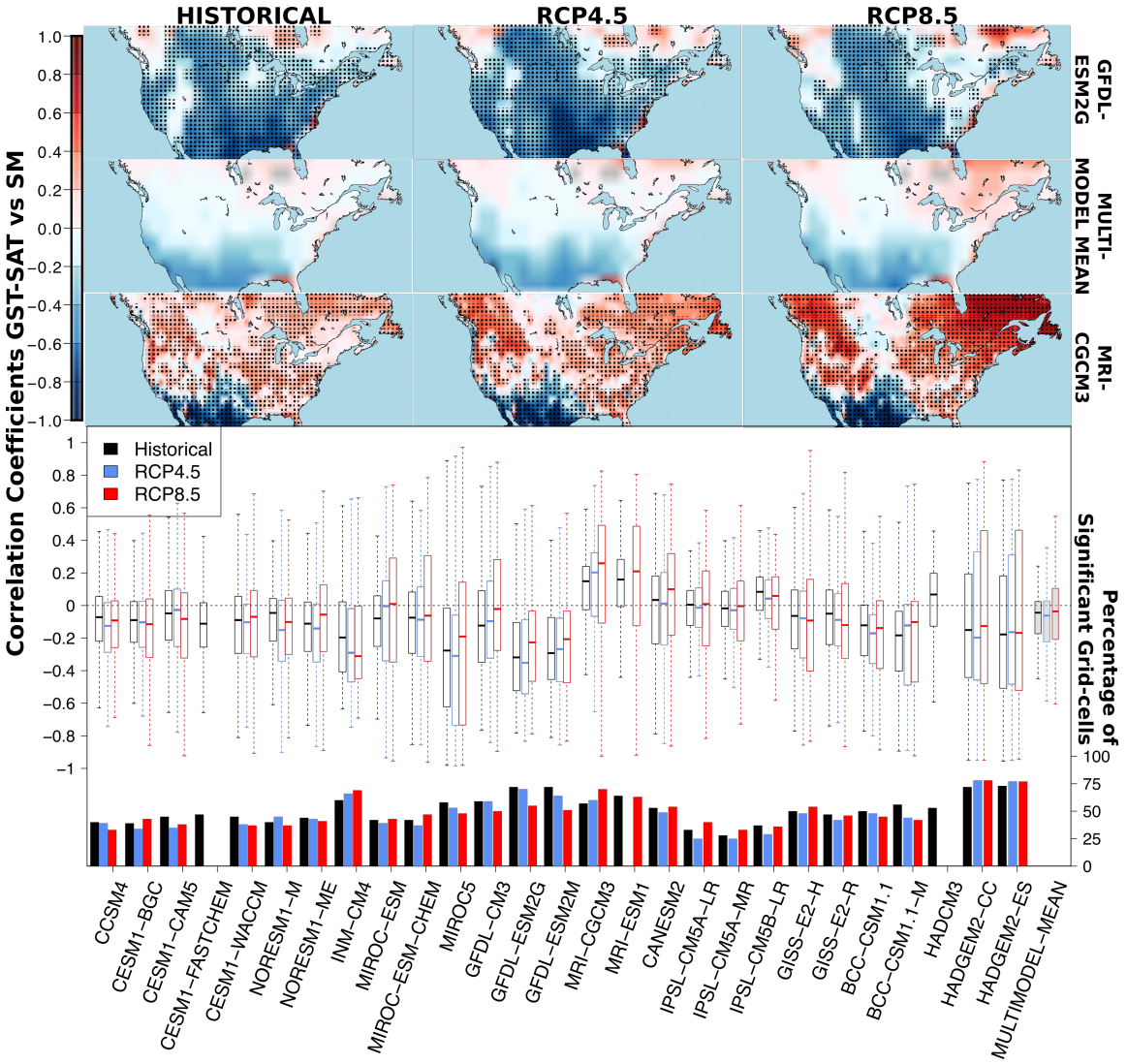

Figure A.20: Temporal correlation, point to point, between the annual mean of monthly soil moisture at the first 10 cm (SM) and the absolute values of the annual temperature difference of each model, GST-SAT. (bottom) Boxplots (75th and 25th spatial percentiles (boxes), medians (center line), maximums and minimums (extremes of dashed lines)) of the correlation maps, using Historical (1860-2005) (black), RCP4.5 (blue) and RCP8.5 (2006-2099) (red) simulations. Outliers (values located 1.5 times the interquartile range above the upper quartile and bellow the lower quartile) are not included. Bars at the bottom of the boxplots indicate the percentages of grid-cells with significant correlation at the 95% level using a phase-randomizing bootstrapping technique with 1000 Monte Carlo runs (Ebisuzaki, 1997). (top) Maps correspond to the strongest (INM-CM4, top) and the weakest (MIROC5, bottom) mean correlations and the multimodel mean of the correlation coefficients (center), for the Historical simulation (left), the RCP4.5 (center) and the RCP8.5 (right). Dots indicate significant correlation at the 95% level.

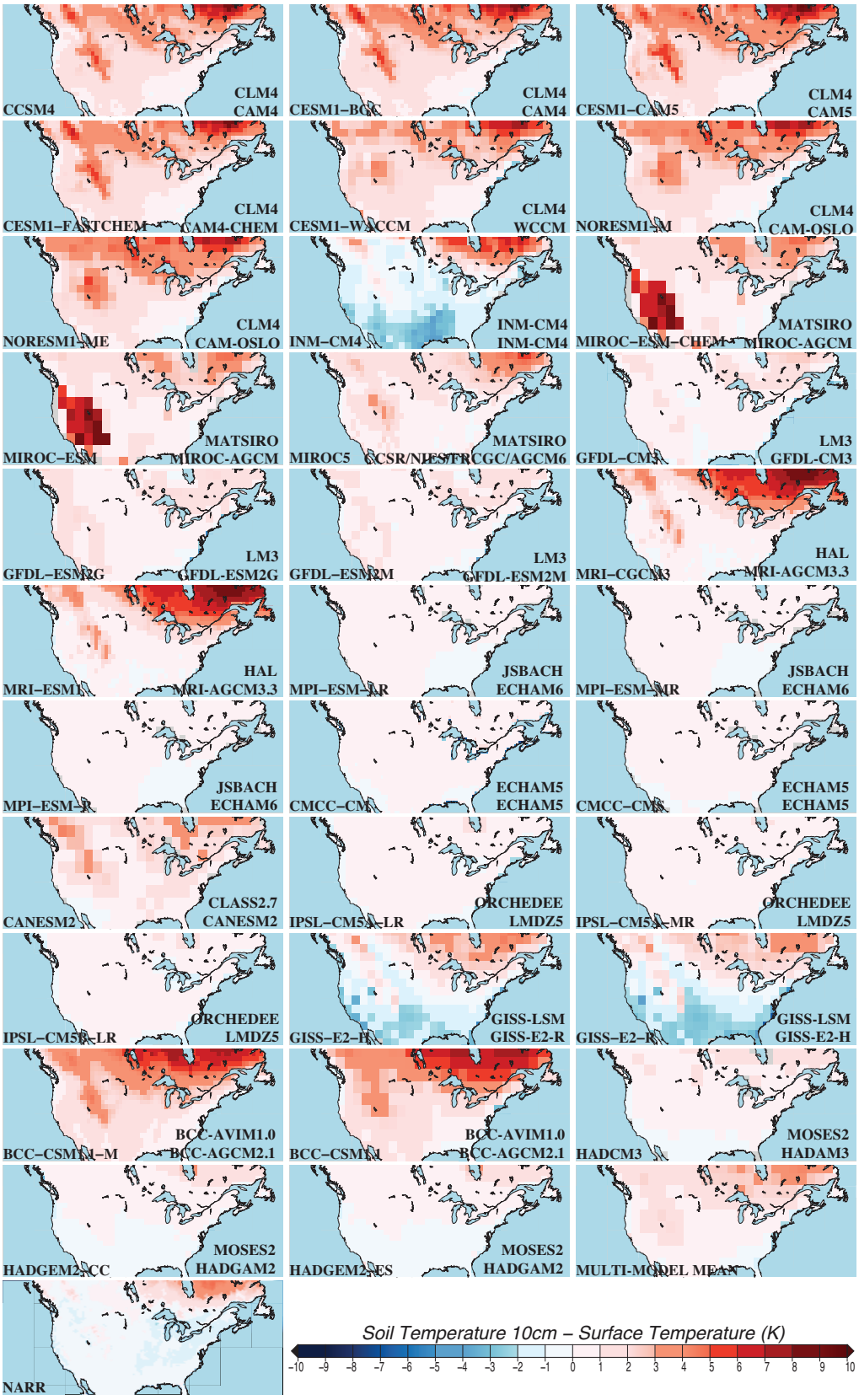

Figure A.21: Annual mean difference between GST at 10cm and ST from 1979 to 2001 for the CMIP5 GCMs, the multimodel mean and the NARR.

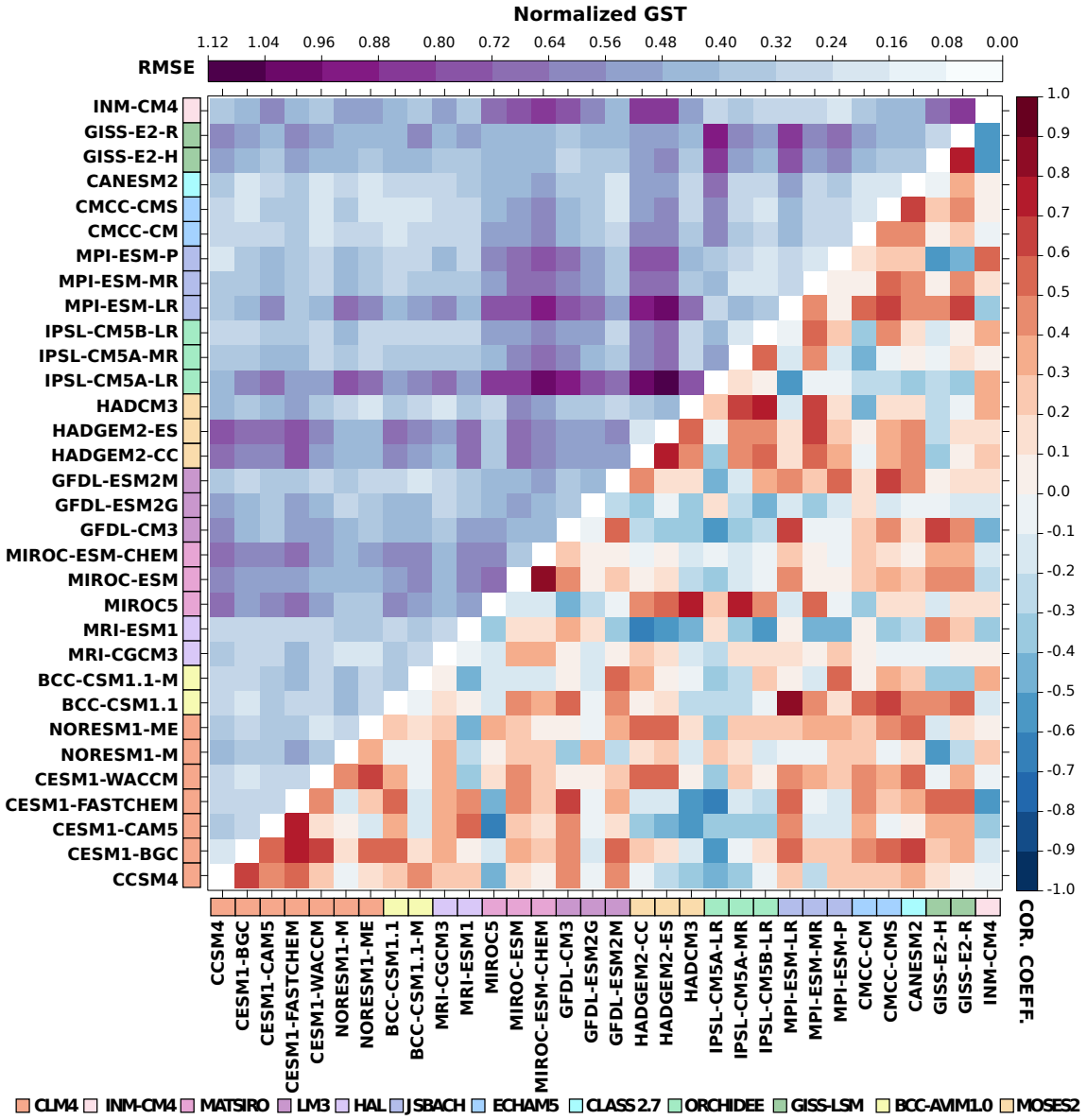

Figure A.22: Spatial correlation coefficients and RMSE values of the annual normalized GST 10cm for each pair of models within the CMIP5 ensemble for the period 1979-2001. The LSM employed by each model is indicated using a different color next to the models' name.

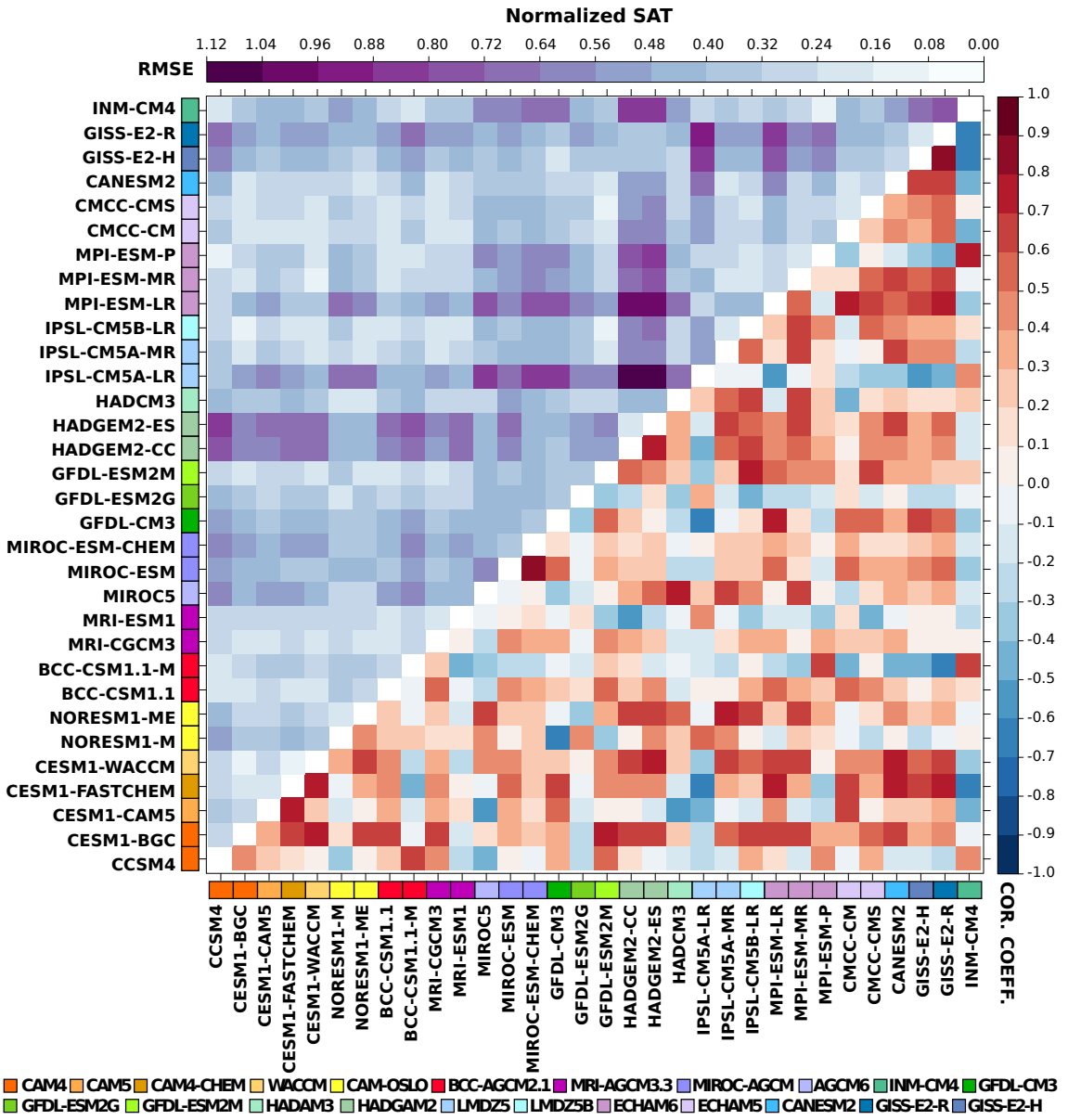

Figure A.23: Spatial correlation coefficients and RMSE values of the annual normalized SAT for each pair of models within the CMIP5 ensemble for the period 1979-2001. The atmospheric model employed by each model is indicated using a different color next to the models' name.

Bibliography

Ebisuzaki, W. (1997). A Method to Estimate the Statistical Significance of a Correlation When the Data Are Serially Correlated. *Journal of Climate* **10**(9), 2147–2153. DOI: doi:10.1175/1520-0442(1997)010<2147:AMTETS>2.0.CO;2.

Appendix B

Supporting Information for Chapter 3

Table B.1: Information on the visited websites for retrieving data or detailed information.

Product	Website	Date of access
ETCCDI	https://www.climdex.org/learn/indices/	December, 2018
NA-CORDEX	https://www.earthsystemgrid.org/search/cordexsearch.html	December, 2018
NARR	https://nomads.ncdc.noaa.gov/data/narr/	August, 2017
ARW-WRF Version 3.9	http://www2.mmm.ucar.edu/wrf/users/download/get_source.html	August, 2017

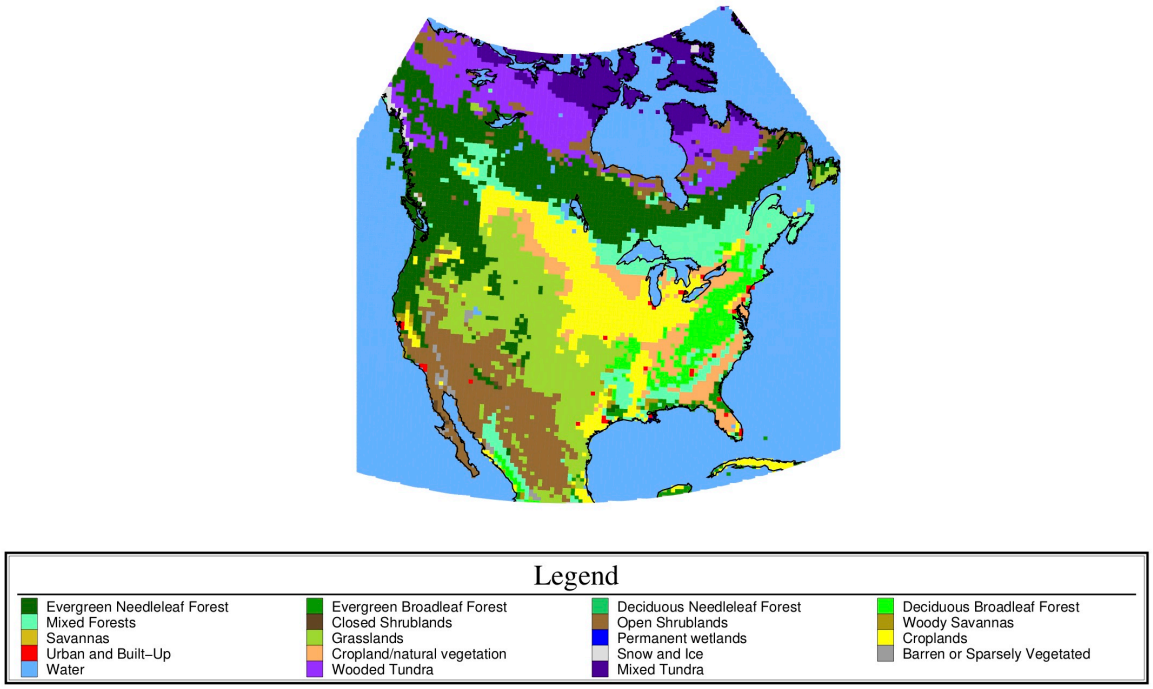

Figure B.1: Land use categories used in all our four simulations with different LSM configurations. These land use categories are derived from the Moderate Resolution Imaging Spectroradiometer (MODIS, Barlage et al., 2005).

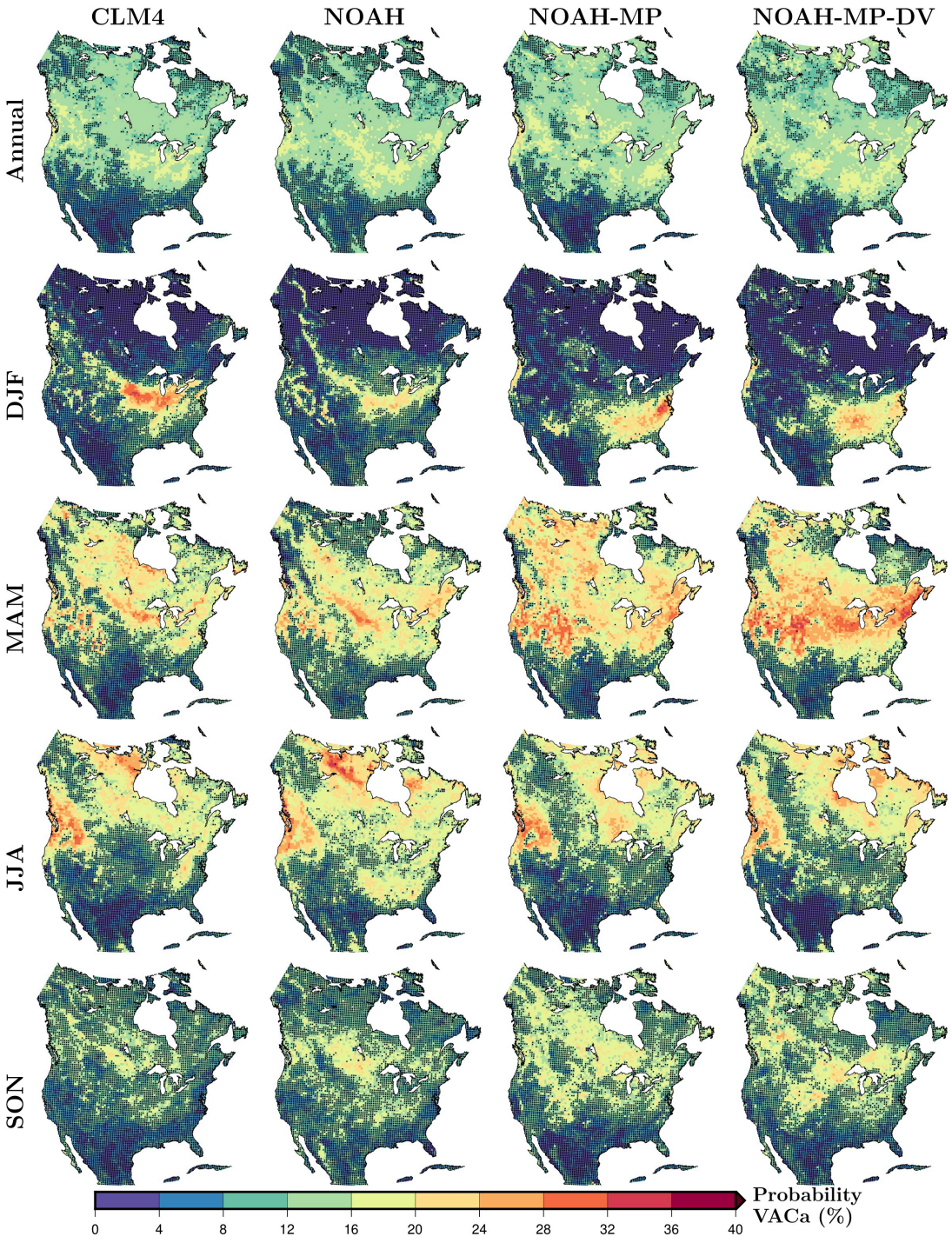

Figure B.2: Frequency of occurrence for the VAC_a category associated with atmospheric control events for each simulation annually and seasonally; DJF, MAM, JJA and SON. Black dots in the maps indicate VAC values lower than the 95th percentile of the randomly generated series, and therefore areas with no significant probabilities.

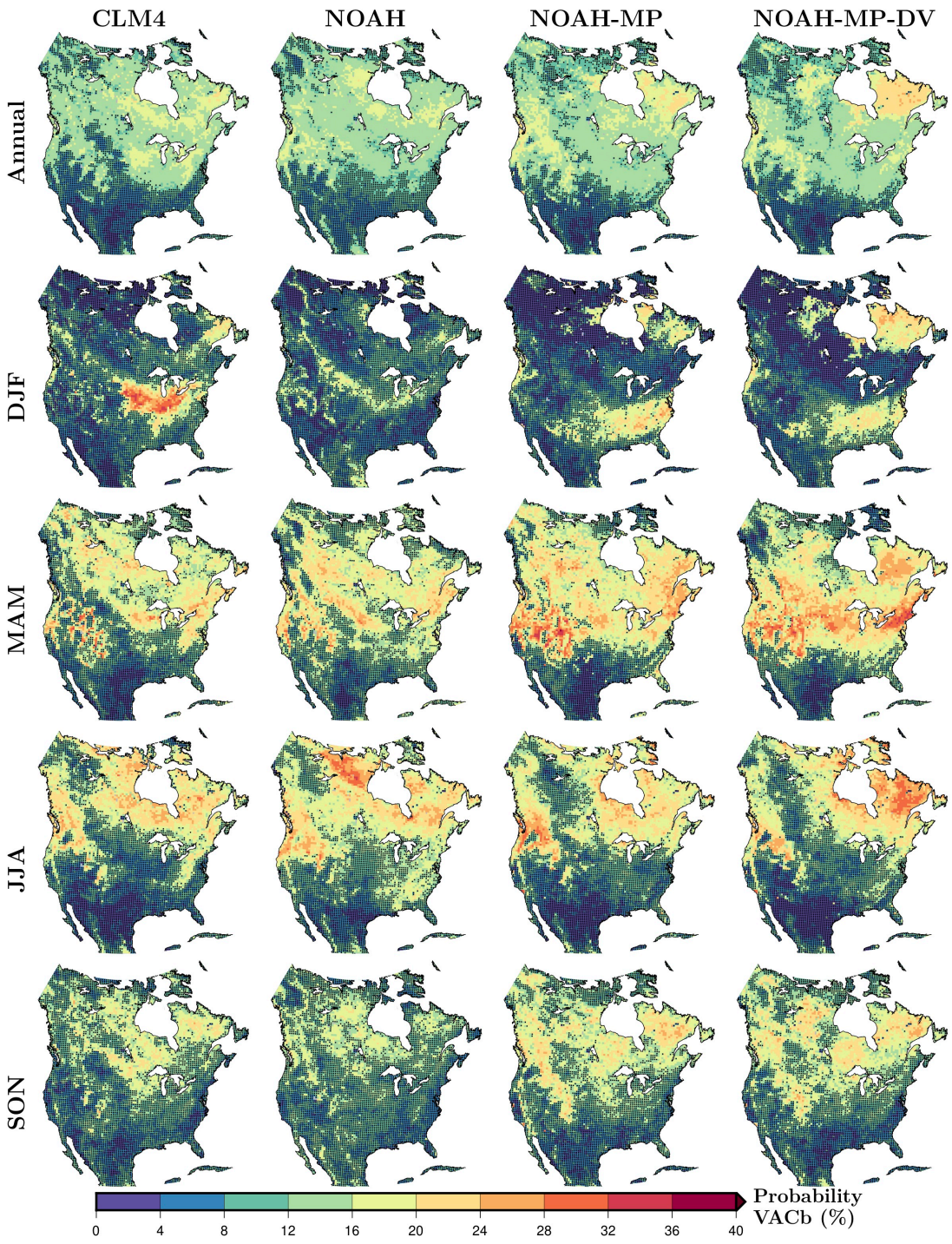

Figure B.3: As in Figure B.2 but for the VAC_b category.

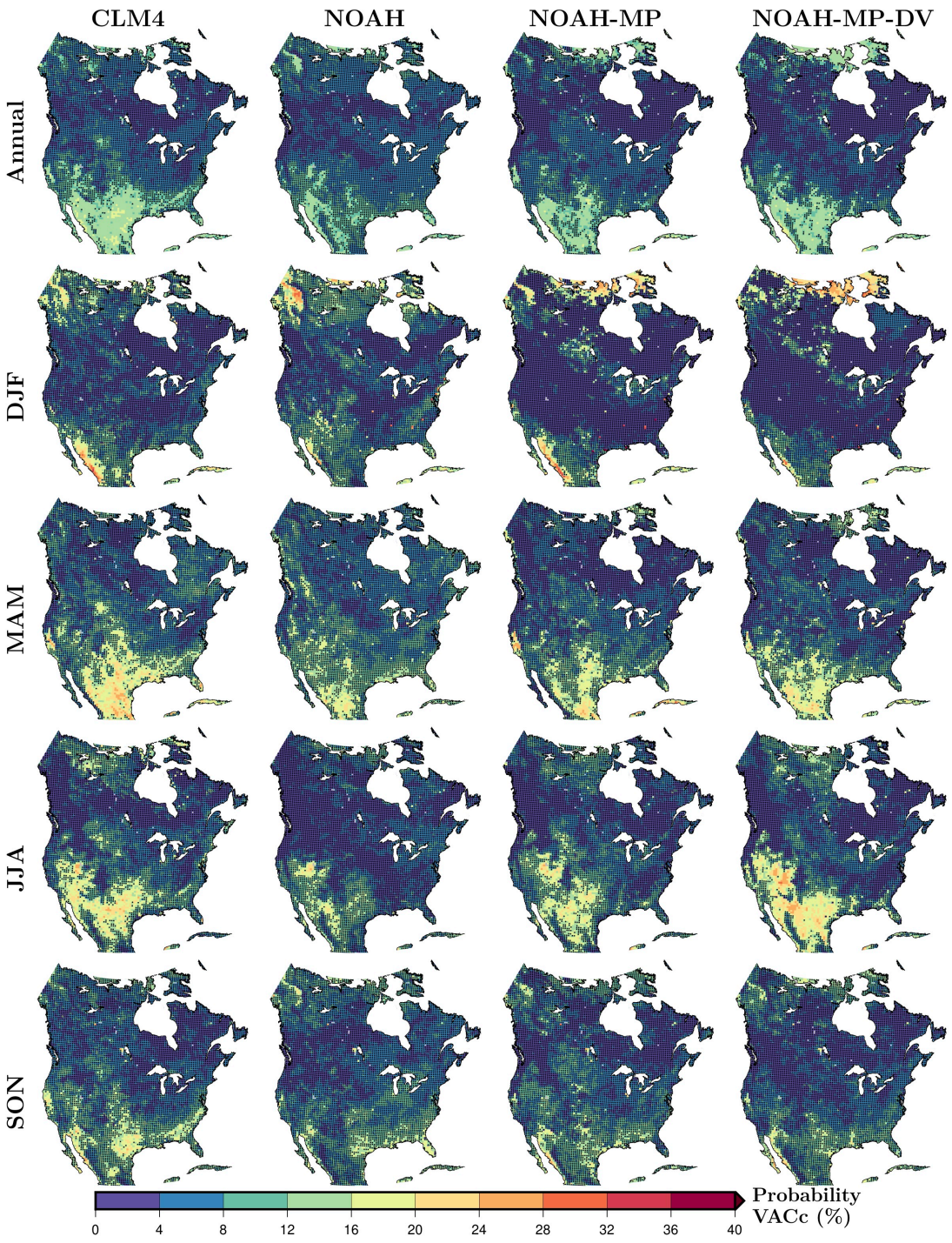

Figure B.4: As in Figure B.2 but for the VAC_c category.

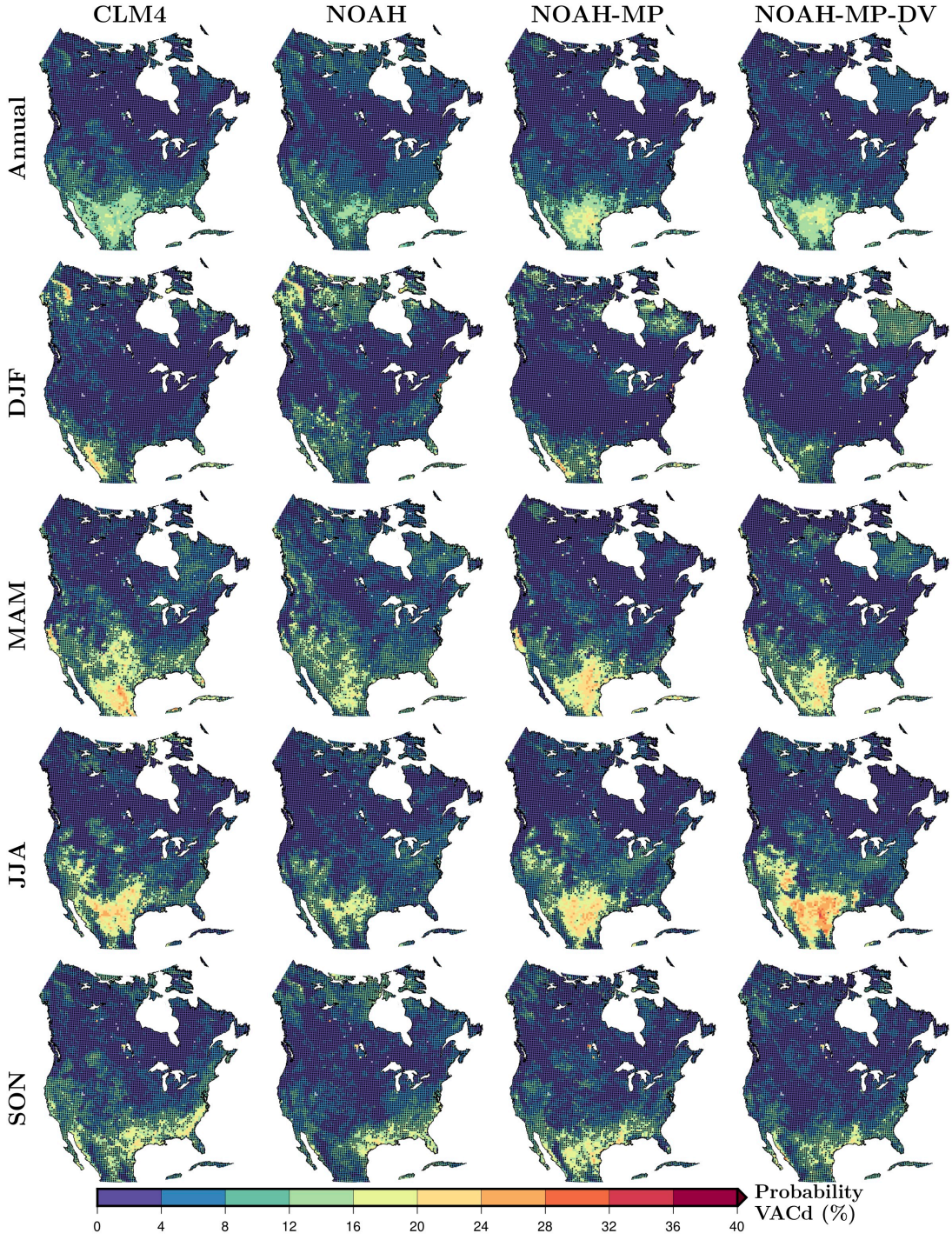

Figure B.5: As in Figure B.2 but for the VAC_d category.

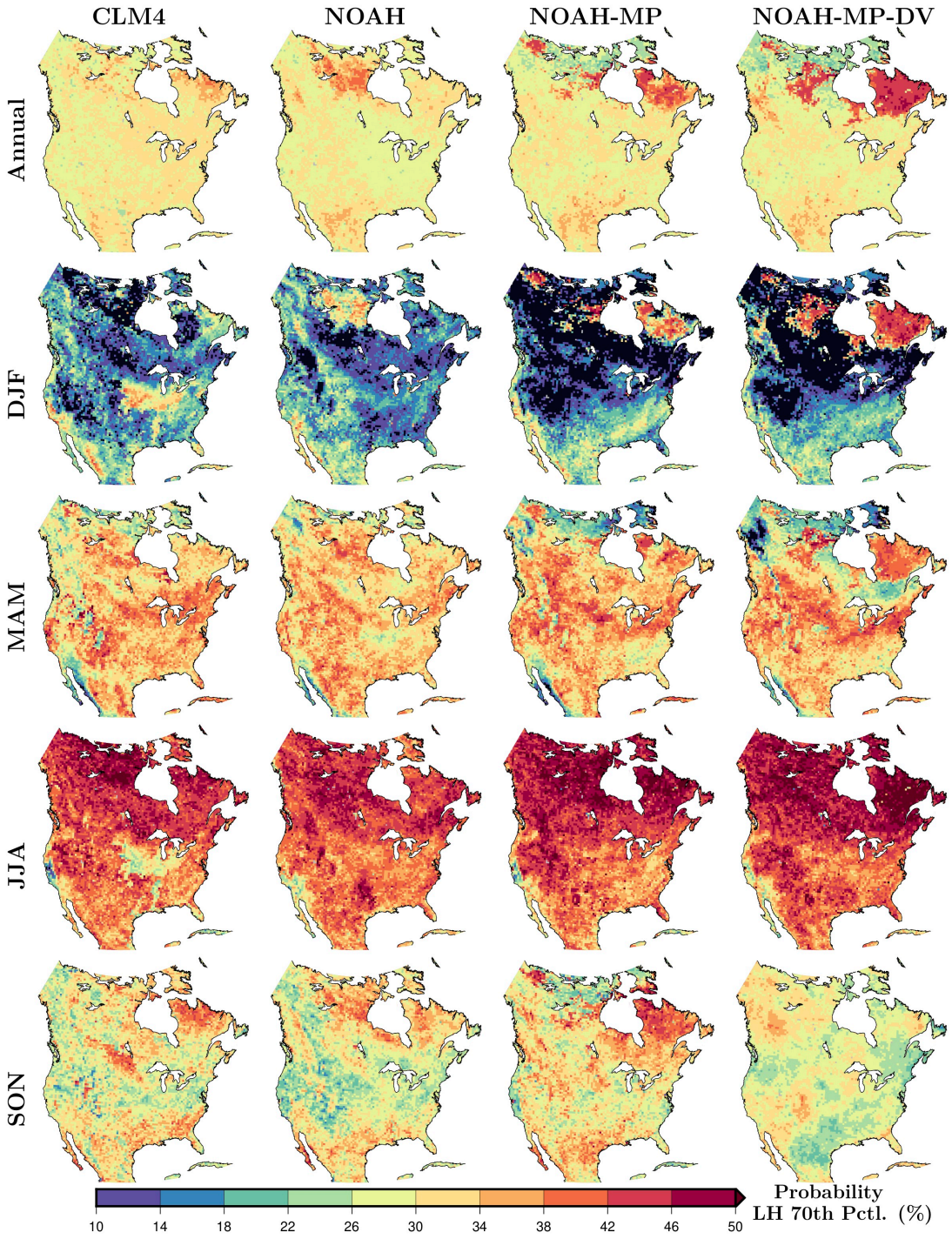

Figure B.6: Frequency of occurrence for the extreme high latent heat flux for each simulation annually and seasonally; DJF, MAM, JJA and SON. Extreme high latent heat flux events are defined as values higher than the 70th percentile of the latent heat flux time series from 1980 to 2000 at each grid cell.

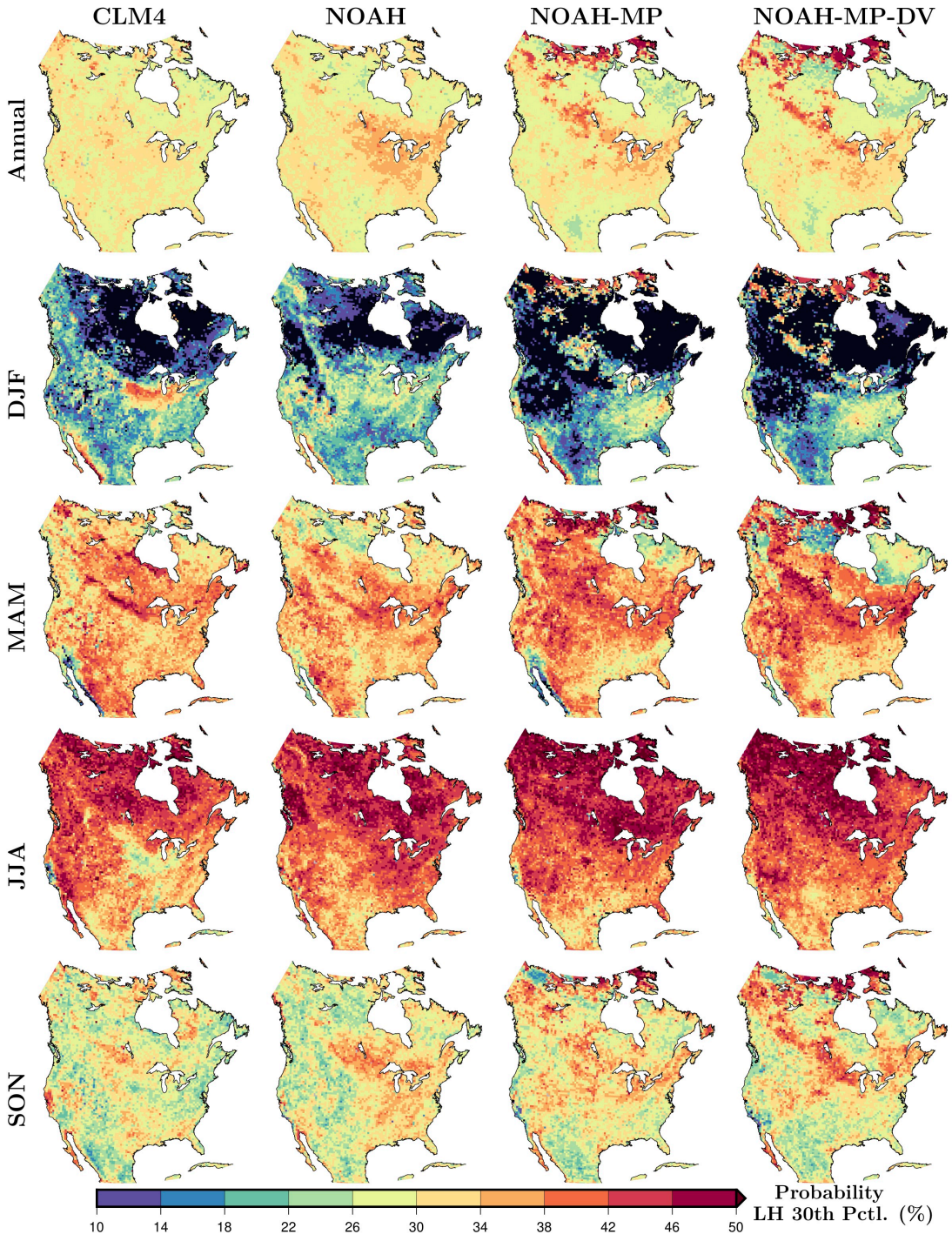

Figure B.7: Frequency of occurrence for the extreme low latent heat flux for each simulation annually and seasonally; DJF, MAM, JJA and SON. Extreme high latent heat flux events are defined as values lower than the 30th percentile of the latent heat flux time series from 1980 to 2000 at each grid cell.

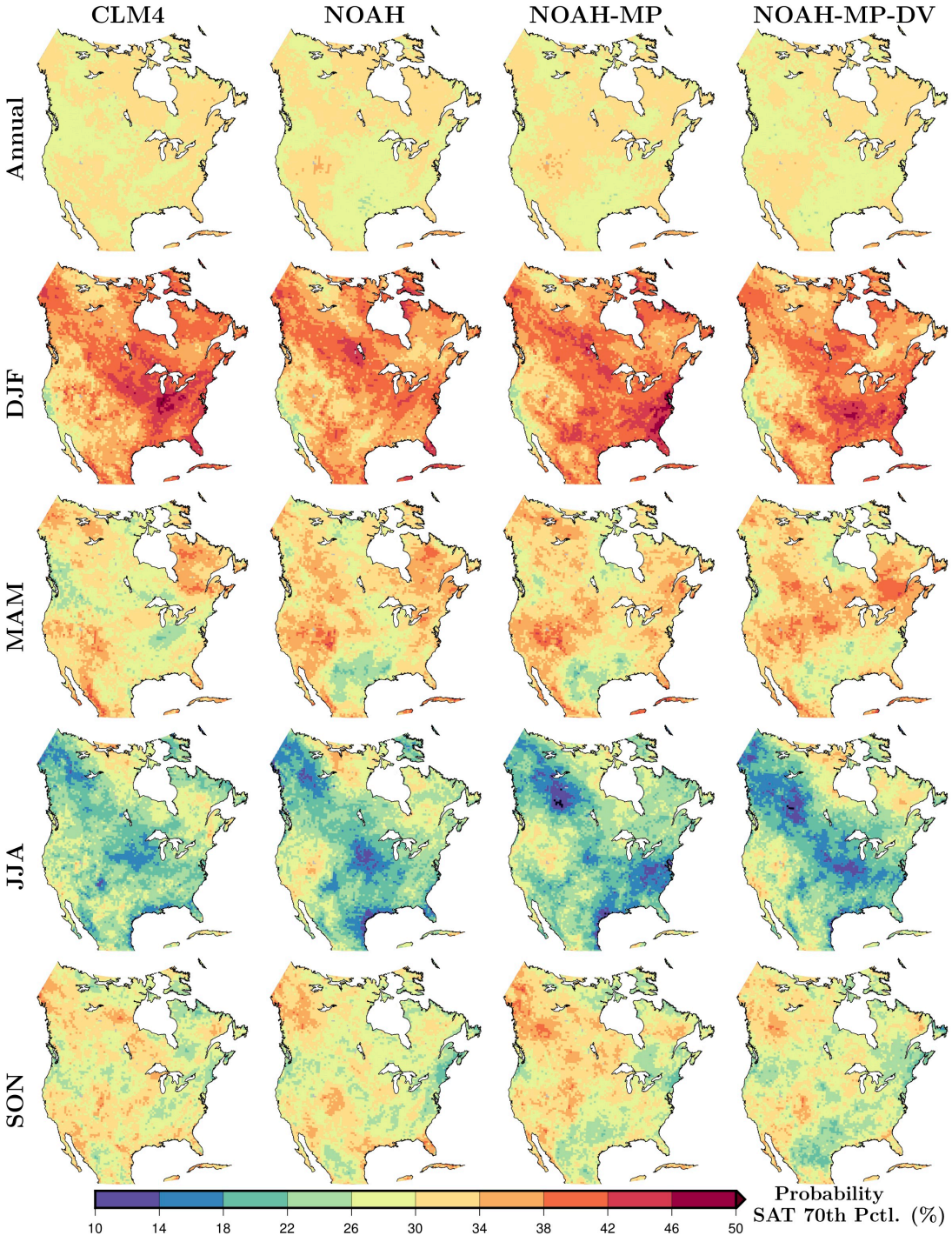

Figure B.8: As in Figure B.6 but for Surface Air Temperature (SAT.)

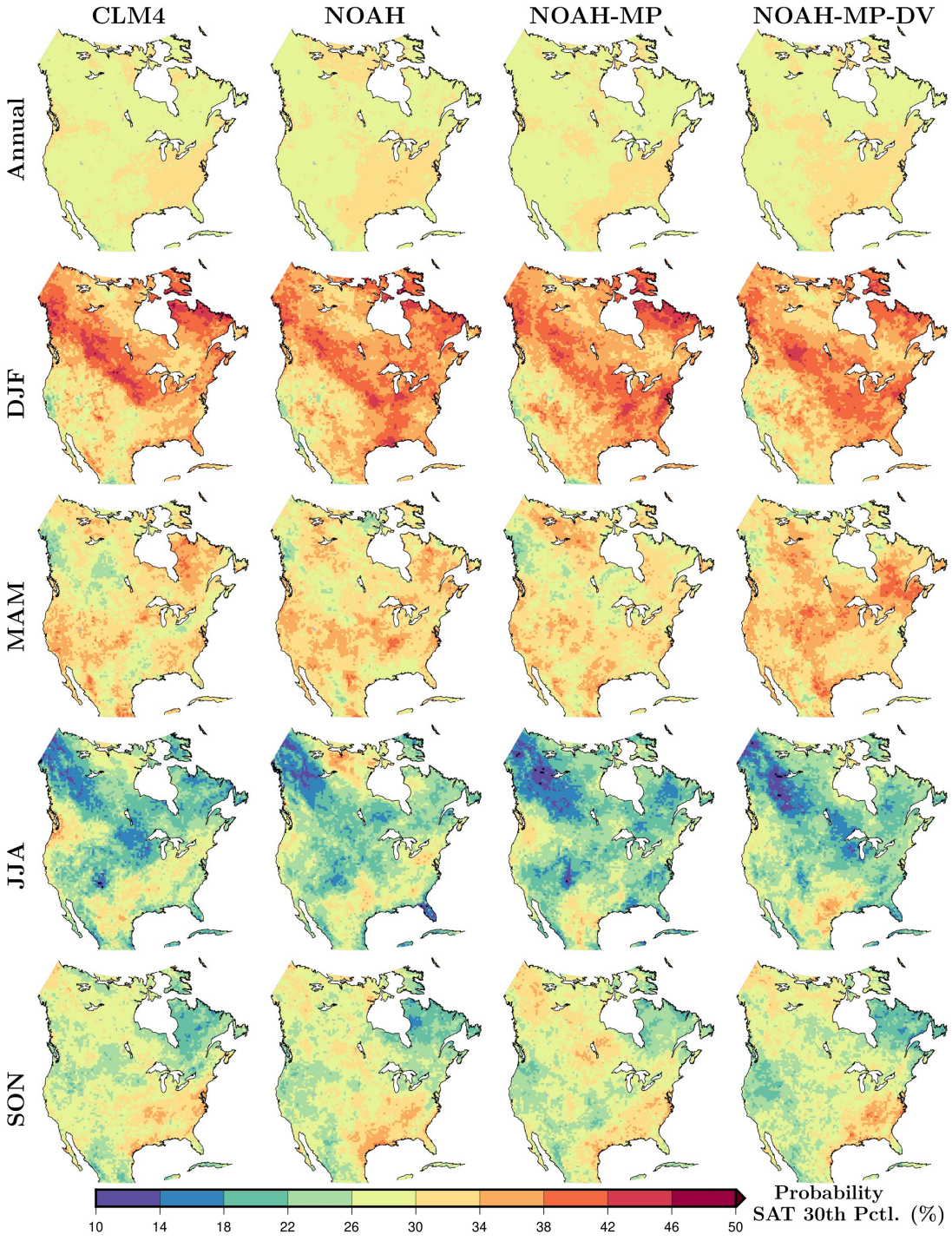

Figure B.9: As in Figure B.7 but for Surface Air Temperature (SAT.)

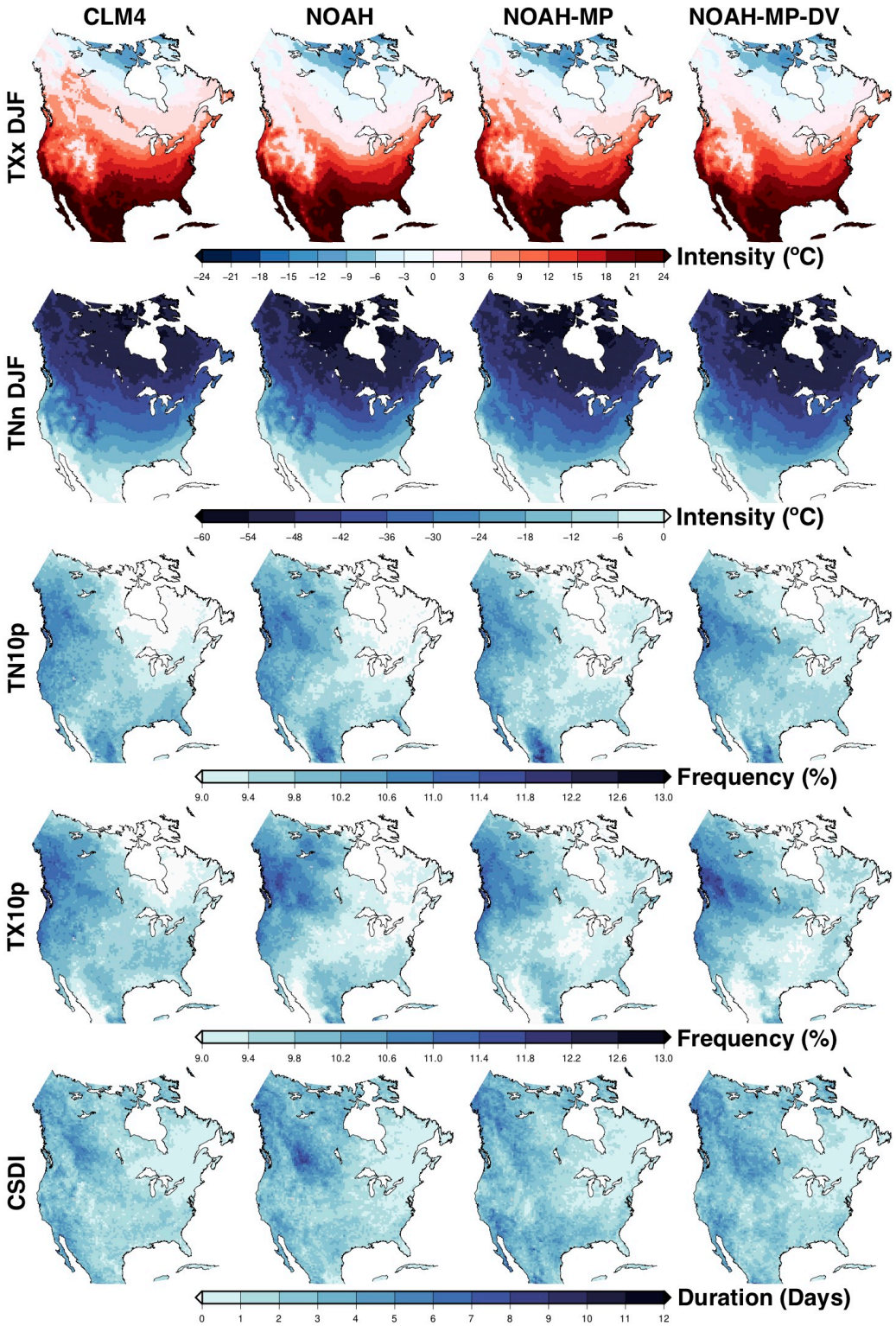

Figure B.10: Climatologies of extreme indices associated with intensity, frequency, and duration of cold extreme temperature events for each simulation separately (Table 3.2). The indices are computed using the mean of each index from 1980 to 2012 for each simulation.

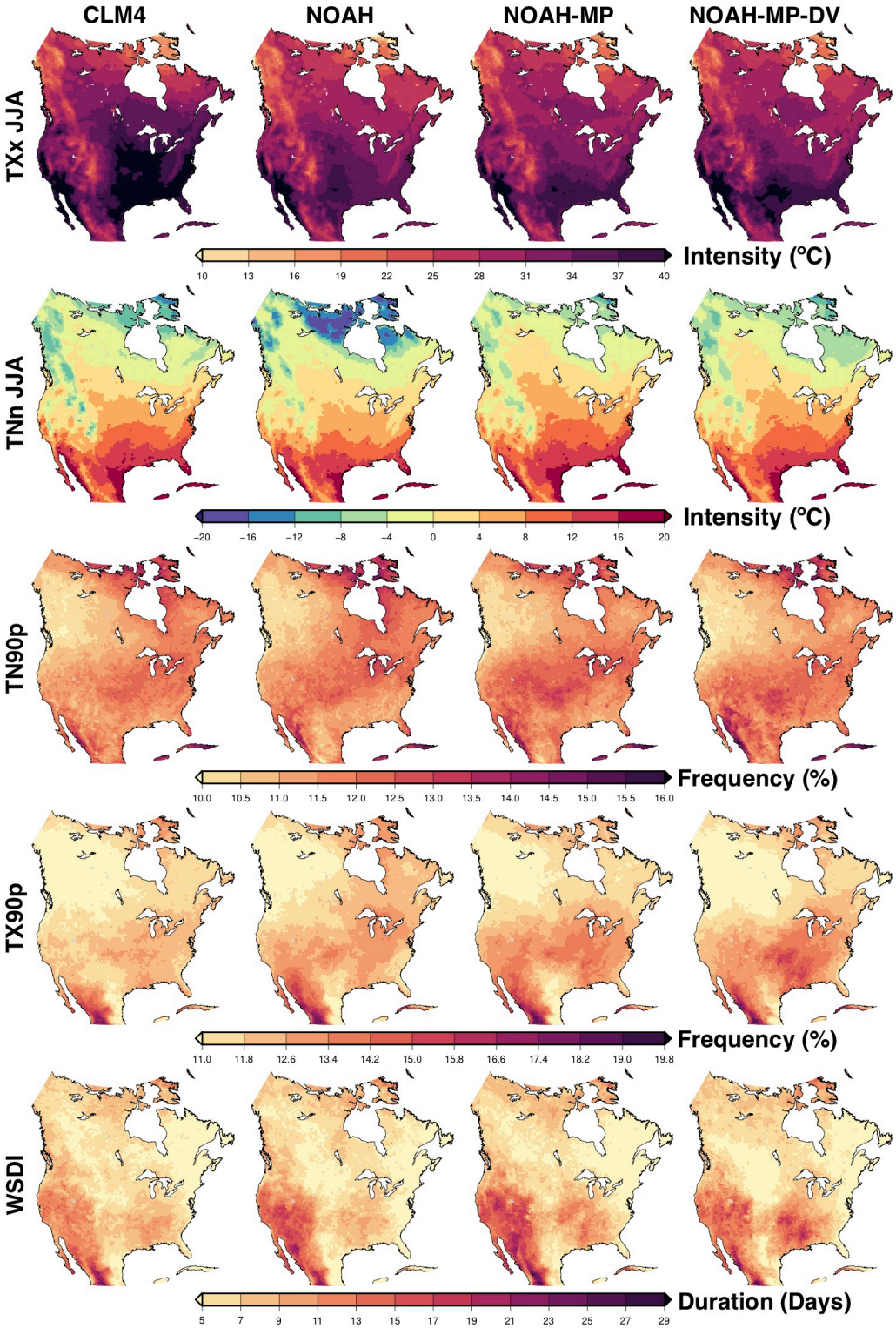

Figure B.11: As in Figure B.10 but for warm extreme temperature events.

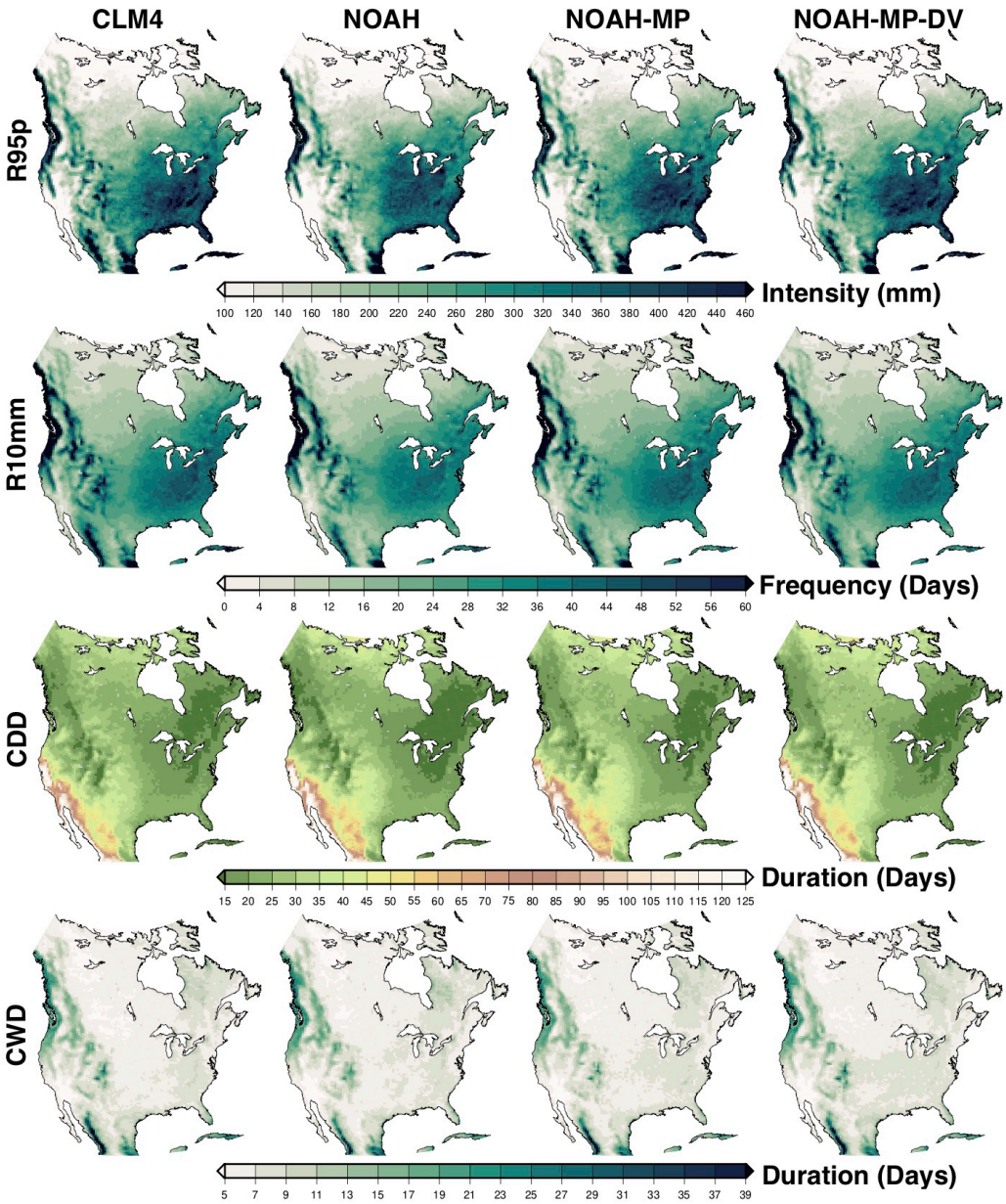

Figure B.12: As in Figure B.10 but for extreme precipitation events.

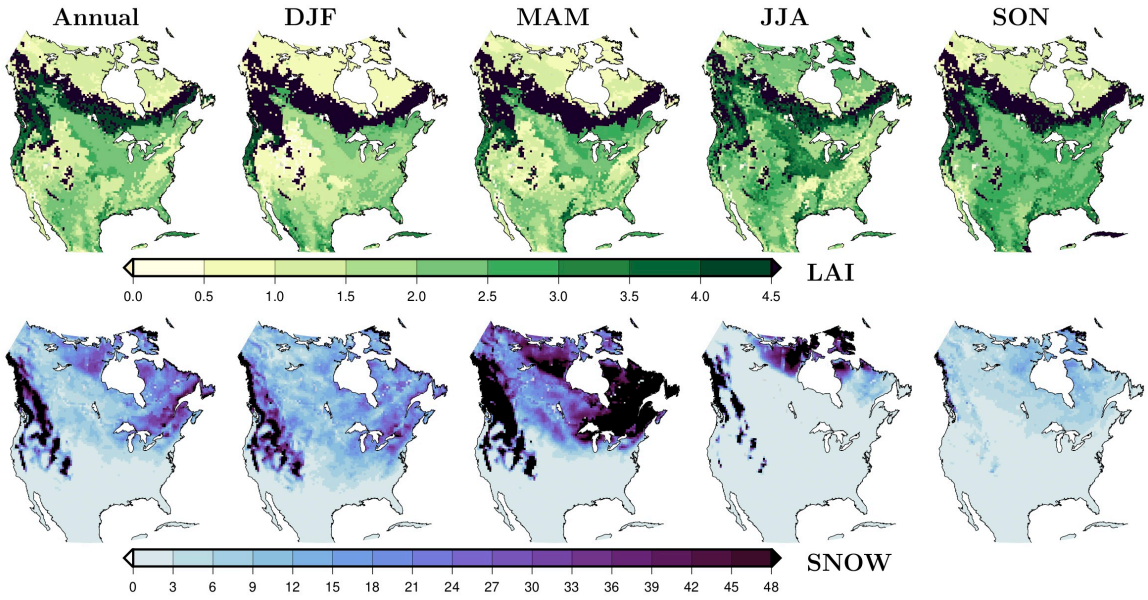

Figure B.13: Ranges across the WRF simulations (i.e., difference between the highest value and the lowest value of the simulation ensemble at each grid cell) of Leaf Area Index (LAI, m^2/m^2) and snow water equivalent (kgm^2) annually and for each season. The range among simulations is computed using the mean of each index from 1980 to 2012 for each simulation.

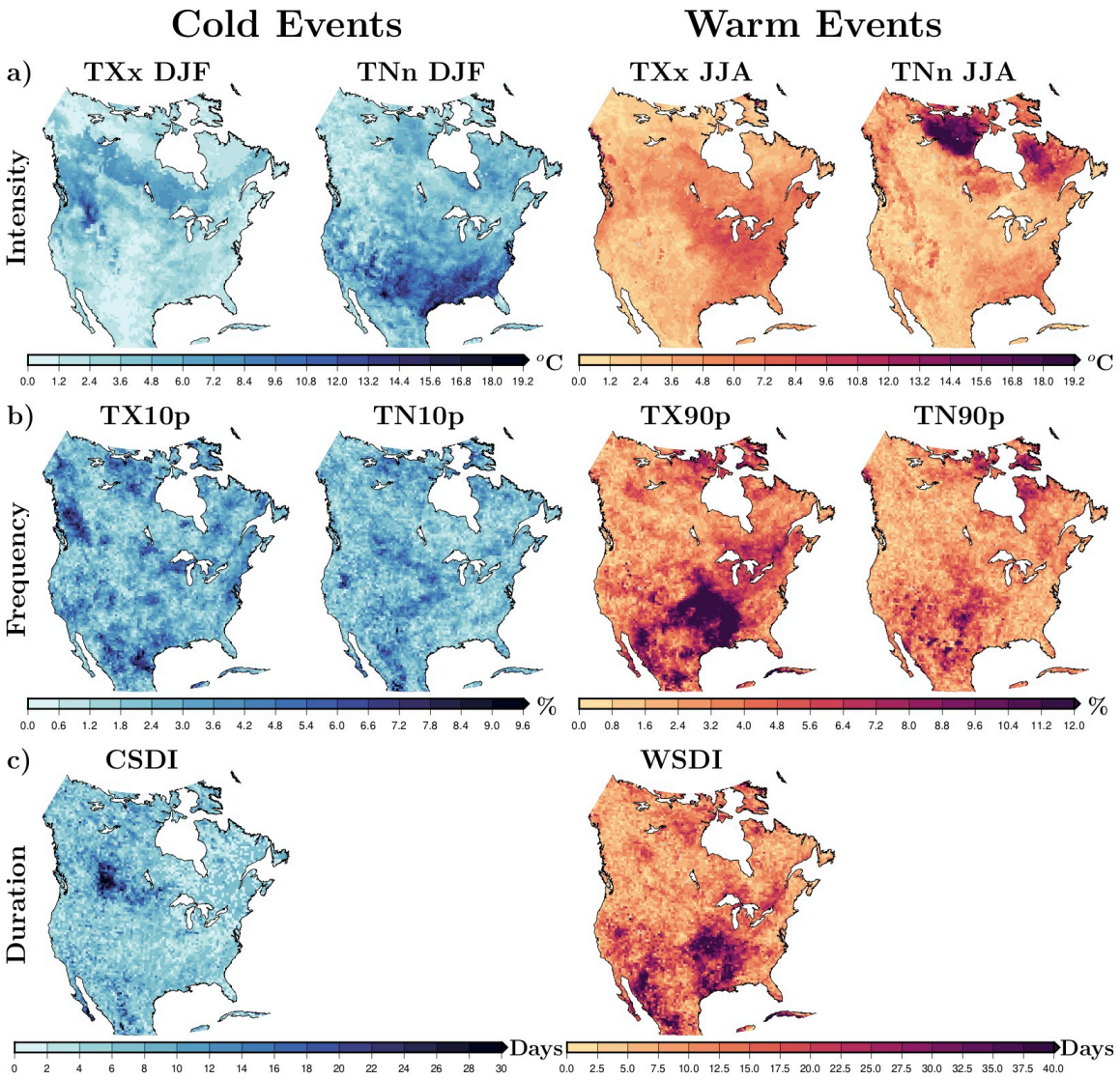

Figure B.14: Ranges across the WRF simulations (i.e., difference between the highest value and the lowest value of the simulation ensemble at each grid cell) of extreme indices associated with the intensity (a), frequency (b), and duration (c) of cold (left) and warm (right) extreme temperature events (Table 3.2). The range among simulations is computed using the 95th percentile of each index from 1980 to 2012 for each simulation, except for the TNnDJF and TNnJJA index for which the 5th percentile of the period was employed.

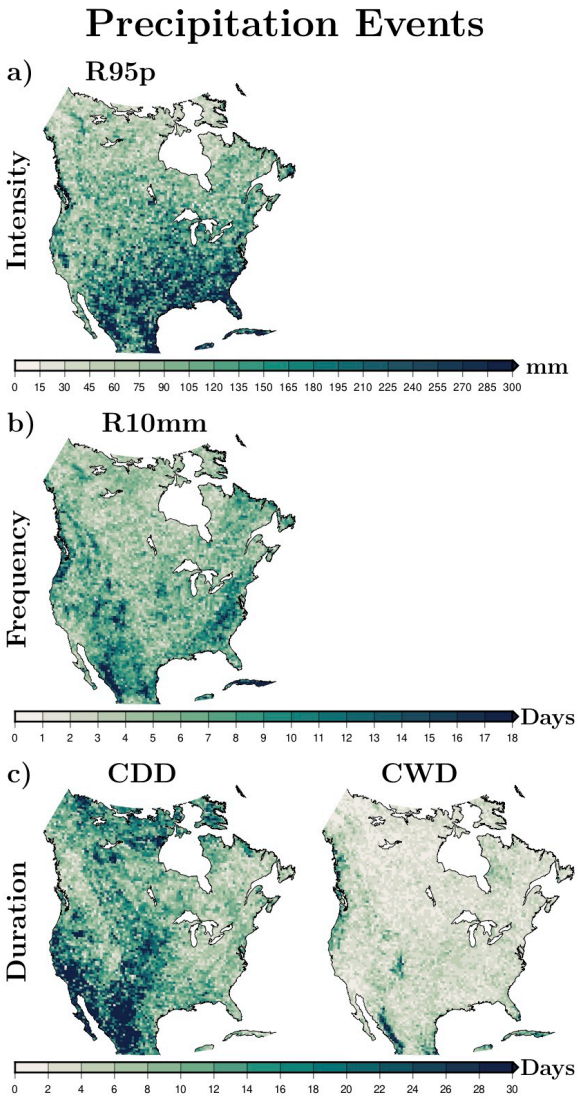

Figure B.15: Multi-model ranges across the WRF simulations (i.e., difference between the highest value and the lowest value of the simulation ensemble at each grid cell) of extreme indices associated with the intensity (a), frequency (b), and duration (c) of extreme precipitation events (Table 3.2). The range among simulations is computed using the 95th percentile of each index from 1980 to 2012 for each simulation.

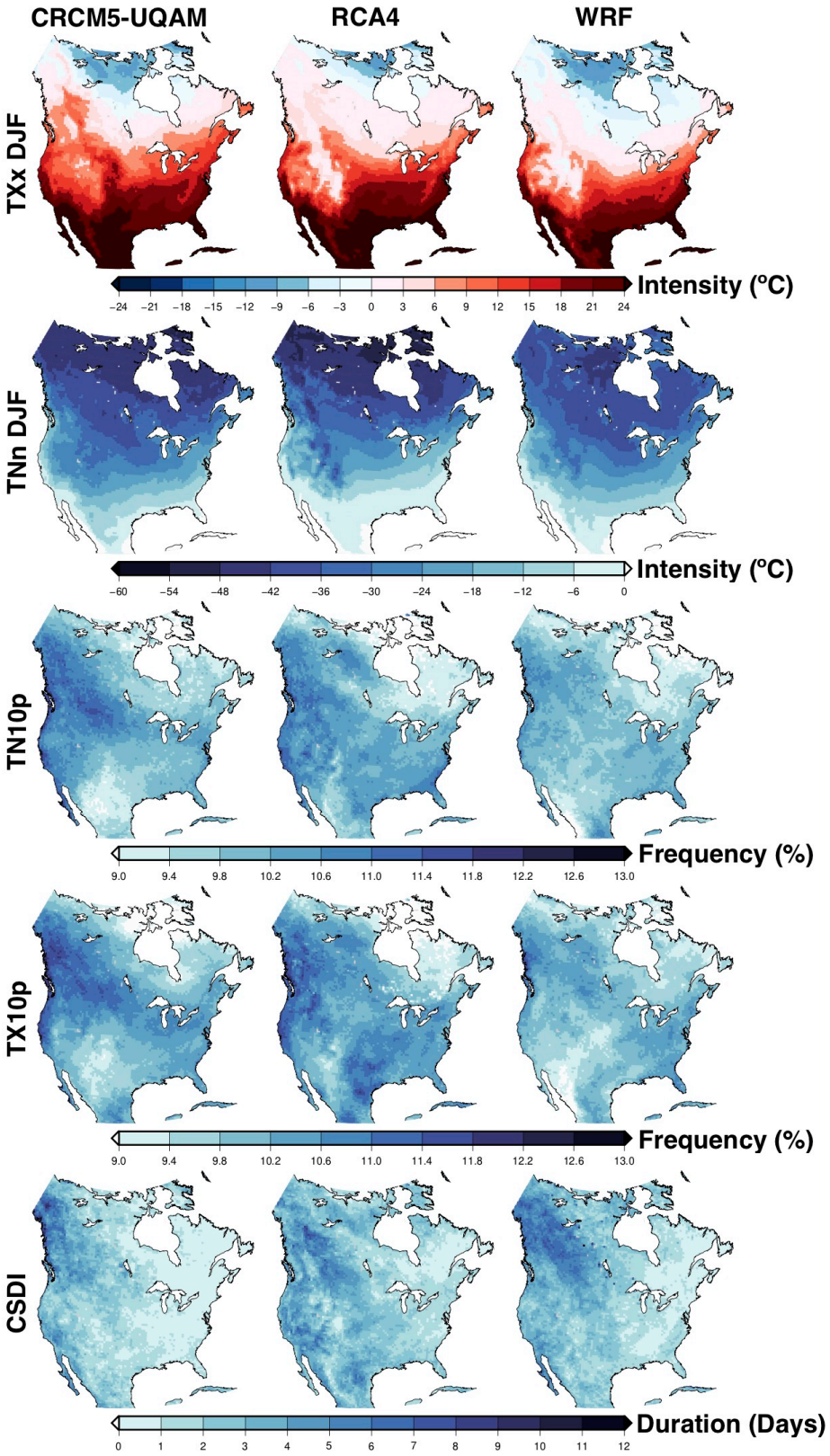

Figure B.16: Climatologies of extreme indices associated with intensity, frequency, and duration of cold extreme temperature events for each CORDEX simulation separately (Table 3.2). The indices are computed using the mean of each index from 1980 to 2012 for each simulation.

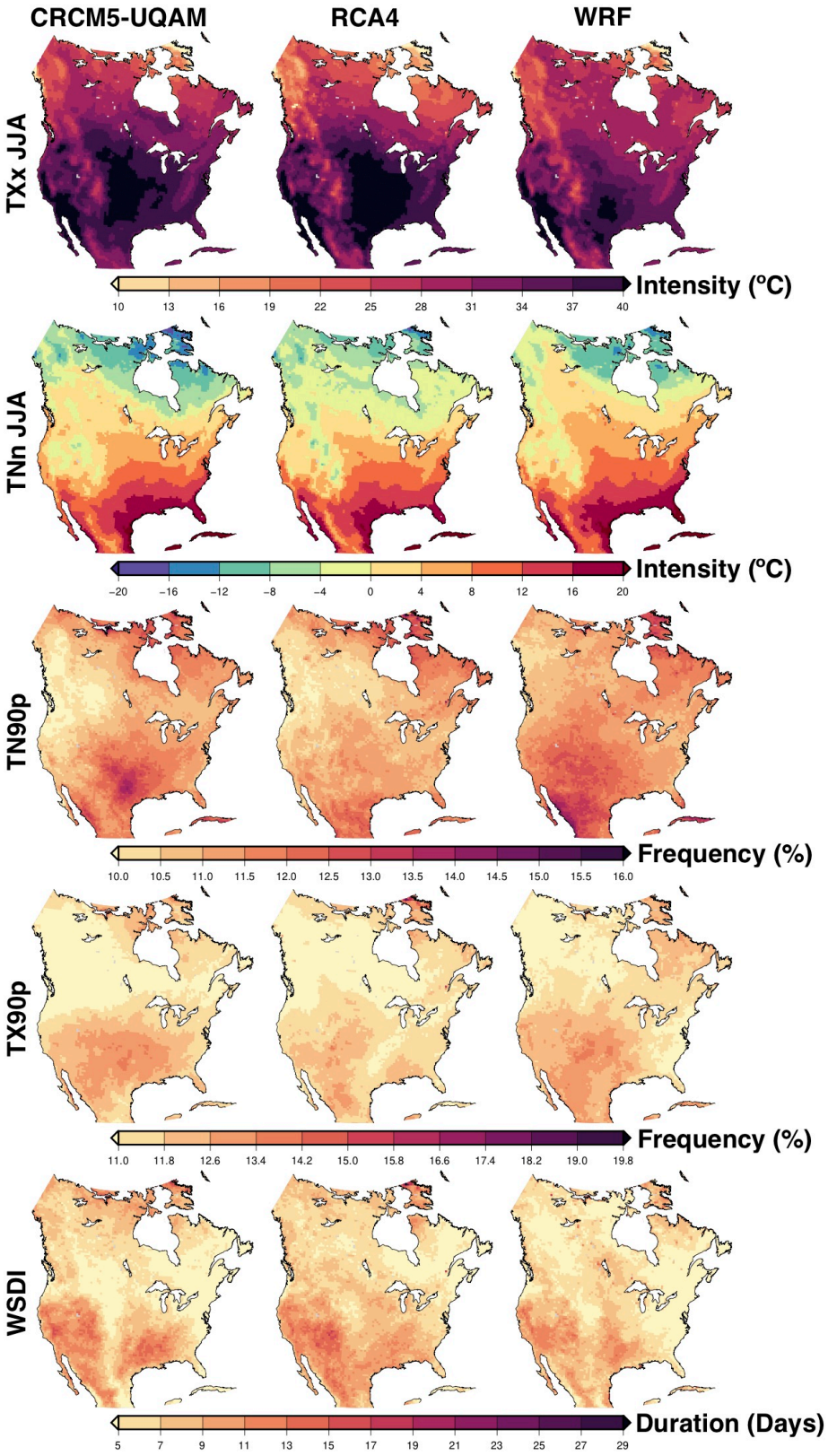

Figure B.17: As in Figure B.16 but for warm temperature extremes.

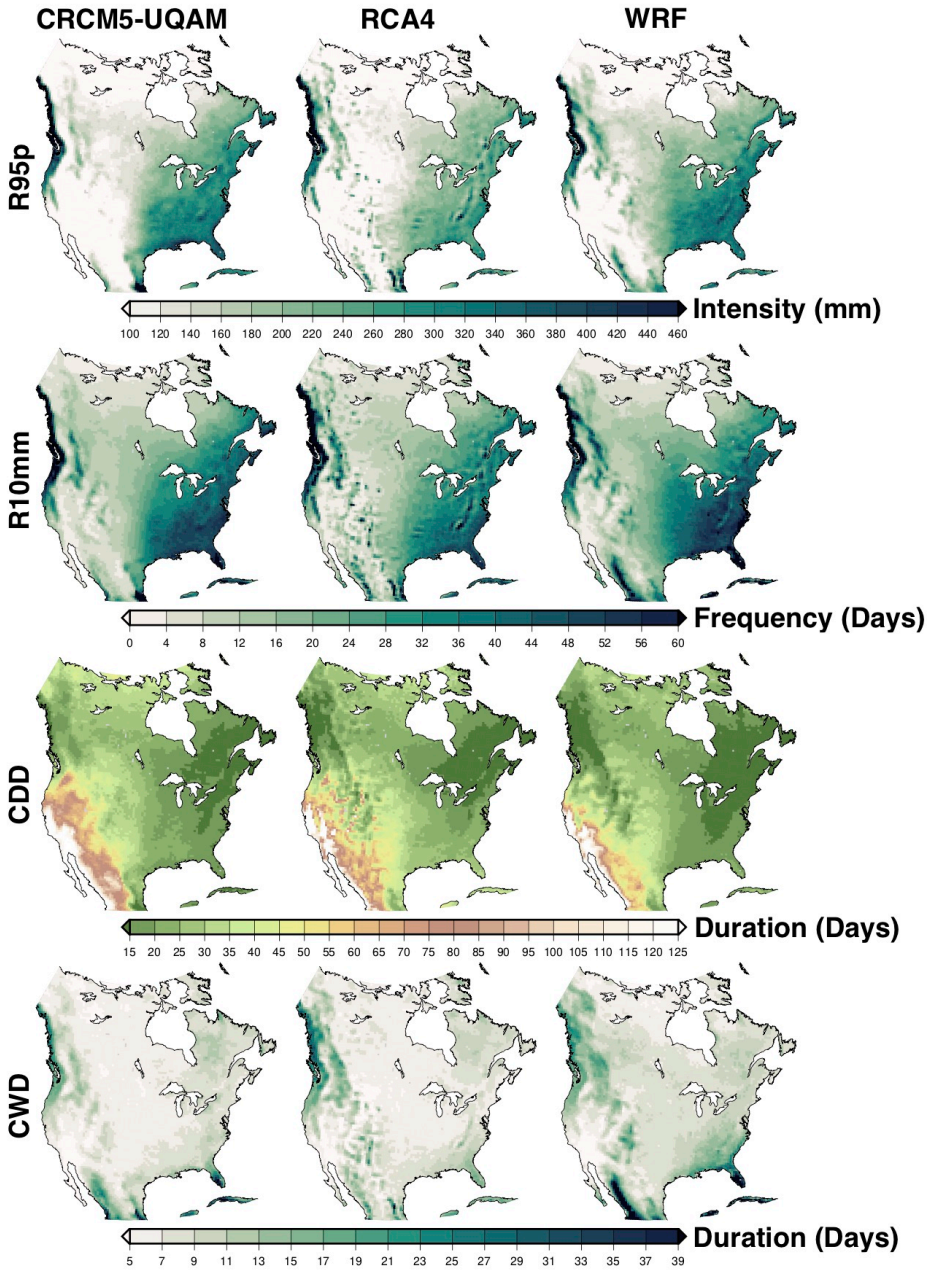

Figure B.18: As in Figure B.16 but for precipitation extremes.

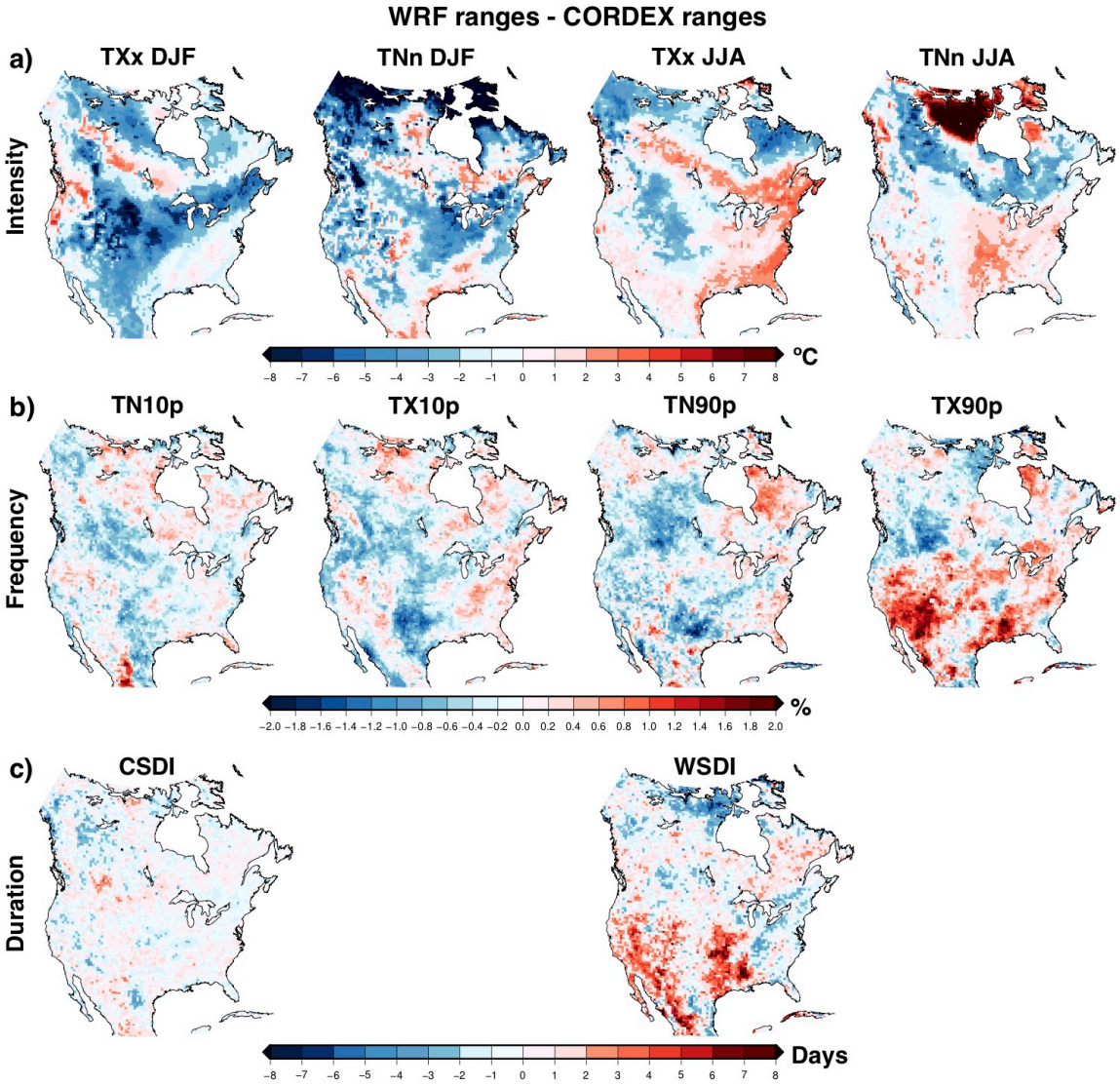

Figure B.19: Differences between the range among the WRF simulations and the range among three CORDEX simulations in representing extreme indices related to intensity (a), frequency (b), and duration (b) of cold (left two columns) and warm (right two columns) extreme temperature events (Table 3.2). Ranges across each simulation ensemble are computed using the mean of each index from 1980 to 2012 for each simulation. Red color means larger rages among the WRF simulations than among the CORDEX simulations, white color means comparable values for ranges among the WRF simulations and the CORDEX simulations and blue color means larger ranges among the CORDEX simulations than among the WRF simulations.

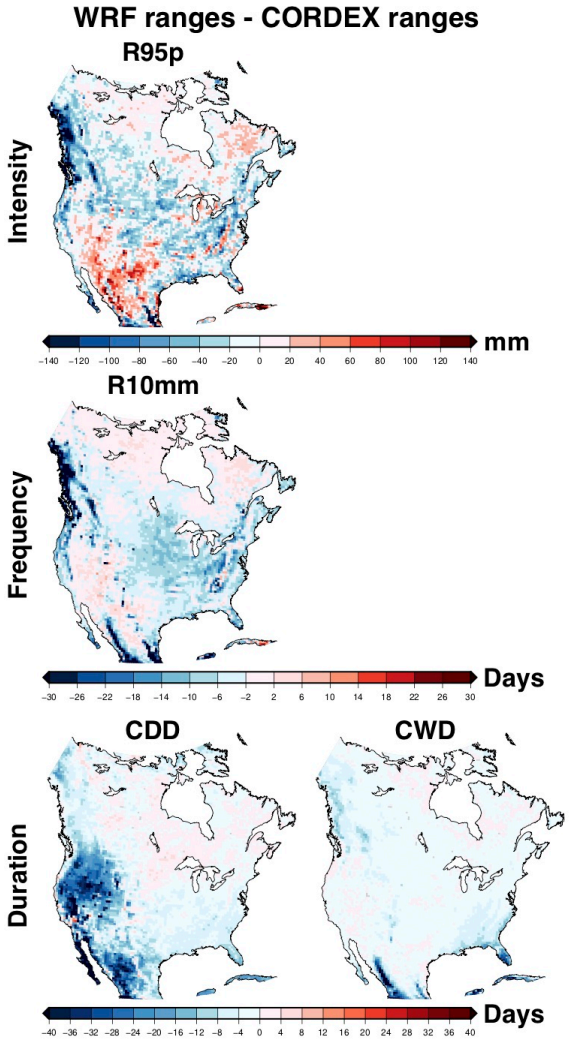

Figure B.20: As in Figure B.19 but for precipitation extremes.

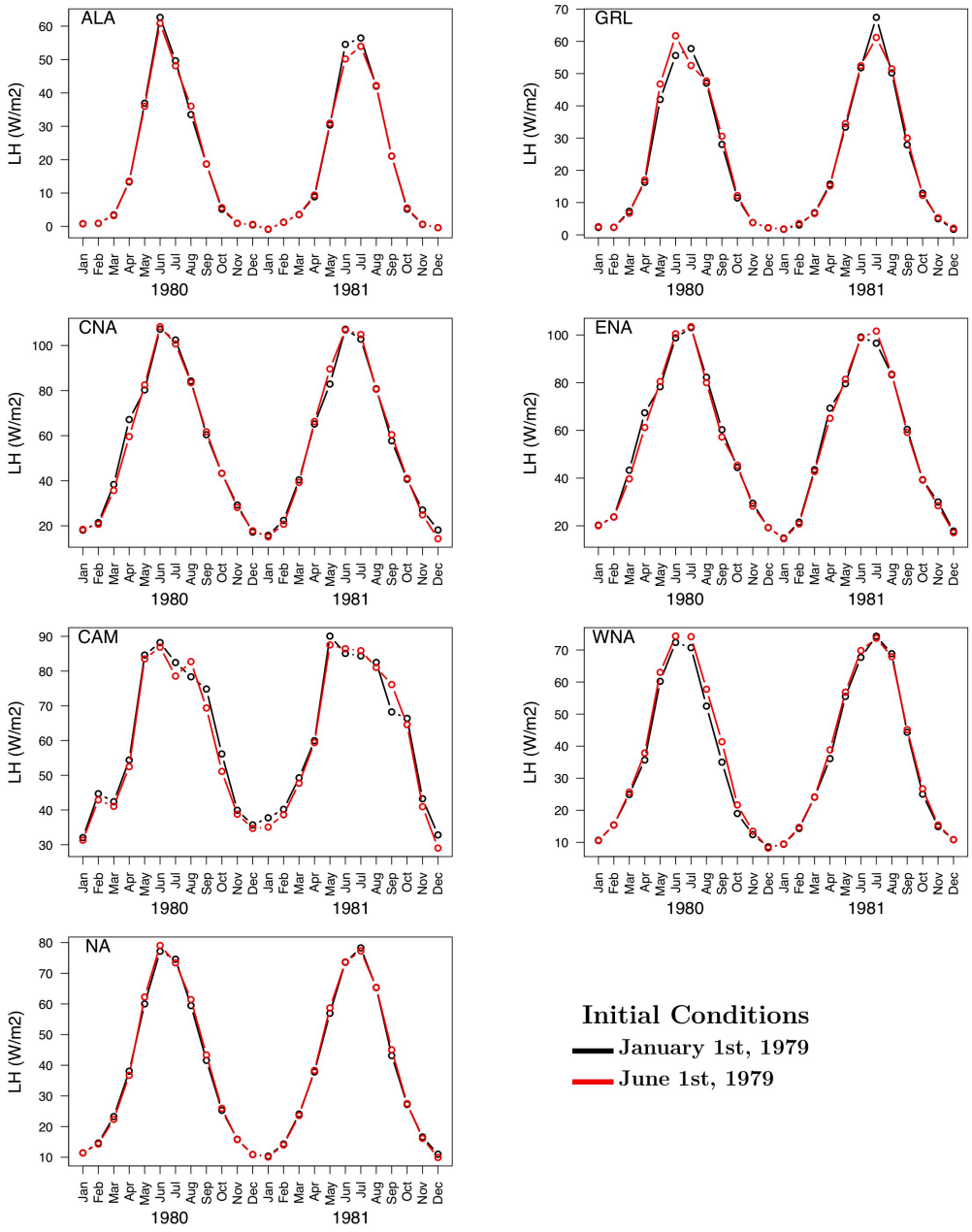

Figure B.21: Monthly latent heat (LH) flux from 1980 to 1981 averaged over North America (NA) and the subdomains included in this analysis. The black line represents the outputs from the WRF-CLM4 simulation with initial conditions on January 1st, 1979. The red line represents the outputs from a WRF-CLM4 simulation with initial conditions on June 1st, 1979.

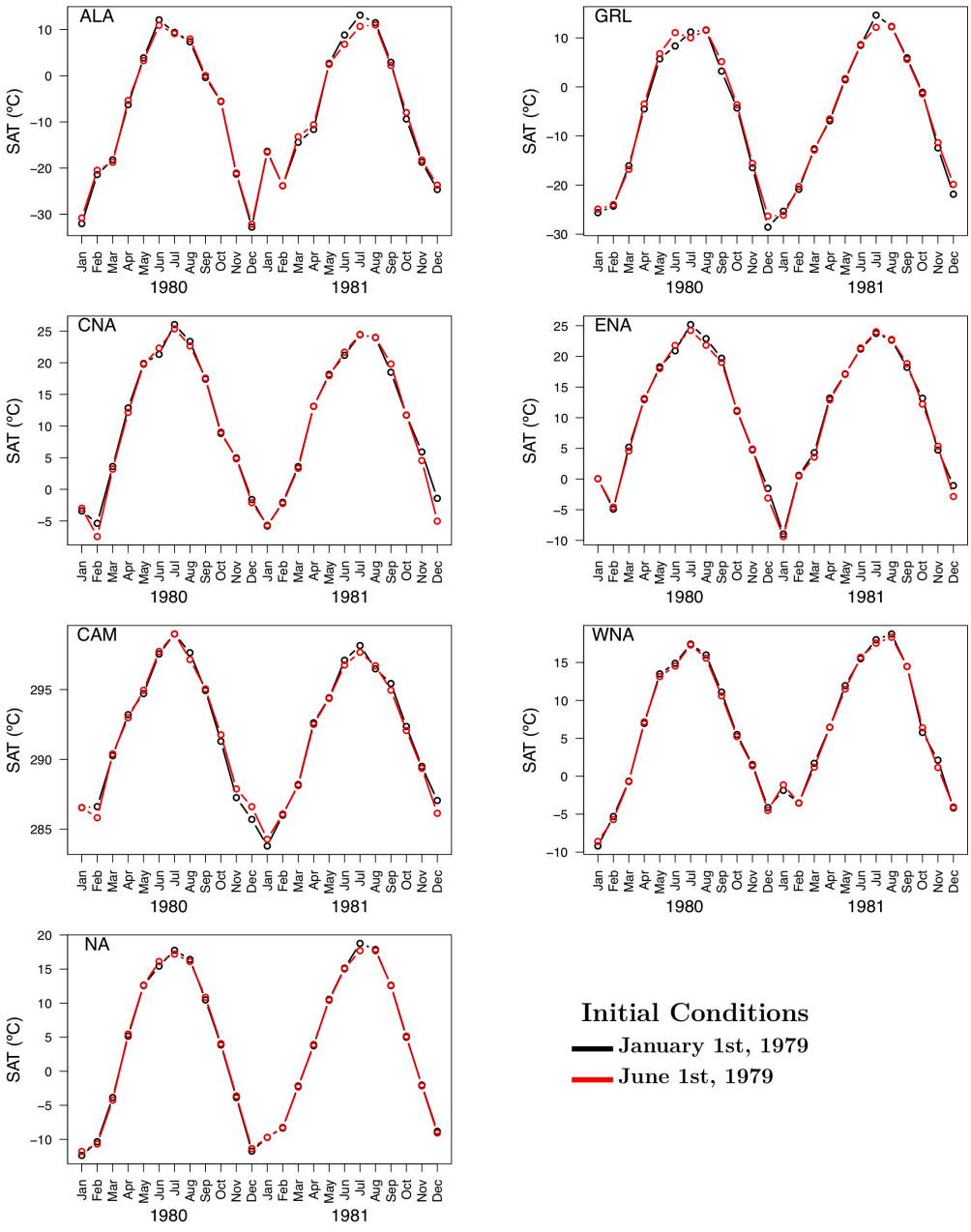

Figure B.22: As in Figure B.21 but for monthly Surface Air Temperature (SAT).

Bibliography

Barlage, M., Zeng, X., Wei, H., and Mitchell, K. E. (2005). A global 0.05 ° maximum albedo dataset of snow-covered land based on MODIS observations. *Geophysical Research Letters* **32**(17).

Appendix C

Supporting Information for Chapter 4

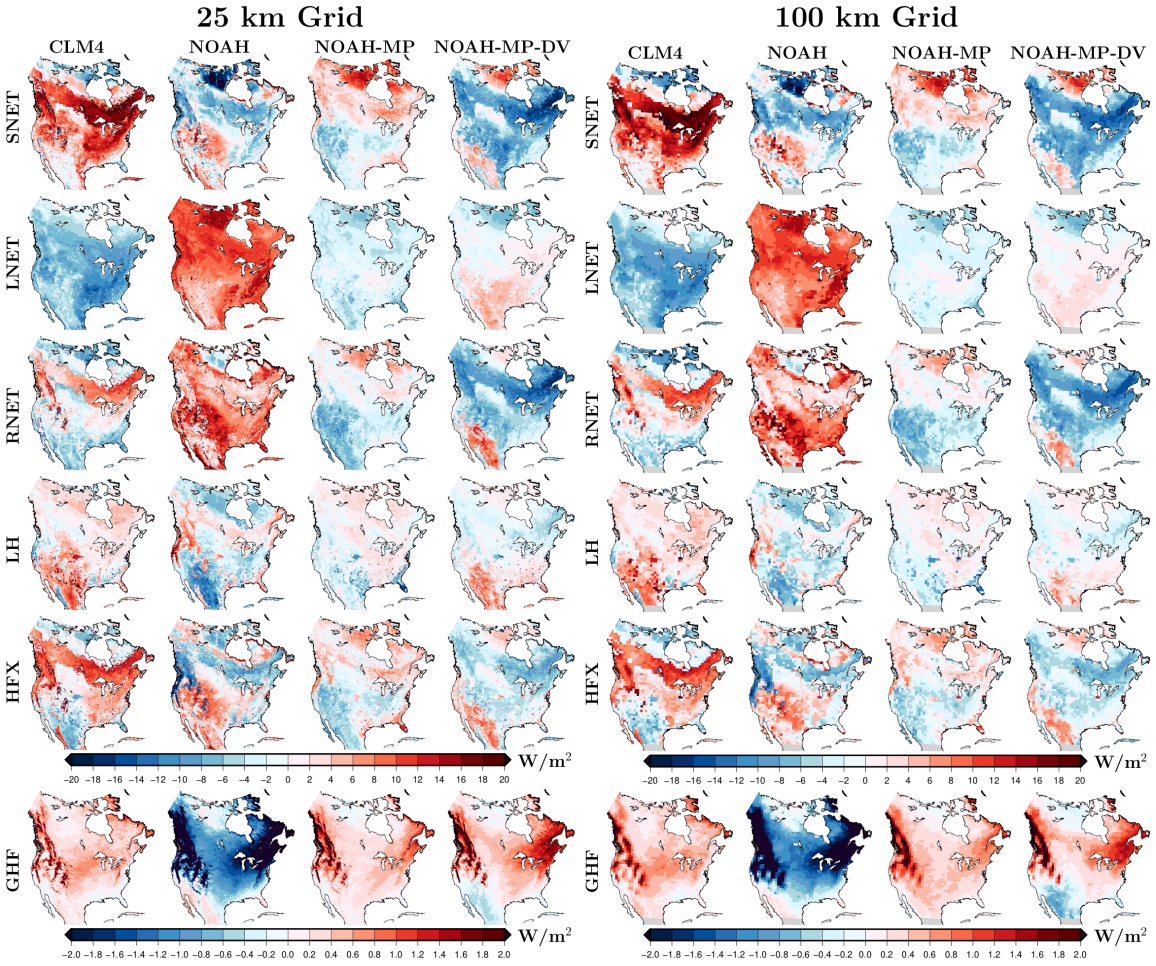

Figure C.1: Climatology of energy terms at the surface (net shortwave radiation SNET; net longwave radiation LNET; soil net radiation RNET; latent heat flux LH; sensible heat flux HFX; and ground heat flux GHF) for each LSM simulation relative to the multi-model mean for each energy term. Climatologies are estimated as the temporal average for the period 1980-2013 using simulations performed with 25 km resolution (left) and 100 km resolution (right).

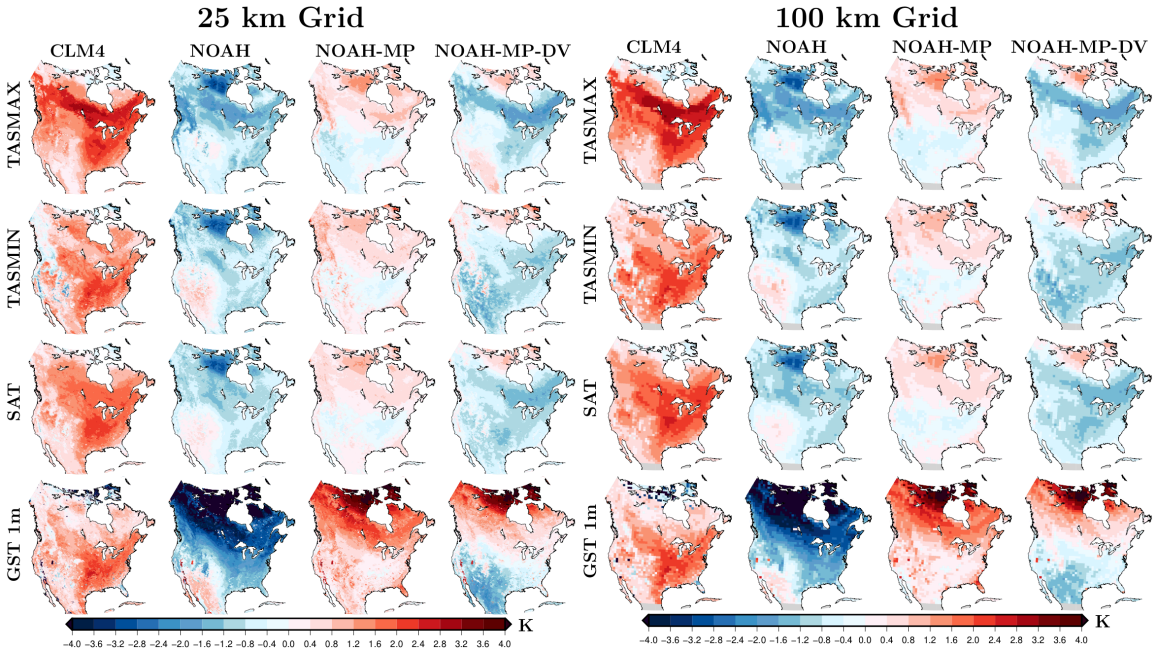

Figure C.2: Climatology of near-surface temperature conditions (maximum temperature TASMAX; minimum temperature TASMIN; surface air temperature SAT; and soil temperature at 1m depth GST 1m) for each LSM simulation relative to the multi-model mean for each energy term. Climatologies are estimated as the temporal average for the period 1980-2013 using simulations performed with 25 km resolution (left) and 100 km resolution (right).

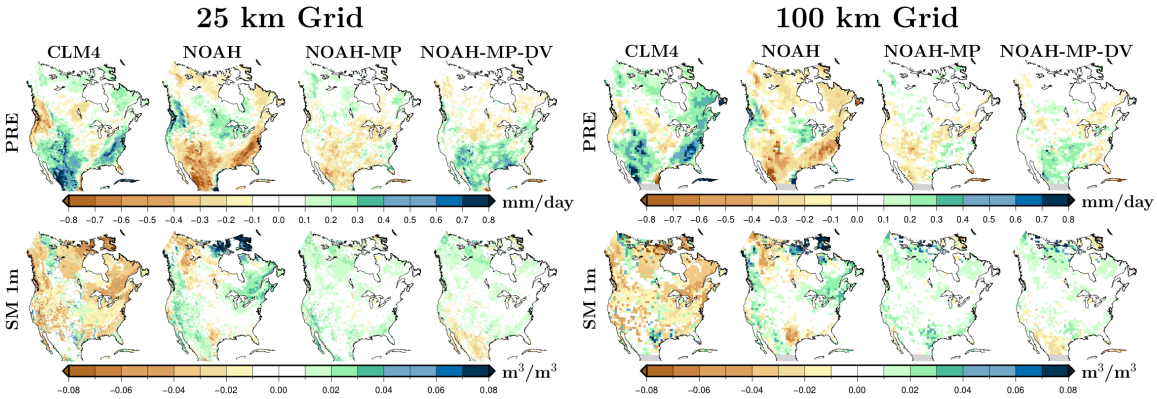

Figure C.3: Climatology of near-surface humid conditions (accumulated precipitation at the surface PRE; and soil moisture contained in the first soil meter SM 1m) for each LSM simulation relative to the multi-model mean for each energy term. Climatologies are estimated as the temporal average for the period 1980-2013 using simulations performed with 25 km resolution (left) and 100 km resolution (right).

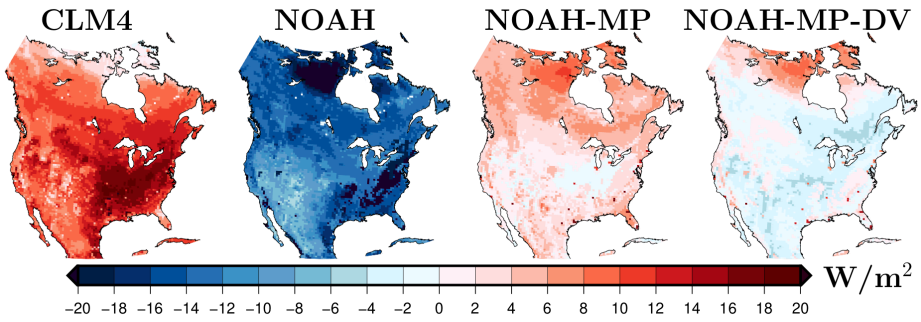

Figure C.4: Upward component of the longwave radiation climatology at the ground surface for each LSM simulation. Climatologies are estimated as the temporal average for the period 1980-2013 using simulations performed with 50 km resolution.

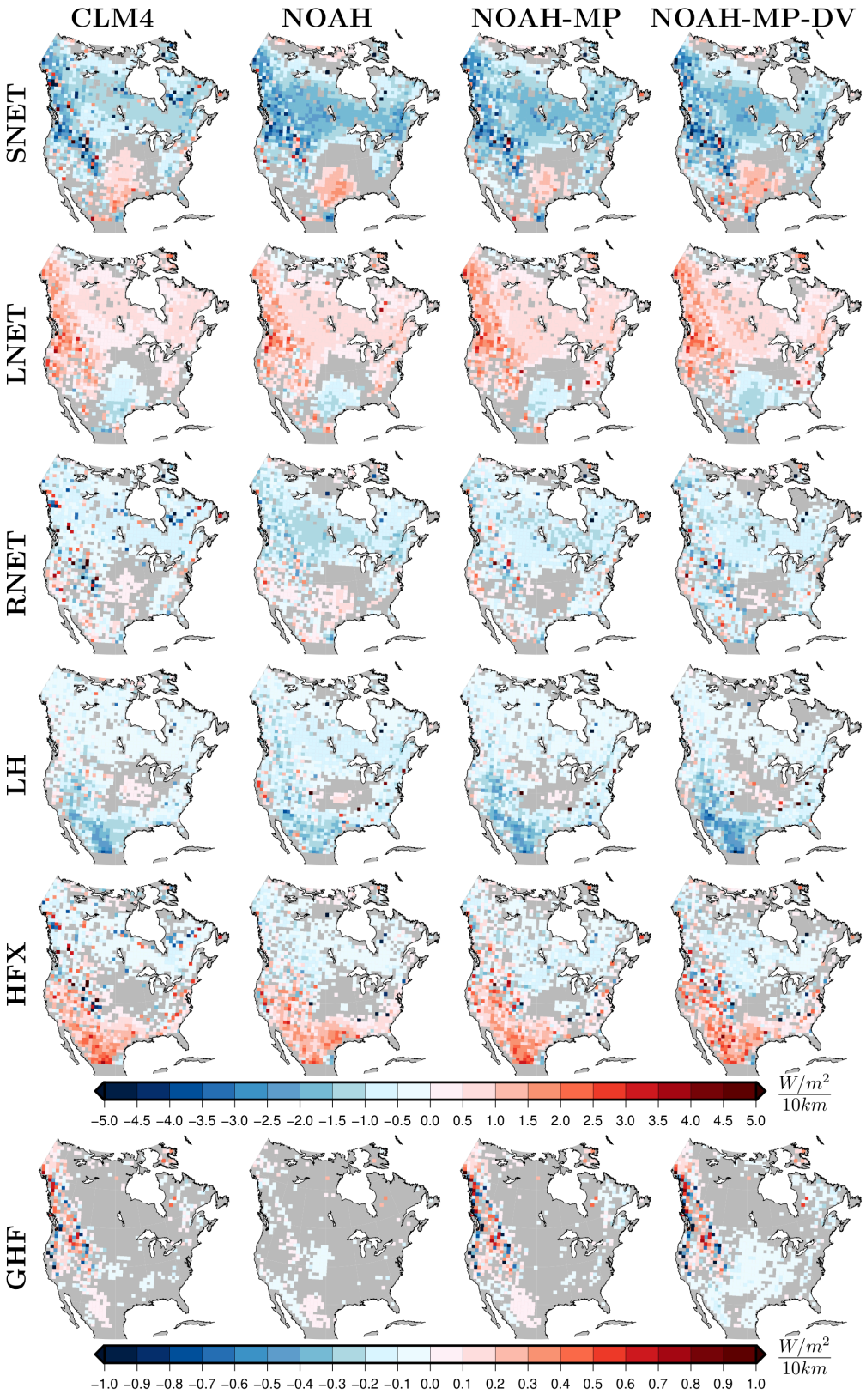

Figure C.5: Annual mean change in surface energy fluxes per 10 km reduction in horizontal resolution (coarser resolutions) for each LSM set of simulations for the analysis period 1980-2013. Only grid cells where the response is significant at the 95% level are plotted.

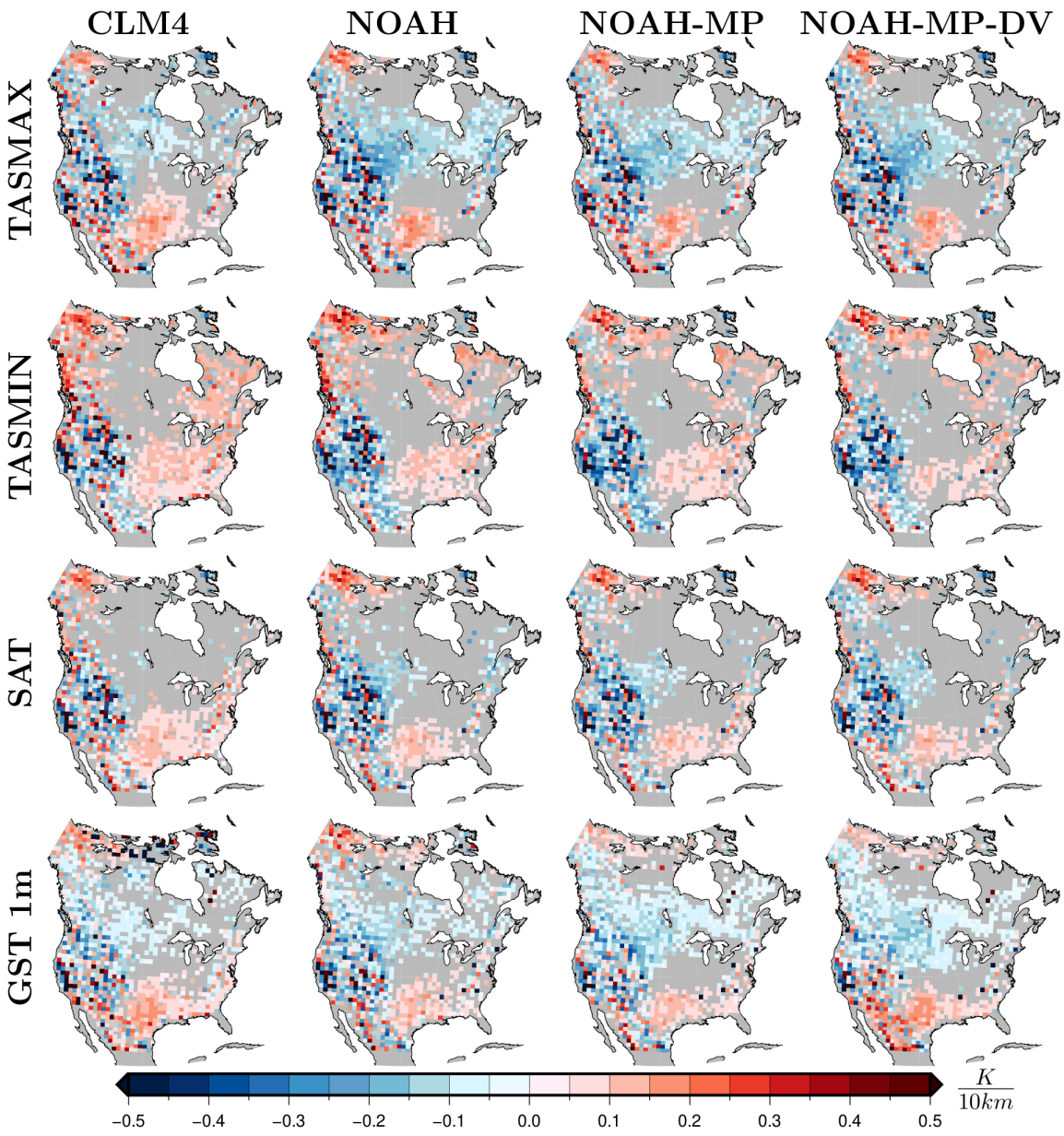

Figure C.6: Annual mean change in near-surface conditions per 10 km reduction in horizontal resolution (coarser resolutions) for each LSM set of simulations for the analysis period 1980-2013. Only grid cells where the response is significant at the 95% level are plotted.

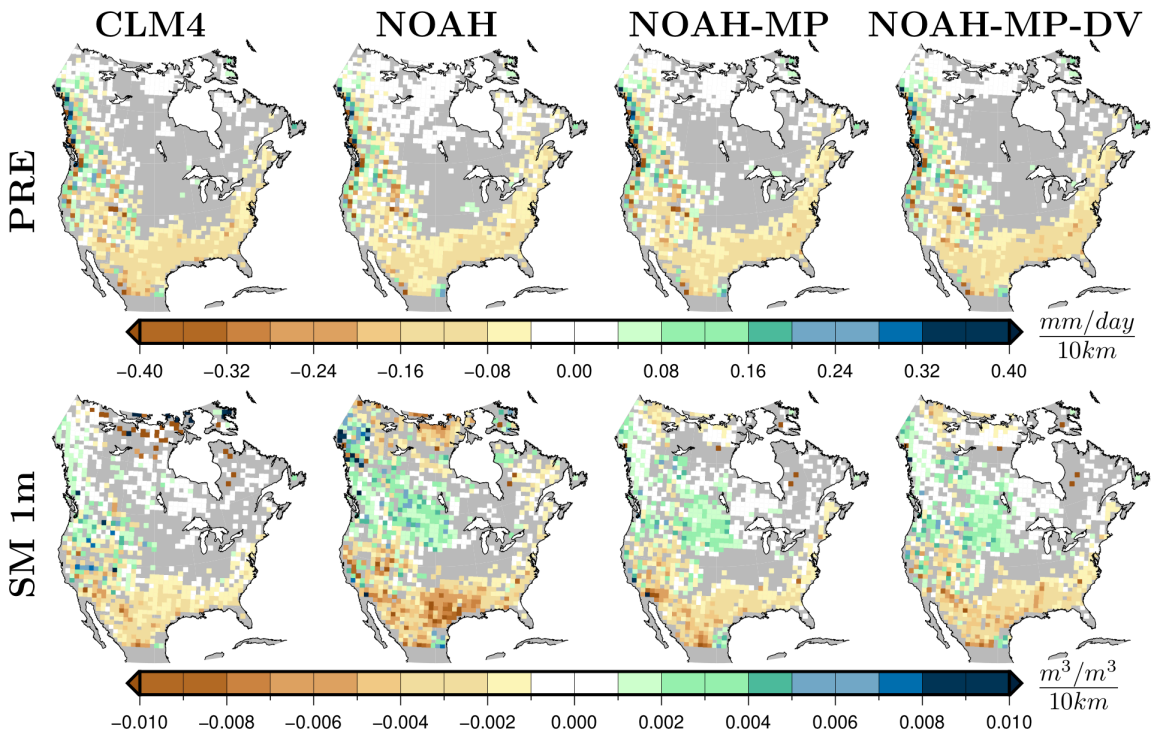

Figure C.7: Annual mean change in accumulated precipitation at the surface and soil moisture per 10 km reduction in horizontal resolution (coarser resolutions) for each LSM set of simulations for the analysis period 1980-2013. Only grid cells where the response is significant at the 95% level are plotted.

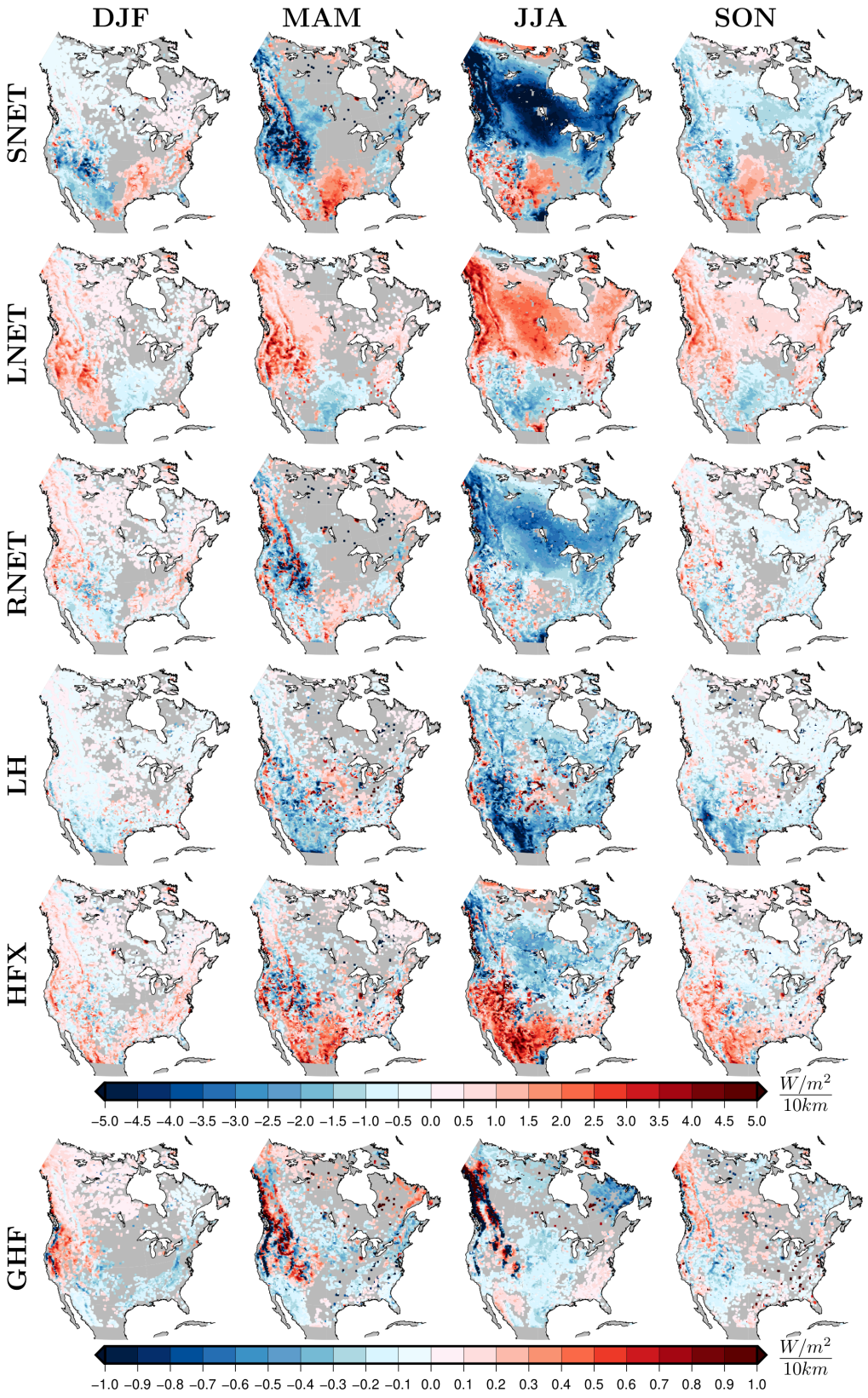

Figure C.8: Seasonal mean change in surface energy fluxes per 10 km reduction in horizontal resolution (coarser resolutions), using the NOAH-MP-DV simulations for the period 1980-2013 previously interpolated to the 25 km grid. Only grid cells where the response is significant at the 95% level are plotted.

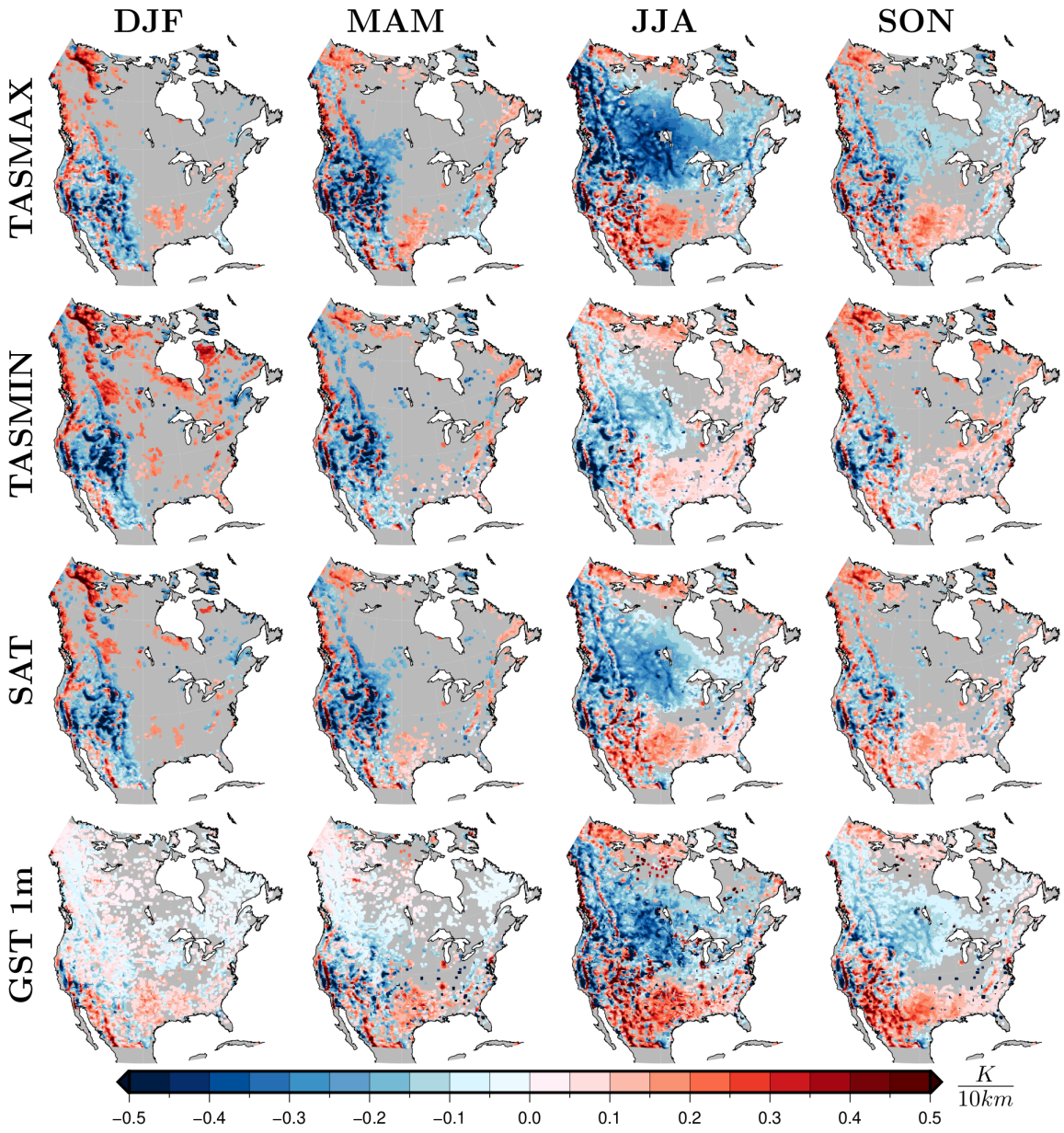

Figure C.9: Seasonal mean change in near-surface temperature conditions per 10 km reduction in horizontal resolution (coarser resolutions), using the NOAH-MP-DV simulations for the period 1980-2013 previously interpolated to the 25 km grid. Only grid cells where the response is significant at the 95% level are plotted.

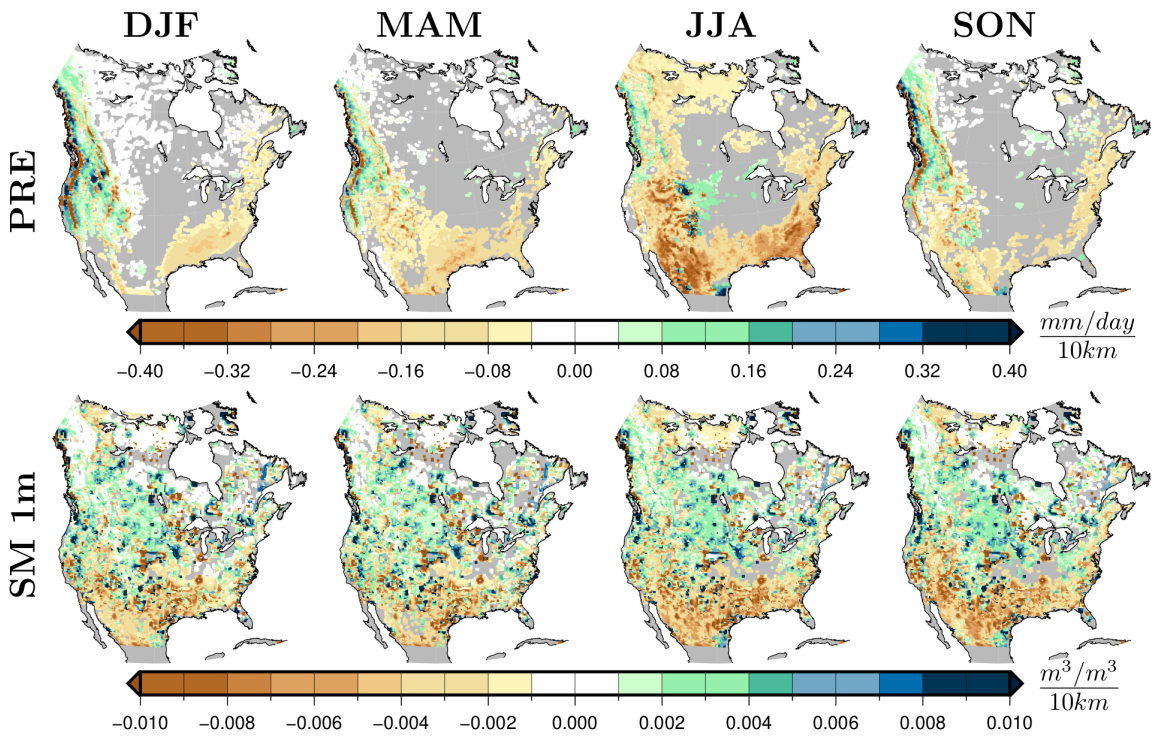

Figure C.10: Seasonal mean change in accumulated precipitation at the surface and soil moisture per 10 km reduction in horizontal resolution (coarser resolutions), using the NOAH-MP-DV simulations for the period 1980-2013 previously interpolated to the 25 km grid. Only grid cells where the response is significant at the 95% level are plotted.

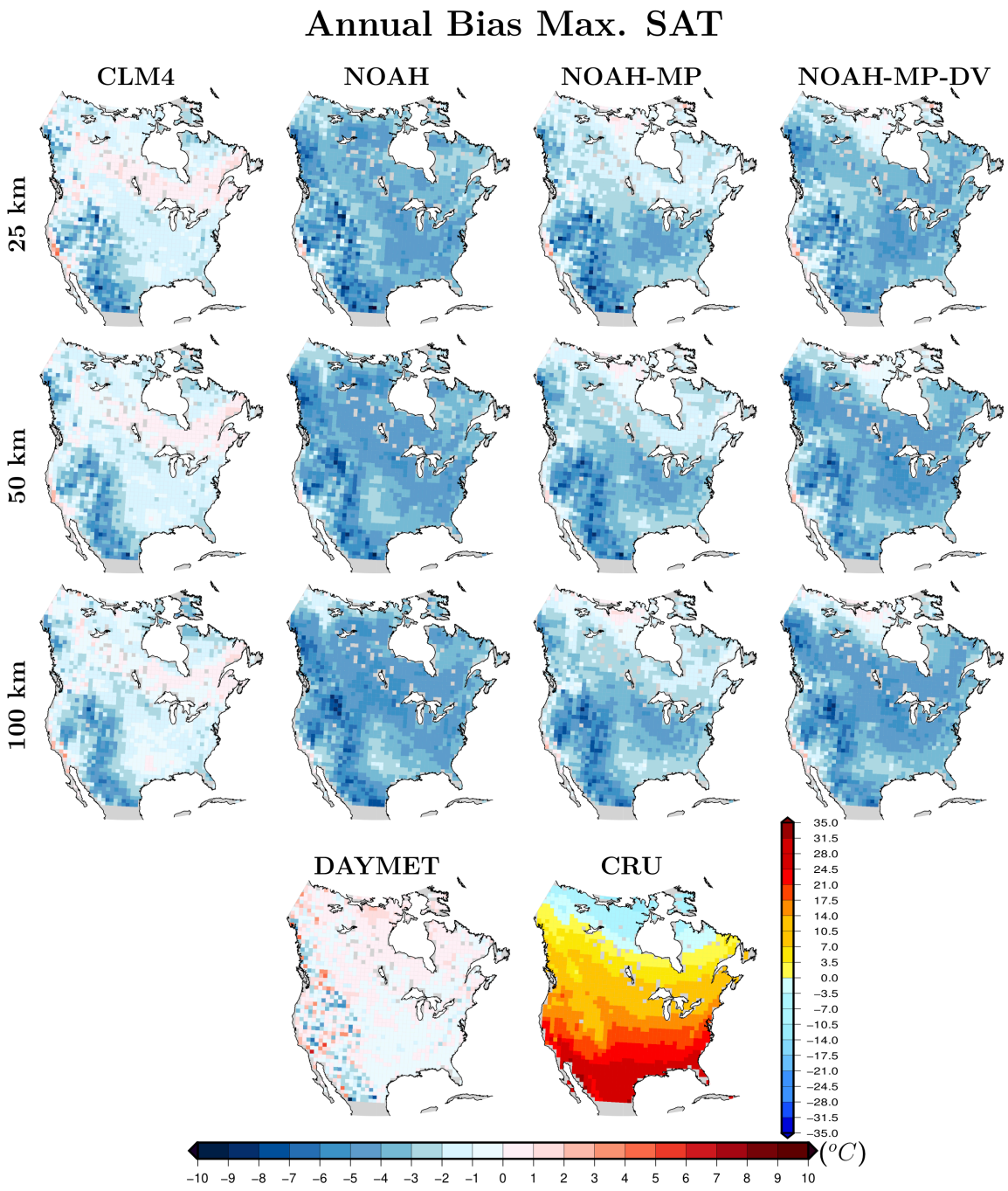

Figure C.11: Annual bias in maximum temperature climatology (^oC) for all experiments and the DAYMET data product relative to the CRU database from 1980 to 2013.

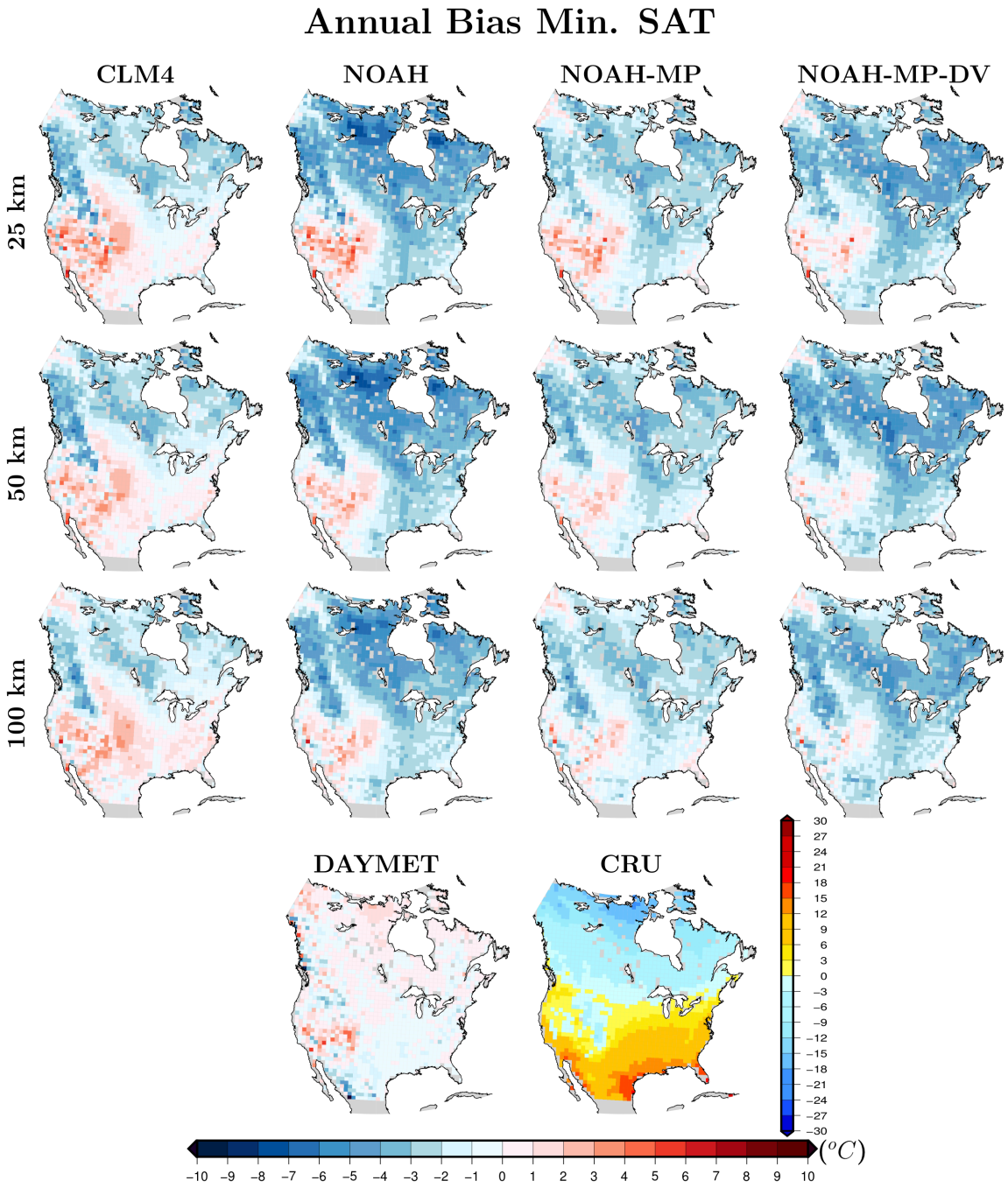

Figure C.12: Annual bias in minimum temperature climatology (^oC) for all experiments and the DAYMET data product relative to the CRU database from 1980 to 2013.

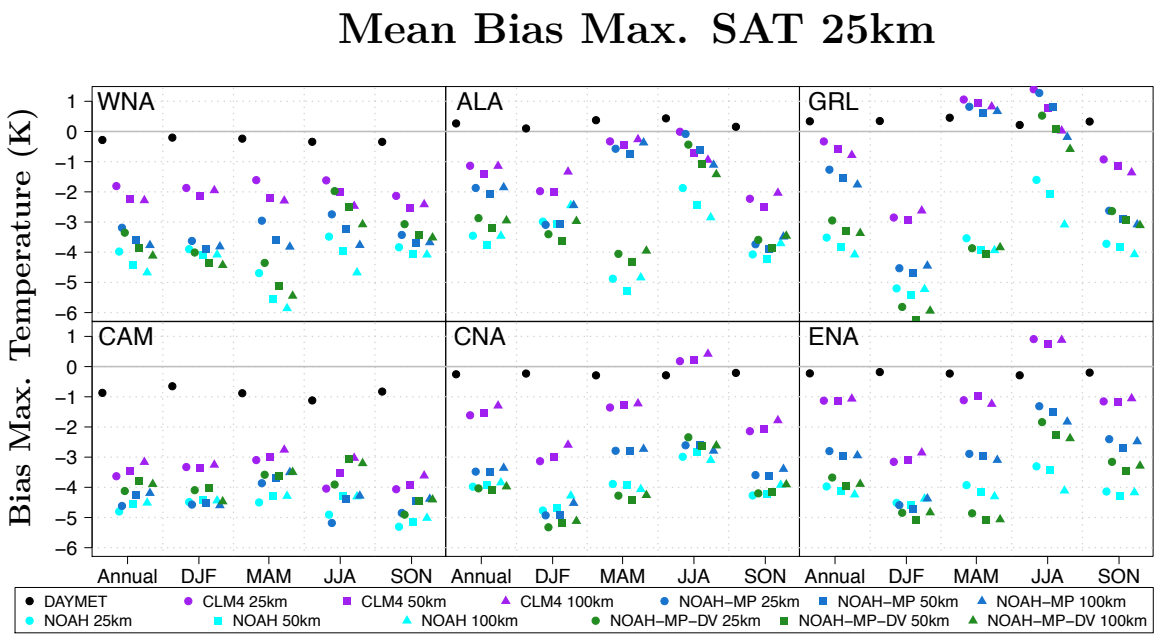

Figure C.13: Mean annual and seasonal bias in maximum temperature climatology (^oC) for all experiments and the DAYMET data product relative to the CRU database from 1980 to 2013. All experiments and databases are interpolated to a 25 km grid before any calculation. Biases are estimated over six subregions (Figure 4.2) adapted from Giorgi et al., 2000: Central America, CAM; Western North America, WNA; Central North America, CNA; Eastern North America, ENA; Alaska, ALA; and Greenland, GRL.

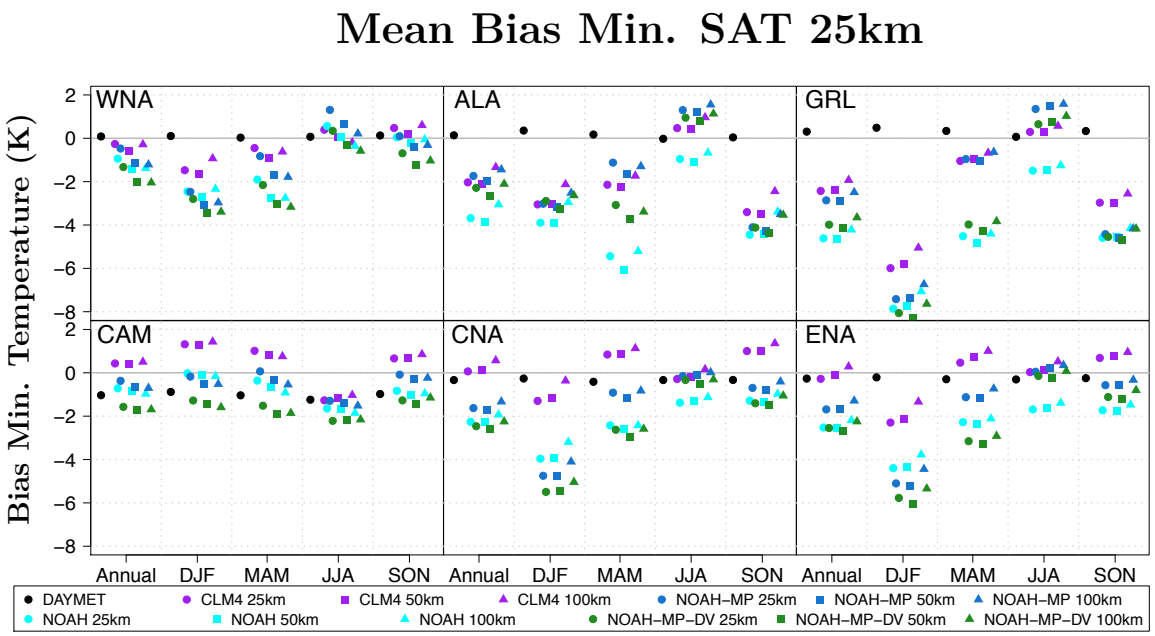

Figure C.14: Mean annual and seasonal bias in minimum temperature climatology (^oC) for all experiments and the DAYMET data product relative to the CRU database from 1980 to 2013. All experiments and databases are interpolated to a 25 km grid before any calculation. Biases are estimated over six subregions (Figure 4.2) adapted from Giorgi et al., 2000: Central America, CAM; Western North America, WNA; Central North America, CNA; Eastern North America, ENA; Alaska, ALA; and Greenland, GRL.

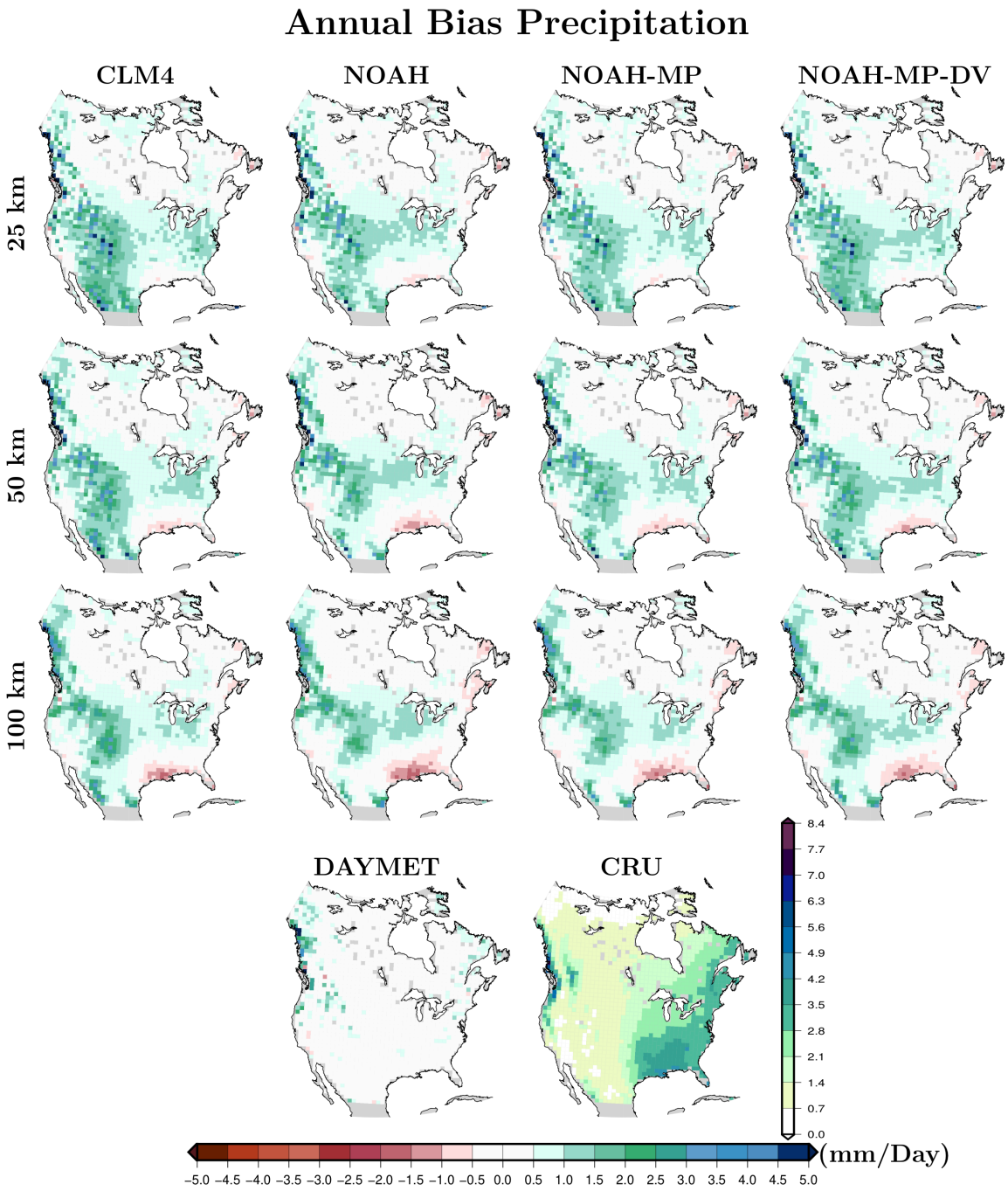

Figure C.15: Annual bias in precipitation climatology (mm/Day) for all experiments and the DAYMET data product relative to the CRU database from 1980 to 2013.

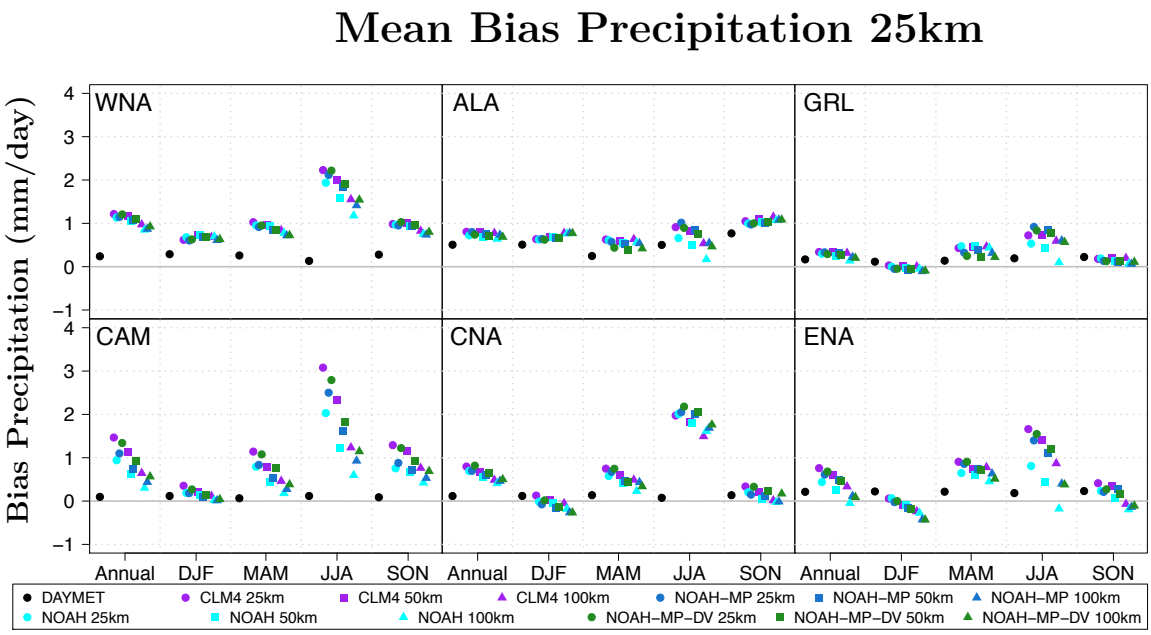

Figure C.16: Mean annual and seasonal bias in precipitation climatology (mm/day) for all experiments and the DAYMET data product relative to the CRU database from 1980 to 2013. All experiments and databases are interpolated to a 25 km grid before any calculation. Biases are estimated over six subregions (Figure 4.2) adapted from Giorgi et al., 2000: Central America, CAM; Western North America, WNA; Central North America, CNA; Eastern North America, ENA; Alaska, ALA; and Greenland, GRL.

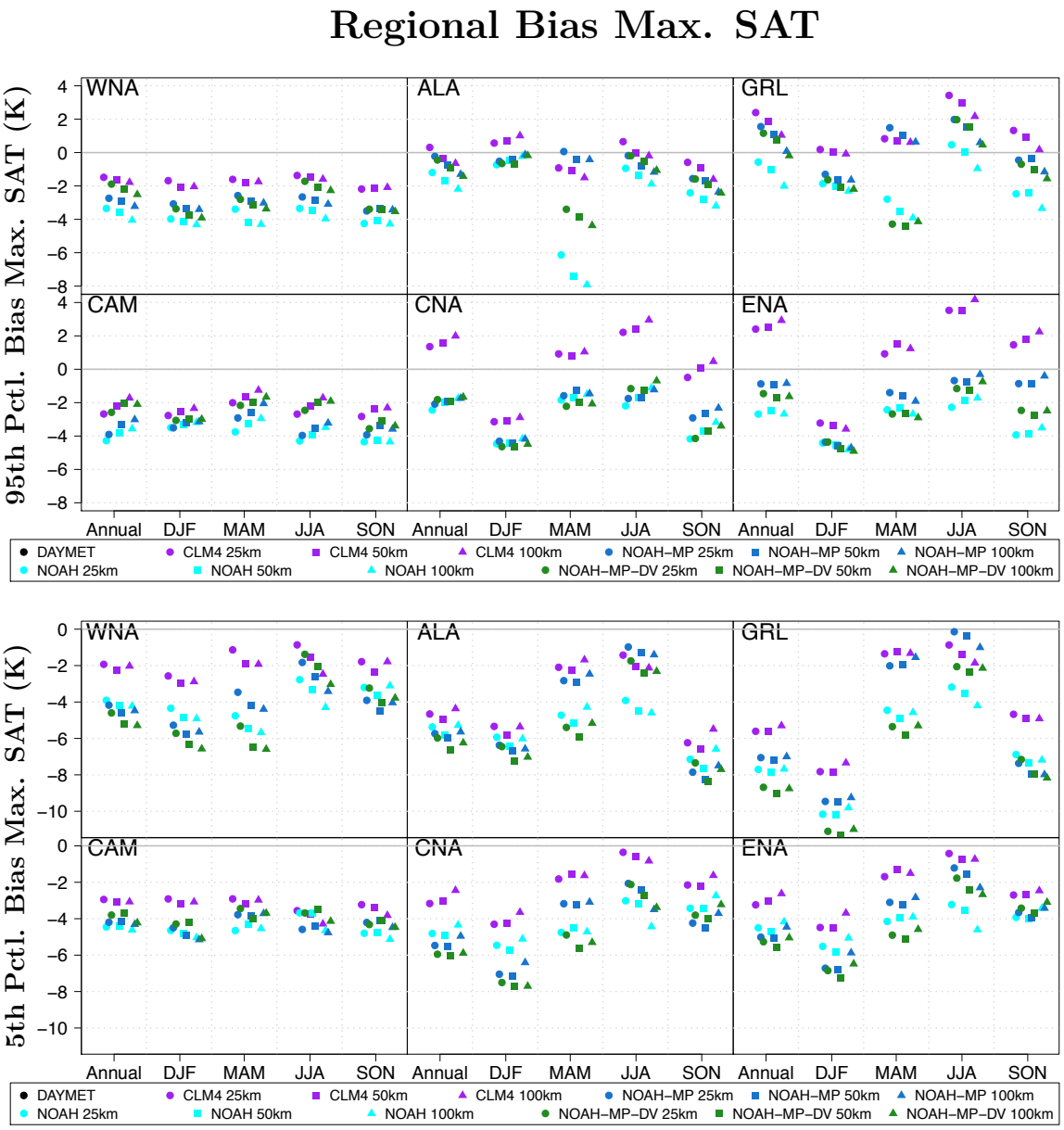

Figure C.17: Mean annual and seasonal bias in the 95th (top panels) and 5th (bottom panels) percentile of daily maximum temperatures (^oC) for all experiments and the DAYMET data product relative to the DAYMET database from 1980 to 2013. All experiments and databases are interpolated to a 100 km grid before any calculation. Biases are estimated over six subregions (Figure 4.2) adapted from Giorgi et al., 2000: Central America, CAM; Western North America, WNA; Central North America, CNA; Eastern North America, ENA; Alaska, ALA; and Greenland, GRL.

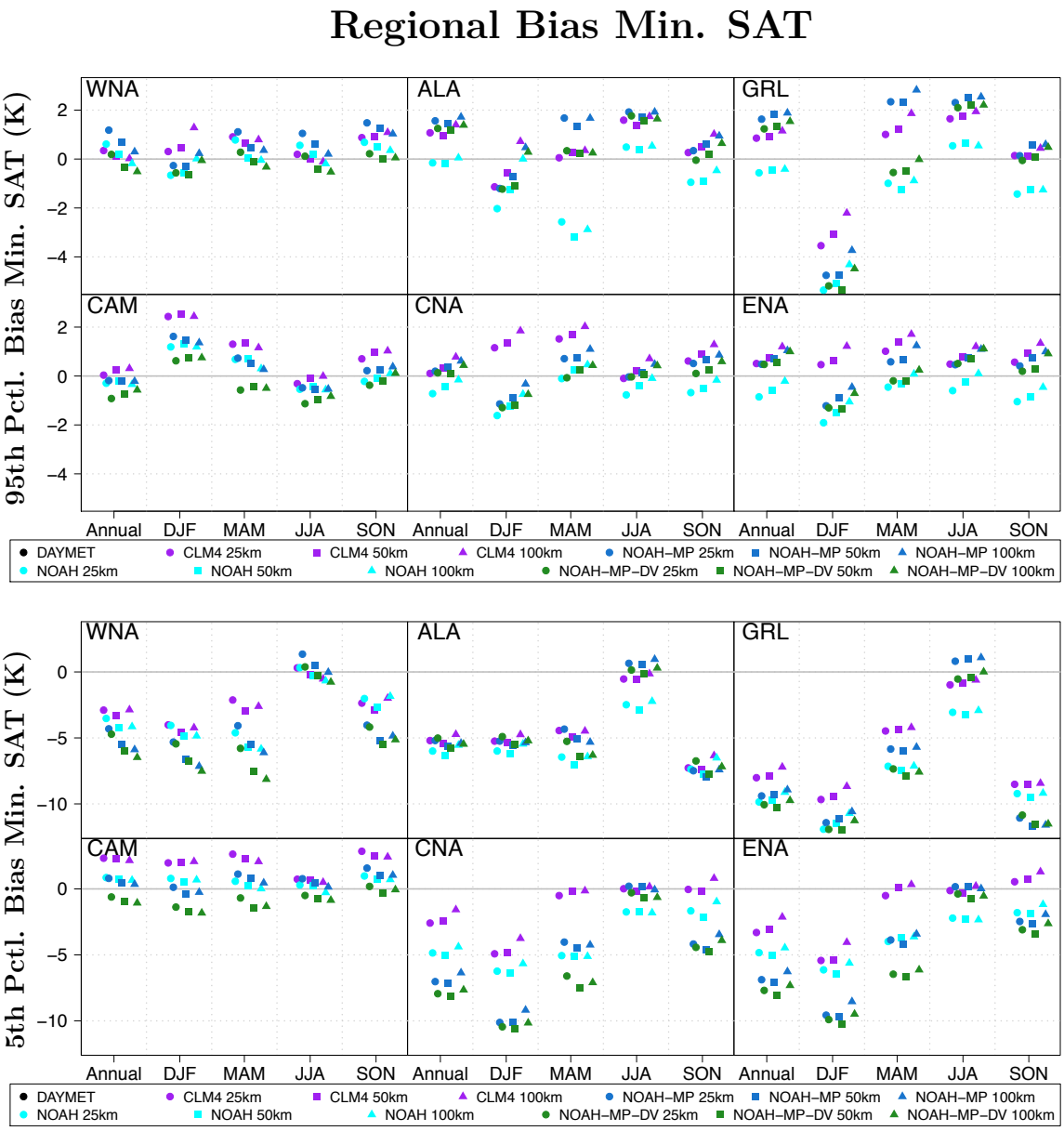

Figure C.18: Mean annual and seasonal bias in the 95th (top panels) and 5th (bottom panels) percentile of minimum daily temperatures (^oC) for all experiments and the DAYMET data product relative to the DAYMET database from 1980 to 2013. All experiments and databases are interpolated to a 100 km grid before any calculation. Biases are estimated over six subregions (Figure 4.2) adapted from Giorgi et al., 2000: Central America, CAM; Western North America, WNA; Central North America, CNA; Eastern North America, ENA; Alaska, ALA; and Greenland, GRL.

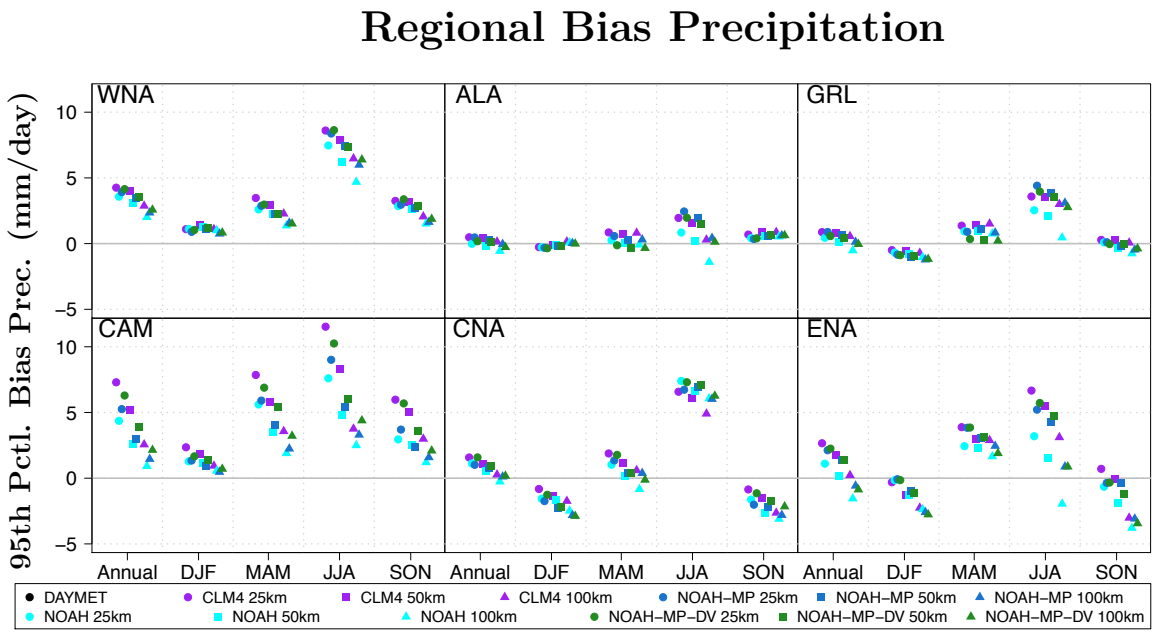

Figure C.19: Mean annual and seasonal bias in the 95th percentile of daily accumulated precipitation (mm/day) for all experiments and the DAYMET data product relative to the DAYMET database from 1980 to 2013. All experiments and databases are interpolated to a 100 km grid before any calculation. Biases are estimated over six subregions (Figure 4.2) adapted from Giorgi et al., 2000: Central America, CAM; Western North America, WNA; Central North America, CNA; Eastern North America, ENA; Alaska, ALA; and Greenland, GRL.

Bibliography

Giorgi, F. and Francisco, R. (2000). Uncertainties in regional climate change prediction: a regional analysis of ensemble simulations with the HADCM2 coupled AOGCM. *Climate Dynamics* **16**(2), 169–182.